Karlsruher Institut für Technologie

ETP-KA/2025-01

System and Integration Tests with 2S Module Prototypes for the Phase-2 Upgrade of the CMS Outer Tracker

Lea Stockmeier

Zur Erlangung des akademischen Grades eines
DOKTORS DER NATURWISSENSCHAFTEN (Dr. rer. nat.)
von der KIT-Fakultät für Physik des
Karlsruher Instituts für Technologie (KIT)

angenommene

Dissertation

von

M.Sc. Lea Stockmeier
aus Heidelberg

Tag der mündlichen Prüfung: 09.05.2025

Referent: Prof. Dr. Ulrich Husemann Institut für Experimentelle Teilchenphysik
Korreferent: Prof. Dr. Thomas Müller Institut für Experimentelle Teilchenphysik

Lea Stockmeier:
System and Integration Tests with 2S Module Prototypes for the Phase-2 Upgrade of the CMS Outer Tracker
March 2025

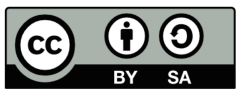

To Britta Wecker-Carsten

Contents

Part I.

Introduction and Basics

1 Introduction

The *Large Hadron Collider* (LHC) is currently the largest particle accelerator in the world. It is located near Geneva and operated by the *European Organization for Nuclear Research* (CERN[1]). ATLAS and CMS are two multi purpose particle detectors located at the LHC. With them, the last missing particle of the *standard model of particle physics* – the Higgs boson – was discovered in 2012 [ATL12; CMS12b]. To increase the physics potential at the LHC, it will be upgraded to the *High Luminosity LHC* (HL-LHC) with first beams expected in 2030. As the name of the upgrade suggests, the instantaneous luminosity of the HL-LHC will be increased by a factor of 3.5 compared to the luminosity of the LHC. The particle collision rate is proportional to the luminosity.

The *Compact Muon Solenoid* (CMS) experiment is one of the four main experiments at the LHC. As assumable by the name, a solenoid providing a magnetic field of 3.8 T is part of CMS. For the operation of the CMS detector at the HL-LHC CMS will be upgraded as well to maintain the current performance. This upgrade of the CMS experiment for the data taking during HL-LHC operation is called the *Phase-2 Upgrade*. As part of the Phase-2 Upgrade, the CMS silicon tracker will be fully replaced. The HL-LHC and the CMS Phase-2 experiment are described in more detail in chapter 2.

The outermost part of the new tracker is called *CMS Phase-2 Outer Tracker*. It will be built of p_{T}-modules that will enable the contribution of transverse momentum information to the *Level-1 Trigger system* of CMS. These modules are built with two back to back oriented silicon sensors at close distance of few millimeters. The signals of both silicon sensors are read out with the same readout chips. The magnetic field inside the CMS experiment bends the trajectories of charged particles. Particles with high transverse momentum p_{T} will curve less in the magnetic field and therefore cross both sensors at nearly the same position. By combining the hit information of both sensors on the readout chip level, the information of close hits in both sensors, called *stub*, can be used to discriminate particles with high p_{T}. The stub information is used in the Track Finder of the Level-1 Trigger system, but the full hit information is read out when receiving an L1 trigger signal. In the inner part of the Outer Tracker, *PS modules* with one macro-pixel and one strip sensor will be mounted while in the outer part *2S modules* with two strip sensors will be used. A detailed description of the CMS Phase-2 Outer Tracker Upgrade can be found in chapter 3.

The *Institute of Experimental Particle Physics* (ETP) at the *Karlsruhe Institute of Technology* (KIT) is one of eight 2S module *assembly centers*. The Outer Tracker module production started in late 2024, but full-size prototype versions were built already since 2016 to test all components before the start of the mass production. Within this thesis, the two latest 2S prototype module versions were investigated. They are the first modules with the final outer dimensions and optical readout and were available since the beginning of this thesis in 2021. Also, during the time of this thesis, the Outer Tracker Phase-2 Upgrade Project was moving from the R&D to the production phase. Thus, the number of 2S prototype modules available within the CMS Tracker community increased. The increased number of modules and the

[1] **C**onseil **e**uropéen pour la **r**echerche **n**ucléaire

close to final design made it possible to mount 2S modules on final subdetector structures to perform functional tests in such larger systems. These tests are called *integration tests*. Within this thesis, measurements in the laboratory, at a test beam facility and integration tests were performed with 2S module prototypes. The 2S module is introduced in detail in section 3.3.

Measurements in the laboratory are discussed in chapter 4. They focus mainly on noise measurements and explain module specialities during the prototyping phase that are needed to understand the subsequent test results. Also, software and firmware developments are explained in section 4.2.

To probe the full readout chain of the 2S modules starting at the charge generation by crossing particles in silicon, the particle detection with 2S modules was tested in a muon hodoscope and at the test beam facility of *Deutsches Elektronen-Synchrotron* (DESY) in Hamburg. By stacking the modules on top of each other in a laboratory setup and placing one scintillator below and one above the modules for triggering on crossing particles, the angular distribution of cosmic muons can be reconstructed. This is presented in section 5.1. More detailed stub and hit efficiency studies can be performed when mounting the 2S modules in between an upstream and a downstream telescope arrangement at a beam line. With the pixelated telescope planes, the expected position of hits on the 2S modules can be reconstructed and compared to the hit and stub information in the 2S modules. By rotating the modules with respect to the beam, bent particle trajectories can be emulated. Beam tests at DESY were already performed with earlier 2S module prototypes but here, the results with the latest ones are presented in section 5.2.

Within this thesis, several integration tests were performed. Depending on the purpose of the test, it can focus on electrical, mechanical and thermal aspects. After the assembly of the modules, they will be shipped to *integration centers* where the modules will be mounted on subdetector structures. The integration tests of this thesis were performed in collaboration with the integration centers *Hubert Curien pluridisciplinary Institute* (IPHC[2]) in Strasbourg and DESY in Hamburg. Two integration tests focused on the thermal performance of the *ladders* on which the 2S modules will be mounted in the barrel region of the Outer Tracker. For these tests, a 2S module with irradiated sensors was used. The cooling performance with a radiation damage level as expected at the end of the HL-LHC operation was measured. The tests and results are presented in section 6.1. Also, for the first time a ladder got fully equipped with twelve 2S modules that were read out synchronously. The measurements performed during this test targeted the electrical performance of the modules at such close distances. The setup and results are introduced in section 6.2. A first integration test with PS and 2S modules on a *dee*, which is a substructure of the endcap region of the Outer Tracker, was performed. The corresponding results are explained in section 6.3.

[2]**I**nstitut **p**luridisciplinaire **H**ubert **C**urien

2

The High-Luminosity Large Hadron Collider (HL-LHC) and the Phase-2 Upgrade of the Compact Muon Solenoid (CMS) Experiment

The *Large Hadron Collider* (LHC) at *CERN* is currently the largest and most powerful particle accelerator. It is located in a tunnel with a circumference of 27 km near the French-Swiss border and Geneva. Four experiments observe particle collisions at the interaction points of the LHC, namely *A Large Ion Collider Experiment* (ALICE), *A Toroidal LHC ApparatuS* (ATLAS), *Compact Muon Solenoid* (CMS) and *Large Hadron Collider beauty* (LHCb). As general purpose experiments, ATLAS and CMS discovered the Higgs boson in 2012 [ATL12; CMS12b]. The Higgs boson was the last missing particle of the Standard Model of Particle Physics.

To fully exploit the physics potential of proton interactions at LHC energies, the accelerator will be upgraded until 2029 to the *High-Luminosity Large Hadron Collider* (HL-LHC). Rare phenomena like double Higgs couplings and further Higgs studies as well as physics beyond the Standard Model like large extra dimensions can be searched for with the HL-LHC. Being sensitive to rare processes requires that the LHC must produce many more collisions. This can be done by squeezing more protons into both beam to allow for more collisions per bunch crossing. In order to cope with the new challenges of the increased number of collisions within the same bunch crossing (also called *pileup*) the detectors at the LHC have to get upgraded as well when starting with the HL-LHC operation.

The HL-LHC upgrade is further described in section 2.1 while section 2.2 describes the upgrade of the CMS experiment.

2.1. The HL-LHC

To achieve the 14 TeV center-of-mass-energy of the colliding protons at the LHC, the injected particles have to pass an accelerator chain depicted in figure 2.1. Starting with negative hydrogen ions (H^-) which get accelerated by the *Linear accelerator 4* (Linac4) to 160 MeV they get injected into the *Proton Synchrotron Booster* (BOOSTER). During that injection the hydrogen ions are stripped of their two electrons leaving protons in the BOOSTER. When they are at 2 GeV they get transferred into the *Proton Synchrotron* (PS). After being accelerated to 26 GeV they are injected to the *Super Proton Synchrotron* (SPS) in which they reach 450 GeV, ready to enter the LHC. The injector chain was already upgraded in the second long shutdown of the CERN accelerator complex from 2018 to 2021 to provide reliable pre-acceleration for the HL-LHC.

The performance of a particle collider can be described by its center-of-mass energy and the luminosity $\mathcal{L}$, which is defined as

$$\frac{\mathrm{d}N_i}{\mathrm{d}t} = \mathcal{L} \cdot \sigma_i \,, \tag{2.1}$$

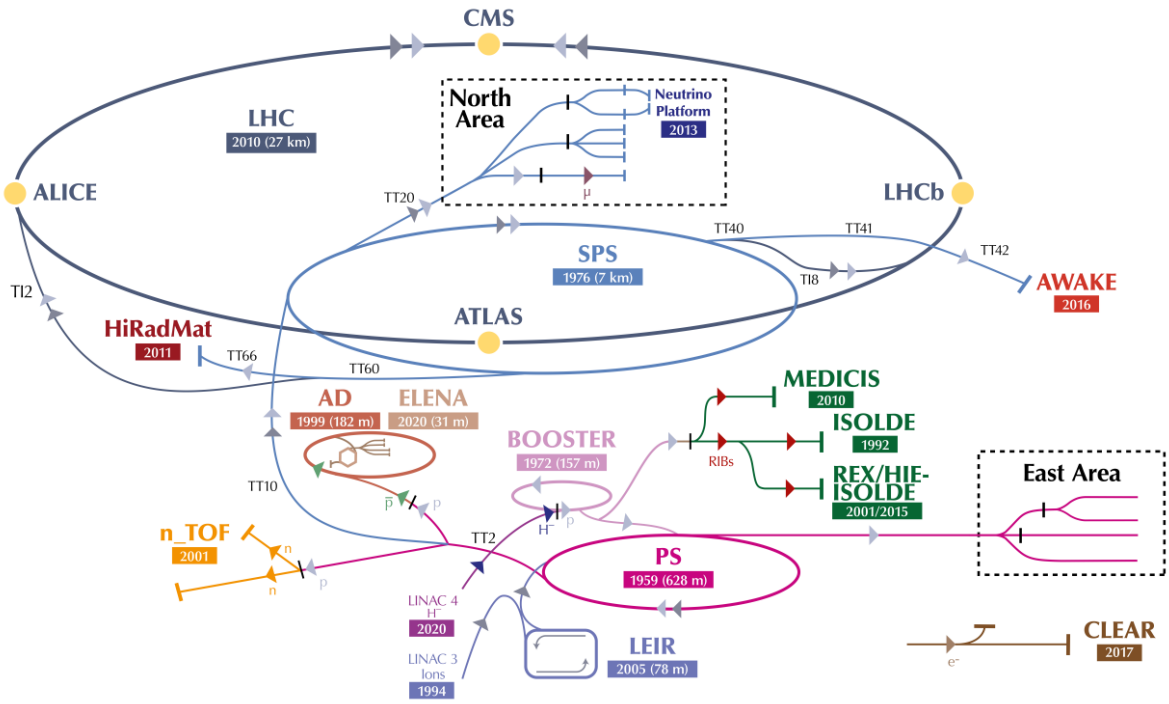

Figure 2.1.: The CERN accelerator complex. Before entering the LHC, negative hydrogen ions (H^-) pass the Linac4 from which they get injected to the BOOSTER. During this injection they get stripped of their electrons, which leaves bare protons to be further passed the PS and SPS before they get injected to the LHC. Adapted from [Lop22].

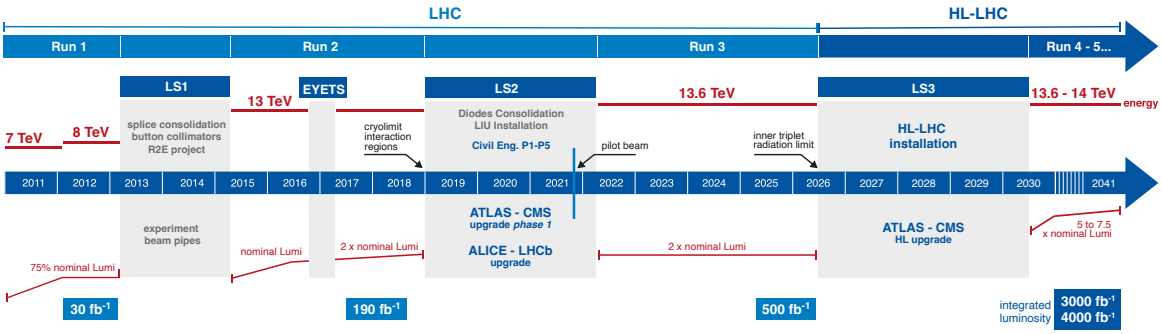

Figure 2.2.: Schedule of the LHC and HL-LHC program. The program is split into runs and shutdown periods. During runs the experiments are taking data while the long shutdowns (LS) are there for maintenance and upgrade work. The center-of-mass energy, luminosity and integrated luminosity is depicted in the schedule. Adapted from [CER25].

where σ_i denotes the cross section of the process i and $\frac{\mathrm{d}N_i}{\mathrm{d}t}$ is the number of events per second produced through that very process. With the equation

$$\mathcal{L} = \frac{n_1 n_2 f N_\mathrm{b}}{A} \tag{2.2}$$

the luminosity $\mathcal{L}$ of two colliding beams can be described. The number of particles per bunch is indicated by n_i ($i \in \{1, 2\}$), N_b denotes the number of colliding bunches and f is the revolution frequency. The overlapping cross section of the beam profiles is indicated with an A. [HM06]

The integrated luminosity $\mathcal{L}_\mathrm{int}$ is used to calculate the number of observable events N_i of a process i with a cross section σ_i during a measurement time T according to

$$N_i = \sigma_i \cdot \int_0^T \mathcal{L}(t)\,\mathrm{d}t = \sigma_i \cdot \mathcal{L}_\mathrm{int}\,. \tag{2.3}$$

In order to increase the statistics for rare processes, according to equation (2.3) either the cross section σ_i or the integrated luminosity $\mathcal{L}_\mathrm{int}$ must be increased. The cross section could be increased by increasing the center-of-mass energy. The integrated luminosity can be increased by either increasing the measurement time or increasing the luminosity given in equation (2.2). Since the center-of-mass energy is at the LHC already at the maximum of 7 TeV per colliding beam with a bending power of 8.33 T per dipole magnet [Ros03], the increase of the luminosity has to be addressed within the upgrade of the LHC to the HL-LHC. As visible in the timeline of the LHC and HL-LHC project in figure 2.2, the operation of the HL-LHC will start in 2030. The project is split in runs and shutdown periods. From the beginning of the LHC data taking in 2011 until the *long shutdown 2* (LS2) in 2019, an integrated luminosity of 190 fb^{-1} was achieved. Another 310 fb^{-1} are expected to be collected until the end of run 3 in mid 2026. Thus, the total integrated luminosity of the LHC will be 500 fb^{-1}. The nominal luminosity of the LHC is $1 \times 10^{34}\,\mathrm{cm}^{-2}\mathrm{s}^{-1}$, but it is operated at luminosities up to $2 \times 10^{34}\,\mathrm{cm}^{-2}\mathrm{s}^{-1}$. The nominal luminosity of the HL-LHC will be increased by a factor of five compared to the nominal LHC luminosity. Thus, an integrated luminosity of 3000 fb^{-1} can be achieved within ten years. Nevertheless, the HL-LHC is designed to handle luminosities up to $7.5 \times 10^{34}\,\mathrm{cm}^{-2}\mathrm{s}^{-1}$ in the *ultimate scenario*. This would lead to an integrated luminosity of 4000 fb^{-1} within the runtime of the HL-LHC. The majority of the upgrades of ATLAS and CMS will happen in LS3 starting mid of 2026 and last until beginning of 2030.

The higher luminosity at the HL-LHC will lead to increased radiation damage at the accelerator components and detectors. Quadrupole and higher order magnets are more likely to fail at higher luminosities. Thus, further collimators will be added, and existing collimators will be replaced by collimators with increased performance. Twelve more powerful quadrupole magnets will be installed at the ATLAS and CMS experiments to provide better final focusing of the beams before the collisions. Crab cavities will be installed next to the interaction points of ATLAS and CMS to tilt the beam before the collision. Thus, the luminosity is increased according to equation (2.2) due to a reduced beam cross section A. More detailed information about the HL-LHC upgrade can be found in the Technical Design Report (TDR) [Apo+17].

2.2. The Phase-2 Upgrade of the CMS Experiment

The CMS experiment is one of the four main experiments at the LHC. It is a multipurpose detector with different subdetector systems arranged cylindrically around the interaction point, as shown in figure 2.3. From inside out these are the silicon tracker, the electromagnetic calorimeter (ECAL), the hadron calorimeter (HCAL) and the muon chambers. A superconducting solenoid is located in between the HCAL and the muon chambers. Muon chambers are embedded in steel return yokes. For energy measurements at high pseudorapidity $|\eta|$[1] regions, a forward calorimeter is present as well.

The superconducting solenoid magnet can provide a central magnetic flux density of up to 4 T, but it is operated at 3.8 T to ensure longevity. The magnet has a diameter of 6 m and a length of 12.5 m. The presence of a magnetic field inside the detector allows determining the charge-to-mass ratio of charged particle. The tracks of charged particles are bent in the magnetic field. The lower the bent of the trajectory is, the higher is the transverse momentum of the particle. This allows for measuring the transverse momentum of charged particles within CMS by tracking their paths through the entire detector. CMS aimed for a high magnetic field strength to also provide accurate momentum measurements of highly-energetic particles that are the most interesting for the physics processes investigated with CMS. [Her00]

To cope with the increased pileup of 140 to 200 and harsher radiation environment during the HL-LHC operation, the CMS experiment has to be upgraded. Depending on the subdetector either the complete subdetector will be replaced or the existing one will be improved. This upgrade is called *Phase-2 Upgrade* and will be performed during LS3 from 2026 to 2029. The current and future subdetector systems of CMS are described briefly from inside out in the following subsections. More detailed information about the Phase-2 Upgrade of the CMS experiment can be found in the TDR [Bal24].

2.2.1. Tracker

The current silicon tracker with pixelated sensors in the inner region and microstrip sensors in the outer region will be fully replaced by a new silicon tracker that is depicted in figure 2.4. The *Inner Tracker* (IT) will consist of three parts with high granularity silicon pixel modules: The *Tracker Barrel Pixel Detector* (TBPX), the *Tracker Forward Pixel Detector* (TFPX) and the *Tracker Endcap Pixel Detector* (TEPX). New 3D sensors will replace the innermost layers of the inner tracker (depicted in black in figure 2.4) allowing for significant increases in radiation hardness and n-in-p type pixelated silicon sensors (indicated in green and orange in figure 2.4) will be mounted in the outer layers of the inner tracker. The readout chips of these new sensors were developed within the RD-53 collaboration [CER20] as a common-project for the Phase-2 pixel detector upgrades of ATLAS and CMS. Being the innermost part of CMS, the radiation

[1] $\eta = -\ln\left[\tan\left(\frac{\theta}{2}\right)\right]$ with the polar angle θ measured from the beam axis to the particle trajectory.

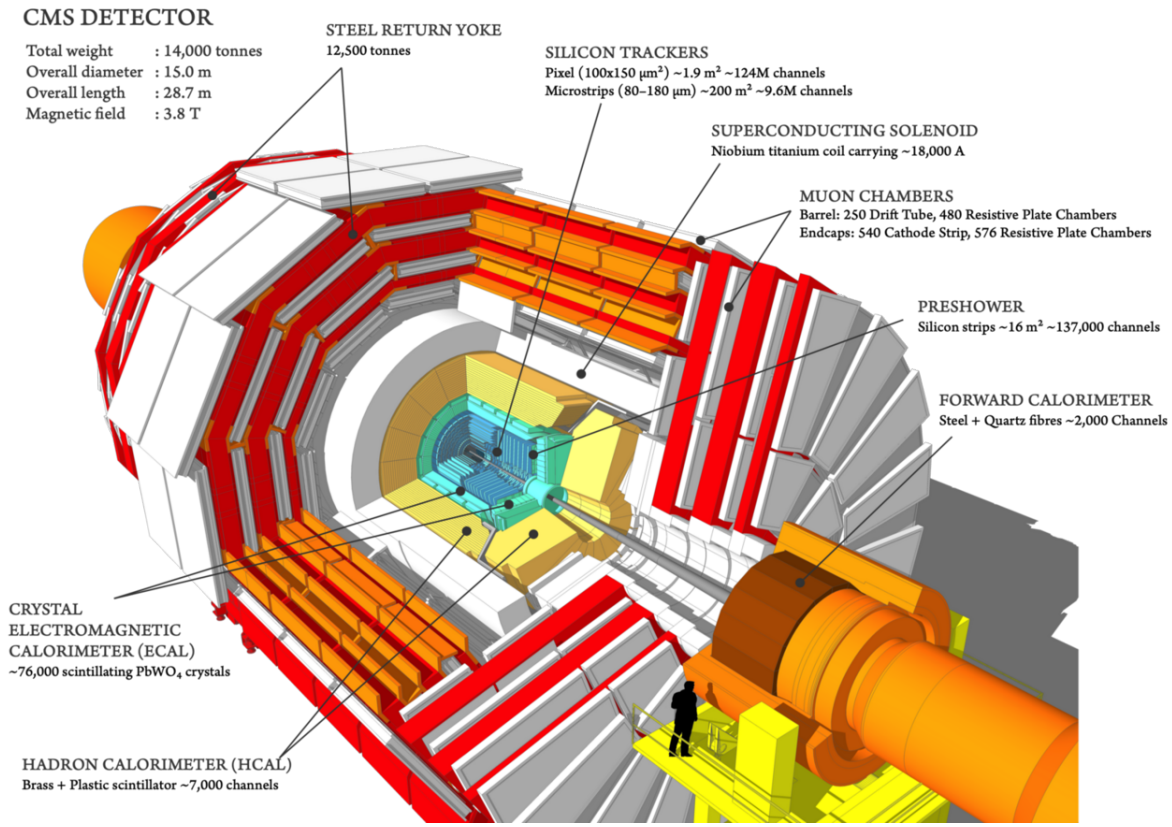

Figure 2.3.: Illustration of the CMS detector. The CMS detector consists of different subdetector systems arranged cylindrically around the interaction point. From inside out these are: silicon tracker, ECAL, HCAL, the superconducting solenoid and muon chambers with steel return yokes. A forward calorimeter is present for energy measurement in the high η regions. Taken from [Sak19].

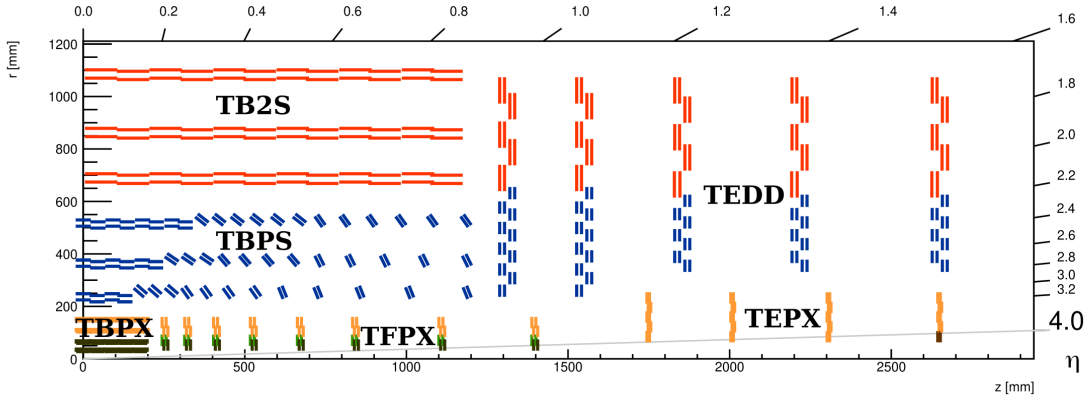

Figure 2.4.: Sketch of a quarter of the CMS Phase-2 Tracker. The Phase-2 Tracker will consist of the Inner Tracker (IT) and the Outer Tracker (OT). The IT consists of three parts: The TBPX, the TFPX and the TEPX. The OT is made of the TBPS, the TB2S and the TEDD. 3D pixel modules are depicted in black, pixel modules using other technologies in green and orange, PS modules in blue and 2S modules in red. The interaction point is at the origin (0/0) of this sketch. Adapted from [tkL23].

environment of the pixel detector is harsher compared to the Outer Tracker. Thus, the Phase-0 pixel detector [CS09] that was installed before the start of the runtime of CMS in 2009, was already replaced once by the Phase-1 pixel detector [Ada+21b; CMS12a] in LS2 from 2019 to 2021. The Phase-2 pixel detector will have about 2000 million channels and pixel sizes of $25 \times 100\,\mu m^2$ and $50 \times 50\,\mu m^2$ [CMS17f]. The *Outer Tracker* (OT) will be made of *PS modules* with one silicon macro-pixel and one strip sensor each and *2S modules* with two strip sensors each. The PS modules with higher granularity are located in the inner part and the 2S modules in the outer part of the OT. The barrel region is split into the *Tracker Barrel with PS modules* (TBPS) and the *Tracker Barrel with 2S modules* (TB2S). The endcap is called *Tracker Endcap Double-Discs* (TEDD). Both, the TB2S and TEDD, are described in more detail in sections 3.2.1 and 3.2.2.

The Phase-2 Tracker will have larger pseudorapidity coverage ($|\eta| < 4$) and a higher granularity than the current tracker. Also, the silicon strip sensors of the Phase-2 Outer Tracker will be n-in-p type in Phase-2 instead of p-in-n type which will prevent type inversion due to radiation damage and increase the signal strength after irradiation [Ada+17]. The planar pixel sensors in the outer regions of the Phase-2 inner tracker will be n-in-p type [Orf20] instead of n-in-n as in the Phase-0 and Phase-1 inner tracker. The heart of the CMS Phase-2 Tracker Upgrade is the track trigger that generates p_T information at the bunch crossing rate as input for the Level-1 trigger of CMS. This allows triggering several subdetector systems at the L1 trigger stage on high p_T particles. The trigger system of CMS and its upgrade is further described in section 2.2.5. The special concept of the Phase-2 Outer Tracker modules described in section 3.1 allows for this new L1 track trigger feature.

2.2.2. Calorimeter

The CMS calorimeter system consists of two main parts, the *electromagnetic calorimeter* (ECAL) and the *hadronic calorimeter* (HCAL). The ECAL has three parts, the barrel (EB) section, two endcaps (EE) and a silicon strip preshower (ES) detector belonging to the endcap sections. The EE and EB are made of about 76 000 lead tungstate ($PbWO_4$) crystals and the scintillation light produced by particle interactions is read out by avalanche photodiodes

(APDs) in the EB and vacuum phototriodes in the EE. The EB covers a pseudorapidity region of $|\eta| < 1.48$ and the EE covers a region up to $|\eta| = 3$. The HCAL for measuring the energy, angle and position of hadronic showers is made of four subsystems: the barrel (HB), the endcap (HE), the outer and the forward (HF) calorimeter. They cover a region up to $|\eta| < 5$ [Bil16]. The calorimeter system of CMS will be upgraded or replaced as described in the following paragraphs.

The front-end electronics of the EB will be replaced as well as the off-detector electronics of the EB and HB. The photodetectors and lead tungstate crystals of the EB as well as the absorber, active material and front-end electronics of the HB will be retained during HL-LHC operation. [CMS17b]

The current EE based on lead tungstate ($PbWO_4$) and the plastic scintillator based HE were designed for an integrated luminosity of $500\,\mathrm{fb}^{-1}$. To withstand the harsher radiation environment of the HL-LHC, both parts and the ES will be replaced by a *high granularity calorimeter* (HGCAL). A sketch of one half of one endcap of the HGCAL can be found in figure 2.5. It will consist of an electromagnetic (CE-E) and hadronic part (CE-H). Silicon sensors are used in the CE-E part and in the inner high radiation regions of the CE-H (depicted in green in figure 2.5). In the outer regions of the CE-H, scintillator tiles equipped with *silicon photomultipliers* (SiPM) are used (depicted in dark blue in figure 2.5). The CE-E uses lead as main absorber material but the copper cooling plate and copper-tungsten baseplates also contribute to the absorption. The CE-H uses steel as absorber material and the copper cooling plate contributes as well. The silicon cells of HGCAL have a cell size of about $0.5\,\mathrm{cm}^2$ to $1\,\mathrm{cm}^2$ and the outer plastic scintillators have a cell size of $4\,\mathrm{cm}^2$ to $30\,\mathrm{cm}^2$. This results in a total of about 6 million silicon channels at $620\,\mathrm{m}^2$ silicon sensors. The scintillators cover an area of $370\,\mathrm{m}^2$. The HGCAL will be operated at $-30\,^\circ\mathrm{C}$, cooled by CO_2, and covers an η region of $1 < |\eta| < 3$. [CMS17c] With these improvements of the calorimeter regarding the larger granularity, it will be possible to measure the development of a particle shower in much higher detail than before. The HGCAL will provide timing information for showers with a resolution of about 20 ps [CMS24b] and will enable tracking of showers while measuring their energy.

The HF will not be upgraded, but it will be continued to be operated at the HL-LHC. [Bil16]

2.2.3. Timing Layer

The about 200 simultaneous pileup interactions per bunch crossing do, due to the longitudinal and transversal extent of the beams, not happen at the exactly same time and z-position. This allows to associate tracks to vertices by combining tracking and time information even though the vertices are very close to each other in space. To do this, a new timing layer which measures with a precision of 30 ps to 40 ps the production time of *minimum ionizing particles* (MIP) will be added to CMS for the Phase-2 operation. It is called *MIP Timing Detector* (MTD) and will disentangle the nearly-simultaneous pileup interactions occurring in each bunch crossing. The MTD will consist of two parts, the *Barrel Timing Layer* (BTL) and the *Endcap Timing Layer* (ETL). Both parts are briefly introduced in the next two paragraphs, but more information can be found in the TDR [CMS19].

The BTL is located between the tracker and the ECAL. It has a total thickness of 4 cm and covers up to $|\eta| = 1.48$. The BTL will be made of Cerium-doped Lutetium Yttrium Orthosilicate crystals (LYSO:Ce) which will be read out by SiPMs.

The ETL will cover a pseudorapidity range of about $1.6 < |\eta| < 3$ and is shown in purple in figure 2.5. It will be mounted at the nose of the CE in a separated thermally isolated volume. The volume will be flushed with cold dry air allowing independent operation of the ETL to the CE. The separate volume also allows for accessing the ETL for maintenance and repair work during the cold operation of the CE detector. The ETL will be operated with *low-gain*

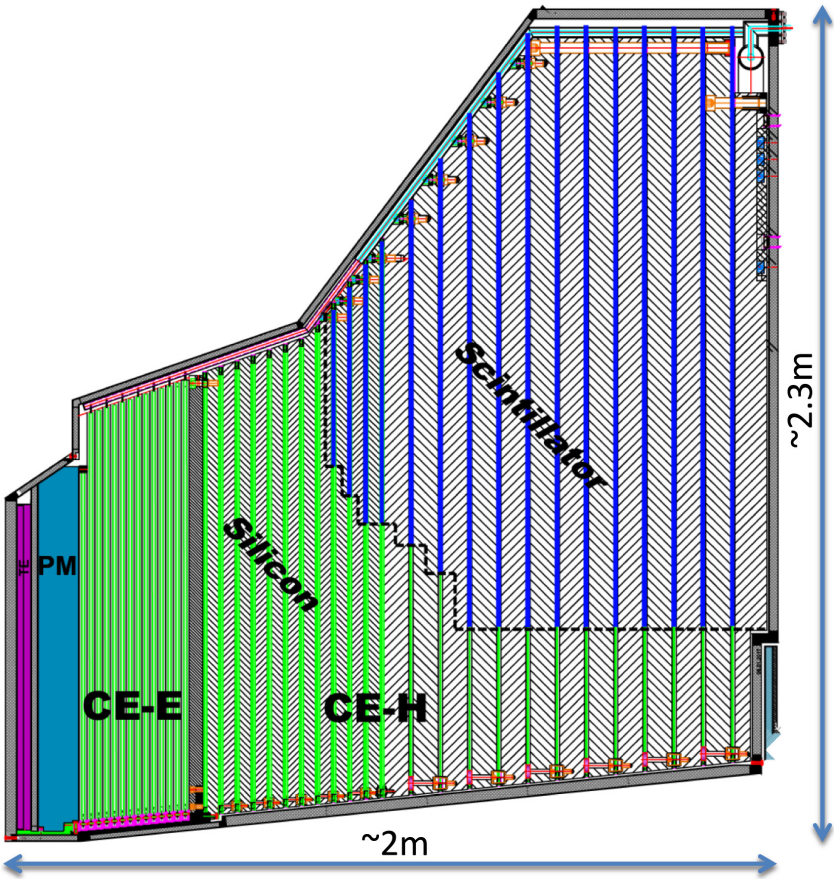

Figure 2.5.: Longitudinal cross section of one half of one endcap of the HGCAL. The two parts of the HGCAL are shown. The electromagnetic parts (CE-E) and the inner region of the hadronic part (CE-H) will consist of silicon (depicted in green) while the outer region of CE-H will be made of scintillators (depicted in dark blue). The Endcap Timing Layer (ETL, in the sketch shown in purple and labeled with TE) is located between the silicon tracker and the HGCAL. It is further described in section 2.2.3. The polyethylene neutron moderator (PM) is shown in light blue. The dimensions of the half of one endcap are indicated in the picture. Taken from [Yoh20] and adapted from [CMS17c].

avalanche diodes (LGADs) read out with a dedicated readout ASIC called ETROC [Tor22]. LGADs are specially doped silicon sensors that have a better temporal resolution due to their small thickness while achieving a high signal to noise ratio.

2.2.4. Muon System

The muon system of CMS provides information for identification, triggering and track reconstruction of muons. A sketch of its components can be found in figure 2.6. It is the outermost detector system of CMS and is made of three gaseous detector technologies: *Drift Tubes* (DTs), *Resistive Plate Chambers* (RPCs) and *Cathode Strip Chambers* (CSCs). DTs and RPCs are used in the barrel region while RPCs and CSCs are used in the endcap region. CSCs cover the inner high $|\eta|$ regions.

During the upgrades of the CMS experiment, *Gas Electron Multiplier* (GEM) detectors are being installed in the forward region of the muon system. The GE1/1 GEM detector (depicted in red in figure 2.6) is needed during HL-LHC operation to contribute to the L1 trigger to reduce the L1 muon trigger rate. The ME0 is another GEM detector (depicted in orange in figure 2.6) that will extend the η-coverage of the muon system up to $|\eta| = 2.8$. The GEM detectors developed for the upgrade are optimized for the occupancy and radiation damage requirements.

RPCs get also upgraded within the Phase-2 Upgrade to maintain the performance of the muon system during the HL-LHC operation. [CMS17e] These *improved RPCs* (iRPCs) are depicted in purple in figure 2.6.

2.2.5. Trigger System

When the LHC is running about one billion proton-proton interactions per second are happening inside the CMS detector. Thus, CMS produces about 40 TB of data per second by its frontend electronics. To reduce the amount of data to a storable amount with just the potentially interesting event candidates, a two stage trigger system is used. The first stage is called *Level-1 Trigger* (L1 Trigger). The L1 Trigger decides on hardware level within 4 µs if a trigger signal is sent to the readout electronics. The data get buffered from each subdetector for this time and the readout rate gets reduced from 40 MHz to 100 kHz. The second stage is a software based trigger system called *High-Level Trigger* (HLT). For each event, objects like electrons, muons and jets are reconstructed, and different selection criteria are applied to select the events of possible interest for data analysis. A readout rate of a few kHz is achieved. [CMS17a]

For the Phase-2 Upgrade of CMS, the L1 Trigger will be upgraded to cope with the increased pileup during the HL-LHC operation. The main enhancement is the inclusion of Outer Tracker data to the L1 Trigger. This will be achieved by including local *transverse momentum* (p_T) measurements performed by the detector front-end electronics. This concept is sufficient for lowering data rates because about 97 % of the particles created in proton-proton collisions have $p_\mathrm{T} < 2\,\mathrm{GeV/c}$ [CMS17d]. The Outer Tracker module concept allowing for the p_T measurement is described in detail in section 3.1. Hits compatible with a transverse momentum above 2 GeV/c are used as input for the L1 track finding algorithm, which will be implemented in *Field Programmable Gate Arrays* (FPGAs). First, track fragments, called *tracklets*, are formed and then combined to track candidates via Kalman filter fitting. [Bro24] Such a track trigger has never been used before and is a novelty in particle physics experiments at hadron colliders. Together with the HGCAL, it is the heart of the CMS Phase-2 Upgrade.

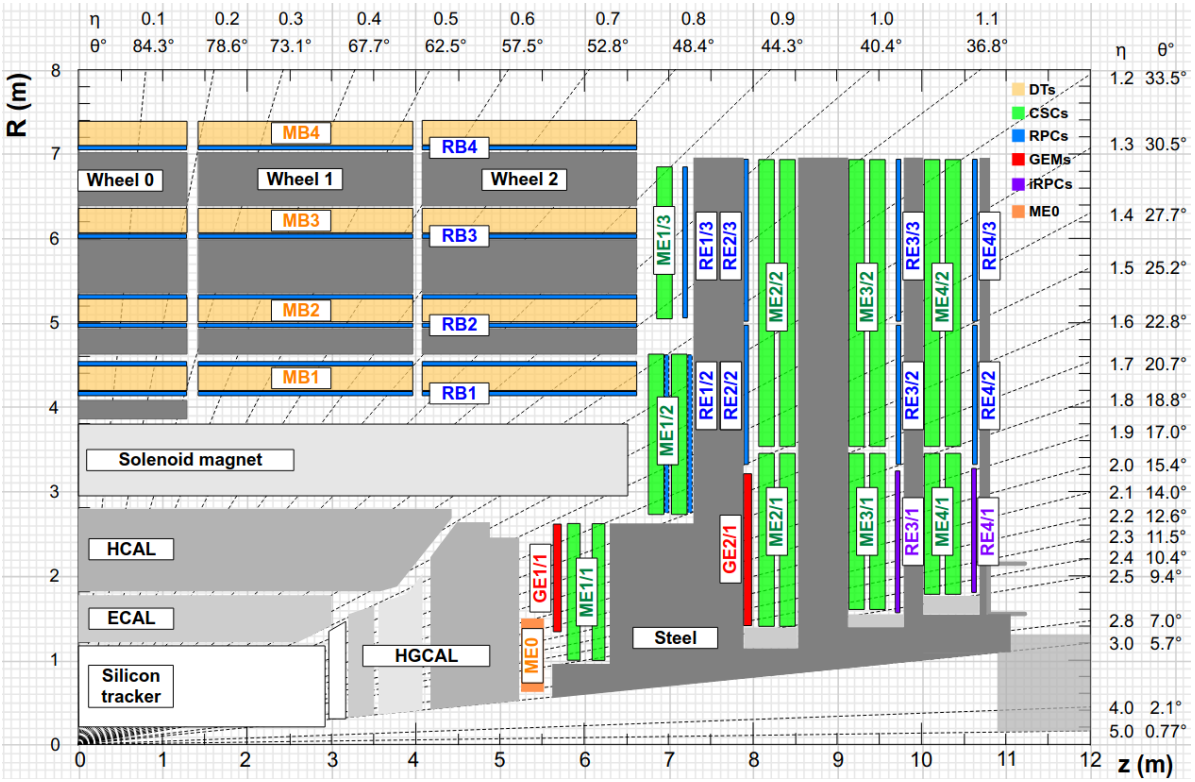

Figure 2.6.: Sketch of a quadrant of the CMS Muon System and its Phase-2 Upgrade. The sketch shows the different parts of the muon system. It consists of four detector types namely Drift Tubes (DTs, yellow), Cathode Strip Chambers (CSCs, green), Resistive Plate Chambers (RPCs, blue and purple) and Gas Electron Multipliers (GEMs, red and orange). The Phase-2 Upgrades include improved RPCs shown in purple (RE3/1 and RE4/1) as well as GEMs shown in red (GE1/1 and GE2/1) and orange (ME0). The magnet return yokes are indicated with the dark gray areas. Taken from [CMS17e].

3
The Phase-2 Upgrade of the CMS Outer Tracker

At the heart of the research conducted in this thesis are the 2S module prototypes developed for the CMS Phase-2 Outer Tracker upgrade. Before a detailed description of the system and integration tests can be provided, an overview of the Phase-2 Outer Tracker upgrade and the 2S modules is needed. This chapter provides exactly that, starting with the general concepts which motivate the module in section 3.1, continuing with the general layout of the Outer Tracker in section 3.2, and then giving a detailed overview of the components and electronics of the 2S modules in section 3.3.

3.1. The p_{T} Module Concept

In a coordinate system with the beam pipe along the z-axis, the transverse momentum p_{T} of a particle is defined as

$$p_{\mathrm{T}} = \sqrt{p_x^2 + p_y^2}\,. \tag{3.1}$$

For collisions in CMS, the transverse momentum of the accelerated particles is known and, up to small p_{T} of partons inside the protons, approximately zero before the collision. Due to momentum conservation, the sum of the p_{T} of all particles after the collision has to be approximately zero as well. Due to that and the unknown p_{z} of the colliding particles, the p_{T} is often used in analyses as a variable describing the particles generated during the collisions and a precise measurement of the p_{T} of the charged particles in CMS is important. Also, triggering on particles with high p_{T} is a sufficient way to reduce the trigger rate within CMS while not losing the events with physical interest away.

Due to the increased particle density during the HL-LHC operation compared to the LHC, the CMS trigger system needs to be upgraded. The concept to achieve the rate reduction in the trigger is the p_{T} discrimination of tracks on module level. For that, the Outer Tracker modules are assembled with two back to back oriented silicon sensors. The distance between the sensors is in the millimeter range and depends on the position of the modules in the tracker. By using the same set of chips to read out both sensors, the integrated circuits can search for pairs of *clusters*, called *stubs*, in similar regions in both sensors of the module. A cluster is a group of adjacent strips with hits in the same event. It is defined by the position of its center and the width in units of strips. To form a valid stub, the cluster in the *correlation layer* has to lay within a predefined *correlation window* with respect to the position of the cluster in the *seed layer*. The sensor closer to the interaction point is used as the seed layer, which can, depending on the position of the module in the tracker, either be the top or the bottom sensor of the module. The stub concept is visualized in figure 3.1. A stub can be described by its *position* in the seed layer and the distance between the center of the correlation cluster and the center of the seed cluster. This distance is called *bend* and is evaluated with half-strip resolution.

The magnetic field of 3.8 T inside the CMS detector bends the trajectories of charged particles via the Lorentz force. The higher the curvature of a track, the lower the transverse momentum of

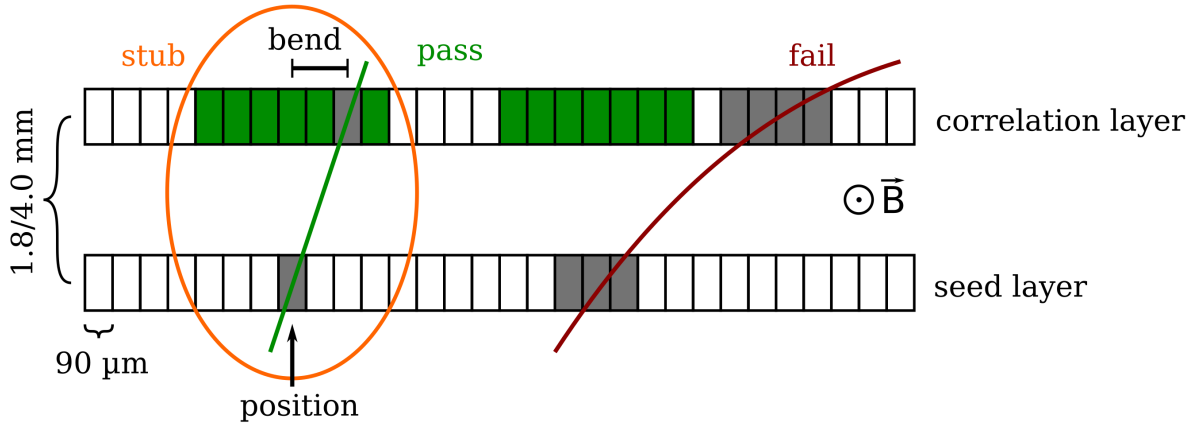

Figure 3.1.: Stub concept of 2S modules. The sketch depicts the seed and correlation layer of a 2S module. The trajectory of a charged particle with high p_T is shown in green while the trajectory of a low p_T particle is shown in red. The combination of clusters leads to a stub when the cluster in the correlation layer lies within a predefined correlation window (depicted in green) with respect to the position of the cluster in the seed layer. In this example, the green high p_T trajectory leads to a stub while the other does not. A stub can be described by the position of the cluster in the seed layer and the distance of position of the cluster in the seed and correlation window, called bend. Adapted from [Sto21].

the particle. Thus, high p_T-particles with $p_T \geq 2\,\text{GeV}$ produce stubs whereas low p_T-particles will not. Including the stub information to the Level-1 Trigger system, allows to trigger on a minimum transverse momentum of charged particles. This leads to the same physics performance of the CMS experiment in HL-LHC operation as during the LHC operations.

In the Outer Tracker, this concept of p_T discrimination is implemented with two different module types: The 2S and PS modules. Renderings of both can be found in figure 3.2. The 2S module consists of two silicon strip sensors while the PS module is built with one silicon strip sensor and one macro-pixel sensor each. The 2S module sensors are n-in-p type sensors with a thickness of 290 µm [Ada+21a] and a strip pitch of 90 µm. The sensors have outer dimensions of about 9.4 cm in width times 10.3 cm in length. The strips have half the length of the sensor so that the signal from each sensor side can be read out individually by the corresponding frontend chips. The strip sensors of the PS module are half the size of the 2S module sensors resulting in shorter strips of about 2.3 cm length and a pitch of 100 µm. The macro-pixel sensors have a pixel length of 1.5 mm and a pitch of 100 µm and are used to increase the granularity in the innermost layers of the Outer Tracker. The distances of the sensors are different depending on the position of the module in the tracker to ensure the desired p_T discrimination. 2S modules exist in the 1.8 mm and 4.0 mm version while PS modules are built with sensor spacings of 1.6 mm, 2.6 mm and 4.0 mm. [CMS17f] The next section 3.2 describes the positioning of the 2S and PS modules in the Outer Tracker as well as the radiation environment they will be exposed to during the operation of the HL-LHC.

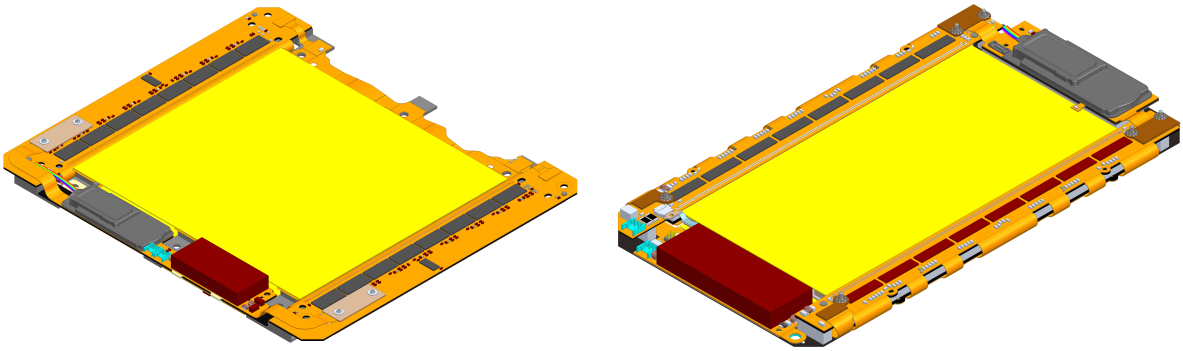

(a) 2S module

(b) PS module

Figure 3.2.: Rendering of a 2S and PS Outer Tracker Module. The silicon sensors of the 2S (a) and PS (b) module are depicted in yellow. Both module types are built with two back to back oriented sensors. Similar to [CMS17f].

3.2. Tracker Layout

The layout of the full Phase-2 Tracker is shown in figure 2.4. The Outer Tracker parts relevant for this thesis are the *Tracker Barrel with 2S modules* (TB2S) and the *Tracker Endcap Double-Disks* (TEDD), which are described in detail in the following sections 3.2.1 and 3.2.2. Being at different distances to the interaction point, the radiation levels of the modules are different depending on where they are located in the tracker. Section 3.2.3 gives an overview of the expected radiation exposure of the Outer Tracker modules.

3.2.1. Tracker Barrel with 2S Modules (TB2S)

In the TB2S, the 2S modules are arranged cylindrically around the beam pipe in three layers at different radii. A rendering of the *support wheel* is depicted in figure 3.3. The radial distance to the beam pipe (z-axis) of layer one to layer three are about 70 cm, 87 cm and 110 cm respectively. The modules themselves are attached to *ladders* mounted inside a support wheel. The interaction point of CMS is located in the center of the wheel. It is twice as long as one ladder so that ladders get mounted to the wheel from both sides. The modules from one side are called z^+-ladders while the others are named z^--ladders. At the coordinate $z = 0$ (radial outwards from the interaction point), the z^+- and z^--ladders overlap to guarantee full coverage of the detector volume. Later in this section, it will be explained how this overlap is mechanically made possible.

The TB2S is built with 372 ladders that house twelve 2S modules of the 1.8 mm variant each. A rendering of a ladder can be found in figure 3.4 with labels of the module and position numbers. C-shaped profiles are connected with crossbars giving the ladders their name. Both structures are made of *Carbon-fiber reinforced plastics* (CFRP). At the inner part of the C-profile, cooling inserts are attached providing the mounting points of the modules. A cooling pipe is routed through the inserts to provide a direct cooling path to the module bridges that act as the main cooling structures for the module readout electronics and silicon sensors. CO_2 in evaporative mode is used as coolant and will be set to an operation temperature of $-35\,°C$ to $-33\,°C$ for tracker operation. As cooling pipe material stainless steel and titanium got tested. The final ladders are made with titanium pipes.

A zoom to the ladder positions 1 to 3 is shown in figure 3.5. To provide full coverage of the tracking volume, the modules have to overlap so that there is no gap between the silicon sensors from neighboring modules. To achieve this, the modules mounted from the top and

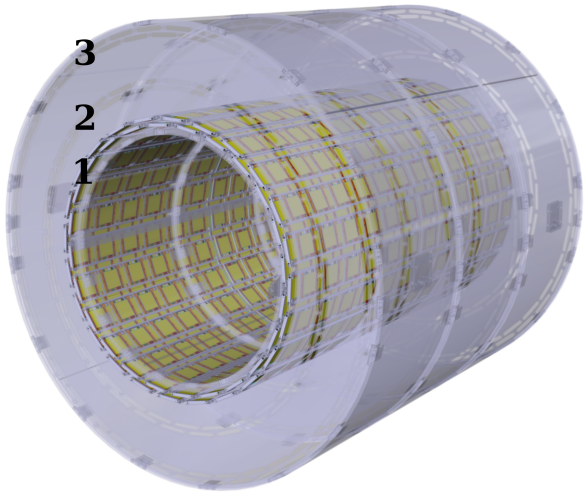

Figure 3.3.: Rendering of the TB2S support wheel. The ladders are arranged in three layers in the support wheel. The layers are labeled from 1 to 3 from inside out. The ladders and modules from layer 2 and 3 are not shown, but the ones from the inner layer can be seen. The interaction point is located in the center of this cylindrical structure. Adapted from [CMS17f].

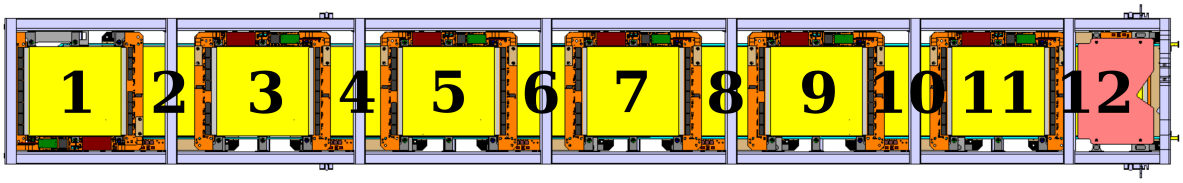

Figure 3.4.: Rendering of a TB2S ladder equipped with twelve 2S modules. The twelve 2S modules of a ladder are mounted from both sides on cooling inserts that surround the cooling pipe of the ladder. The modules on the ladder are labeled from 1 to 12 according to the ladder position they are mounted on. Module 1 and 12 are rotated by 180° compared the other modules that are mounted on the same ladder side.

bottom side of the ladder share common inserts, called *long inserts*. In between the long inserts, the *short inserts* provide additional cooling contact fixation points. Both insert types can be seen in figure 3.5b where the modules 1 to 3 are removed from the CAD model of the ladder.

To achieve this module overlap also at $z = 0$ where the modules 1 from the z^+- and z^--ladders are located, the left side of the modules at position 1 are mounted on so-called *special inserts*. They are marked with red rectangles in figures 3.5a and 3.5b. The special inserts are even longer than the long inserts and provide direct cooling of the middle cooling points of the modules but indirect cooling to the left cooling points. The cooling pipe (visible in light blue in figure 3.5) makes a loop below the module 1 to not clash with the cooling pipe of the overlapping ladder.

Since the special inserts for module 1 come with an indirect cooling path to the left module side, the modules at position 1 will be all build with a sixth cooling point. More details about the sixth cooling point can be found in section 3.3.2. The expected fluence at the innermost layer is much higher than the one at the other layers (see section 3.2.3). Due to that, the ladders of layer 1 (see figure 3.3) are built such that every module mounted on them has six cooling points. The modules mounted on the ladders of layer 2 and 3 have five cooling points except the modules that get mounted to position 1, which have six cooling points.

The power and readout services of the modules on the ladder are called *octopus* and *naked fanout*. Below the module at position 12 and next to module 11, a so-called *service plate* is mounted on the ladder. The service plate is visualized in salmon in figure 3.4. At this service plate, the adapters of the octopus and naked fanout are mounted such that the whole ladder can be connected with just two connections – one for the electrical connection and one for the optical readout connection. At the service plate, the octopus and naked fanout split to twelve cables that are routed through the C-profile. During the integration of the modules on the ladder, short optical and electrical cables are already attached to the modules. They pass through holes in the C-profile and get connected to the octopus and fanout. Each module has its own low and high voltage connection, but outside the CMS cavern, the high voltage lines of groups of four modules will be connected to the same high voltage channel of the power supply.

3.2.2. Tracker Endcap Double-Disks (TEDD)

It is foreseen that the same module types will be used in both the endcap and barrel region of the tracker. In total, 2744 PS modules of the 4.0 mm variant and 424 (2792) 2S modules of the 4.0 mm (1.8 mm) variant will be used in the endcaps. The CAD model of one endcap is shown in figure 3.6. The modules are mounted on so-called dees, which got their name due to their D-shape. As in the barrel region, PS modules are mounted in the inner part of the detector and 2S modules in the outer part. Two dees are connected to form a so-called disc. A disc covers the tracking volume at specific radii from the beam pipe. Two discs covering different radii are mounted at a distance of about 3 cm to form a double-disk structure. One double-disk provides the hermetic coverage of one endcap layer. Each endcap is made of five double-disk layers resulting in identical subdetectors at each side of the interaction point. The two double-disks closer to the interaction point have a smaller inner diameter whereas the remaining three have larger diameter to provide more space for the inner tracker that is larger at this part of the tracker.

Each dee is a composite of two carbon fiber sheets surrounding an inner foam layer. Seven cooling pipe loops pass each dee through the inner foam layer. The cooling of the modules is, as in the barrel region, done with CO_2 in evaporative mode. The cooling contact to the backside of the PS modules is provided by carbon foam blocks while the cooling of the 2S modules is done with six cooling inserts per module. Thus, all 2S modules going to the TEDDs are built with six cooling points.

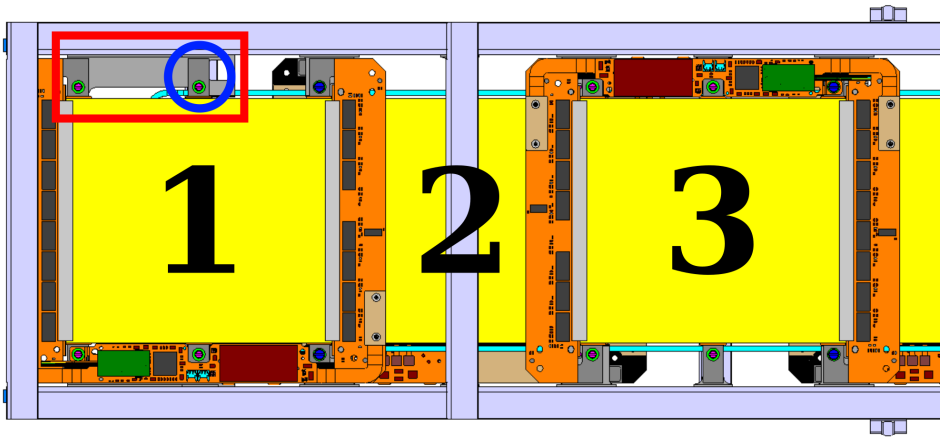

(a) Zoom to the ladder positions 1 to 3

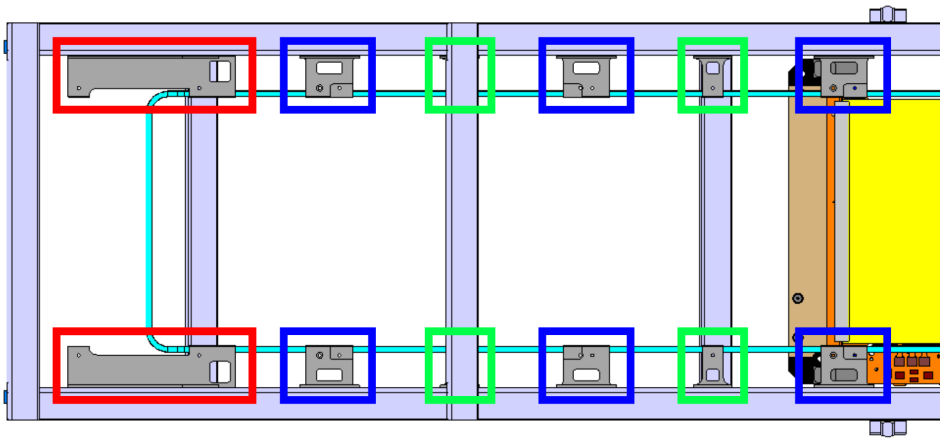

(b) Zoom to the ladder positions 1 to 3 without modules

Figure 3.5.: Zoom to the module positions 1 to 3. (a) The cooling of the left half of module 1 is done with special inserts (marked with a red rectangle) that are longer than the other inserts. For better cooling performance, all modules mounted on position 1 are built with a sixth cooling point (marked with a dark blue circle). (b) In the zoom on the ladder positions 1 to 3, the loop of the cooling pipe below module 1 can be seen when removing the modules 1 to 3 from the CAD model. The different insert types are marked with different colors: special inserts – red, long inserts – blue, short inserts – green. Some special inserts are covered by crossbars. (a) + (b) The cooling pipe is depicted in light blue.

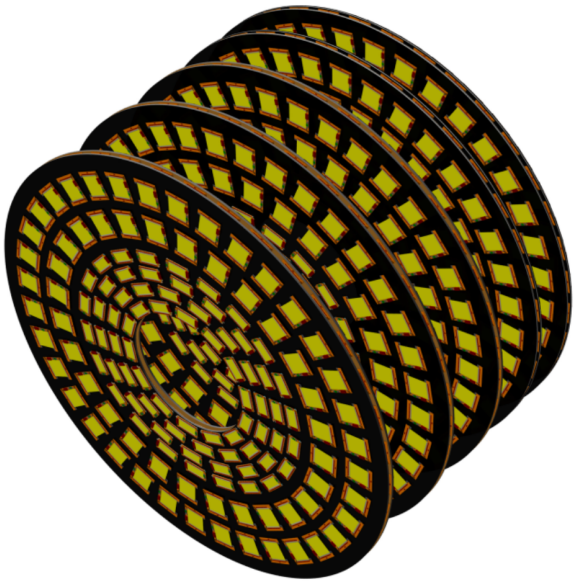

Figure 3.6.: Rendering of a TEDD. One TEDD is made of five double-disks. 2S modules are mounted at the outer part and PS modules in the inner region. In the top right corner of the image the inner part of the second TEDD can be seen. In between those, the TB2S is placed, which is not shown in this picture. Adapted from [CMS17f].

The optical and electrical services for powering and readout are routed radially outwards. Cables from the inner modules are routed through the spaces between the modules and, at some positions, above the hybrids of other modules. During integration of the modules to the dees, the PS modules in the inner part are integrated first.

3.2.3. Radiation Environment

The expected radiation environment in the CMS Phase-2 Tracker is calculated within the *CMS Beam Radiation Instrumentation and Luminosity* (BRIL) project. For the simulations the FLUKA 2011.2b.6 Monte Carlo multi-particle transport code was used [Fer+05]. The resulting expected fluence map is shown in figure 3.7 for an integrated luminosity of $3000\,\mathrm{fb}^{-1}$ and proton-proton collisions at 14 TeV with a total cross section of $\sigma_{\mathrm{pp}} = 80\,\mathrm{mb}$. This radiation scenario is called the *nominal scenario*. The inner layer of the Inner Tracker is, with $3.26 \times 10^{16}\,\mathrm{cm}^{-2}$, exposed to the highest fluences. For the PS (2S) modules of the Outer Tracker the highest expected fluences are $1.04 \times 10^{15}\,\mathrm{cm}^{-2}$ ($3.8 \times 10^{14}\,\mathrm{cm}^{-2}$). The expected fluences in the *ultimate scenario* at $4000\,\mathrm{fb}^{-1}$ are 1.33 times higher – resulting in $1.39 \times 10^{15}\,\mathrm{cm}^{-2}$ for the PS modules and $5.08 \times 10^{14}\,\mathrm{cm}^{-2}$ for the 2S modules. In the TB2S, the highest expected fluence in the nominal scenario is $2.8 \times 10^{14}\,\mathrm{cm}^{-2}$, while it is $3.72 \times 10^{14}\,\mathrm{cm}^{-2}$ in the ultimate scenario. The numbers are taken from the tracker layout [tkL23]. Thermal simulations of the module performance after irradiation are used to validate the cooling concept of the modules. These simulations need to be verified with measurements. Such measurements are performed within this thesis with an irradiated 2S prototype module on a TB2S ladder and described in section 6.1.

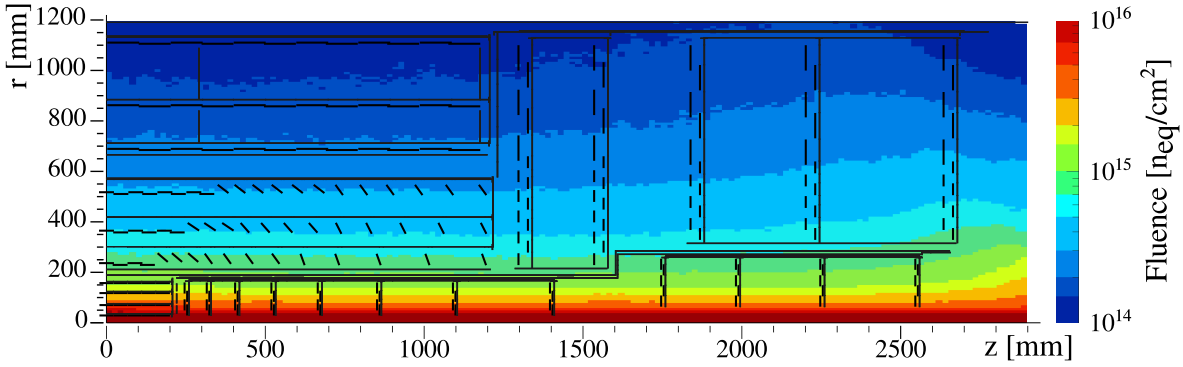

Figure 3.7.: Fluence map of the Phase-2 Tracker. The expected integrated particle fluence in 1 MeV neutron equivalent per cm^2 in the CMS Phase-2 Tracker is shown. The fluences are calculated for an integrated luminosity of 3000 fb^{-1} and proton-proton collisions at 14 TeV with a total cross section of $\sigma_{pp} = 80$ mb. Taken from [CMS17f].

3.3. Outer Tracker 2S Modules

The system and integration tests performed in this thesis use 2S modules. This section describes the modules in detail because each detail may influence tests performed with the modules. Their sensors, mechanics, electronics and readout are described first in sections 3.3.1 to 3.3.4 and then the differences between so-called prototype and kickoff modules are explained in section 3.3.5. Section 3.3.6 introduces the assembly and integration flow during module production and tracker integration beginning in 2025.

3.3.1. Sensors

Since the 1980s, silicon sensors have improved high energy particle physics experiments by providing reliable, precise tracking in high fluence environments [Ber+19]. For the CMS Phase-2 Outer Tracker n-in-p type silicon sensors from the Japanese company Hamamatsu Photonics K.K. (HPK) will be used. The 2S sensors have outer dimensions of $9.4183 \times 10.2700\,cm^2$ resulting in an active area of about $9.1440 \times 10.0548\,cm^2$. They have a physical thickness of 320 µm resulting in an active thickness of 290 µm. The strip pitch is 90 µm and the strips have a length of 4.572 cm.

Signal Generation

The working principle of semiconductor tracking detectors is to use *pn-junctions* operated in *reverse bias mode*. 2D and 3D schematics of silicon strip sensors can be seen in figure 3.8. In a p-doped bulk with a p^{++}-doped backside layer on an aluminum backplane, n^+-doped strips are implanted. The space charge region can be increased by applying a reverse voltage between the implants and the bulk backside. The space charge region grows from the bulk topside and is extended to the volume of the whole bulk at the *full depletion voltage* V_{FD}.

Passing the sensor in reverse bias operation, an ionizing particle will create electron-hole pairs in the bulk. The holes will drift towards the backside while the electrons drift to the strips. As the charges move, they induce charge on the nearest strips. Reading out this charge individually per strip provides the position information for tracking. When the readout chips are directly connected to the strip implants, the readout method is called *DC coupled*. In the *AC coupled* readout mode, a thin passivation layer of SiO_2 is added between the strips and

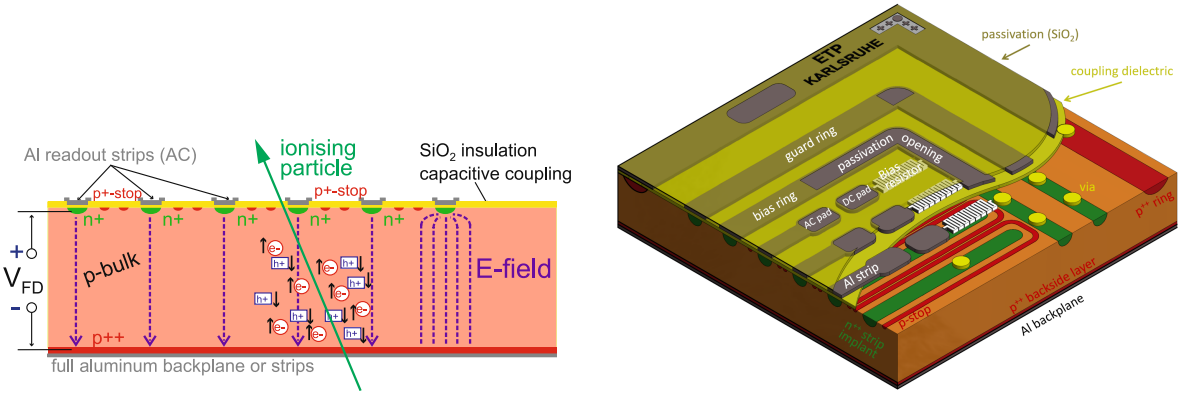

(a) 2D schematics of a silicon strip sensor **(b)** 3D schematics of a silicon strip sensor

Figure 3.8.: 2D and 3D schematics of silicon strip sensors. (a) A n-in-p silicon strip sensor with a passivation layer for AC coupled signal readout is shown. The space charge region fills the complete bulk since the full depletion voltage V_{FD} is applied to the sensor backside. An ionising particle creates charge carriers in the bulk that induce signal in the n^{+}-strips when being separated by the electric field in the space charge region. (b) Spots without the passivation layer allow probing and wire-bonding on the sensors that are used in CMS. Taken from [Kop22] and adapted from [Har17].

the readout chips. This layer electrically isolates the strips from the readout chips. Thus, the induced signal of the strips couples capacitively to the readout chips.

Figure 3.8b shows a 2S silicon strip sensor as it will be used in the 2S modules. There is a dielectric layer above the whole bulk and the n++ strips. Above this, aluminum strips are located on top of the n^{++} strip implants. Thus, bonding the readout chips to these AC pads results in AC readout of the signal. But there are also DC pads allowing for DC readout. These pads are connected directly to the strip implants by vias inside the dielectric coupling layer. Another SiO_2 passivation layer is added to the whole sensor except at some positions to allow probing and wire bonding.

Noise

The number of electrons and holes in silicon sensors underlies statistical fluctuations. These statistical fluctuations are called *noise* and can be described by the *equivalent noise charge* (ENC) Q_{n}. It is the quadratic sum

$$Q_{\mathrm{n}} = \sqrt{Q_{C_d}^2 + Q_{I_L}^2 + Q_{R_p}^2 + Q_{R_S}^2} \tag{3.2}$$

of different noise contributions.

- The *load capacitance* term

$$Q_{C_d} = a + b \cdot C_d \tag{3.3}$$

  is dependent of the load capacitance C_d and two preamplifier-specific parameters a and b. The load capacitance is mainly dependent on the strip length.

- The *shot noise*

$$Q_{I_L} = \frac{e}{2}\sqrt{\frac{I_L \cdot t_P}{q_e}} \tag{3.4}$$

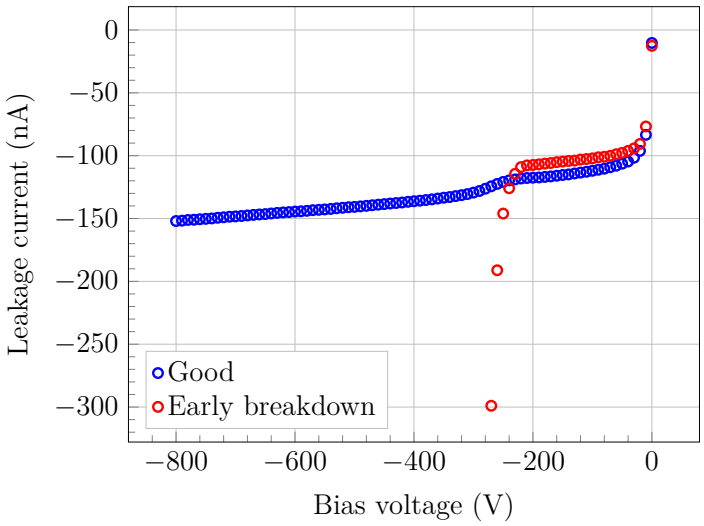

Figure 3.9.: IV characteristic of a 2S silicon sensor. The leakage current is shown in dependence of the bias voltage. The comparison of an IV curve with the expected behavior (blue) and early breakdown (red) is plotted.

is caused by the leakage current I_L and depends further on the peaking time t_P. e refers to the Euler number and q_e to the electron charge.

- The *parallel thermal noise*

$$Q_{R_p} = \frac{e}{q_e}\sqrt{\frac{k_B T \cdot t_P}{2R_P}} \tag{3.5}$$

is temperature T dependent and results from the current through the bias resistance R_P. The Boltzmann constant k_B is part of the equation.

- The second temperature dependent term is the *serial thermal noise*

$$Q_{R_S} = C_d \cdot \frac{e}{q_e}\sqrt{\frac{k_B T \cdot R_S}{6t_P}} \tag{3.6}$$

from the aluminum strip resistance R_S.

Further information on noise can be found in [Har17].

IV Curves

The current-voltage characteristic (or short *IV curve*) is the dependency of the leakage current of the applied reverse bias voltage. To measure this, high voltage has to be applied to the sensor backside and the current from the backside to the grounded bias ring (see figure 3.8b) is measured. Figure 3.9 shows two exemplary IV curves measured on the same sensor. The IV curve labeled with “Good” shows the expected behavior while the other one (label “Early breakdown”) shows a step increase of the leakage current at a bias voltage of about −220 V. Such an early breakdown behavior can be caused by high humidity for the sensors used in 2S modules. [Wit23] Also, mechanical stress on a silicon sensor can increase the leakage current. [Mur+16] Sensors being damaged during the assembly or integration can be spotted by increased leakage current as well.

Within this thesis, the high voltage applied to sensors or modules has always a negative sign because n-in-p sensors are used. For readability, this thesis uses from now on the convention of absolute voltage and current values.

The sensors from Hamamatsu undergo the so-called *sensor quality control* (SQC, described in detail in [Wit23]) procedures. Measuring IV curves of random samples of sensors from each production lot is part of the SQC. The IV curves of all sensors that will be used for module assembly have to look "good". Currently, "good" is defined by three criteria. The leakage current at a bias voltage of 600 V has to be below 7.25 µA, the breakdown voltage has to be at voltages higher than 800 V and the ratio of the leakage current at 800 V and 600 V $I_{800\mathrm{V}}/I_{600\mathrm{V}} < 2.5$ has to be fulfilled. [Wit23] Also, during the module assembly and integration process (see section 3.3.6) IV curves of single sensors and both sensors combined in a module are taken at several steps. During functional module tests and integration tests the IV characteristic of the sensors of a module can be taken to evaluate if there is mechanical stress on the silicon sensors of a module which would result in higher leakage current at a given voltage. [Mur+16]

Radiation Damage and Annealing

The leakage current of silicon sensors increases with increasing radiation. [Mol99] The increase of the leakage current at 21 °C can be described as

$$\Delta I(21\,^\circ\mathrm{C}) = \alpha \cdot \Phi_{\mathrm{eq}} \cdot V_{\mathrm{sensor}}\,. \tag{3.7}$$

The annealing factor α depends on the annealing time t at room temperature and Φ_{eq} describes the radiation level the sensor got exposed to. The active volume V_{sensor} is

$$V_{\mathrm{sensor}} = 91.488\,\mathrm{mm} \cdot 100.703\,\mathrm{mm} \cdot 290\,\mu\mathrm{m} = 2.669\,\mathrm{cm}^3 \tag{3.8}$$

for the sensors of 2S modules. [CMS17f]

The annealing factor α can be calculated according to

$$\alpha = \alpha_{\mathrm{initial}} \cdot \exp\left(\frac{-t}{\tau_{\mathrm{initial}}}\right) + \alpha_0 - \beta \cdot \ln\left(\frac{t}{t_0}\right)\,. \tag{3.9}$$

The annealing time is denoted with t. The parameters $\alpha_{\mathrm{initial}}$, τ_{initial}, α_0 and β depend on the annealing temperature T in Kelvin and were measured by [Mol99] with diodes as

$$\begin{aligned}
\alpha_{\mathrm{initial}} &= 1.23 \times 10^{-17}\,\mathrm{A/cm} \\
\tau_{\mathrm{initial}} &= \exp\left(\frac{12.9 \times 10^3\,\mathrm{K}}{T} - 34.1\right)\,\mathrm{min} \\
\alpha_0 &= \left(-8.9 \times 10^{-17} + \frac{4.6 \times 10^{-14}\,\mathrm{K}}{T}\right)\,\mathrm{A/cm} \\
\beta &= 3.07 \times 10^{-18}\,\mathrm{A/cm} \\
t_0 &= 1\,\mathrm{min}\,.
\end{aligned} \tag{3.10}$$

The resulting annealing factors depending on the annealing time in days are plotted in figure 3.10.

The dependency of the leakage current I of the temperature T is given by

$$I(T) = T^2 \cdot \exp\left(\frac{-1.21\,\mathrm{eV}}{2 \cdot k_{\mathrm{B}} \cdot T}\right) \tag{3.11}$$

with the Boltzmann constant k_{B} and the effective energy $E_{\mathrm{eff}} = -1.21\,\mathrm{eV}$ of silicon. [Chi13]

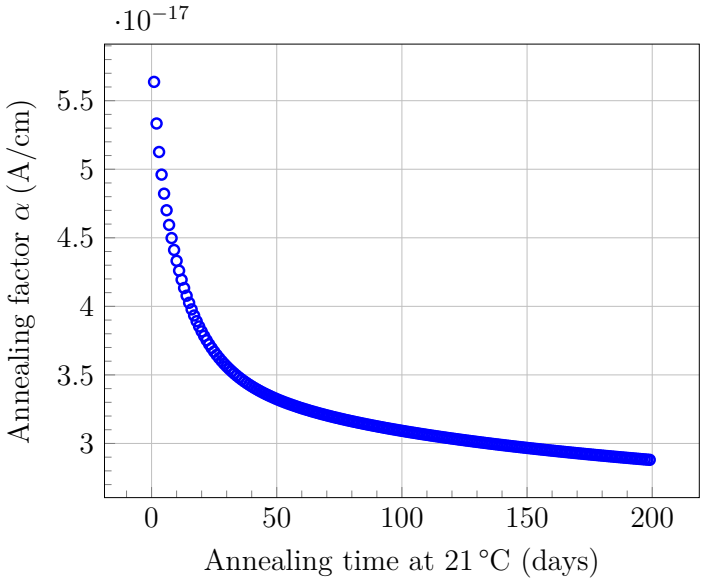

Figure 3.10.: Annealing factor dependency of the annealing time in days at room temperature (21 °C). The annealing factor is shown as a function of the annealing time in days.

The expectation of the leakage current at a temperature T is thus given by

$$\Delta I(T) = \Delta I(21\,^\circ\mathrm{C}) \cdot \frac{I(T)}{I(21\,^\circ\mathrm{C})}\,. \tag{3.12}$$

Radiation damage in silicon sensors can either be bulk or surface damage. Bulk damage mostly increases the bulk resistivity, full depletion voltage and leakage current while lowering the charge collection efficiency. The defects are mobile and can thus either recombine or combine to larger defects. The mobility is very small at temperatures below 0 °C but at higher temperatures the *annealing* of the defects becomes relevant due to higher mobility. There are two types of annealing, the *beneficial annealing* lowering the depletion voltage and increasing the charge collection efficiency and the *reverse annealing* leading to the contrary effects. For the 2S silicon sensors with a physical thickness of 320 µm resulting in a 290 µm depletion zone, the reverse annealing becomes relevant for very long annealing times and high fluences.

3.3.2. Mechanics

An exploded view of the final 2S module design can be found in figure 3.11. The central structure of a 2S module is provided by two back to back oriented silicon sensors. They are glued on *carbon fiber reinforced aluminum* (Al-CF) structures called *bridges*. These bridges provide the correct spacing of the silicon sensors, the main cooling path of the module and the mechanical fixation points for mounting the modules on the larger detector structures such as TB2S ladders and TEDD dees. There are two kinds of bridges with different thicknesses for the 1.8 mm and 4.0 mm modules. The bridge below the service hybrid is shorter than the long bridges below the frontend hybrids and thus called *stump bridge*. Depending on the position of the module in the tracker, they will be built with five or six cooling points. The sixth cooling point is given by a second stump bridge attached on the opposite of the first stump bridge. All 4.0 mm modules will be built with six cooling points to partially compensate for the worse cooling performance of the thicker bridges. The 1.8 mm modules will be built in both types.

During operation, the backside of the silicon sensors is connected to high voltage of up to 800 V. To electrically isolate the rest of the module components from this high potential, polyimide foils are attached on the sensor backsides at the positions of the bridges. The high voltage is connected to the sensor backsides by *high voltage tails* (HV tails). The HV tails are plugged into the HV circuit of the service hybrid at one end and glued to the sensor backside at the other end. The electrical connection to the sensor backside is done with wire-bonds. The HV tail of the top sensor has a second tail at which a thermistor is mounted. The thermistor is located next to the bond pad and has thus direct thermal contact to the sensor. With this, the silicon sensor temperature can be monitored during module operation in the tracker which is useful to monitor the sensor temperature and thus cooling performance after irradiation. The assembly of silicon sensors with the HV tails and polyimide strips attached to the module bridges is called *bare module*. The strip rotation between the upper and lower sensor of a bare module must be smaller than 400 µrad for accurate p_{T} measurements.

The combination of two *frontend hybrids* (FEHs) and a *service hybrid* (SEH) is called a *skeleton*. Both electronic structures are explained in more detail in section 3.3.3. They are made of flexible electronic circuits folded around a CFRP stiffener. This material within the electronic components provides – together with the bridges – the cooling path of the electronic components. Also, it ensures the mechanical stiffness of the electronic components.

A full 2S module is made of one skeleton and one bare module. The skeleton is glued to the bridges of the bare module. A *light shield* is mounted on the Versatile Transceiver Plus (VTRx+) located on the SEH. This is further explained in the following section 3.3.3. To reduce the electronic noise of the 2S modules, a *ground balancer* connects the module ground on the SEH far side. For more details see section 4.1.2.

3.3.3. Electronics

The electronic components of the 2S modules are mounted on electronic circuit boards, called *hybrids*. The hybrids are glued to the module bridges at dedicated fixation points. There are two kinds of hybrids mounted inside a 2S module: The *frontend hybrids* (FEHs) and the *service hybrid* (SEH).

The Frontend Hybrids

Two frontend hybrids (FEHs) are connected to each module. Looking from the SEH to the module, one is on the right and one on the left side. On each of the FEHs, eight *CMS binary chips* (CBCs) are placed. They are bump bonded to the FEHs and are responsible for the readout of 254 channels each. 127 of these channels belong to the top and bottom sensor each. A fold-over from the top side of the FEH to the bottom side allows wire bond connections from the AC pads of the top and bottom sensor to bond pads on the FEH. The channels are routed along the fold-over such that the CBC channels are connected alternately to strips of the top and bottom sensor. Thus, the stub finding algorithm can be applied on readout chip level and will be used as input for the Level-1 trigger of CMS. The hit information of neighboring CBC chips is exchanged to have clean stub detection across the whole FEH. The final chip version is the CBC3.1 [Pry19].

The signal is processed via analogue frontends for each channel, which is illustrated in figure 3.12a. There is a pre- and a post-amplifier at each analogue frontend. The signal level of each channel can be shifted with an 8-bit offset register before comparing the pulse with a chip-wide programmable threshold in internal DAC units $\mathrm{V_{CTH}}$. The chip is designed such that the ENC is less than 1000 electrons reading out the 5 cm long strips of a 2S sensor.

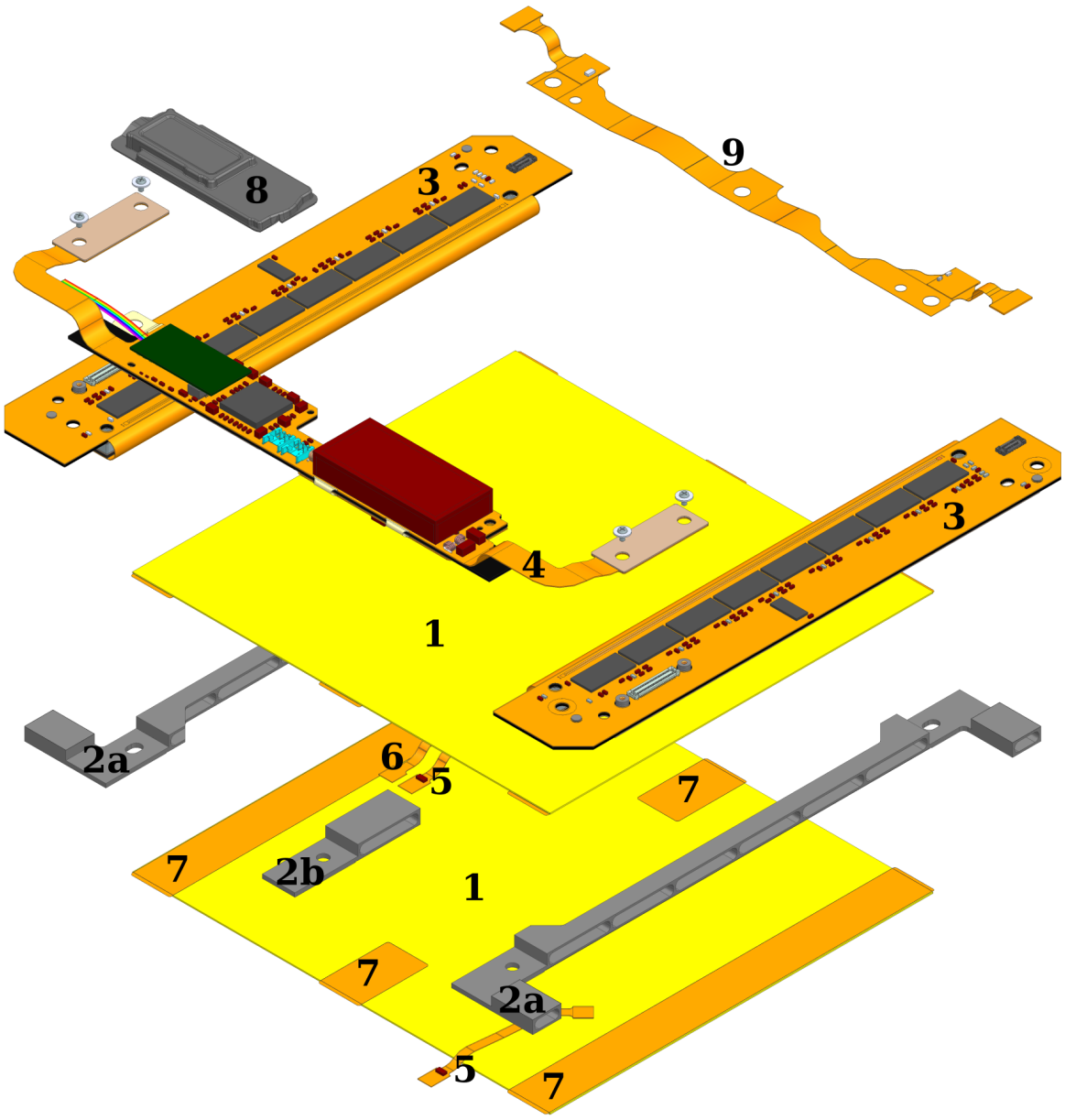

Figure 3.11.: Exploded view of a 2S module. A 2S module with sensor spacing of 4.0 mm and two stump bridges is shown. The parts of the 2S module are: 1 – silicon sensors, 2 – bridges, 2a – long bridges, 2b – stump bridges, 3 – frontend hybrids, 4 – service hybrid, 5 – high voltage tails, 6 – thermistor, 7 – polyimide foil, 8 – light shield, 9 – ground balancer.

Figure 3.12b shows the main signal processing blocks within the CBC. The output of the analogue frontend is passed to the *Hit Detect* block that is operated at 40 MHz. The binary hit information is written to a 512 bunch crossings deep pipeline as well as transferred to a stub detect logic. The hits are read out at two data paths – the triggered or L1 data and the stub data. The triggered data are read out when receiving an L1 trigger signal while the stub data are piped out continuously at 40 MHz.

The 512 deep pipeline corresponds to 12.8 µs at 40 MHz bunch crossing rate, which is also the time, the trigger system of CMS will have to decide whether the full hit data of the event should be read out or not.

The first part of the stub detect logic is the *OR254* block that passes the result directly to the *Data Packet Assembly & Transmission* block. This flag shows if at least one of the 254 channels of the CBC detected a hit. The next step is the *Top & Bottom Channel Swap* that can account for changing the seed and correlation layer for modules that are mounted in the Tracker with the top side facing to the interaction point. To be able to also detect stubs that span across the boundary of neighboring CBCs, the nearest strips from neighboring CBCs are taken into account in this step. In the *Cluster Width Discrimination* all clusters with a width larger than the programmable maximum width are rejected. The maximum possible width is four strips. The *Offset Correction & Correlation* logic searches for stubs in the remaining clusters according to the stub logic described in section 3.1. The correlation window size can be programmed in total window sizes of one strip up to a total window size of 15 strips. The position of the correlation window can be offset in half channel steps up to ±3 channels in four independently programmable regions per chip. With this, the geometrical offset due to the position of the module in the Tracker can be accounted for. The stub position as well as the bend information have half strip resolution. The chip internal 5-bit bend information is reduced to a 4-bit value according to a programmable lookup table to further reduce the data output rate.

The CBC stub data are sent out continuously at 320 MHz. The data are sent out in packets at five *scalable low-voltage signalling* (SLVS) lines that get generated in the *Data Packet Assembly & Transmission* block. This is illustrated in figure 3.13a. Each packet has a width of eight clock cycles at 320 MHz. There is one stub data packet per bunch crossing (25 ns). The stub packets contain data from up to three stubs. The address is given by an 8-bit value and the bend information is decoded in a 4-bit word. A synchronization bit allows for synchronizing the stub data stream with the L1 data stream. Three more 1-bit flags are part of the stub packages. The *Stub Overflow Flag* (SoF) indicates if there were more than three stubs in the respective bunch crossing. The *OR254* flag indicates a hit in any of the 254 channels per CBC and the *Flags* bit is the logical OR of the *FIFO Full Flag* and the *Latency Error Flag*. The Latency Error Flag is high if the value stored in the latency register differs from the difference of the write counter and trigger counter. The FIFO Full Flag is set to high if the number of items in the Buffer SRAM reaches 32. Both flags are separately part of the triggered L1 data.

The L1 or triggered data are sent out via a sixth SLVS line. Its data format is shown in figure 3.13b. It consists of a 2-bit header, two error bits, a 9-bit pipeline address, the 9-bit L1 ID as well as the channel data from the 254 channels. The *L1 ID* is counting the number of received L1 triggers. It can be reset by an own dedicated reset command, called *Orbit Reset*. Since the L1 counter gets incremented when receiving a trigger, the first L1 event in an orbit will have an L1 ID of 1. Just in the cases where the reset is sent simultaneous with a trigger or one clock cycle later, the L1 ID of that event will be 0.

On each FEH, a *Concentrator Integrated Circuit* (CIC) [Ber+24] is bump bonded that combines the data of the eight CBCs to two single data paths per FEH. It gets the output data of each CBC as input that are divided in the stub and the L1 data as illustrated in figure 3.13.

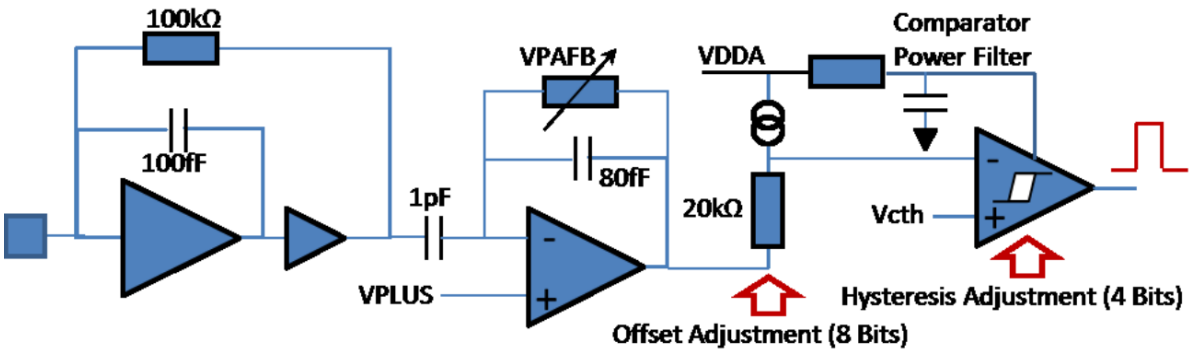

(a) Diagram of the analogue frontend of the CBC3.1 chip

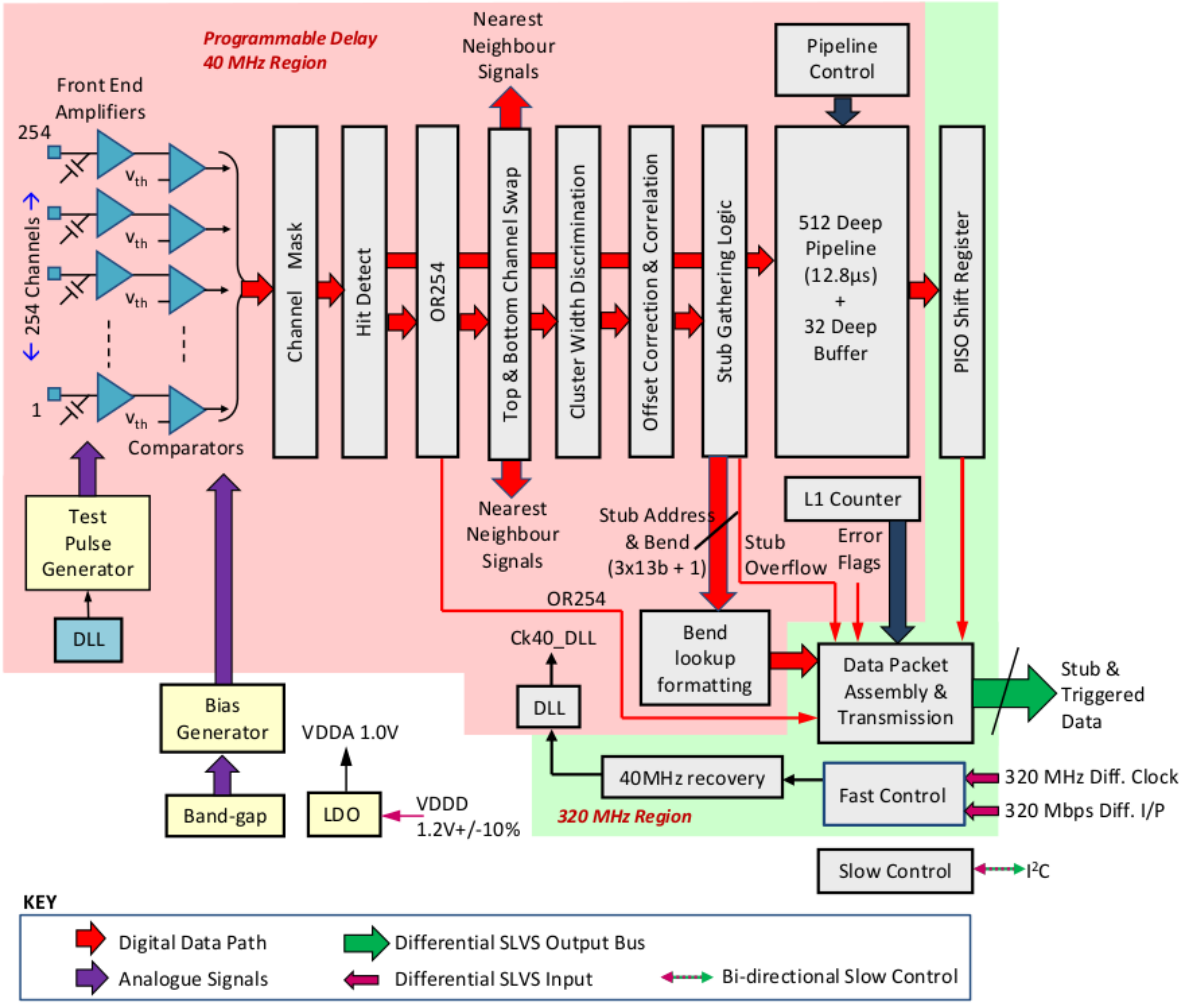

(b) Block diagram of the CBC3.1 chip

Figure 3.12.: Diagram of the analogue frontend and block diagram of the CBC3.1 chip. (a) The analogue frontend of the CBC3.1 chip consists of a pre- and post-amplifier and a comparator that creates a digital output of the analogue sensor signal. (b) The block diagram shows the main circuit blocks processing the analogue and digital signals of the CBC3.1 chip. Taken from [Pry19].

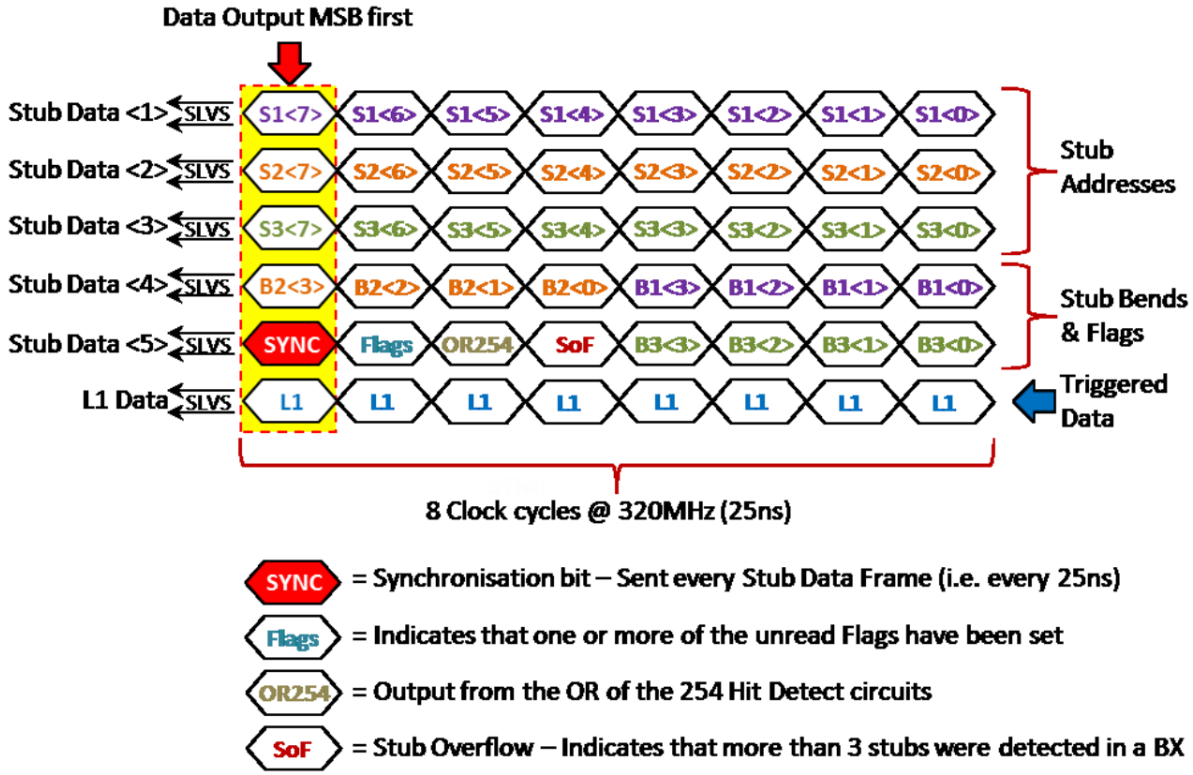

(a) CBC stub data format

header	error	pipeline address	L1 ID	channel data
2 bits	2 bits	9 bits	9 bits	254 bits

(b) CBC L1 data format

Figure 3.13.: CBC stub and L1 data format. (a) Illustration of the stub data packet. Each stub packet has a width of eight clock cycles at 320 MHz. It contains the 8-bit address and 3-bit bend data of up to three stubs (depicted in purple, orange and green) as well as a synchronization bit and three flag bits at five SLVS lines. The meaning of the flags is explained in the figure and the text. The stub data span over five SLVS lines. The sixth line is for the transmission of the L1 data. Taken from [Pry19]. (b) The format of the CBC L1 data is shown. For each part the number of bits in the data stream is given. Taken from [Ber+24].

The output stub data format of the CIC is shown in figure 3.14a. The stub data from the CBCs are first phase and word aligned. Then, the incoming stub data are buffered for eight bunch crossings within the CIC and sorted by increasing stub bend. In case of a CIC buffer overflow, low bend stubs are prioritized. There are two readout configurations, called *FEC5* and *FEC12*. The reason are two different schemes for the *forward error correction* (FEC) in data transmission of the Low Power Gigabit Transceiver (lpGBT, for more details see next subsection The Service Hybrid) that receives the data of the two CICs of one module. With this, error control is obtained in data transmission. FEC12 provides more transmission robustness compared to FEC5. [Pau24] In the FEC5 (FEC12) readout, six (five) output lines are used for the CIC stub output data. Both output data formats are visualized in figure 3.14a. In total, the CIC transmits up to 16 (19) stubs per eight consecutive bunch crossings in the FEC12 (FEC5) mode. By the option to skip the transmission of the bend information, this number of stubs per CIC within eight bunch crossings can be increased. The CIC stub package includes also nine status bits, one for each CBC and one for the CIC itself, and a *bunch crossing ID* (BX ID or BCID/Bclk ID in figure 3.14a) that is incremented every bunch crossing. Since the stubs of one packet span over eight bunch crossings, a 3-bit bunch crossing offset is part of each stub data packet to be able to assign it to the correct bunch crossing.

In the case of CBCs connected to the CIC, the output L1 data of the CIC can either be in the *unsparsified* or *sparsified* mode. The unsparsified (or deserialized) mode is for debugging purposes and means that the CIC transmits the CBC raw data. This works up to an L1A rate of 100 kHz. In the sparsified readout mode, the CIC creates clusters from the CBC hit data. The corresponding data format is visualized in figure 3.14b. A cluster is described by the 8-bit address and the 3-bit width. At maximum, 31 clusters per CBC can be reconstructed. If there are more, the clusters corresponding to the lowest addresses are dropped. The sparsified readout mode can be enabled with a 1-bit read-write CIC slow control register.

The CIC has readout limits that are summarized below and investigated in more detail in [Dro21]. The bandwidth of the module readout is 320 Mbit/s, which corresponds to a readout capability of 8 bits/clock cycle for clock cycles of 25 ns. To read out one event it takes

$$S = \frac{H + 14\,\text{bits/cluster} \cdot n_{\text{cl}}}{8\,\text{bits/clock cycle}} \tag{3.13}$$

where S is the number of clock cycles. The information about each cluster is 14 bits long. Three bits for the chip ID, eight bits for the address of the cluster from 0 to 253 and three bits for the width. The size of the event header H is given by $H = 54$ bits. The maximum readable number of clusters per *frontend* (FE) and event at a given trigger separation S can thus be written by

$$n_{\text{cl}} = \frac{8\,\text{bits/clock cycle} \cdot S - H}{14\,\text{bits/clock cycle}}\,. \tag{3.14}$$

This limit is also called *CIC Level-1 bandwidth limit* and becomes relevant for trigger frequencies above 100 kHz. Up to 100 kHz the hard *CIC cluster limit* of 127 clusters/FE/event is valid.

The Service Hybrid

The service hybrid (SEH) is connected to the two FEHs with two fine-pitch connectors on flexible tails. It is made of a flexible electronic circuit board that sits on a carbon-fiber-reinforced polymer stiffener. The SEH houses different components which have individual tasks. The *Low Power Gigabit Transceiver* (lpGBT) [Mor+24] receives data from the CICs of the module. It serializes the data and transmits them to the *Versatile Transceiver Plus* (VTRx+) [Ola+20] for opto-electrical conversion. Optical fibers provide the connection from the VTRx+ to the FPGA module readout board. I^2C-commands can be sent to the FEHs with the lpGBT. During the

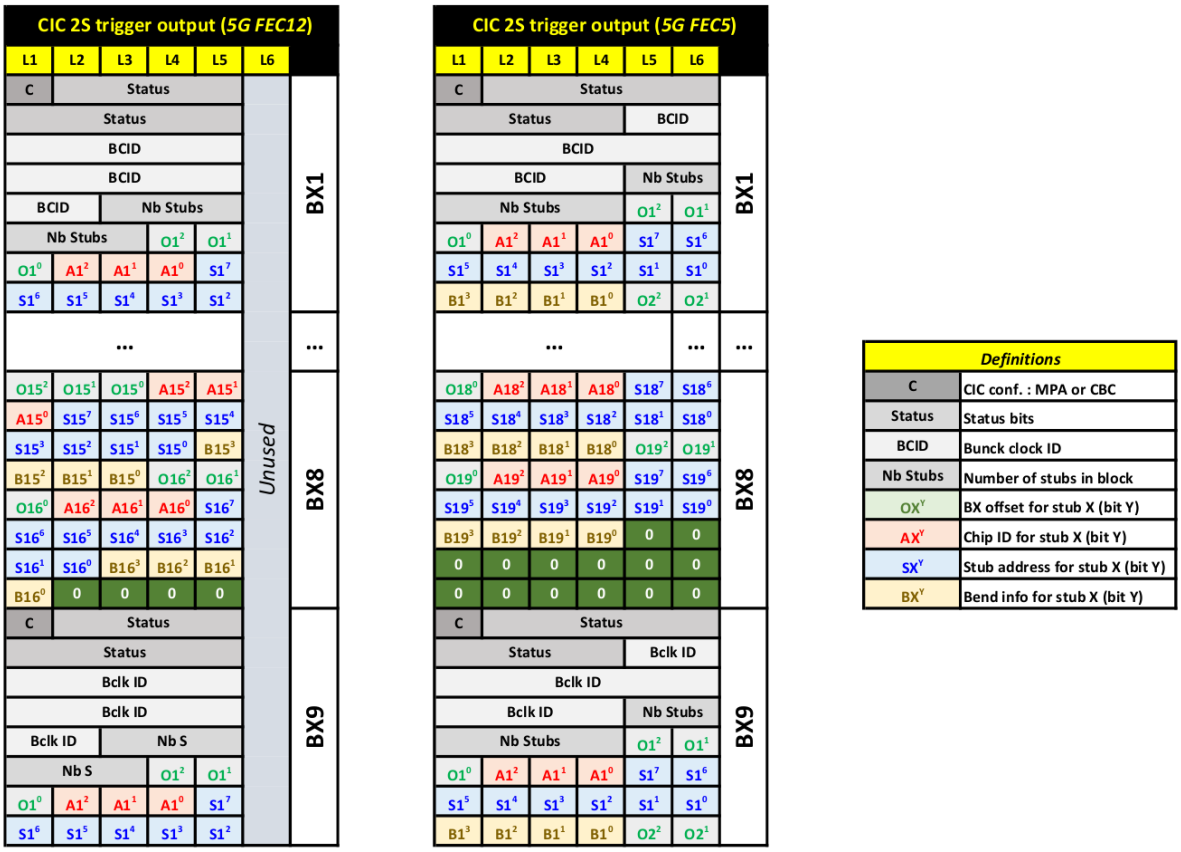

(a) CIC stub output data format

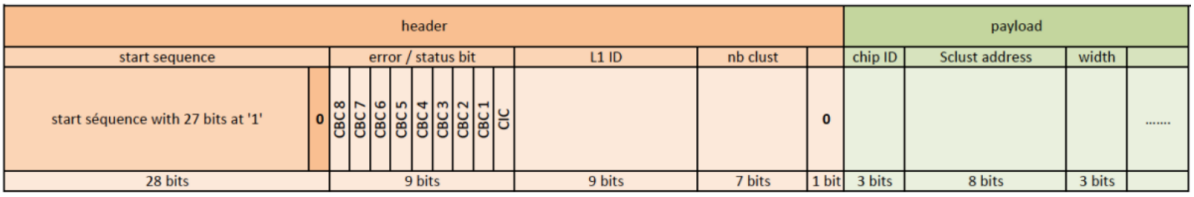

(b) Sparsified CIC L1 output data format

Figure 3.14.: CIC stub and sparsified L1 output data format. (a) A CIC stub data packet spans over eight consecutive bunch crossings. Depending on the readout mode (FEC12 on the left and FEC5 on the right), the maximum number of transmitted stubs per CIC differs. (b) The sparsified CIC L1 data consist of a 54 bits long header and a payload containing the cluster information. The information of each cluster data is 14 bits long. Taken from [Ber+24].

opto-electrical conversion of the module data during operation, the VTRx+ emits light. This increases the leakage current drawn by the module. To reduce the light seen by the silicon sensors, a plastic light shield is attached to the VTRx+ on the modules (see section 3.3.2).

To reduce the material budget of cables in the Outer Tracker and to reduce the electrical power losses in the cables, all on-module electronics get powered with one low voltage line at about 10 V to 11 V. During the measurements shown in this thesis, the low voltage was always set to 10.5 V. Two on-module DC-DC converters in series provide the needed voltages. The bPOL12V converter [CER24a] provides the 2.55 V for the VTRx+ module. The bPOL2V5 converter [CER22] creates 1.25 V from the 2.55 V to power all the other on-module chips. The DC-DC stages are shielded with an aluminum cover that acts as a Faraday cage to protect the rest of the module from electromagnetic noise. The high voltage is attached to the SEH via a connector at the SEH top side and then routed through the HV circuit of the SEH to its bottom side where it is connected to the high voltage tails that are glued to the sensor backsides

3.3.4. Readout

During the Phase-2 Tracker operation, the optical readout of the modules will be done with a *Serenity* FPGA board [Ros+19] which can handle up to 72 Outer Tracker modules per board. As the Serenity board was within the development and prototyping phase, it was not used for the measurements presented in this thesis. Also, all measurements that will be performed during the module assembly and integration procedure described in more detail in section 3.3.6 will be done with an FC7 board as explained in the next paragraph.

The prototype modules that are investigated within this thesis are read out optically. For this, an *FC7 evaluation board* [Pes+15] is used. This µTCA [PIC25a] compatible *Advanced Mezzanine Card* allows FPGA based multi-gigabit transceiver operation. For powering, the FC7 board can either be plugged to a µTCA crate [PIC25b] or self-made nanoCrate that houses a similar power board as the µTCA crate but is much smaller and thus easier to handle during beam and integration tests. Each FC7 can support up to two *FPGA Mezzanine Cards* (FMCs). They can either house optical transceivers in which the optical fibers of modules can be plugged or maintain an external trigger interface. As external trigger interface, the *DIO5* FMC [BWL23] and the *AMC13* [Haz+13] are used in this thesis. External signals from, e.g., scintillators can be fed to an input channel of the DIO5, which can then be used to trigger the module readout. Depending on the aimed readout configuration regarding the trigger source, module prototype and number of modules, dedicated firmware versions can be uploaded to the FC7 board. The AMC13 can provide high rate triggers that are distributed to the FC7 via the backplane when both are inserted in a µTCA crate.

The *d19c-firmware* [CMS25] is the firmware that is used to read out 2S modules with FC7 boards. It is constantly evolving during the prototyping phase of the Outer Tracker modules.

The *CMS Tracker Phase-2 Acquisition & Control Framework* (Ph2_ACF) [CMS24a] is a software framework written in C++. It is developed to read out the CMS Outer and Inner Tracker modules during the prototyping and integration phase of the tracker upgrade. The Ph2_ACF enables communication between the computer and FC7 via Ethernet so that the computer can send commands and receive data from the modules. There are different routines for the module readout implemented in the Ph2_ACF.

To be able to detect crossing particles in the same way independent of the position of the hit in the 2S module, all channels have to respond similarly at a specific threshold and the electronic noise has to be known to be able to set a suitable threshold for detecting the particles but not counting too many noise hits. To achieve these requirements two steps have to be executed one after the other – the *offset trimming* and the *noise measurement*.

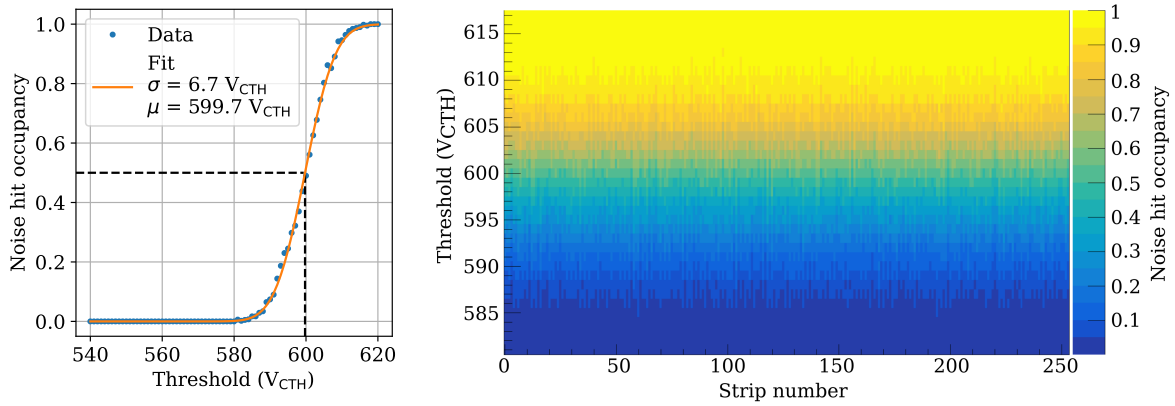

(a) (b)

Figure 3.15.: S-curves of 2S module channels. (a) S-curve of a 2S module channel. With increasing threshold the noise occupancy decreases. Lower internal thresholds in V_{CTH} correspond to higher physical thresholds in electrons. The fitting parameters are given in the plot where σ is the channel noise and μ the pedestal. The pedestal is indicated with dashed lines. (b) 2D histogram of S-Curves of 2S module channels belonging to one CBC readout chip. After the offset trimming, the pedestal values of all channels are at the same threshold value.

Noise Measurement and Offset Trimming

Since the modules are read out binary, a threshold scan is performed to measure the noise of each channel. At different threshold values, n events are recorded, and it is counted how often each channel gets a noise hit. This noise hit occupancy defined in equation (3.17) of each readout channel has an S-curved shape which can be seen in figure 3.15a. Low internal threshold values in V_{CTH} correspond to high physical threshold values in electrons. This S-curve is the integral of the channel noise. Assuming only Gaussian noise it can be described by

$$f(x) = \frac{1}{2} \cdot \left(1 + \operatorname{erf}\left(\frac{x-\mu}{\sqrt{2}\sigma}\right)\right) \tag{3.15}$$

with the threshold x, the pedestal μ and the width σ. The width σ is referred to as the channel noise and the pedestal μ is the threshold value at which the noise hit occupancy is at about 50 %.

By tuning the offset values of each channel individually, the pedestals of each channel can get equalized. This procedure is called offset trimming. Figure 3.15b shows threshold scan results of the channels of one sensor and CBC after the offset trimming. The pedestals (green) are at the same threshold for all channels and thus, all channels will show similar response at a specific threshold.

The channel noise of all 4064 channels of a 2S module is depicted in figure 3.16. The top sensor shows, in general, a lower noise level than the bottom sensor since the foldover of the FEHs to the bottom sensor induces additional capacitive noise to the bottom sensor channels. Also, the edge strips of the sensors, often show increased noise of about $8\,V_{CTH}$. To further compress the noise information of all channels of a module in comparison plots like figure 4.3, it is plotted as *candle plots* in chapters 4 to 6. A detailed description of these plots is given in section 4.1. The mean value of the noise of all channels of a module is referred to as the *module noise*. To convert V_{CTH} units to electrons a conversion factor of $156\,e^-/V_{CTH}$ is used [Mai19].

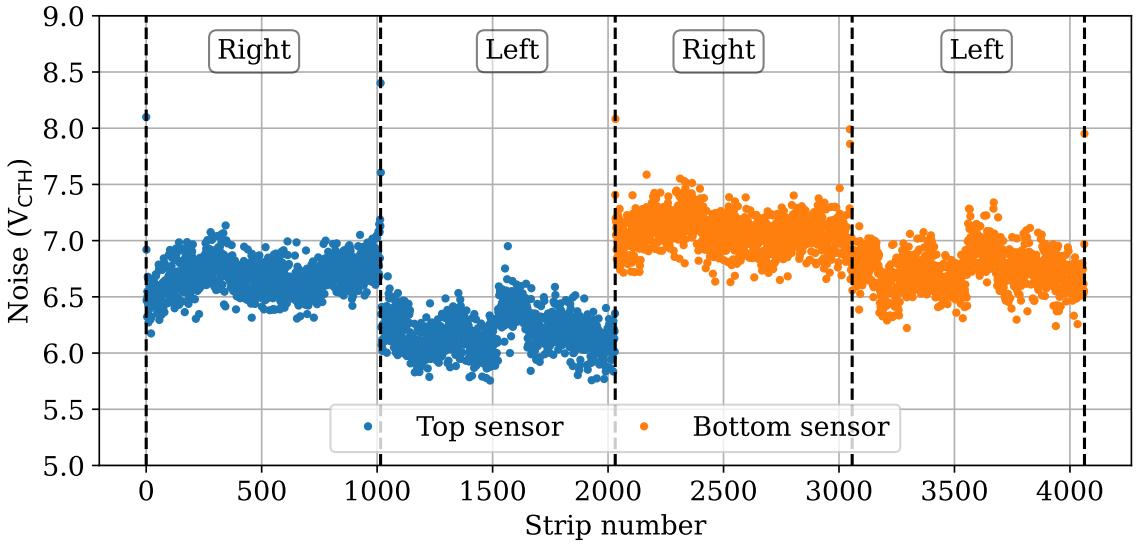

Figure 3.16.: Noise over strip number of a 2S module. The strip noise of a 2S module is shown for all 4046 channels. The strip numbering is chosen such that the four different parts of the module – top right, top left, bottom right and bottom left – are shown separately. The vertical dashed lines indicate the borders between the module parts.

Latency Scan

Taking data with external triggers requires additionally a latency scan to determine how far inside the data buffer the event corresponding to the trigger signal can be found. The *latency* is the time delay between writing the L1 data in the CBC buffer and the arrival of the trigger signal at the CBC. Due to the different data streams for L1 hit data and stub data, a second latency scan has to be performed to determine the *stub delay* between the stubs in the FC7 data buffer and the L1 trigger in the FPGA state machine. The latency for the readout can be changed in steps of bunch crossings (25 ns).

Definitions

The *relative threshold* t_{rel}

$$t_{\text{rel}} = \frac{\mu - t}{\sigma} \tag{3.16}$$

can be used to quantify the threshold setting during a measurement. It expresses the real threshold setting t in units of the noise σ of the system. It can be used to compare data of different module parts or modules.

The *hit occupancy* η per channel is defined as

$$\eta = \frac{\#\text{ hits}}{\#\text{ events} \cdot \#\text{ channels}} . \tag{3.17}$$

If there is no source or beam generating the hits in the silicon but just the noise of the module is measured, this quantity is called the *noise hit occupancy* η_{n}.

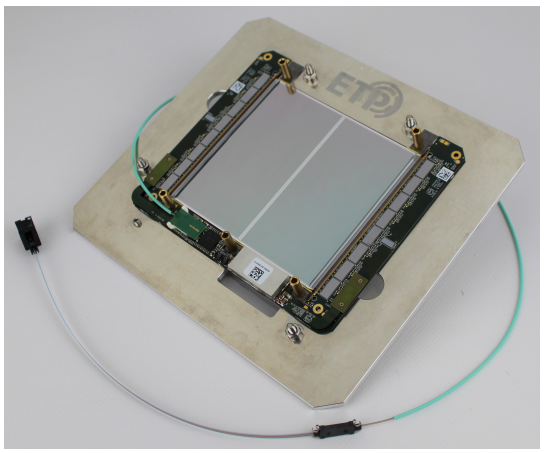

(a) 2S prototype module

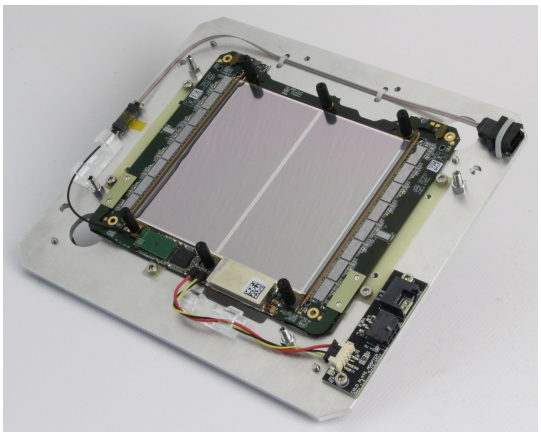

(b) 2S kickoff module

Figure 3.17.: Pictures of 2S prototype and kickoff modules. The most recent 2S module prototypes are shown mounted on aluminum carriers for easier and safe handling. Both have the same outer dimensions as the production modules will have.

3.3.5. Prototype and Kickoff Modules

During the preparation for the Phase-2 Upgrade of the CMS Outer Tracker, several 2S module prototypes were built over the years. The first prototypes were read out electrically. Then, optically read out prototype modules were built. The first optically read out 2S module prototypes are called 8CBC3 2S modules. The hybrids of these modules were larger than foreseen in the final module design. They are not further explained here since this thesis does not show measurements with these modules. For detailed explanations and (noise) measurements with 8CBC3 2S modules see [Kop22]. Since 2021, 2S modules with the final outer dimensions were built within the CMS Tracker community. With these modules, tests on final subdetector structures got possible. There are two versions, called *2S prototype modules* and *2S kickoff modules*. Both are pictured in figure 3.17. The measurements presented in this thesis are all performed with either prototype or kickoff modules.

Prototype Modules

A 2S prototype module can be seen in figure 3.17a. This is the first module type during module prototyping where the CIC chip is bump bonded onto the frontend hybrids. Some modules were built with FEHs assembled with CIC chips of the version CIC2 and others with the version CIC2.1. Both – the CIC2 and CIC2.1 – fulfill the requirements for the CMS Phase-2 Outer Tracker. [Vir+22] bPOL chips [CER24a; CER22] are used to control the DC-DC converter stages. The lpGBT chip on the SEHs are either of the version v0 [lpG22] or v1 [lpG24; Mor+24]. The forward error correction of the lpGBT is set to FEC5 in the prototype modules. The opto-electrical conversion for the output signals of the modules is performed with the VTRx+ module [Ola+20]. On some prototype modules, I^2C-problems were observed that prevented reading data from both FEHs at the same time. This was solved by bypassing the I2CM0 by connecting the VTRx+ I2C master to the left FEH I2C bus. With this soldered connection (I^2C patch), the affected modules could be read out with a small software fix without any problems. [FK21]

Kickoff Modules

The noise of the prototype modules turned out to be higher than foreseen by the hybrid design. Due to that it was decided to have another prototyping round before starting with the pre-production. These modules are called kickoff modules (see figure 3.17b). A 100 Ω resistor was added to the high voltage tails of the kickoff modules (for more details see section 4.1.1) and the thermistor for reading the temperature on the silicon sensor was modified to 1 kΩ. Additionally, the SEH design changed compared to the prototype modules. The design changes address mainly the grounding scheme of the SEH and have the purpose to reduce the noise on the kickoff modules. Two SEH variants were introduced, the *common plane SEH* and the *split plane SEH*. In the split plane SEHs, "the [ground] plane is split to block the common-mode voltage difference generated by the return currents of the switching activity" [Kov+23]. All SEHs are equipped with an lpGBT of the version v1. The forward error correction of the lpGBT is set to FEC12 in the kickoff modules. To further reduce the noise, the FEHs were changed to be able to connect a so-called *ground-balancer* visible in figures 3.11 and 3.17b. This connects the ground and 1.2 V lines of the left and right FEH. Light shields like in figure 3.11 were just connected to some modules during some measurements. Even though they reduce the leakage current of the module by shielding the light emission of the VTRx+, the noise is not significantly changed by the light shield. The effect of the reduced shot noise (see equation (3.4)) on the total noise is too small. The stub data readout of the right FEH does not work for the 2S kickoff modules because one stub data e-link was not routed properly to the lpGBT when changing the SEH design from FEC5 to FEC12 readout. [Pau24]

Common plane SEHs will be used for the pre-production and production modules. The pre-production started in October 2024 and the production will start in 2025.

Measured Modules

Within this thesis, system and integration tests were performed with 2S prototype and kickoff modules. All prototype modules used in this thesis are listed in table A.1, while a list of all used kickoff modules can be found in table A.2. The CMS internal official module names are given in the tables as well as the information in which test they were used at which position. The position labeling of each test can then be found in the respective chapter. Also, other information like the lpGBT version is listed. An example of an official 2S prototype module name is 2S_18_5_KIT-00001. *2S* indicates the module type and *18* the sensor distance of 1.8 mm. The next number *5* means that this module has five cooling points. *KIT* is the acronym for the module assembly center that this specific module built. The modules used in this thesis are from the following assembly centers: Aachen (AAC), Brussels (BEL), Brown (BRN), Fermilab (FNL), Perugia (IPG), Karlsruhe (KIT) and Islamabad (NCP). The last five-digit number after the hyphen is an incrementing number per module assembly center. Numbers with the structure 000yz are used for prototype modules while 001yz is used for kickoff modules. The (pre-)production module numbers are structured like 1$wxyz$.

3.3.6. Assembly and Integration Flow

The construction of the Phase-2 Outer Tracker will happen in several steps executed at different institutes all over the world. The assembly and integration flow is depicted in figure 3.18. The 2S and PS modules will be first assembled at so-called *assembly* centers. After the assembly, the modules undergo the *burn-in* procedure in which they are cycled several times between 20 °C and −35 °C during a time span of about 48 hours. Passing also this test, the modules get integrated to the subdetector structures in the *integration* centers. The integrated subdetectors get then shipped to the *Tracker Integration Facility* (TIF) at CERN where the subdetector

parts are combined to the full TBPS, TB2S and TEDD. From there, they come to *Point 5* at the HL-LHC where the CMS experiment is located. The whole Phase-2 Outer Tracker will be mounted into CMS starting with the barrel parts and continuing with the endcaps. After the placement of the tracker, it can never again be accessed during the whole operation time of about 10 years. Thus, it is extremely important to test the modules before the construction of the tracker very well.

The CMS community has seven assembly centers for 2S modules and five assembly centers for PS modules. The assembly centers get the silicon sensors from six *sensor quality control* (SQC) centers. The FEHs and SEHs are tested at CERN before they get distributed to the assembly centers. Nevertheless, the assembly centers make a reception test of all the components before they start with the assembly of a module. The assembly consists of subsequent steps that are each followed by a quality control measurement. Detailed descriptions of the module assembly can be found in [Mai19; Kop22].

The *Institute of Experimental Particle Physics* (ETP) at the *Karlsruhe Institute of Technology* (KIT) is one of the 2S module assembly centers and pledged to build about 1300 2S modules for the Outer Tracker. It could be that this number will be even increased to about 2000 modules. The production started in October 2024 and will last about two to three years. For the module assembly at KIT, a large clean room is used to have all steps of the assembly near to each other. The modules assembled at KIT will also be thermally cycled at KIT in a burn-in station that can house up to eight 2S modules at once. The burn-in setup is not located in the same clean room. Part of this thesis was to participate in the setup procedure of the burn-in station and to perform the first burn-in measurements with the pre-production modules from October 2024. As visible in figure 3.18, the modules from KIT will be shipped to the integration centers DESY (Hamburg, Germany), Lyon (France) and IPHC (Strasbourg, France). DESY and Lyon are TEDD dee integration centers while the IPHC is an integration center for TB2S ladders.

To guarantee equivalent conditions for the module measurements at different locations an *Outer Tracker Module Test Station* was developed within [Kop22]. It will be used for the tests of the fully assembled modules before and after wire-bond encapsulation at all assembly sites as well as for the reception tests that are performed at the integration centers after receiving the module and before the integration. A picture of this test station installed in the module assembly clean room at KIT is shown in figure 3.19. 2S and PS modules can be tested in this setup mounted on their aluminum carriers. High and low voltage can be applied to the modules using any laboratory power supply. The fibers for optical module readout are connected to an FC7 board that is either plugged to a µTCA crate or a nanoCrate. Dry air can be flushed to the setup. This setup was used for several measurements during this thesis. The other setups used in this thesis are described when the results are presented. They all have in common that they deliver dark and dry environment for the modules. The power supplies differ from setup to setup, but the modules are always read out with an FC7 board.

The Phase-2 Outer Tracker project transitioned from the R&D to the production phase during the time of this thesis. The first 2S modules with the final outer dimensions were assembled in 2021, which made integration tests on the final detector structures possible. Since the integration centers IPHC and DESY are the closest to KIT, the integration tests performed within this thesis took place there or at CERN in cooperation with the IPHC group. This allowed also the people from the integration centers to learn about the module readout and to train the integration with real modules instead of dummy modules. The combined knowledge of all contributing groups with their own special fields of expertise made the tests possible.

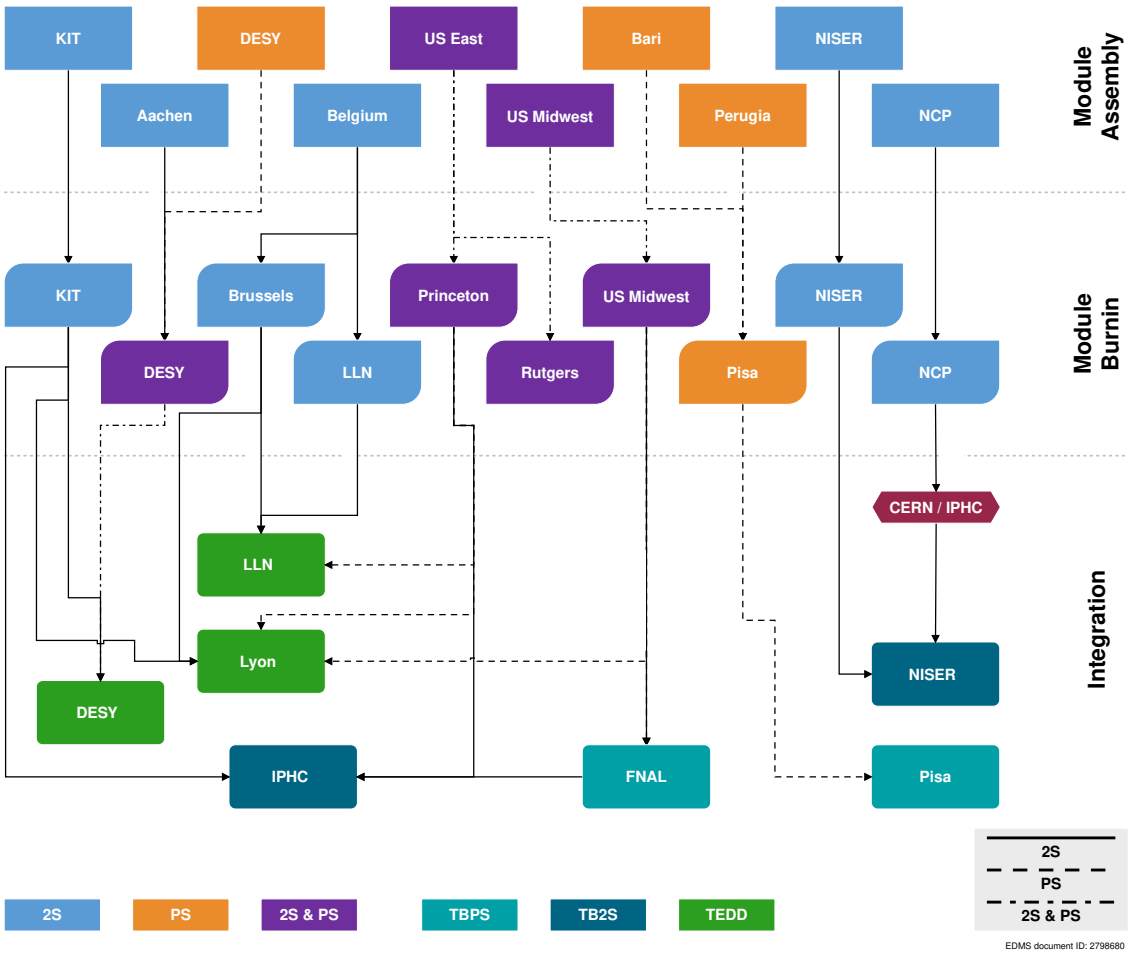

Figure 3.18.: 2S and PS module assembly and integration flow. The module assembly and integration flow is shown starting with the module assembly, continuing with the module burn-in and ending with the integration. The color of the assembly (burn-in) centers indicates whether 2S, PS or both module types are assembled (thermally cycled) at this center. The color of the integration center indicates the integrated subdetector system TBPS, TB2S or TEDD. The line style of the flow charts represents as well the module types that get shipped between the centers. Adapted from [CMS24c].

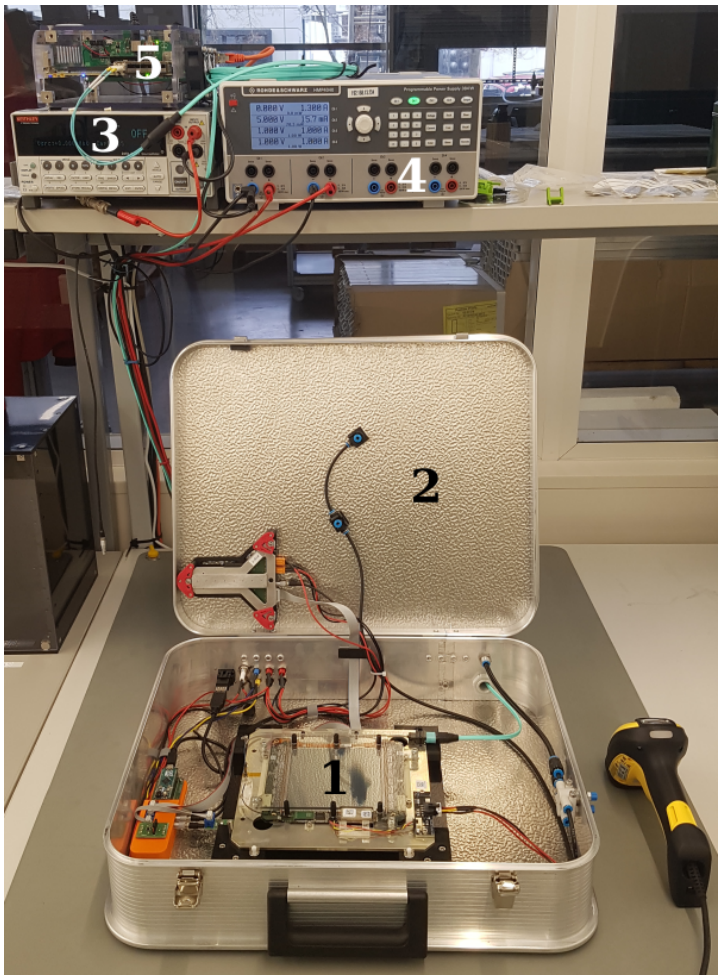

Figure 3.19.: The Outer Tracker Module Test Station. A pre-production module (label "1") is placed inside the Outer Tracker Module Test Station (label "2") in the clean room for module production at ETP. Laboratory power supplies provide the high voltage (label "3") and low voltage (label "4") for the module operation and an FC7 board in a µTCA crate (label "5") is used to read out the module.

Part II.

Main

4

Single Module Characterizations and Multi-Module Readout

The laboratory tests performed within this thesis have the purpose to characterize individual 2S modules before they are used in hodoscope arrangements and beam tests as described in chapter 5 as well as before performing large scale functional module tests on subdetector structures shown in chapter 6. Section 4.1 describes noise measurements performed with prototype and kickoff modules while section 4.2 introduces the software and firmware developments for the 2S module readout that were implemented for the module tests performed in this thesis.

4.1. Noise Measurements

How noise measurements are performed on 2S modules using threshold scans was already explained in section 3.3.4. For the results shown in the following, 1000 events per threshold step were recorded. The results shown in section 4.1.1 were obtained in preparation for the Full TB2S Ladder Integration Test while the measurements of section 4.1.2 are a CMS Tracker Group wide effort, which are shown here to explain noise features of the 2S kickoff modules that are needed in chapter 6.

4.1.1. Additional Resistance on High Voltage Tails

The 2S prototype module noise was unexpectedly about $1\,\mathrm{V_{CTH}}$ higher than the noise of the previous 8CBC3 2S modules (see section 3.3.5). [Kop22] This must be related to the changed hybrid design of the 2S prototype modules compared to the previous 8CBC3 2S modules. [Zog+22] During very detailed noise studies with 2S prototype modules it was shown that "[by] introducing resistors into the HV tails, the module noise level can be improved" [Kop22]. A simplified version of the HV circuit with the additional $100\,\Omega$ resistance is depicted in figure 4.1. At the SEH side, the high voltage passes a low-pass filter before reaching the sensor backplanes via the HV tails. The assumption is that the $100\,\Omega$ resistance increases the impedance of a loop that is formed by the two HV tails connected at the SEH. This loop can pick up a time-varying magnetic field from the DC-DC converters escaping through the PCB of the SEH. Large noise currents get generated by a small electromotive force that appear in the analogue frontends as noise. [Zog+22] Also, the insertion of $100\,\Omega$ in just one of the sensors HV circuits would then increase the impedance and thus reduce the noise of the module. The $100\,\Omega$ resistor was not yet added to the HV tails of the prototype modules but for kickoff modules.

Since many results shown in this thesis are based on noise measurements it is important to have as little noise as possible during the measurements. Even though the observable is a change of the noise, lower noise can increase the sensitivity of the modules noise to grounding and setup specific issues. For the purpose to reduce the module noise, the prototype modules got equipped with so-called *high voltage tail adaptors* (HV tail adaptors) as depicted in figure 4.2a. They are a small flex PCB piece adding additional $100\,\Omega$ resistance to the HV circuit of the 2S

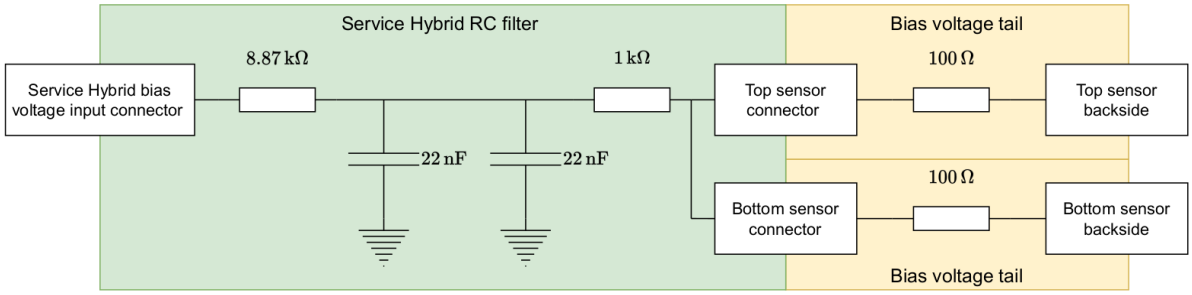

Figure 4.1.: Simplified diagram of the 2S module HV circuit. The bias voltage connected to the SEH reaches the top and bottom silicon sensor backside via a low-pass RC filter (left green part). The 100 Ω resistor in the bias voltage tails were added to the schematics for reducing the module noise (right yellow part). Taken from [Pau24].

(a)

(b)

Figure 4.2.: HV tail adaptor. (a) An HV tail adaptor for 2S prototype modules is shown individually. (b) Two HV tail adaptors are connected to the top and bottom sensor HV tail of a 2S prototype module.

prototype modules. One end fits to the connector on the SEH side and one on the connector of the HV tails that are wire-bonded to the sensor backside. Two HV tail adaptors get attached to each module, one for the top sensor and one for the bottom sensor. This can be seen in figure 4.2b. The size of the adaptors is such that the modules still fit on a TB2S ladder for the measurements presented in section 6.2, but spacers had to be added to the inserts of the prototype TEDD dee to allow mounting 2S prototype modules on such structures (see section 6.3).

Figure 4.3 shows the strip noise of the twelve modules that were mounted on a TB2S ladder prototype during the full ladder integration test described in section 6.2 before and after the attachment of the HV tails. The strip noise distribution is shown with boxes extending from the first to the third quartile and whiskers extending to the farthest data points lying within 1.5 times the interquartile range. The median is represented by the stroke within the box. The data points outside the whiskers are outliers and also shown. The plot shows that the noise levels of the modules are about $1\,V_{CTH}$ to $2\,V_{CTH}$ reduced when the HV tail adaptors are

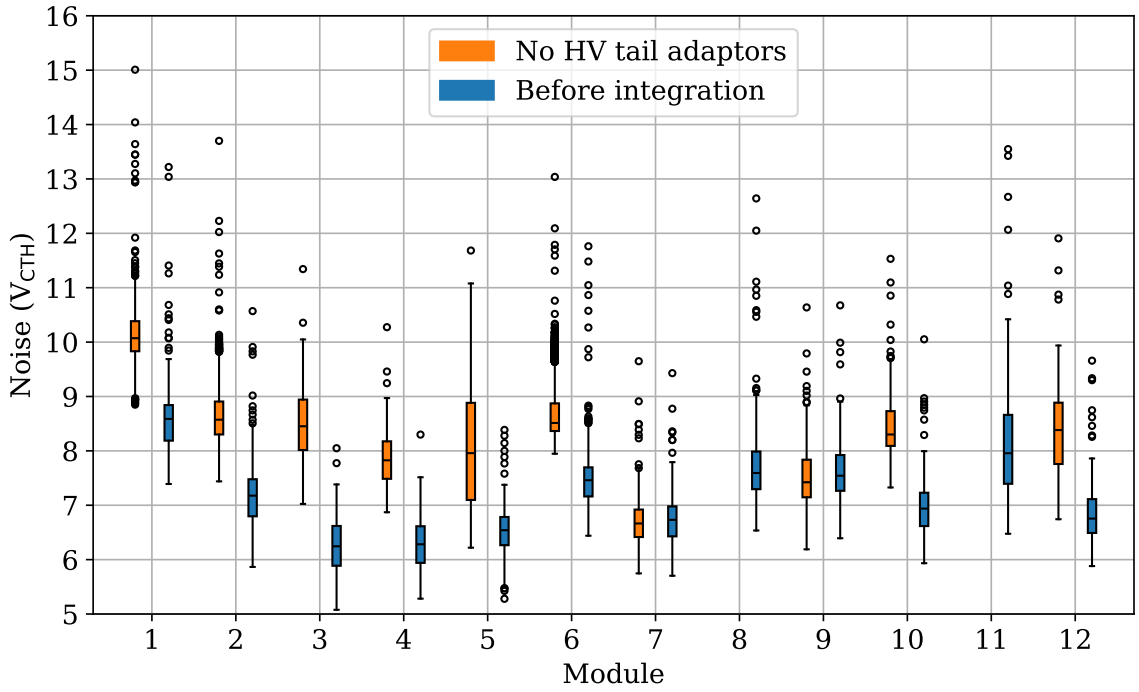

Figure 4.3.: Noise reduction by HV tail adaptors. The noise with and without HV tail adaptors is plotted for all modules used during the full ladder integration test (see section 6.2). Specialities of the individual modules are described in the text. A zoomed out version of the plot showing all outliers can be found in the appendix in figure B.1.

attached to the HV circuit of the modules. Being in the prototyping phase of the modules there are specialities for some modules. The connector at the SEH to plug in the HV tail of the bottom sensor was broken on module 1 and 2. Thus, the high voltage was connected to the bottom sensor with a special soldered hotfix that connected the HV tail to the SEH with a small cable. Due to this, the HV tail adaptor could just get plugged to the top sensor. However, a noise reduction of both sensors is, as expected, observed. Module 7 and 9 had already other self-made HV tail adaptors attached so that the first measurement shows the noise values with those and the second measurement the noise with the adaptors visible in figure 4.2. Both adaptors lead to the same improvements regarding the module noise. The HV tail adaptor of module 8 got already attached to the module before the integration test so that no measurement without tail adaptors is available from this test. Module 11 was built with the new HV tail design where the 100 Ω resistors are already included. It is not understood why this module has higher noise than the other modules with the HV tail adaptors. A zoomed out version of the plot in figure 4.3 can be found in the appendix in figure B.1 showing additional outliers due to unconnected and noisy strips.

Summarizing, a noise reduction of $1\,V_{CTH}$ to $2\,V_{CTH}$ was observed by adding an HV tail adaptor with 100 Ω to the HV powering scheme of the prototype modules. To all prototype modules used for the following tests presented in chapters 5 and 6, an HV tail adaptor was added beforehand. The resulting lower module noise provides higher sensitivity to grounding effects that could influence the module noise during the performed tests. Kickoff and (pre-)production modules were and will be built with HV tails of a new design in which this resistance is already

part of the HV tail. Thus, the measurements of kickoff modules presented in the following section 4.1.2 and chapters 5 and 6 were also performed with the 100 Ω resistance.

4.1.2. Kickoff Modules

After the observation of the about 1 V_{CTH} increased noise of the prototype modules, the SEH design was scrutinized again. The hybrid designers found some weaknesses in the design and redesigned the SEH. The new design exists in two versions, the common plane and the split plane design. Both are explained in section 3.3.5. A very detailed description of the different SEH designs during the development and prototyping phase can be found in [Pau24]. Additional to the SEH design changes, ground balancers and new HV tails with the 100 Ω resistance are used for the kickoff modules. To provide as many measurements with different combinations as possible, the SEHs were not glued to the bridges during the module assembly. At each assembly site, all SEHs were attached to all "incomplete" modules of silicon sensors and FEHs. This allowed for a larger number of measurements at different modules with the limited number of parts for the kickoff modules. These measurements were then used to define the final SEH design for the (pre-)production modules.

Measurements with and without ground balancers for both SEH designs – common plane and split plane – were performed at room temperature and −35 °C. These results as well as measurements from prototype modules are plotted in figure 4.4 [DM24]. The measurements are a CMS Tracker Group wide effort to come up with a solution for the final SEH design as fast as possible.

The first two data points show the noise measured on the prototype modules. The mean value of about 6.8 V_{CTH} is higher than the expected design value of 1000 e^- corresponding to 6.4 V_{CTH} for a conversion factor of 156 e^-/V_{CTH} [Mai19]. The results with a ground balancer connected show reduced noise. The measurements with the common plane SEHs show similar noise values as the prototype modules. The measurements at −35 °C have further reduced noise in general. Also in the measurements performed in cold, the noise reducing effect of the ground balancers can be observed. The mean noise of the split plane SEH modules is unexpected with 7.8 V_{CTH} (9.1 V_{CTH}) with (without) a ground balancer even higher than the prototypes modules noise.

Based on these tracker community wide measurements it was decided to use the common plane SEH design for the modules in the final Phase-2 Outer Tracker, and to attach a ground balancer to every module.

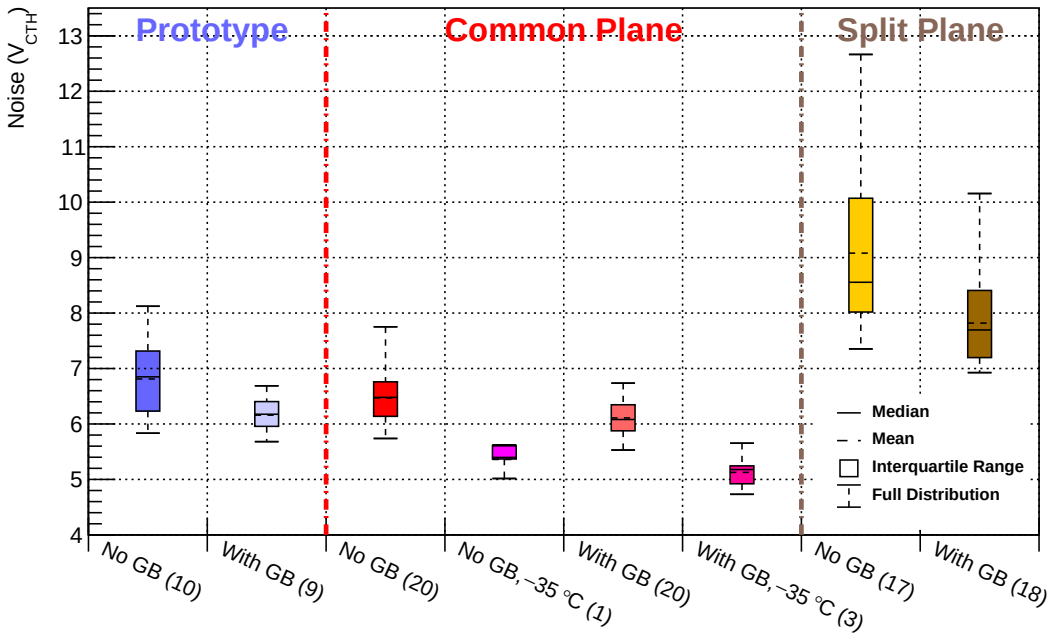

Figure 4.4.: Noise of 2S prototype and kickoff modules in different configurations. The measurements are performed at 350 V bias voltage and either at room temperature or at −35 °C as indicated in the axis label. The ground balancer (GB) connects the GND and 1.2 V lines of the left and right FEH. "Common Plane" and "Split Plane" refers to the SEH version used in the kickoff modules. The boxes and whiskers represent the distribution of all individual channel noise measurements and include measurements from several modules of different assembly sites. Module quantities are indicated in parentheses. Taken from [DM24].

4.2. Software and Firmware Changes for the Multi-Module Stub Readout

In order to properly read out more than one hybrid or module at the same time, some changes were needed in the firmware for the FC7 board and in the readout software. The changes were originally implemented by Sarah Seif El Nasr-Storey (University of Bristol/CERN) for the measurements during the full TB2S ladder integration test described in section 6.2. Since they were never merged to the master branches of the firmware and software repositories, I took care of reimplementing the changes with help from Guido Magazzù (INFN-PISA/CERN) on the firmware side and Fabio Ravera (FNAL) on the software side.

When reading out multi-module systems, the challenge is to align all stub and L1 data from the different CICs properly. During the readout with the Serenity board, this is done all in FPGA but for the FC7 readout, some parts of these steps are performed in the readout software Ph2_ACF.

The stub data output of the CICs is organized in packages (eight *boxcars* (BXC) transmitted in eight consecutive clock cycles) as depicted in figure 3.14a. To be able to reconstruct to which bunch crossing each stub belongs, a 3-bit *bunch crossing offset* (BX offset) is part of the stub data. To properly read out stub data, the first boxcar of the stub data package has to be identified. In the Serenity board, this is done directly in the FPGA. In the FC7 readout a scan needs to be performed in order identify the first boxcar that contains the BX ID. Figure 4.5 illustrates the stub data readout with a correctly set stub package delay while figure C.1 depicts the same with a wrong stub package delay. When a *BC0 command*, that resets the BX ID counter, is sent to the FE, the *finite-state machine* (FSM) in the CIC reader, originally in the idle state, goes in a wait state. It remains in the wait state for a number of clock cycles defined as *stub package delay* plus one clock cycle. Data can be properly decoded only if the first boxcar of the stub package is detected during the first clock cycle in the run state. This situation is shown in figure 4.5. A wrong stub package delay does not start the run state of the FSM in the CIC reader at the correct time (see figure C.1). As soon as the read stub data are reasonable, as explained later, the current value of the stub package delay is stored for this module and used for further data taking. The BX ID contained in the CIC stub data is used to check if the stub package delay scan worked and if the module stub data are read out properly. The BX IDs of the two hybrids of a module have to be the same for the same event and the BX IDs of subsequent triggered stubs need to have a trigger frequency dependent difference. This difference is 400 for the internal trigger rate of 100 kHz that is used during the stub package delay scan in the Ph2_ACF.

The L1 and stub data flow is depicted in figure 4.6. The *latency* is defined as the number of clock cycles between the write operation of the L1 data in the FE data buffer and the arrival time of the L1A trigger in the FE. This is in principle module dependent, e.g., when the modules are connected to the FC7 with fibers of different lengths. In the presented measurements, the correct latency was always the same for all read out modules, which were all connected to the FC7 with fibers of the same length. The correct latency is determined by scanning the latency with the Ph2_ACF software. The L1 data are read out at each latency value and the latency at which the expected data are found is used for the further data taking. The *stub delay* is the number of clock cycles between the write operation of the stubs in the FC7 data buffer and the arrival time of the L1A trigger in the FC7. It is also determined by a scan with the Ph2_ACF software that is performed after the stub package delay scan. Thus, the correct stub package delay is already set for all modules when the scan of the stub delay is performed and the stub data that are read out are correctly decoded. The stub delay is changed in steps of bunch crossings and at each value, the stub data are read out. The stub delay, at which

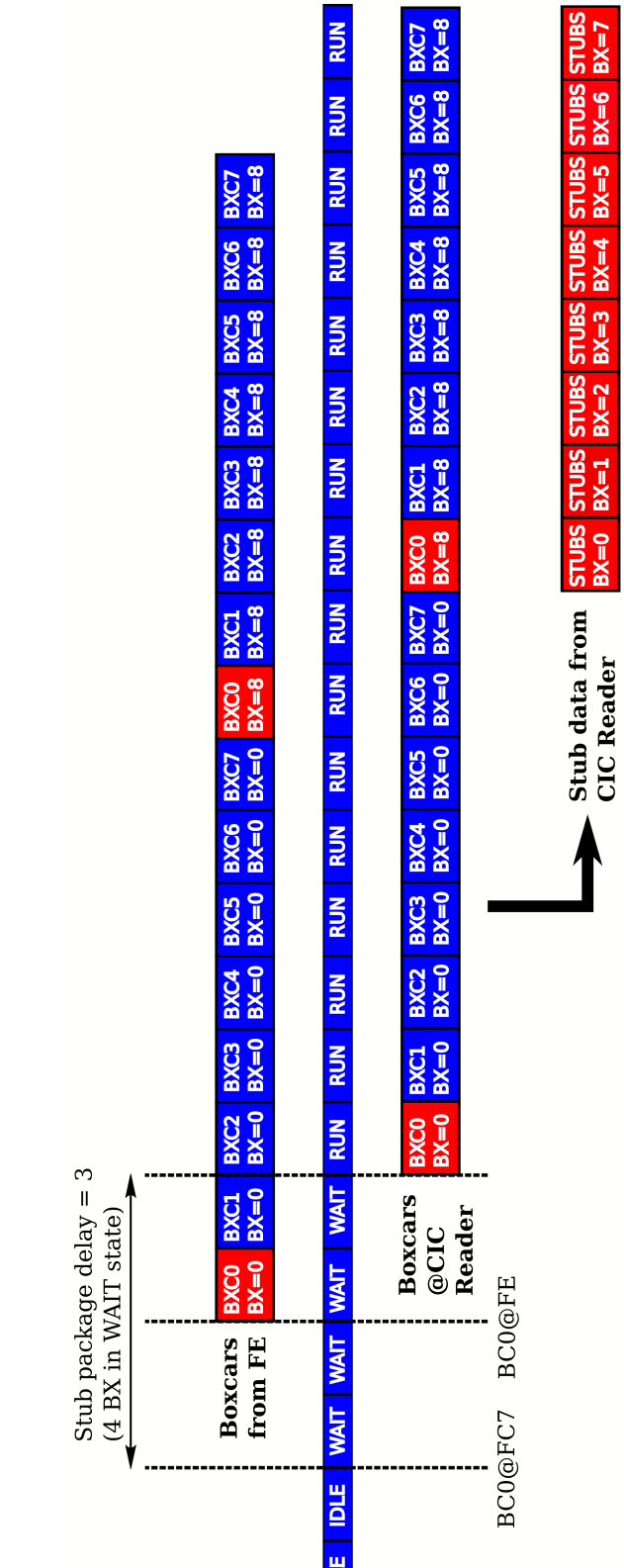

Figure 4.5.: Illustration of the stub readout with a correct stub package delay. A BC0 command resets the BX ID counter in the FE. When the BC0 command arrives at the FC7, the finite-state machine (FSM) of the CIC reader goes from the idle to the wait state. It remains there for the number of clock cycles equal to the stub package delay plus one. Then, the run state is entered, and the stub data are read out. The stub data are reasonable when the CIC reader starts reading the stub data at the boxcar 0 (BXC0). In this figure this is the case since the stub package delay is set to the correct value of 3 bunch crossings. Adapted from [Mag24].

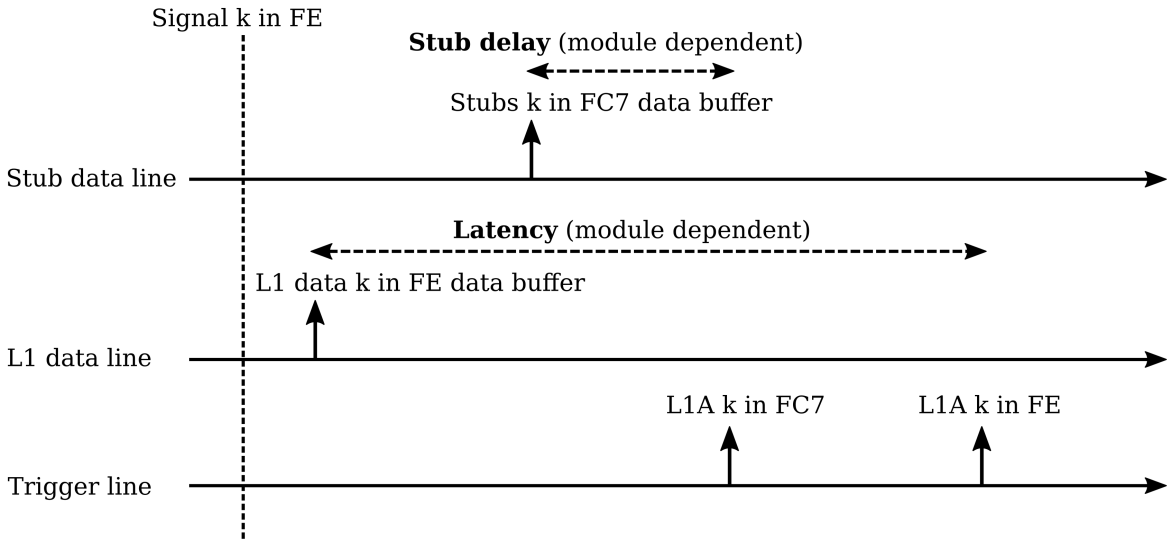

Stub delay: Number of clock cycles between the write operation of the stubs in the FC7 data buffer and the arrival time of the L1A trigger in the FC7

Latency: Number of clock cycles between the write operation of the L1 data in the FE data buffer and the arrival time of the L1A trigger in the FE

Figure 4.6.: Illustration of the stub delay and latency. The stub data line, L1 data line and trigger line are shown. The meaning of the stub delay and latency is depicted and explained in the text. Both are module dependent and have to be handled separately for each module during the readout. Adapted from [Mag24].

the expected number of stubs at the expected positions is found, is then used for the following data taking. For both, the latency and stub delay scan, real data with actually present hits in the L1 data and stubs are needed. The data can either come from test pulses or particles like Sr^{90}-electrons, cosmic muons or particles from a test beam. Test pulses are injected into the frontend amplifiers by using on-chip capacitors. They can be used to measure the channel response to a known signal and to test the L1 and stub data readout with known expected hit and stub positions.

The developments for the multi-module stub readout in software and firmware addressed the individual handling of the stub package delay and stub delay per module. Now, there are two 32-bit registers used for the stub package delay. The first contains the stub package delay values from module 0 to 9, which uses 30 bits of the 32-bit register, and the second contains the stub package delays of module 10 and 11. For the 9-bit stub delay four 32-bit registers are now used. The first contains the stub delay values from module 0 to 2 and so on. With this, 27 bits of each of the four 32-bit registers are used. Also, the size of some variables of the software was changed from 8-bit to 16-bit.

With these changes, the 2S and PS module stub readout during the beam tests presented in section 5.2 and the data taking during the integration tests presented in chapter 6 was possible. The developments are also needed for all measurements in the module burn-in setups as well as for the measurements during the subdetector integration at the integration sites.

During tracker operation, the modules will be read out by Serenity boards (see section 3.3.4) on which the described module data synchronization will be handled all in FPGA.

5 Particle Detection with 2S Modules

Stand-alone 2S modules are able to detect the position of a charged particle when crossing the silicon sensors. By the p_T-module concept described in section 3.1, they can also measure hits in both sensor layers with low spacial distance. With several layers and in the magnetic field in CMS, they will track charged particles. Thus, testing the whole data readout of 2S modules beginning with the charge deposition by charged particles in the silicon sensors is very important. During this thesis, this was done with a muon hodoscope at ETP and during a beam test at DESY. The measurement setups, analysis steps and results of both measurement campaigns are described in the following sections.

5.1. 2S Muon Hodoscope

In the laboratory, particle tracking with 2S modules can be realized by detecting cosmic muons with a hodoscope setup. For that, a muon hodoscope made of three 2S modules was set up at ETP as described below. In addition to research, it can also be used in teaching, e.g., for a laboratory exercise for Master students of a detector lecture. Students gain hands-on experience in constructing their own tracking detector.

5.1.1. Experimental Setup

For the 2S muon hodoscope the same setup as described in [Sto21] was used to stack three 2S modules on top of each other. Two scintillators are placed on the top and the bottom of the module stack. This is shown in figure 5.1b. The whole experimental setup can be seen in figure 5.1a. The modules are powered with low voltage at 10.5 V and a bias voltage of 350 V. The scintillators are powered with low voltage at 3.3 V and their signal is processed with a Zedboard [Dig14]. The firmware and software used for the signal processing with the ZedBoard are developed and described in [Gos24]. To trigger on particles crossing the setup, the coincidence signal of both scintillator signals is used as trigger input for the 2S modules. The module readout is performed with an FC7. In addition to the FMC card for connecting the modules, a DIO5 is plugged to the FC7 for triggering the module readout with the output of the trigger logic programmed with the Zedboard. During data taking, the measurement box is constantly flushed with dry air to keep the humidity low.

5.1.2. Angular Simulation

The expected angular distribution of cosmic muons that can be measured with the 2S muon hodoscope was simulated with the Monte Carlo method taking the known angular distribution of cosmic muons and the detector geometry of the 2S muon hodoscope into account. Since this angular simulation does not take multiple scattering into account, this approach is a first order simulation. For more detailed studies, a full Geant4 [Ago+03] simulation of the 2S muon hodoscope would be needed. This subsection describes the performed angular simulation step by step.

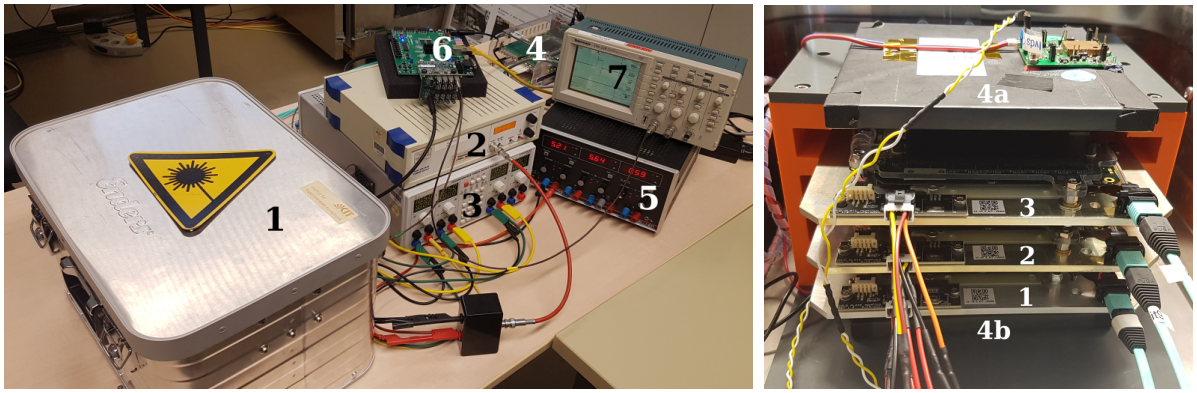

(a) Full setup **(b)** Inside the box

Figure 5.1.: Pictures of the 2S muon hodoscope. (a) The whole muon hodoscope setup is shown. The individual parts are labeled as follows: 1 – Measurement box, 2 – HV power supply, 3 – LV power supply, 4 – FC7 for module readout, 5 – Scintillator power supply, 6 – Trigger FPGA board, 7 – Oscilloscope (b) Three 2S Modules are stacked in between two scintillators. The modules mounted in the hodoscope are labeled according to table A.1 starting at number 1 with the lowest module. They are stacked with the same strip orientation in between a top scintillator (label "4a") and a bottom scintillator (label "4b").

Cosmic Muons

Muons are part of the secondary cosmic rays. They are produced when primary cosmic rays enter the atmosphere and collide with air molecules. When scattering with the air molecules, protons produce pions. Charged pions then decay into muons and neutrinos. These muons can reach the Earth's surface and can be detected with particle detectors.

The differential flux of cosmic muons at sea level as a function of the detection area A, the measurement time t and the solid angle Ω is given by

$$\frac{\mathrm{d}N}{\mathrm{d}A\mathrm{d}t\mathrm{d}\Omega} = I_0 \cos^2 \phi \,, \tag{5.1}$$

where ϕ is the zenith angle and the flux I_0 at $\phi = 0$ is $I_0 \approx 70\,\mathrm{m}^{-2}\mathrm{s}^{-1}\mathrm{sr}^{-1}$ [Kat+23].

Simulation Steps

A drawing of the geometry of the muon hodoscope is depicted in figure 5.2. The defined coordinate system is indicated as well. The variables characterizing the 2S muon hodoscope are the width of the quadratic scintillators $w = 15\,\mathrm{cm}$, the width $w_{\mathrm{sensor}} = 9.144\,\mathrm{cm}$ and length $l_{\mathrm{sensor}} = 10.0548\,\mathrm{cm}$ of the silicon sensors (see section 3.3.1), the z-positions of the sensors $z_{\mathrm{sensors}} = [3.8\,\mathrm{cm}, 3.98\,\mathrm{cm}, 6.6\,\mathrm{cm}, 7\,\mathrm{cm}, 9.5\,\mathrm{cm}, 9.9\,\mathrm{cm}]$ as well as the z-positions of the scintillators $z_{\mathrm{scintillators}} = [0\,\mathrm{cm}, 13.7\,\mathrm{cm}]$.

The simulation of the angular distribution of the cosmic muons measured in the 2S muon hodoscope is performed with the Monte Carlo method. The zenith angle ϕ is randomly generated from $-60°$ to $60°$ according to the $\cos^2\phi$-distribution given in equation (5.1). The range of the zenith angle ϕ is chosen such that the maximum detectable angle given by the acceptance of the two scintillators equation (5.5) is within the range. Additionally, an isotropic polar angle α distributed from $0°$ to $360°$ and x_0- and y_0-coordinates in the plane of the upper scintillator are generated. The angle α is not added to the drawing. The coordinates x_0 and y_0

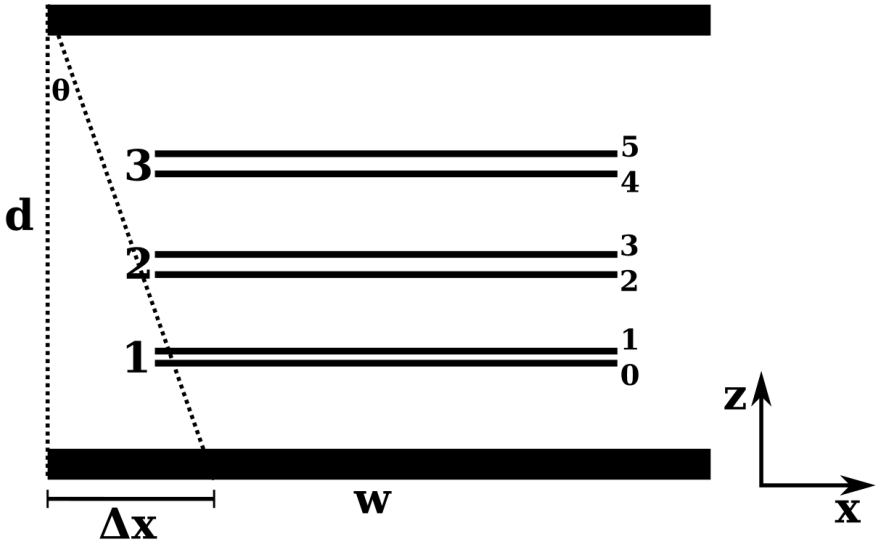

Figure 5.2.: Drawing of the 2S muon hodoscope geometry. The three 2S modules are labeled from 1 to 3 from bottom to top. The bottom module has a sensor spacing of 1.8 mm while the other modules have a spacing of 4.0 mm. The six silicon sensors of the modules are labeled from 0 to 5 from bottom to top. The angle θ is the projection of the zenith angle ϕ as given in equation (5.3). The dimensions describing the detector acceptance equation (5.4) and maximum angle equation (5.5) are indicated in the sketch.

are chosen such that they lie within the area of the upper scintillator. With this, the x- and y-coordinate of a straight track can be calculated for all values of z according to

$$\begin{aligned} x(z) &= \tan(\phi) \cdot \cos(\alpha) \cdot z + x_0 \\ y(z) &= \tan(\phi) \cdot \sin(\alpha) \cdot z + y_0 \,. \end{aligned} \tag{5.2}$$

With calculating the coordinates in the plane of the lower scintillator, tracks can be selected that would produce a hit in both scintillators. These tracks are considered as triggered tracks, and they are counted with n_{trigger}. In the notation of data taking, triggered tracks are called events since these would create a trigger signal by crossing both scintillators. The zenith angles that belong to the triggered events are denoted with ϕ_{trigger}. For some of these events, no hits are expected in the silicon layers since the area of the scintillators is larger than the area of the silicon sensors. The number of empty events is called n_{empty}. The number of events with hits in all layers is given by n_{all}. For checking if hits are expected in the individual silicon sensors, their x- and y-position is considered to be exactly in the middle of the scintillators, and it is assumed that the scintillator and silicon planes are all parallel to each other and the ground surface. The angles that would produce a hit in each of the six silicon layers are called ϕ_{all}.

With a strip length of about 5 cm the three equally orientated 2S modules of the hodoscope are only able to measure a projected angle θ of the zenith angle ϕ. The projection on a plane perpendicular to the strips is given by [Bla12]

$$\theta = \arctan\left(\tan(\alpha) \cdot \cos(\phi)\right) \,. \tag{5.3}$$

This projection is performed for all angles ϕ_{all} that fulfill the criterion of generating a hit in each of the six sensors and is denoted by θ_{all}.

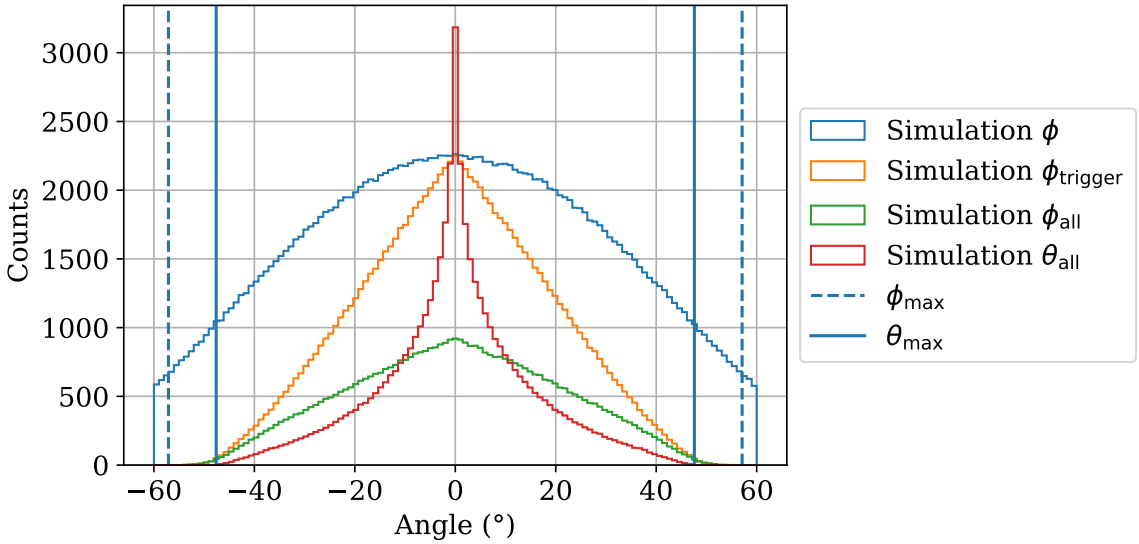

Figure 5.3.: Simulated angular distributions for the 2S muon hodoscope. The distributions of the zenith angle ϕ, the angles that resulted in a trigger ϕ_{trigger}, the angles that hit each of the six silicon sensors ϕ_{all} and the projection to the plane perpendicular to the strips θ_{all} is plotted. The maximum expected angles ϕ_{max} and θ_{max} from equation (5.5) are indicated with vertical lines.

Simulation Results

The distributions of all the angles defined above are plotted in figure 5.3. In the distribution of the zenith angle ϕ the $\cos^2$-shape can be seen. With the constraint of hitting both scintillators, ϕ_{trigger} has a triangular shape that is even flatter when taking the additional constraint of producing a hit in each of the six layers for ϕ_{all}. The smaller the angle ϕ_{trigger} the higher is the probability that the track does not hit the silicon sensors. The projection θ_{all} has a sharp peak at 0° since the projected angle is always smaller than the real one and nearly all possible angles can be projected to 0° depending on the uniformly distributed polar angle α. The maximum detectable angles are plotted with vertical lines and further explained in the next subsection.

In total, $n_{\text{trigger}} = 2095541$ events were simulated resulting in $n_{\text{all}} = 1000000$ events with hits in all layers and $n_{\text{empty}} = 715952$. Thus, about 48 % of the triggered events are expected to generate a hit in each of the six sensor layers and about 34 % of the triggered events are expected to be empty.

Acceptance and Maximum Angles

The angular simulation described above already takes into account the scintillator trigger acceptance

$$A = \frac{w - \Delta x}{w} = 1 - \frac{d \cdot \tan(\theta)}{w} \tag{5.4}$$

with w as the width of the scintillators and d the distance of the scintillators (see figure 5.2). The maximum detectables angles ϕ_{max} and θ_{max} are the angles where the detector acceptance

is zero:

$$\begin{aligned} \phi_{\max} &= \arctan\left(\frac{w_\mathrm{d}}{d}\right) = 57.1^\circ \\ \theta_{\max} &= \arctan\left(\frac{w}{d}\right) = 47.6^\circ\,. \end{aligned} \tag{5.5}$$

For $\phi_{\max}$ the width of the scintillators along the diagonal $w_\mathrm{d} = 21.2\,\mathrm{cm}$ is used while the width $w = 15\,\mathrm{cm}$ is used for the maximum value of the projected angle $\theta_{\max}$.

The analysis was split into a multi module and a single module analysis. Both are described in the following subsections.

5.1.3. Multi Module Analysis

The data presented in this subsection were recorded during a measurement time of about nine and a half days. The data were recorded in subsequent runs with 10 000 events each. In total, 830 210 events were recorded, which results in a mean trigger rate of 1 Hz. For vertical incident muons, the trigger rate expected by the flux equation (5.1) on the scintillator area is about 1.5 Hz. Thus, the measured trigger rate is less than expected which could be a result of potential less efficient areas in the scintillators. 215 847 empty events were observed, thus, the fraction of empty events of 25 % is lower than the expectation of 34 % from the simulation. The simulation does not take noise hits into account. Considering also the 30 144 events with exactly one cluster in one of the six sensors as empty, the fraction of empty events in the data is about 30 %, which is closer to the expectation. It is very likely that a single cluster in one of the sensors does not result from a muon track but from noise.

During data taking with the muon hodoscope in [Sto21], it occurred that the BX ID was different for FEHs of the same module. This was due to a bug in the firmware and software which is now fixed meaning that both sides of one module can now be read out synchronously. Nevertheless, the stub data taking regarding the stub latency setting was not enabled properly during the data taking resulting in different BX IDs of FEHs belonging to different modules. Since the goal of these measurements was to analyze the L1 data, the missing stub data do not impact the result. The stub readout chain is further analyzed in section 5.2.

For the multi module analysis that takes the hits in all modules into account, the hits in the edge strips are also masked because they showed higher noise than the other strips. Then, all events with exactly one cluster in each of the six sensors are used for further analysis. This corresponds to the cut that was also used in the simulation. With cluster efficiencies well above 99.8 % of unirradiated 2S modules in beam test measurements at the same threshold [Kop22; Wit23], this cut looses $1 - 0.998^6 = 1.19\,\%$ of events with tracks that crossed all silicon layers but were not detected in one of the six layers.

Alignment

The first step of this analysis is an *alignment* of the sensors that is performed as following. For the alignment the first 100 000 events are taken. A track is calculated by a linear regression through the cluster positions. The distance between the track and the actual position of the cluster in the sensor in the direction perpendicular to the strip in x-direction is depicted in figure 5.4. The binning is done such that each bin corresponds to 45 µm, which is the cluster position resolution in the 2S sensor with a pitch of 90 µm. A Gaussian fit is performed to the histogrammed data of each sensor and the mean value of the distribution is used to correct all cluster positions during the data analysis. The displacement of the sensors of the middle module resulting from this alignment is with about 300 µm above the specifications of 100 µm [HRM22].

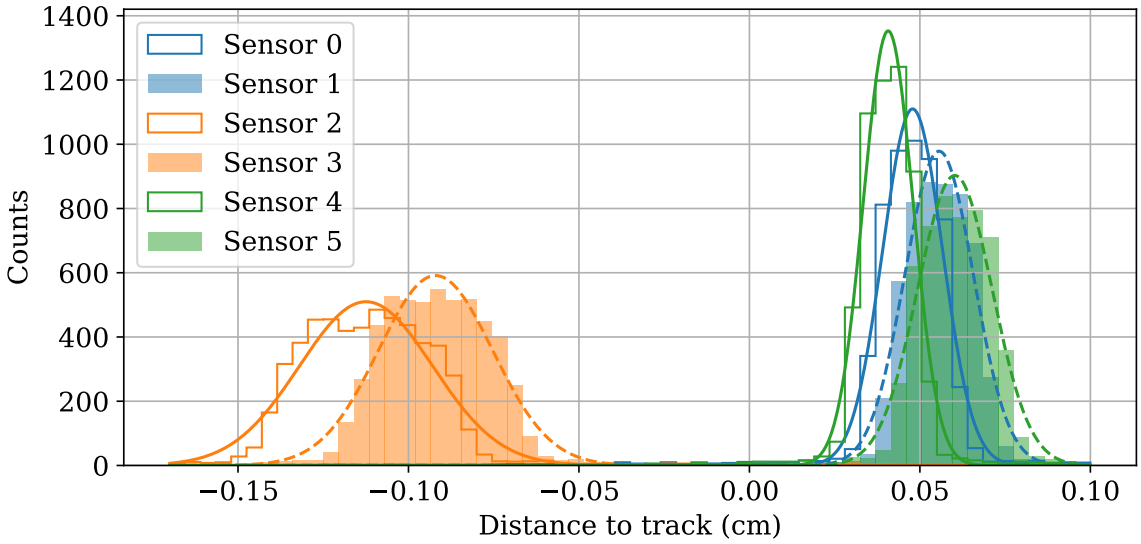

Figure 5.4.: Histogram of the distance of the cluster position to the calculated expected position from the track. For each silicon sensor beginning with number 0 at the bottom, the distance between the actual cluster position and the calculated position from the fitted track are histogrammed. The binning is chosen such that each bin width corresponds to the cluster position resolution of 45 µm. The result of the Gaussian fit to the distribution is also shown.

The displacement of the sensors of all modules is measured during the assembly procedure, and it was within the specifications for all modules measured within this thesis. Thus, the observed displacement cannot be real and is a hint that the used alignment procedure delivers too rough values.

This alignment procedure assumes that the sensors are parallel to each other and that they are not rotated in the polar angle. Also, it does not catch the telescope weak mode where all three modules are slightly shifted in the same direction perpendicular to the strips. Such an orientation of the modules would later result in an angular distribution that is not centered around 0° but shifted by some degrees depending on the shift of the modules.

Angular Distribution Measurement

For the analysis of the muon angles detected with the 2S muon hodoscope, all events with exactly one cluster in a predefined number of layers are used to get a track from a linear regression through all cluster positions. If the difference of the position of one of the clusters to the track is larger than 405 µm, this event is not included in the angular plot since the track is then most likely not just from a muon track but probably includes a noise hit. This cut allows still deviations between the cluster and track position of 4.5 strips.

The angular distributions for events with at least two layers with hits is shown in figure 5.5. It can be seen that the overall shape of the angular distribution is maximal around 0° and reduces to higher angles until the maximum angle from the detector acceptance of about 47° is reached. The stricter the cut on the minimum number of sensors with hits, the fewer events fulfil the selection criterion. Module 1 showed overall less hits and therefore contribute mostly module 2 and 3 to the tracks with hits in less than five layers. For all cuts, a shift of about −2° to negative angles can be observed that could result from the very rough alignment of the

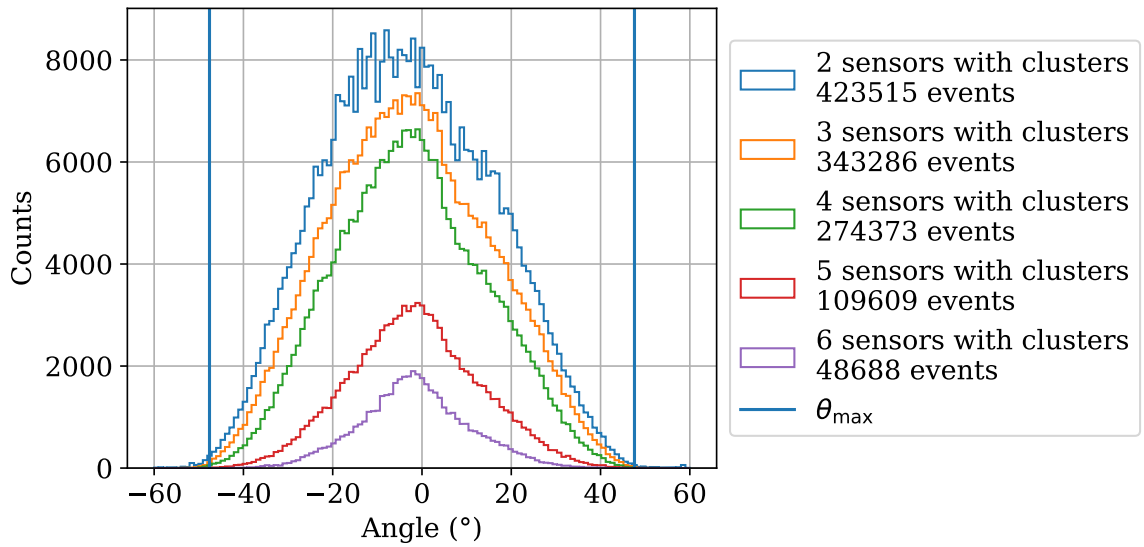

Figure 5.5.: Angular distribution measured with the 2S muon hodoscope for different cuts on the number of sensors with clusters. The angular distribution is shown for different cuts on the number of silicon sensors with clusters.

sensors that takes just shifts perpendicular to the strips into account but no displacements of the sensors along the z-axis or any rotations of the sensors. Most likely, the sensors of all modules were shifted to one direction, which was introduced in section 5.1.3 as a telescope weak mode that could not be detected by the performed alignment procedure. A shift of 1 mm to the same direction between the top and middle as well as middle and bottom module would already result in a shift of the angular distribution by the observed 2°. This difference is compatible with the tolerances of the carrier placement in the setup and the module fixation on the carriers. A not perfectly horizontal table alone cannot explain the angle shift since the 2° offset corresponds already along the sensor width to a difference of about 3 mm in height at both sensor edges. The dip at about 0° which was present in the measurements shown in [Sto21] is not present anymore. Most likely, this was there due to a mistake in the tracking algorithm and not due to a problem with the modules itself.

In figure 5.6, the simulated angular distribution already shown in figure 5.3 is plotted in comparison to the measured angular distribution with the requirement of exactly one hit in each of the sensor layers that was already shown in figure 5.5. Also, the measured angular distribution shifted by 2° is shown in figure 5.6. The simulated angular distribution is weighted such that its integral is the same as from the measured distribution. The data match the simulated distribution roughly. In the data, hits at angles about 0° as well as angles at the edges at about $20° < |\theta_{\text{all}}| < 47°$ are missing. Nevertheless, the measured angular distribution is closer to the simulated projected angle θ_{all}, that is plotted in figure 5.6 as well, than to the simulated not projected angle ϕ_{all} and the by 2° shifted distribution is symmetric around 0°. Possible reasons for the differences could be inefficient areas in the scintillators. Adding a shift of the scintillators of 1 cm to the simulation, results in very small angular distribution difference. Thus, deviations from the distribution by adjusting the scintillators by eye above and below the modules can be excluded as a reason for the differences. Also, the angle resolution of the hodoscope setup is not perfect. This effect is not yet considered in the purely geometrical simulation of the expected angle. Cluster detection inefficiencies from the 2S modules itself are

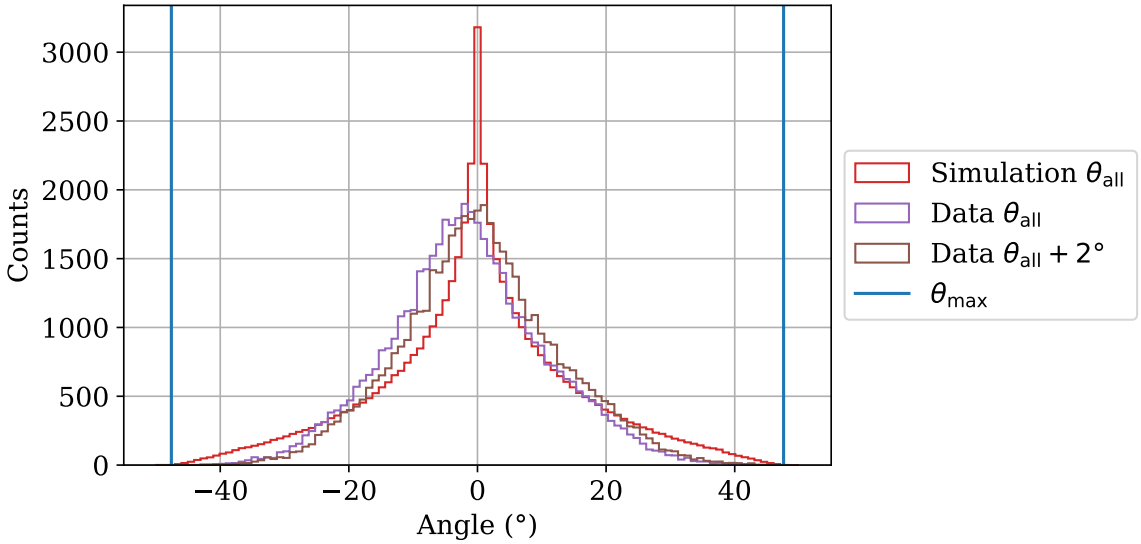

Figure 5.6.: Angular distribution measured with the 2S muon hodoscope for one cluster in each of the six sensors. The simulated muon angle as well as the projection to a plane is shown. The measured angular distribution is shown for events with exactly one cluster in each of the six silicon sensors.

not probable since they were also tested multiple times in test beam setups showing cluster efficiencies above 99.8 % [Kop22; Wit23].

5.1.4. Single Module Analysis

Another way to analyze the data from the muon hodoscope is to look at the data of each module individually. First, hits in all edge strips are masked because they have higher noise than the other strips. During later tracker operation, the offset trimming of the edge strips of the 2S modules could be adjusted such that they show the same noise hit occupancy as the other strips by applying the same threshold. In this way, these channels would not have to be masked entirely, but their signal detection efficiency would drop slightly. Then, the events with exactly one cluster in each of the two sensors of the analyzed module are taken. The cluster data of the remaining events are used for further analysis of the events.

Cluster Sizes

The cluster sizes of the clusters in all six sensors of all modules are depicted in figure 5.7. The sensors are labeled from 0 to 5 beginning with the bottom most sensor at number 0 as depicted in figure 5.2. The histograms are normed to an area of one such that differences in the cluster sizes between the modules are visible. Overall, module 1 shows more small clusters than the other modules and the percentage of the clusters measured by this module with cluster sizes larger than one strip is smaller than for the other modules. Also, the counts of the cluster sizes are nearly the same for sensor 2 to 5 but the number of clusters in the bottom module is just half about the number of clusters in the other two modules. This can be seen in the not normed version of the plot shown in the appendix in figure D.1. The reason for that is not found, but it could be that the missing clusters of the bottom module could have been observed at another latency if the timing of the modules during data taking was in an unlucky condition.

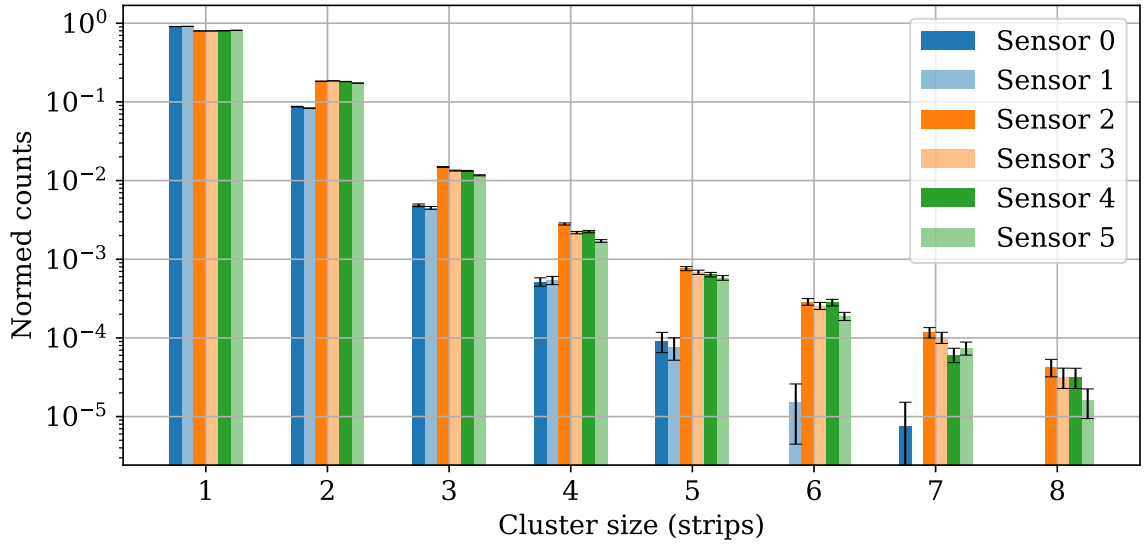

Figure 5.7.: Cluster sizes of the sensors in the muon hodoscope. The cluster sizes of all six sensors of the hodoscope are histogrammed. Sensors with the same color but different opacity belong to the same module. The sensor with the lower number and higher opacity is the bottom sensor of the module. Sensor 0 and 1 belong to the bottom module 1 and so on. The histograms are normed to an area of one. A not normed version of the plot is depicted in the appendix in figure D.1.

Offset Distribution

Instead of calculating the angle of the cosmic muons from the cluster offset in the top and bottom sensor of the module, the offsets can be investigated directly. The cluster offset has a half-integer resolution in units of strips since it is an integer value if the size of both clusters is the same or differing by an even number of strips and a half-integer number if the cluster sizes of both sensors of the module differ by an odd integer number. The cluster offset distributions of module 1 (1.8 mm module) and 2 (4.0 mm module) are shown in figure 5.8 while the results of the second 4.0 mm module 3 are shown in the appendix in figure D.2. The binning is chosen in half-integer steps so that each possible strip offset is displayed separately.

The general shape of the offsets is, as expected, maximal at an offset of zero strips and reducing to larger absolute offsets. This gives another hint that the individual modules were parallel to the ground during the data taking and that the offset by 2° observed in the angular distribution in the previous section 5.1.3 resulted from the telescope weak mode of shifted modules along the x-axis. Different combinations of cluster sizes in both sensors are plotted with different colors. The respective cluster sizes in the top and bottom sensor are given in the legend as a tuple.

Underlying the general shape that is maximal at an offset of zero strips and reducing to larger offsets, there is a subshape with two maxima at an offset of about ±7.5 strips for module 1 and ±15.5 strips for module 2. This underlying shape results from cluster combinations with a cluster size of one in one of the two sensors and a cluster size of two in the other sensor. The probability of this cluster size combination increases with larger incidence angle of the muons since the length of the path of the particles in the silicon sensors increases with increased angle. With even more increasing angles the probability of two clusters with a width of two strips

each increases. The amount of this cluster combinations with two strip clusters in each sensor reduce again to even higher angles. This effect is mainly caused by the overall reduced event number with crossing muons at such large angles.

The angle corresponding to the offsets in figure 5.8 is shown in a second x-axis. With the offset o, pitch p and sensor spacing s of the module, the angle θ is given by

$$\theta = \arctan\left(\frac{o \cdot p}{s}\right) . \tag{5.6}$$

Using the maximum detectable angle $\theta_{\text{max}} = 47.6°$ from equation (5.5) to calculate a maximum detectable offset o_{max} for modules with a sensor spacing s of 3.91 mm and 1.71 mm and a pitch $p = 90\,\mu\text{m}$ leads to

$$\begin{aligned} o_{\text{max}} &= \frac{\tan(\theta_{\text{max}}) \cdot s}{p} \\ o_{\text{max,4.0}} &\approx 48\,\text{strips} \\ o_{\text{max,1.8}} &\approx 21\,\text{strips}\,. \end{aligned} \tag{5.7}$$

The maximum offsets are shown in figure 5.8 with vertical lines. It can be seen that the data fit to that expectation of the maximum detection angle given in equation (5.5).

Summary of 2S Muon Hodoscope

Summing up, the measurements presented in this section showed successful tracking of cosmic muons with three 2S prototype modules read out synchronously. The measured angular distribution does not fit perfectly to the expectation but the basic shape peaking at 0° and smearing out at the maximum detection angles was observed. Analyzing the data of each module separately showed also consistent results. The 2S muon hodoscope can be used for a laboratory exercise for Master students taking a detector lecture. A benefit of the setup is that no additional particle source is needed. It allows students to understand tracking with silicon sensors and gives the students the chance to work with real, state-of-the-art detectors in the prototyping phase. Cosmic muons are also used for the alignment of the current and future CMS Tracker in addition to the particles from collisions to circumvent weak modes. [CMS14] Within the next years, up to three fully populated TB2S ladders will be placed in a cosmic rack by the CMS Tracker collaboration. The presented measurements show which kind of analyses could be performed with those data even though a more precise alignment will be needed in the cosmic stack with ladders.

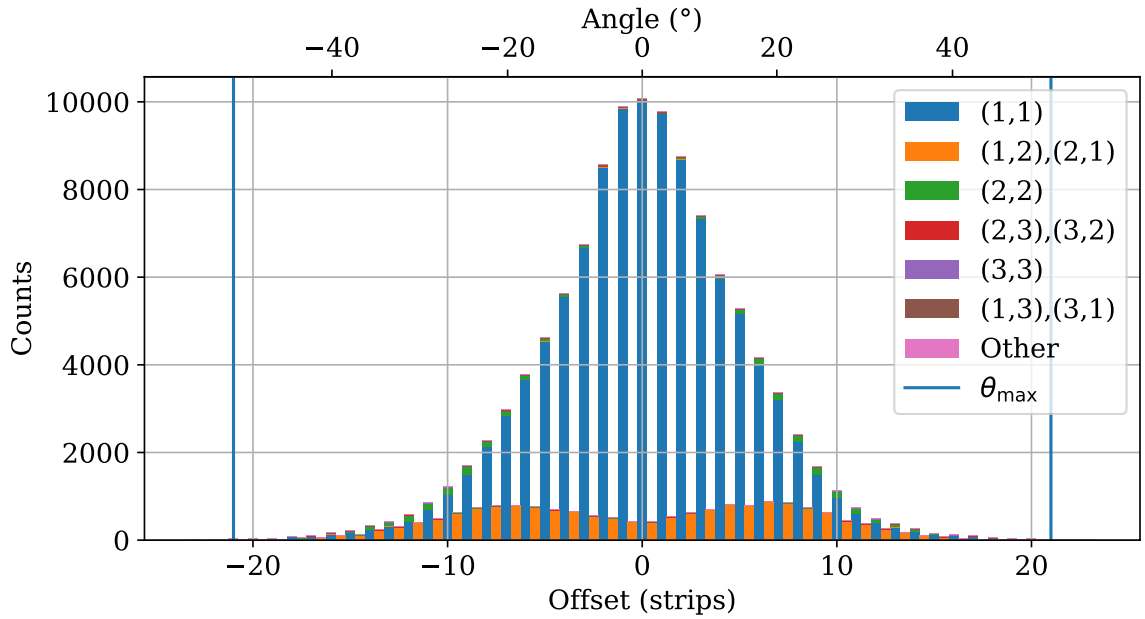

(a) Module 1 (1.8 mm module)

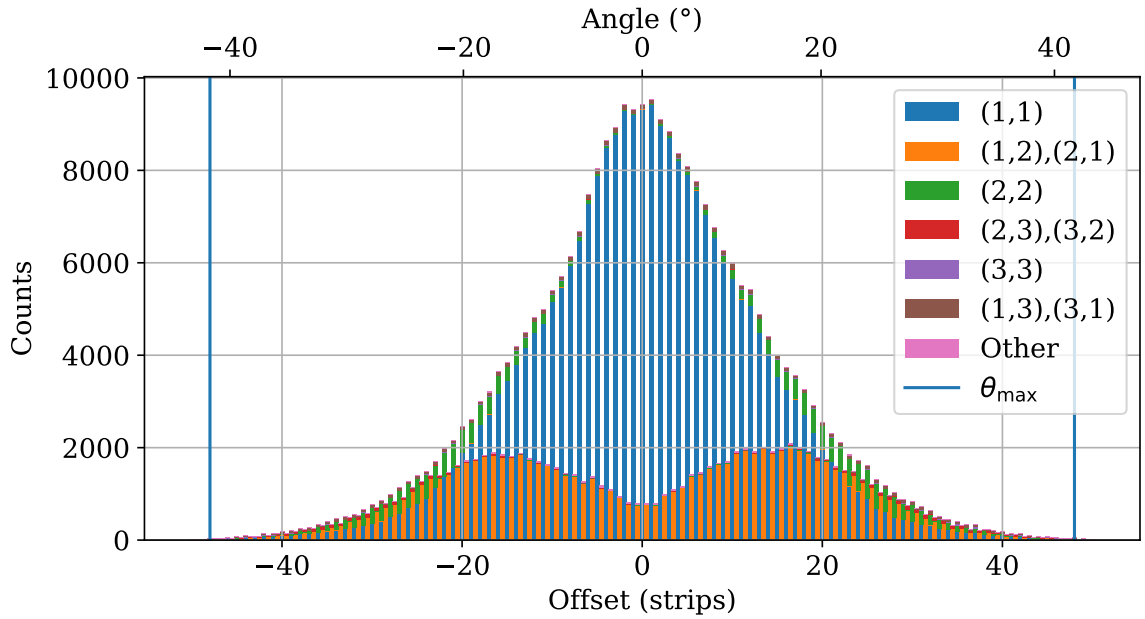

(b) Module 2 (4.0 mm module)

Figure 5.8.: Offset of the clusters in the top and bottom sensor for module 1 and 2. The offset values are plotted stacked for different combinations of the cluster width in the top and bottom sensor of each module. The cluster widths of both sensors are given as tuples in the legend. Cluster size differences of an even integer number result in integer offset values while cluster size differences of odd integer numbers result in half-integer offset values. The binning is chosen in half-integer steps so that each possible strip offset is displayed separately.

5.2. Beam Test

Between 2019 and 2022, several beam tests were performed to evaluate the performance of full-size 2S module prototypes. The beam test facility at *Deutsches Elektronen-Synchrotron* (DESY) in Hamburg, Germany, is one of the facilities used for these tests. Results of beam tests with 2S prototype modules can be found in [Wit23]. During this thesis, a beam test at the DESY II facility was performed with three 2S kickoff modules in February 2024. The aim was to test the performance of the 2S modules with the latest components and to compare the results with previous measurements.

5.2.1. Experimental Setup

The test beam facility where these measurements were performed is operated at the electron synchrotron *DESY II* [Die+19] at DESY in Hamburg. To generate the beam at the beam facility, the primary DESY II electron beam is guided onto a carbon fiber target to produce bremsstrahlung photons. These get converted to electron-positron-pairs via a metal plate. The resulting particles are focussed and guided by a magnetic field and enter the three user beam lines. The users can choose between electron and positron beams with energies between 1 GeV and 6 GeV.

Hardware at the Beam Line

The setup at the beam line can be seen in figure 5.9. The *devices under test* (DUTs) are mounted in a light tight box in between an upstream and a downstream beam hodoscope, called telescope in the following, with three layers each. The telescope layers are MIMOSA 26 monolithic active pixel sensor planes [Bau+09]. The pixels have a size of 18.4 µm × 18.4 µm providing an active area of about 2 cm × 1 cm. The telescope planes are used to reconstruct the tracks of the electrons or positions passing through the DUTs. The MIMOSA 26 planes are read out separately column by column, resulting in an integration time of 115.2 µs. Additionally, two data frames are read out together by the data acquisition system, resulting in a timing granularity larger than 200 µs. To get tracking information with the 25 ns time resolution of the 2S modules, an additional timing layer is used. In this beam test a *CMS Phase-1 BPIX* module [Ada+21b] was used as timing layer. For triggering, two crossed scintillator panels are placed before the first layer of the upstream and behind the last layer of the downstream telescope. An EUDET-type *trigger logic unit* (TLU) [BCG19] is used to combine the signals of the scintillators to a trigger signal for the data acquisition. During this test the coincidence signal of all four scintillators was used as trigger signal. For all measurements presented in the following, an electron beam was used, and the beam energy was set to 5 GeV. As DUTs, either a PS module or three 2S modules were mounted. The DUTs are mounted on a rotation stage that is movable in x- and y-direction and allows for rotation of the DUTs around the y-axis. The coordinate system is indicated in figure 5.9a as well. The results of the measurements with the 2S kickoff modules are presented in the following while some PS module results can be found in [Ras24].

Data Acquisition

The EUDAQ framework [Liu+19] is used for data acquisition. Each hardware component is read out by its own dedicated readout software. In these software packages, a EUDAQ *producer* is implemented for initialization, configuration and readout of the dedicated detector type. The EUDAQ framework provides a *RunControl* module that coordinates the data taking of all detector components. They get first initialized and configured for the data taking by the

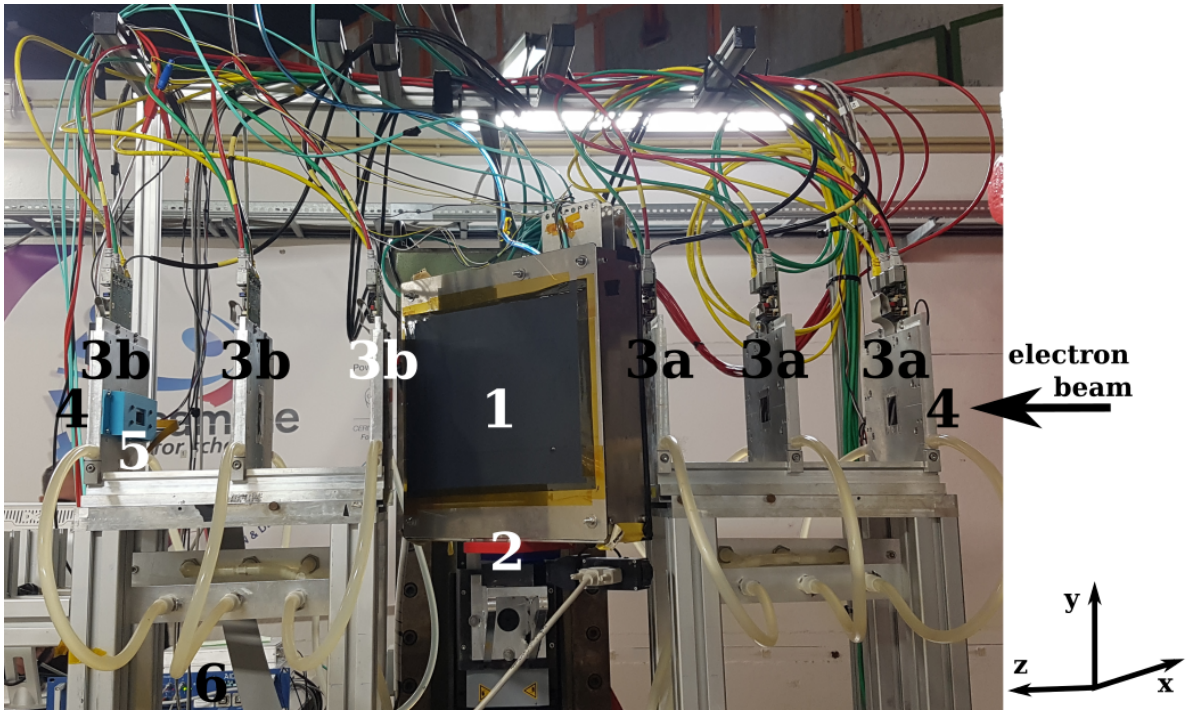

(a) Setup

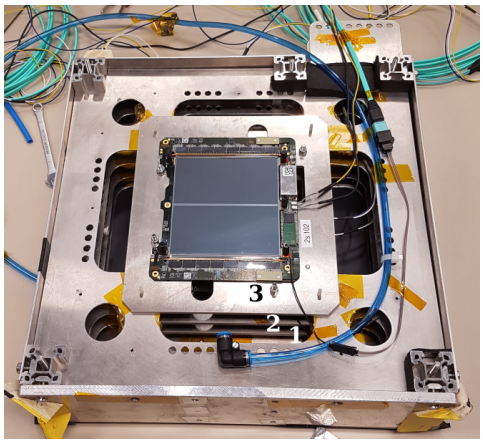

(b) 2S kickoff modules

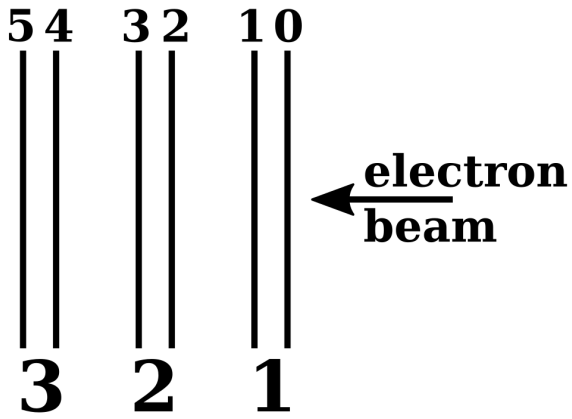

(c) DUT numbering

Figure 5.9.: Setup at the DESY II test beam facility. (a) The three 2S kickoff modules (DUTs) are mounted in a light tight box (label "1") on a rotation stage (label "2") in between an upstream (label "3a") and a downstream telescope (label "3b") with three layers each. Two crossed scintillators before and after the telescope allow for triggering on the electrons (label "4", not visible in the picture). A reference plane (label "5") is used to choose the track that belongs to the trigger of the 2S modules. An EUDET-type TLU (label "6") provides the trigger signal for data acquisition. The coordinate system and the electron beam along the z-axis are indicated in the picture as well. (b) View inside the DUT measurement box. The box is mounted in the electron beam such that the bottom sensors of the modules are hit first by the beam. The bottom sensor of module 1 is oriented to the beam. (c) The module and sensor numbering of the DUTs is depicted with respect to the electron beam direction. The sensors are labeled from 0 to 5 with even (odd) numbers denoting the bottom (top) sensors.

EUDAQ producers and then the readout of all detectors can be started by the RunControl. During data taking, the EUDAQ producers collect data from the detectors and send them to the *DataCollector* module via the *Transmission Control Protocol* (TCP). The data streams of all detectors get combined event by event and are stored to result files. These files can be used for offline analysis.

5.2.2. Analysis Steps

The data analysis is done in several steps. The tracks are reconstructed in a first step. As a second step, the DUTs get aligned and then, a detailed analysis of the data can be performed for different purposes. All these analysis steps are described briefly below. For a more detailed description see, e.g., [Kop22].

Offline Track Reconstruction

For the offline track reconstruction, the *EUTelescope* framework [Bis+20] is used. Each step of the track reconstruction is performed with a software module. The EUTelescope framework stores the data in the *Linear Collider I/O* (LCIO) *Event Data Model* [Apl+12]. The results of each analysis steps are also plotted and stored in the data analysis framework *ROOT* [Bru+97]. For track reconstruction, a sequence of software modules is executed. For the presented data analysis, the sequence is given in the following. If not stated differently, they are executed for all telescope planes, the DUTs and the reference plane.

1. **Converter:** Conversion from the custom detector data format to the LCIO format
2. **Noisy channel identification:** A user defined threshold for the hit occupancy (defined in equation (3.17)) is used to identify noisy channels with a hit occupancy above the threshold. The noisy channels are stored so that their hits can be removed later. The thresholds applied for this analysis are 0.1 % for the telescope pixels and 1.5 % for the 2S kickoff modules. With this threshold, none of the 2S module channels was masked.
3. **Clustering:** Hits in neighboring channels get combined to clusters.
4. **Masking:** Clusters with noisy channels get removed.
5. **Hitmaker:** The cluster positions are converted to positions in the telescope coordinate system. The axes are indicated in figure 5.9. The cluster centers are calculates according to
$$x_{\text{center}} = \frac{1}{Q}\sum_i x_i q_i \quad \text{and} \quad y_{\text{center}} = \frac{1}{Q}\sum_i y_i q_i \,, \tag{5.8}$$
where x_i and y_i denote the channel coordinates, q_i the signal charges of each channel in the cluster and Q the sum of all charges q_i. For the binary readout of the MIMOSA sensors and DUTs, the charges q_i are set to one. The z-positions of all detector layers have to be provided in a geometry configuration file. They were measured with a tapeline during the beam test.
6. **Pre-alignment:** The cluster position coordinate measured in the first detector plane is propagated to all others. The difference between the detected and propagated cluster position, called *residual*, is calculated. The mean of the residuals of a subset of events is used to determine correction factors for shifts and rotations of the MIMOSA and reference planes in the reconstruction software. The DUT layers are also pre-aligned regarding a shift in x-direction, but no rotations are taken into account in this step. The z-position

is fixed for all layers during the pre-alignment. The pre-aligned geometry of the layers is stored in a geometry file.

7. **Alignment:** The alignment is performed iteratively. During the presented analysis, it was performed three times. With the *Millepede II* package [Blo07], the track residuals on all telescope planes as well as on the reference plane are minimized simultaneously. Multiple scattering effects are taken into account by using the *General Broken Line* (GBL) approach [Kle12] for track finding and fitting. Besides a shift in z-direction, all possible rotations and shifts are considered for the MIMOSA and reference planes. Regarding rotations, the DUT planes stay fixed during the alignment, but they are treated as passive scattering planes. The DUT alignment is performed separately, which is described in the next subsection.

8. **Track fitting:** The track reconstruction is performed based on the information of all telescope planes on the complete data set. The data are stored in a ROOT [Bru+97] file for further analysis described in the following.

DUT Alignment

The alignment of the DUTs is performed after the automated alignment of the telescope and reference plane described above. During the DUT alignment, all six sensors of the three modules get treated individually. Some constraints of the positions relative to other layers are considered. To check the alignment steps, the residuals of the positions at the track in x-direction are taken into account. The y-residuals are not taken into account since just the left side of the modules was read out during the measurements. This is the consequence of the broken stub readout for the right hybrid of the 2S kickoff modules, as explained in section 3.3.5. The geometry file of the DUTs gets changed according to the x-residuals and then the analysis is performed again to check the new residuals. Since all rotations and shifts that get performed during the DUT alignment influence the results of the previously performed alignment step, a detailed DUT alignment sequence was developed.

As a first step, the x-position is shifted according to the x-residuals x_{res}. Then, the z-position of the bottom sensor of all three modules is shifted in steps of 1 mm from -4 cm to 4 cm and the *root mean square* (RMS) of the x-residuals $\text{RMS}(x_{\text{res}})$ is calculated for all z-positions. Exemplary results for one run can be found in figure E.1. The minimum is extracted by fitting a cubic function to $\text{RMS}(x_{\text{res}})$ and applying the z-shift of this minimum to the original geometry file. All mounted kickoff modules are 1.8 mm modules. Thus, the geometry of the top sensors is adapted to have a z-distance of 1.8 mm to the bottom sensors. Since the shift in the z-direction changes again the x-residuals, the x-position is corrected again once.

The rotation around the z-axis is corrected by checking the slope of the x-residuals plotted over the y-position of the interpolated track. The slope is calculated and then, the rotation around the z-axis is subtracted by the slope, which results in an equal x-residual across the y-coordinate. Again, an x-shift correction has to be performed after this change. Then, the rotation around the y-axis is corrected by changing the angle in the geometry file in steps of 0.1° until the slope of the x-residual over the x-coordinate changes sign. The step size is halved and the procedure is repeated. As soon as the slope is smaller than $8\,\mu\text{m}^{-1}$, the loop is interrupted and the found correction applied. Since this rotation affects again the corrections applied previously, the x-shift, rotation around the z-axis and x-shift is applied again. The resulting RMS values of all aligned runs that are presented in section 5.2.3 can be found in figure E.2.

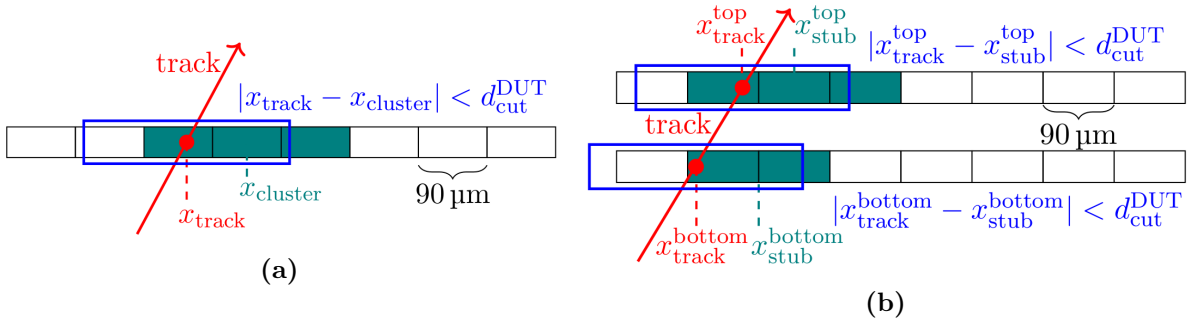

Figure 5.10.: Illustration of cluster and stub cuts used for the efficiency calculations. (a) A cluster is considered as efficient when its x-residual x_{cluster} is closer to the calculated track position x_{track} than a pre-defined distance $d_{\text{cut}}^{\text{DUT}}$. (b) To consider a stub as efficient, its position in the seed layer (bottom sensor) and the positions calculated from the stub bend in the correlation layer (top sensor) has to be closer to the positions of the track as a predefined cut $d_{\text{cut}}^{\text{DUT}}$. Taken from [Kop22].

Analysis Definitions

The noise hit occupancy is defined in equation (3.17) with hits resulting from noise. To measure it, the electron beam was switched off.

To determine which tracks measured by the telescope surrounding the DUTs belong to the time interval in which the DUTs were read out, the tracks that produced a hit in the reference plane are filtered out. This is done by residual cuts for the reference BPIX plane. They were chosen as in [Kop22] as

$$|x_{\text{ref}}^{\text{res}}| \leq 150\,\mu\text{m} \quad \text{and} \quad |y_{\text{ref}}^{\text{res}}| \leq 50\,\mu\text{m}\,. \tag{5.9}$$

Interpolated hit positions in the DUT sensors from all these *reference tracks* that fulfil the criterion in the reference plane given in equation (5.9) are calculated. The number of reference tracks is given by $n_{\text{ref tracks}}$. The modules were mounted in the beam such that all the reference tracks lie well within the left side of the module sensors. The difference between these expected positions and the measured positions are used to declare a cluster (stub) as efficient. This is illustrated in figure 5.10. The maximum difference in positions was set to 180 µm in the presented analysis. No cut on this distance was set on the y-residual of the DUTs due to the large strip length of the 2S sensors. The number of efficient clusters (stubs) is given by $n_{\text{eff clusters}}$ ($n_{\text{eff stubs}}$). The cluster and stub efficiencies are defined as

$$\epsilon_{\text{cluster}} = \frac{n_{\text{eff clusters}}}{n_{\text{ref tracks}}} \quad \text{and} \quad \epsilon_{\text{stubs}} = \frac{n_{\text{eff stubs}}}{n_{\text{ref tracks}}}\,. \tag{5.10}$$

During the operation of the 2S modules in the CMS Phase-2 Outer Tracker, the module readout will be synchronized with the HL-LHC clock. During the beam test the clock of the DESY II accelerator was not synchronized with the 25 ns readout frames of the 2S modules. Thus, the phase between the arrival of individual particles and the sampling of the signal in the CBC frontends is randomly distributed. To account for that, the 25 ns readout time is sampled in the firmware of the FC7 with a 320 MHz clock with a time-to-digital converter resulting in eight *TDC phases*. For each event, the TDC phase is also stored. Depending on the latency and readout settings of the 2S modules, detecting hits is more likely in some TDC phases. To compare the module performance in the beam test with the expected performance during the HL-LHC operation, only the most efficient TDC phase of a run is considered during the data analysis.

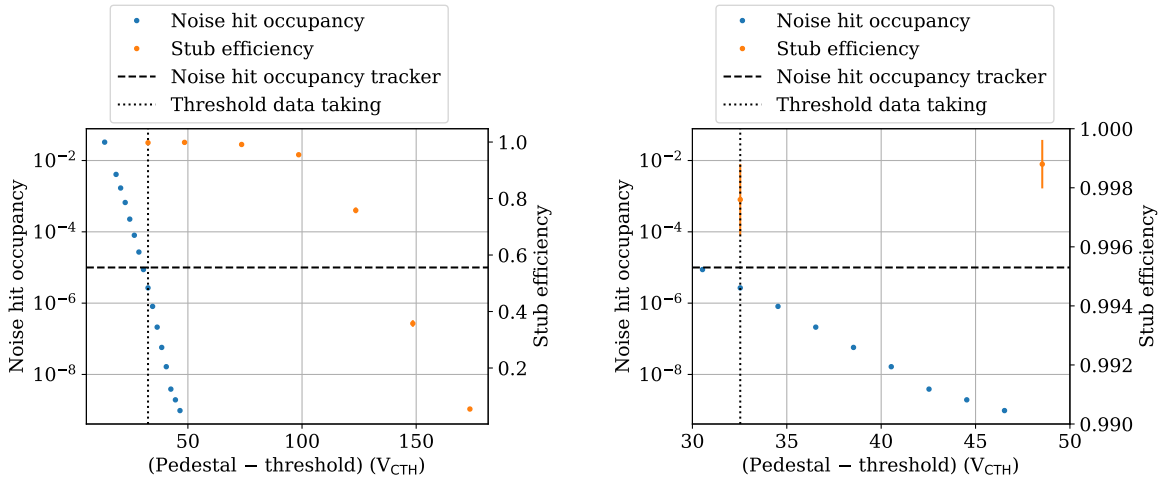

(a) **(b)**

Figure 5.11.: Threshold scan of module 1 during the beam test. The noise occupancy and the stub efficiency (secondary y-axis) are shown as a function of the set threshold relative to the pedestal in V_{CTH}. (b) shows a zoomed version of (a). The threshold for data taking was chosen such that the noise hit occupancy was below 10^{-5} and the stub efficiency above 99.6 %.

5.2.3. Measurements and Results

During the measurements, the low voltage of all three modules was set to 10.5 V and the sensors were biased with 350 V. First, the results of threshold and angular scans are presented. Then, the synchrony of the multi-module stub readout is shown.

Threshold Scan

To determine a sufficient threshold for data taking, two threshold scans were performed. During one, the electron beam was switched off and the noise hit occupancy defined in equation (3.17) was measured. In the second threshold scan, the beam was switched on, and the stub efficiency was measured. The results can be seen in figure 5.11 for module 1 and in the appendix in figure E.3 for module 2 and 3. The noise hit occupancy and stub efficiency are plotted as a function of the difference of the applied threshold and the mean pedestal of all module channels, both measured in the internal DAC units V_{CTH}. The noise hit occupancy decreases with increasing threshold. The stub efficiency decreases for increasing threshold as well. The charge generated by the crossing electrons in the silicon is not high enough anymore to generate a hit at too high thresholds. Figure 5.11b depicts a zoomed version of the plot in figure 5.11a. At the threshold that was set during data taking of the angular scans, the stub efficiency is well above 99.6 % while the noise hit occupancy stays below the value of 10^{-5} required for the Phase-2 Tracker operation. The absolute threshold values of module 1 and 2 differ from the threshold set for module 3 since this has an overall higher noise being built with split plane SEHs (see section 4.1.2). Further details about noise studies with 2S prototype modules can be found in section 6.2.

Table 5.1.: Measurement parameters of the angular scans. The names of the scans as well as the measurement parameters are given in the table. The names refer to the position in the TB2S at which a module with this stub window settings would be placed. [CMS17f]

Name	Stub window size	Stub window offset
AS_Outer	15 strips	0 strips
AS_Inner	10 strips	0 strips
AS_Offset	10 strips	2 strips

Angular Scans

Three angular scans were performed during the beam test. The measurement parameters can be found in table 5.1. The parameters differ by the stub window size and offset. During the angular scan AS_Outer the stub window size was set to 15 strips, which will be the case for the modules that are mounted in layer 3 of the TB2S. Contrary to that, the window size was set to ten strips during AS_Inner. This is close to the window size of nine strips that will be applied to modules in the inner layer of the TBT2S. [CMS17f] In addition, during the AS_Offset, a stub window offset of two strips was applied. This offset can be used to account for different geometrical positions the modules can have in the Outer Tracker (see section 3.3.3). During the angular scans, the entire box with all three DUTs was rotated along the y-axis and at several angles, data were taken with all three modules.

The measured stub efficiencies as a function of the rotation angle of the DUTs are depicted in figure 5.12 for module 1 and in the appendix in figure E.4 for module 2 and 3. The stub efficiency is about 99.6 % at a rotation angle of 0°. With increasing and decreasing angle it stays high until it drops sharply to about 0 %. Depending on the settings for the stub window and offset, the angle at which the stub efficiency decrease occurs, differs. The wider distribution of AS_Outer compared to AS_Inner as well as the shift of AS_Offset are visible. With the equation

$$\theta_{\text{inflection point}\,\pm} = \pm\frac{1}{2}\cdot\left(\arctan\left(\frac{\left(\frac{s}{2}\pm o-\frac{1}{2}\right)\cdot p}{d}\right)+\arctan\left(\frac{\left(\frac{s}{2}\pm o\right)\cdot p}{d}\right)\right) \tag{5.11}$$

with the stub window size s and offset o, the strip pitch p and the sensor distance d, the inflection point angles $\theta_{\text{inflection point}\,\pm}$ can be roughly estimated. It uses that the stub efficiency should be one when the difference of both cluster positions is $\frac{w}{2}\pm o-\frac{1}{2}$ and zero when the difference of both cluster positions is $\frac{w}{2}\pm o$. However, this takes into account just the geometry of the module and no effect of the signal generation in the silicon sensors. For angles for which the stub criterion is no more fulfilled for the electrons of the beam passing the module, the stub efficiency does not drop completely to zero. It stays at stub efficiencies between 1 % and 2 %. This effect is called *stub noise* and was studied in detail in [Kop22]. Multiple track and secondary particle events are the origin of the stub noise.

This *stub turn-on characteristics* can be modeled by the function

$$f(\theta,p_0,p_1,p_2,p_3) = 1-\frac{1}{2}\left(p_0+p_1\cdot\operatorname{erf}\left(\frac{\theta-p_2}{p_3}\right)\right) \tag{5.12}$$

with $\theta \geq 0°$ and $p_2 > 0°$ and erf $\hat{=}$ error function. The shift parameter p_0 is expected to be about one and the scale parameter p_1 allows for scaling the whole function and account for the efficiency in the plateau at 0°. The inflection point is given by p_2 and the width of the turn-on

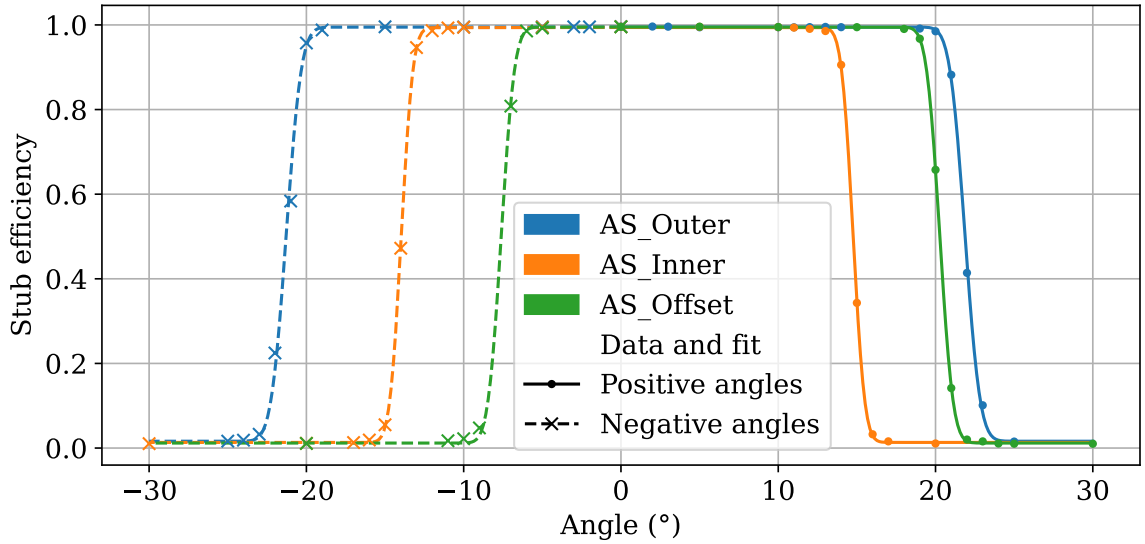

Figure 5.12.: Stub efficiencies of module 1 for the angular scans. The stub efficiencies as a function of the module rotation angle are shown. The fits according to equation (5.12) with the resulting parameters given in table 5.2 are also plotted. The scans are labeled according to table 5.1.

curve is given by p_3. The fit is first performed for the positive angles and then for the absolute values of the negative angles by fixing the parameters p_0, p_1 and p_3 to the values obtained from the fit to the positive angles. The results of the fits are plotted in figures 5.12 and E.4 and the fit parameter results are given in table 5.2 for module 1 and in the appendix in table E.1 for module 2 and 3. The data points and fit results are visualized differently for the positive and negative angles.

Comparison with Simulation

To study the behavior of the stub turn-on characteristics in more detail, the simulation developed within [Kop22] was adapted to also take stub window offsets into account. Tracks at different angles θ are generated with a standard deviation σ_θ. With this standard deviation multiple scattering effects in the upstream telescope and DUT sensor layers are accounted for. The charge signal of the tracks in the two sensors of a 2S module is simulated with the Monte-Carlo method by dividing the track in the active area of the silicon into tracklets of a length of 1 µm each. To obtain the track charge per µm a Landau distributed random number is drawn. Following [Har17], the most probable value of 76 e^-/µm and mean value of 108 e^-/µm is used. For the assignment of the charge of each tracklet to the total charge collected at the two nearest strips, a non-linear charge sharing model according to [Mai19] is applied. The charge sharing model was validated with muon beam test data. The noise is simulated by a normal distribution with a width of the mean noise of the corresponding sensor of the simulated module. This noise charge value is added to each strip charge already obtained from the tracklet charges. Then, the binary readout is emulated by comparing the total strip charge to the threshold set during data taking. For the conversion of V_{CTH} to electrons, the factor 156 e^-/V_{CTH} [Mai19] is used. More details about the simulation can be found in [Kop22].

The simulation was performed with different standard deviations σ_θ and sensor distances. When varying the sensor distance from 1.63 mm to 1.73 mm in steps of 10 µm, $\sigma_\theta = 0°$ was set.

Table 5.2.: Fit parameters of the turn-on characteristics for module 1. The parameters p_0, p_1 and p_3 are obtained from the fit to the positive DUT rotation angles while they are fixed in the fit to the negative angles. The parameter p_2 is given separately for the fit to positive angles $p_{2,\text{pos}}$ and negative angles $p_{2,\text{neg}}$. The statistical uncertainties are shown as well.

Fit parameter	AS_Outer	AS_Inner	AS_Offset
p_0	0.989 ± 0.003	0.993 ± 0.003	0.993 ± 0.001
p_1	0.979 ± 0.003	0.981 ± 0.003	0.983 ± 0.001
$p_{2,\text{pos}}$ in °	21.87 ± 0.02	14.76 ± 0.02	20.27 ± 0.01
$p_{2,\text{neg}}$ in °	21.28 ± 0.04	13.96 ± 0.02	7.61 ± 0.04
p_3 in °	1.07 ± 0.03	0.82 ± 0.03	0.94 ± 0.02

When varying σ_θ from 0° to 1° in steps of 0.1°, the sensor distance was set to 1.68 mm. This is the distance between the middle of both active sensor areas of the module. By design, this should be 1.71 mm, but in [Kop22] detailed sensor distance measurements were performed that showed that at the position where the beam illuminated the 2S kickoff modules, the real sensor distance is about 1.68 mm. From all simulations, the stub turn-on curves are obtained, and the results are fitted by equation (5.12) with p_0 and p_1 set to one since the simulated stub turn-on curves reach a stub efficiency of exactly zero and one due to missing stub noise. Figure 5.13 shows the fit results of the simulated turn-on curves for p_2 and p_3 as a function of the sensor distance d and σ_θ for all three scans for module 1. The turn-on curve fit parameter results p_2 and p_3 of the data are shown as dashed lines. The results from simulation are fitted with an empirical function (polynomial function of degree 4) to retrieve the intersection point of the data fit parameter and the simulation fit parameter. The intersection points (shown as dotted lines) are the simulation parameters that fits the data best. For σ_θ, no intersection between the fit parameter from data and simulation was found for AS_Outer and AS_Offset. Thus, $\sigma_\theta = 0°$ is used for the simulation that matches the measurement conditions best. The physical meaning is that no smearing of the angles is required with this simulation parameters. It is a priori not obvious why this is the case but a combination of the effects of the turn-on width dependency of the angle as described later in this subsection and the fact that the charge sharing parameter used for the simulations was obtained from measurements with muons (see [Mai19]) instead of electrons can explain this. The charge sharing parameter has a significant influence on the simulated cluster sizes that influence the turn-on curve width as explained later. The results for module 2 and 3 are given in the appendix in figure E.5.

The comparison of data and simulation for all three angular scans with the obtained parameters (given in the appendix in table E.2) is shown in figure 5.14 for module 1 and in the appendix in figure E.6 for module 2 and 3. All turn-on curves were shifted such that they are symmetric around 0° to be able to see differences better. The simulation and measurement results match well. It is visible that the plateau is smaller and the turn-on is wider for AS_Offset than AS_Inner, although both have the same stub window size.

To investigate these effects in more detail, the simulation for AS_Offset was also performed with the same parameters d and σ_θ that were used for module 1 and AS_Inner. The results are depicted in figure 5.15. It can be seen that both effects are still there and the curve of AS_Offset shows inflection points at lower absolute angles and a wider turn-on. The fit parameter result p_3 that measures the width is displayed in the legend of figure 5.15. The origin of these effects are studied and described in the following.

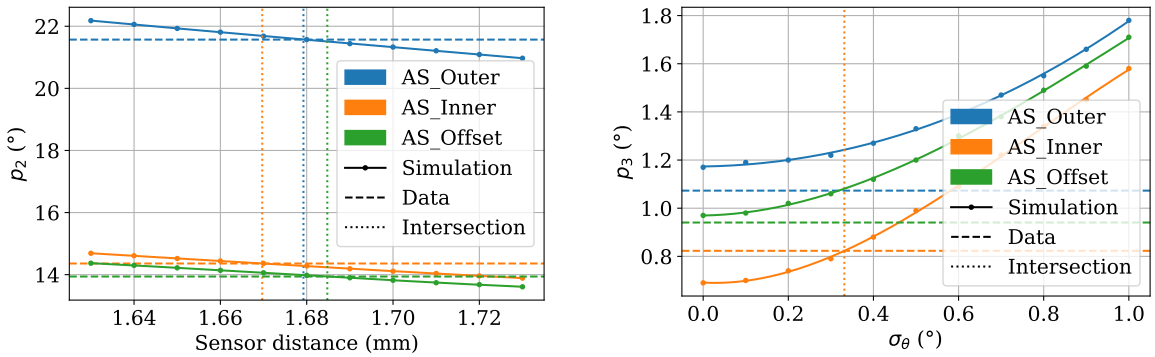

(a) (b)

Figure 5.13.: Comparison of the fit parameters obtained from data and simulation for module 1. The simulation was performed for different sensor distances (a) and standard deviations of the angle σ_θ (b). The fit parameters of the data are plotted as horizontal dashed lines while the intersection with the simulated parameters is depicted with a dotted vertical line.

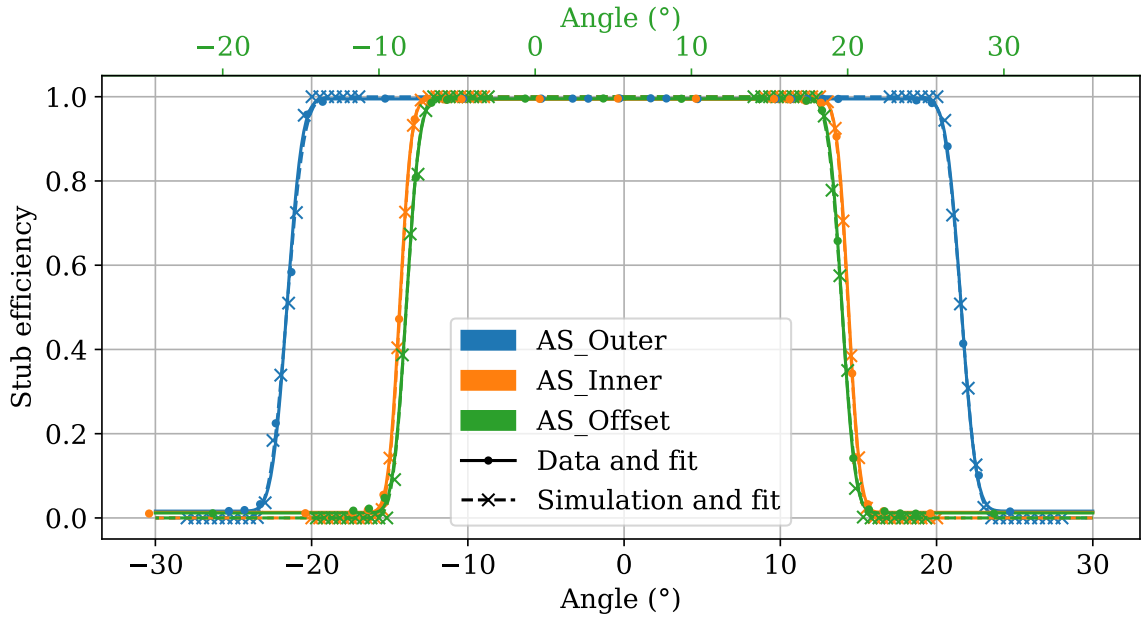

Figure 5.14.: Comparison of data and simulation results for module 1. The measured and simulated stub efficiency turn-on curve is shown for all three angular scans. The turn-on curves were shifted such that they are symmetric around 0°. For AS_Offset, the not shifted angle is also indicated in a secondary x-axis. The simulation results match the measurement results.

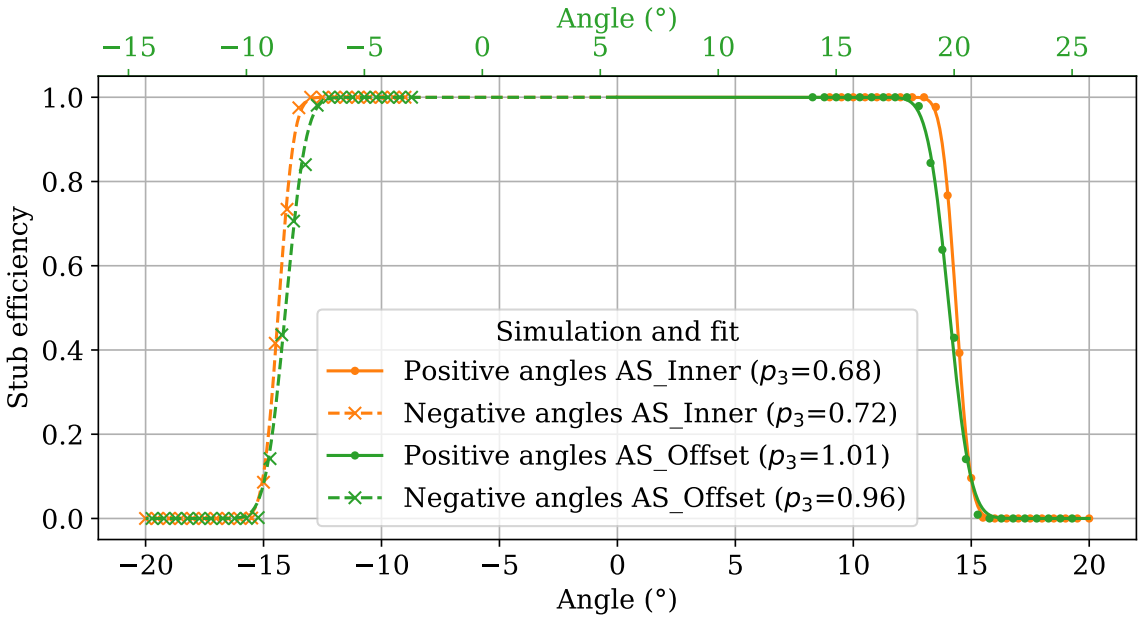

Figure 5.15.: Comparison of angular scans with and without offset in simulation. The simulated stub efficiencies as a function of the rotation angle are shown. For both simulations, the exactly same input parameters were used. Just the stub window offset was set to zero strips for the simulation of AS_Inner and two strips for the simulation of AS_Offset. The turn-on curves were shifted such that they are symmetric around 0°. For AS_Offset, the not shifted angle is also indicated in a secondary x-axis.

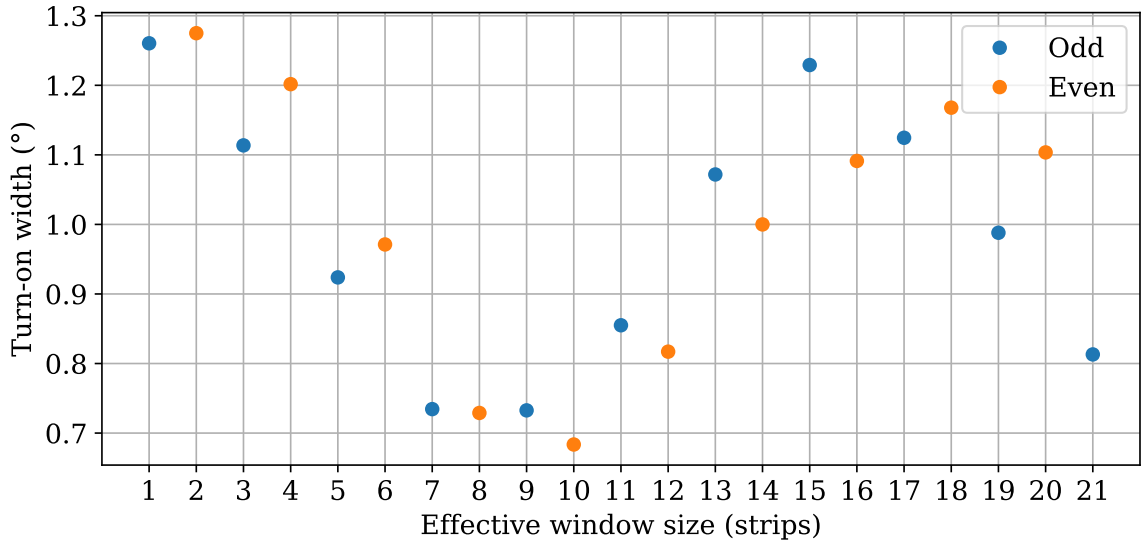

Figure 5.16.: Simulated widths of the turn-on curves of different effective window sizes. The simulated width of the turn-on curves depends on the effective window size and thus angle. It also varies for even and odd effective stub window sizes.

Turn-on curves with an offset of zero strips are symmetric around 0° meaning that the widths and absolute inflection points of the curve at positive and negative angles are the same. Thus, only positive angles can be studied during the investigation of the width of the stub turn-on curves. At positive angles, all window sizes achievable with the CBCs can be set, and, additionally to the maximum window size of 15 strips, an offset up to three strips in half channel resolution can be applied. In the simulation, instead of applying the offset, the window size can also be increased. Thus, the maximum *effective window size* that can be achieved with the settings in a 2S module is 21 strips. For the behavior of the turn-on curve, the angle at which the inflection point of the turn-on curve is located matters. Thus, just the effective window size matters and not the exact combination of the stub window size and offset. To demonstrate this, the simulation was performed for a sensor distance of 1.68 mm and $\sigma_\theta = 0°$ for each possible effective window size that can be achieved with the settings in a 2S module. The turn-on curves obtained from these simulations can be found in the appendix in figure E.7.

The results of the fit parameter p_3 that measures the width of the turn-on curve are depicted as a function of the effective stub window size in figure 5.16. The turn-on width initially decreases with increasing effective stub window size and then increases again at a window size of about nine to ten strips before it decreases again from 17 to 21 strips. The widths observed in figure 5.15 match the turn-on widths shown in figure 5.16, since AS_Inner has an effective window size of 10 strips while the negative (positive) side of AS_Offset has an effective window size of 6 strips (14 strips). As a second effect, the width of the turn-on curve also varies between odd and even stub window sizes (plotted in different colors in figure 5.16). The assumption is that this results from the cluster sizes that are present in the simulation data.

To prove that, the simulation was again performed for all inflection points p_2 that were extracted by the fits to the curves shown in figure E.7. Figure 5.17 depicts the cluster size combinations in the seed and correlation layer for these simulations with 1000 events each. It is visible that with increasing effective window size, and thus angle, the present cluster combinations vary. The larger the angle, the larger the cluster sizes get. Also, the relative

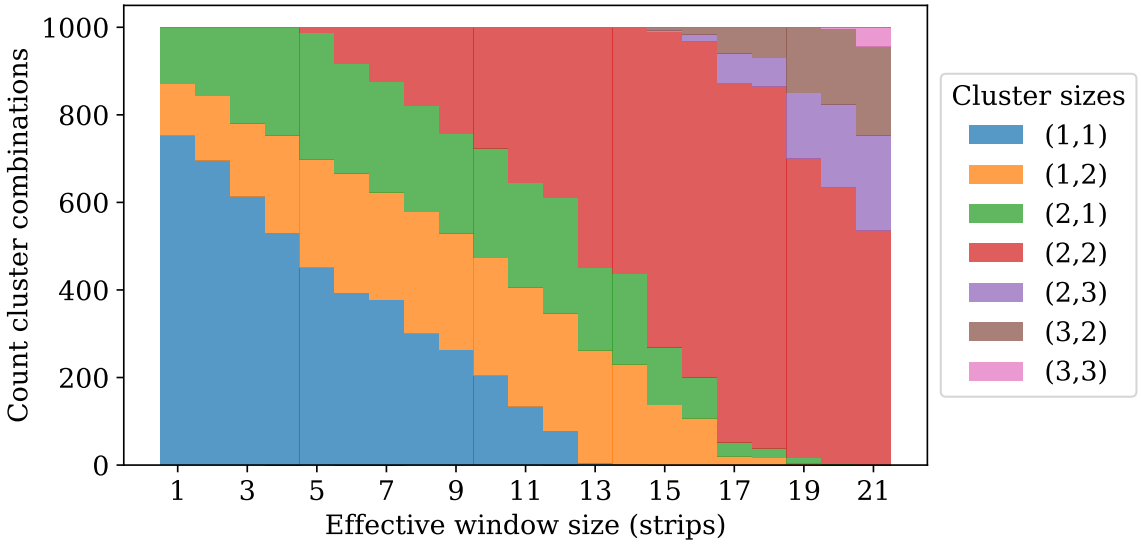

Figure 5.17.: Cluster size combinations at the inflection points of all effective stub window sizes. All cluster size combinations observed in the simulation at the inflection points of all effective stub window sizes are plotted. The simulation was performed with 1000 events at each angle. The cluster sizes are given in the legend as a tuple ("cluster size seed cluster", "cluster size correlation cluster").

fraction of the cluster size combinations varies. Cluster positions can either have an integer or half-integer value in strips. Clusters with an odd number of strips have integer positions whereas clusters with an even number of strips have half-integer positions. For the window size s as defined in this thesis, the edge of the window that is still inside the stub definition, can be calculated by adding $\frac{s-1}{2}$ to the seed cluster position. Thus, the difference between the window edge and seed cluster position is an integer (half-integer) value when the window size is an odd (even) number. To fulfill the criterion of integer (half-integer) cluster position difference, the cluster sizes have to differ by an even (odd) number. Thus, even (odd) cluster size differences between the seed and correlation cluster contribute preferably to the turn-on curve with odd (even) stub window size settings. Due to this, the width of the stub turn-on characteristics depends on the angle at which the effective cluster window becomes relevant and the exact cluster combinations that occur at these angles. Comparing figure 5.16 with figure 5.17 shows that the overall trend of the stub sturn-on width depends on the total fraction of events with the same cluster width in both sensors.

Multi-Module Stub Readout

To prove that the three 2S kickoff modules were actually read out synchronously during the data taking, correlation matrices of the stub positions in all three modules are plotted for a run with about 570 000 events in which the modules were oriented perpendicular to the electron beam. They are depicted in figure 5.18. All stubs are used for the plots independent of being associated with a reference track. Thus, also stubs resulting from noise hits as well as stubs resulting from multiple track and secondary particle events are plotted. For further information about stub noise see [Kop22]. A clear correlation of the stub positions in the modules where the beam is located is visible. This proves that the developments presented in section 4.2 provide synchronized stub readout for multi-module systems.

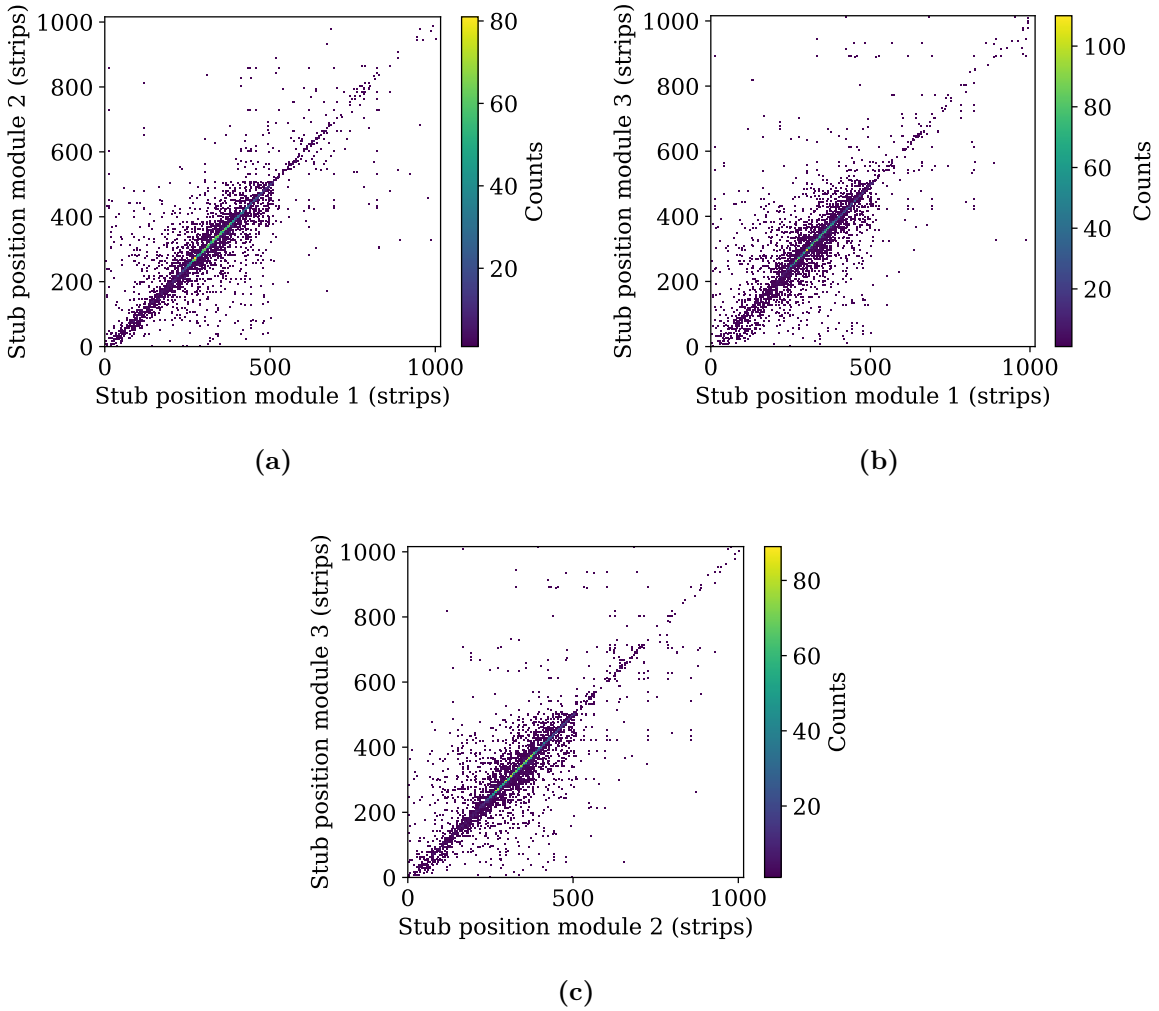

Figure 5.18.: Stub correlation matrices for all three 2S kickoff modules during the beam test. A clear correlation between the stub positions in all module combinations is visible.

Summary of Beam Test

Three modules were mounted at once as DUT in between the telescope layers at the DESY II test beam facility. The stub data of all three modules were read out synchronously proving that the developments shown in section 4.2 work as expected. The turn-on characteristics of the stub efficiency when emulating high p_{T} particles by rotating the DUTs with respect to the beam is very good and behaves as expected. It also behaves as expected when setting a stub window offset other than zero. The results of all three modules are very consistent. The presented measurements show that the most recent prototyping version of the 2S modules, the 2S kickoff modules, show efficient particle detection performance.

6 Integration Tests

During the development and prototyping phase of the modules for the CMS Phase-2 Outer Tracker, many system tests in laboratory and beam test based setups were performed. Within such measurements as presented in chapters 4 and 5, the electrical and thermal behavior of the modules can be tested. Since the modules will be placed inside the tracker mounted on larger structures as described in section 3.2, it is crucial to validate their performance also on these subdetector structures. These types of tests are called *integration tests* and can target different aspects. Generally, the mechanical placement of the modules on the structures and the whole integration procedure itself can be studied during integration tests. To precisely attach the detector modules onto the subdetector structures while at the same time correctly fixing the fragile readout and powering cables to the foreseen positions imposes a large challenge to the integration team. It is crucial to practice this before the start of the integration phase of the Outer Tracker. Then, being mounted on the structures, the electrical performance of the modules with respect to the close distances on the subdetector structures can be tested. Also, common mode noise and crosstalk measurements can be performed. Connecting the subdetector structures to cooling systems, the cooling performance and validation of thermal simulations can be addressed during such measurement campaigns as well. Since integration tests combine the mechanical and electrical aspects of the modules and subdetectors, collaborations between module assembly and integration centers are useful to perform successful integration tests. This also allows to help the experts from the integration centers to gain first integration experience with real modules.

Several integration tests were performed within this thesis. The results of two TB2S ladder integration tests focussing on thermal aspects, a full ladder TB2S integration test and a TEDD dee integration test are described in the following sections 6.1 and 6.3.[1]

6.1. Thermal TB2S Ladder Integration Tests

During this thesis, two thermal TB2S ladder integration tests were performed. The first one took place in March 2022 and the second one in June 2024. Both tests were performed in the Lyon cold room at CERN. The general motivation of these thermal integration tests is to test the mechanical behavior of modules on a CO_2 cooled ladder. Mechanical breakage of the modules due to temperature changes in the expected range during operations must be excluded. During both tests, one of the mounted modules was an irradiated 2S module with which the thermal behavior of the module on the ladder after a fluence corresponding to $4000\,\mathrm{fb}^{-1}$ of luminosity could be tested. This is corresponding to the module behavior at the end of the HL-LHC data taking. These results are used to compare to thermal simulations and to validate them. A validation of the thermal simulations is crucial since the whole design of the cooling structures in the Phase-2 Outer Tracker is based on them.

[1] The CMS collaboration acknowledged my work on the integration tests with a CMS 2023 Award. This honors the "outstanding contributions to the phase-2 upgrade of the CMS Outer Tracker, in particular for a leading role in the Outer Tracker module integration tests." I feel proud of that and would like to thank here all people helping me with the integration tests.

6.1.1. Experimental Setup

Both thermal TB2S ladder integration tests were performed in the Lyon cold room at CERN. The whole room with a ground area of about $55\,\mathrm{m}^2$ can be cooled down to at least $-22\,^\circ\mathrm{C}$. The TB2S ladder with the modules is placed in a light tight and thermally insulated measurement box. Laboratory power supplies were used to power the modules and to monitor the voltages and currents during the whole measurement time. The modules were read out by an FC7 based readout system.

Inside the measurement box, the cooling pipe of the integrated ladder is connected in series with a second ladder to simulate one cooling loop of the TB2S. For the cooling with evaporative CO_2 a TRACI II (Multipurpose Refrigeration Apparatus for CO2 Investigation) [CER24b] cooler is used.

The irradiated module is mounted at position 1 of the ladder. This is the position with the worst cooling performance. For further details see section 3.2.1. Depending on the test, the exact measurement parameters differ. They are briefly described in the following two paragraphs.

The first thermal test was performed with the third prototype ladder, which is also the third ever produced ladder for the TB2S. Besides the irradiated module at position 1, two unirradiated 2S prototype modules were mounted at position 1 and 2. Heating resistors were mounted on the other ladder inserts to emulate the heating power of further irradiated modules. This resulted in a total power of about 65 W across the full ladder. The detailed power calculation can be found in table 6.1. The temperature was monitored at various positions inside the setup during the whole measurement time. A 1-wire temperature and humidity sensor measured the environmental conditions during the measurements. [Mou25b; Mou25a; FHE15] The air temperature inside the cold room but outside the box was also measured. The temperature at the pipe was measured directly upstream and downstream of the modules. In addition to the 16 temperature sensors glued at various positions on the irradiated module, the temperature at the bridge of the left side of the module at position 2 was measured. The monitoring of the environmental conditions was used to prevent operating the ladder at temperatures below the dew point. A pipe with dry air supply was placed inside the measurement box. The air flow was reduced to a minimum during the measurements. To simplify the comparison with thermal simulation, an as much as possible reduced air movement during the measurements is preferred.

During the second thermal test, the first pre-series ladder was fully populated with twelve modules. The irradiated module was mounted at position 1 next to eleven unirradiated kickoff modules. This was the second time operating a fully integrated ladder after the test described in section 6.2. The total power consumption across the ladder was with about 51 W (see table 6.1) less than during the first test. The cold room could not be cooled down during this measurements due to other not removable material inside. Thus, the measurement box was placed inside another thermally insulated box. A freezer was used to pre-cool dry air to about $-19\,^\circ\mathrm{C}$ that could be flushed separately to the outer and inner box. This cold dry air supply in addition to the CO_2 cooling allowed the operation of the irradiated module with high voltage. To better control the environmental conditions during the measurements compared to the first thermal test, the dry air supply to the inner box was switched off during the measurement time.

Irradiated 2S Prototype Module

To be able to measure the performance of an irradiated 2S module, a prototype module got assembled with proton irradiated components. The irradiation was performed with 23 MeV protons at the Karlsruhe compact cyclotron (KAZ) [ZAG24] located at KIT. The top sensor

Table 6.1.: Power consumption across the ladder during the thermal TB2S integration tests. The total power of the unirradiated modules is dominated by the low voltage power while for the irradiated module, the sensor contributes more significantly with 0.6 W of power. The heating resistor power is set to 1.25 W per cooling point to simulate modules with a total power consumption of 6.25 W at five cooling points.

Category	Voltage	Current	Power	Module/position count First test	Second test
Irrad. module LV	10.5 V	0.4 A	4.2 W		
Irrad. module sensor	600 V	1 mA	0.6 W		
Irrad. module total			4.8 W	1	1
Unirrad. module LV	10.5 V	0.4 A	4.2 W		
Unirrad. module sensor	600 V	3.6 µA	2.16 mW		
Unirrad. module total			4.2 W	2	11
Heating resistor cooling point			1.25 W	42	0
Total ladder power				65.7 W	51 W

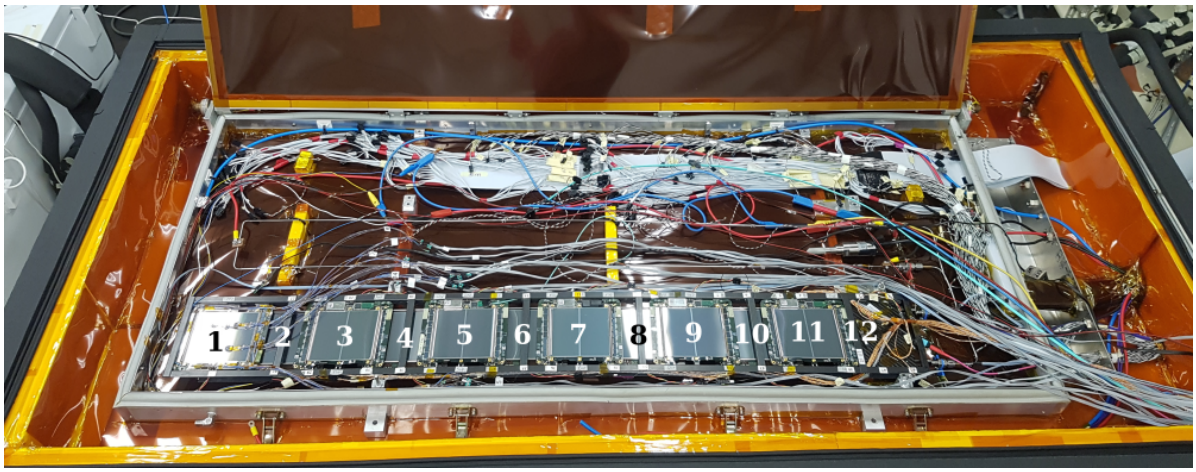

Figure 6.1.: Measurement setup of the full ladder cold test. The irradiated module is mounted at position 1 on the first pre-series ladder (bottom). Eleven unirradiated kickoff modules are mounted at the positions 2 to 12. The cooling pipe of the ladder is connected in series with a second cooling pipe of a ladder (top) to a CO_2 cooling system. Both ladders are placed inside an insulated aluminum box that is placed in a second insulated box. Both boxes can be flushed separately with dry air at about −19 °C.

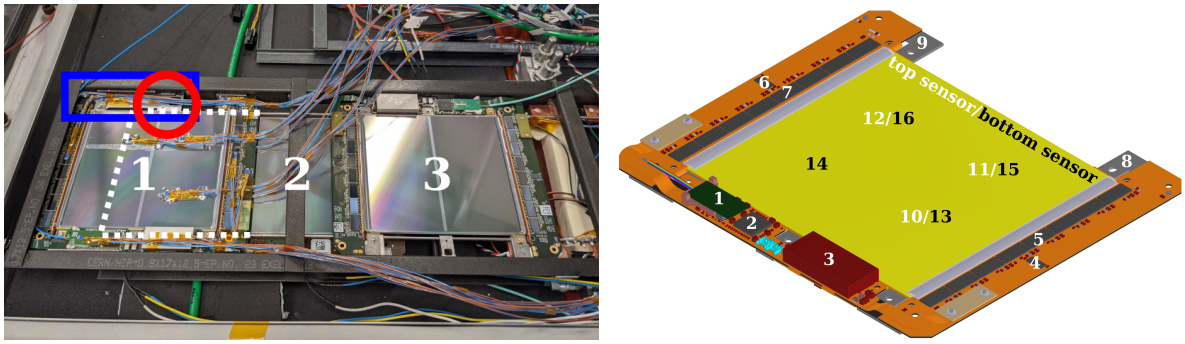

(a) (b)

Figure 6.2.: The irradiated 2S module prototype. (a) The irradiated module with its 16 temperature sensors on the ladder at position 1. One of the special ladder inserts is marked with a blue rectangle and the missing sixth cooling point of the irradiated module on the special insert is surrounded by a red circle. The path of the cooling pipe below the module is drawn with a white dashed line. (b) Numbering of the temperature probes on the irradiated module. The white numbers refer to temperature sensors attached to the top side of the module while the black numbers refer to temperature sensors on the bottom silicon sensor of the module.

was irradiated to a 1 MeV neutron equivalent fluence of $\Phi_{\text{top}} = 5.22 \times 10^{14}\,\text{cm}^{-2}$ while the bottom sensor was irradiated to $\Phi_{\text{bottom}} = 3.77 \times 10^{14}\,\text{cm}^{-2}$. The fluence seen by the FEHs is $\Phi = 1 \times 10^{14}\,\text{cm}^{-2}$, which resulted already in a total ionizing dose of about 150 kGy [tkL23], even higher than the maximum expected dose of 100 kGy. After the irradiation the sensors were annealed to a room temperature equivalent annealing time of 140 days. This corresponds to the expected time of two weeks at room temperature for maintenance each year during the ten years HL-LHC operation. Nevertheless, the module got additionally handled during beam and integration tests so that the actual annealing time was about 154 days during the first cold test and about 168 days during the second cold test. The tracking performance of the module after irradiation was already characterized during a beam test at the DESY II beam test facility. The results can be found in [Wit23]. The SEH of the module was unirradiated since it is built with an lpGBTv0 which is – different from the lpGBTv1 – not radiation hard.

The thermal integrations tests focussed on the thermal performance of the module on the TB2S ladder. Thus, the module got equipped with 16 temperature sensors. The irradiated module mounted on the TB2S ladder as well as the positions and numbering scheme of the temperature probes on the module is depicted in figure 6.2. Three temperature probes are attached to the SEH, one on each, the VTRx+, lpGBT and DC-DC converter shield. Two temperature probes are on each FEH (CIC and one CBC) and one on the left and right bridge at the SEH far side. Temperatures on the top silicon sensor are measured at three positions and at four positions on the bottom sensor.

For the comparison of the measurement results with the simulation, some special features of the module are important to take into account. The module is built with five cooling points only (visible in figure 6.2). Modules at position 1 of the TB2S ladders will normally have a sixth cooling point. The bridges used for this module have an old design, meaning there is not yet extra material which was added to the design for achieving a better cooling performance. A picture of a long bridge and a stump bridge of the old and new design can be seen in figure 6.3. In addition, the fluences of the top and bottom sensor are different and

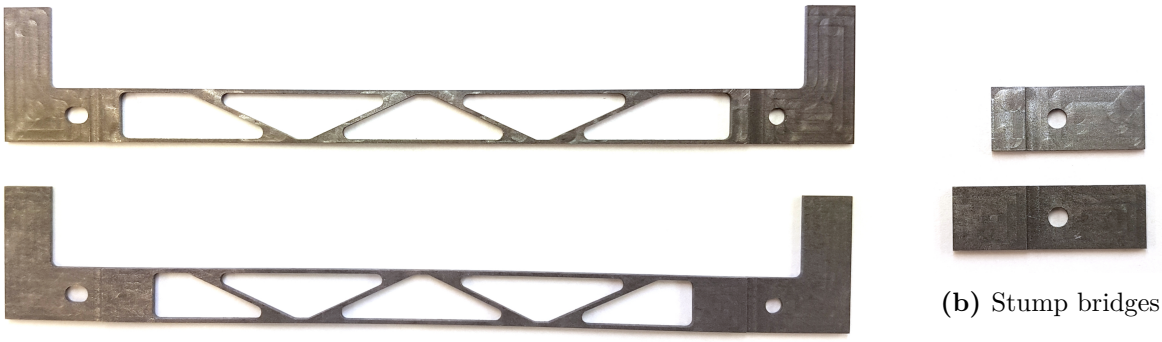

(a) Long bridges

(b) Stump bridges

Figure 6.3.: Picture of the module bridges. The old bridge design is shown in the upper row while the new design in depicted in the lower row. Additional mass was added to the new design resulting in better cooling performance.

with $\Phi_{\text{top}} = 5.22 \times 10^{14}\,\text{cm}^{-2}$ and $\Phi_{\text{bottom}} = 3.77 \times 10^{14}\,\text{cm}^{-2}$ even higher than the maximum expected fluence of $3.7 \times 10^{14}\,\text{cm}^{-2}$ for 2S modules in the TB2S after $4000\,\text{fb}^{-1}$. [tkL23]

6.1.2. Thermal Measurements during Module Operation

To get a general idea of the temperatures on the irradiated 2S module, they are shown in figure 6.4a during a sequence of measurements with the module. From minute 1 to 6 an IV curve is taken from 0 V to 800 V (label "IV").[2] At minute 7 the high voltage is set to 600 V and the low voltage is switched on at 10.5 V (label "LV on"). After stabilization of the temperatures, a calibration run of the module is started at minute 14. This is finished at minute 23 (label "Calibration"). Afterwards the module is in the configured and calibrated state ready to take data. In addition to the temperatures, figure 6.4b shows the power consumption of the irradiated module during the same time range. The power is shown separately for the high and low voltage as well as the sum of both.

During the IV curve the silicon sensor temperatures increase while the other temperatures stay constant. The reason for that is the increasing leakage current with increasing high voltage. The increased current in turn increases the temperature. The total power consumption of the module is $P_{\text{total}} = P_{\text{HV}} = 450\,\text{mW}$ at a bias voltage of $V_{\text{bias}} = 800\,\text{V}$ and a sensor temperature of $T_{\text{sensor}} \approx -26\,^{\circ}\text{C}$.

When switching on the low voltage to 10.5 V and reducing the high voltage from 800 V to 600 V after the IV for the measurements at the same time, all temperatures on the irradiated module increase due to the increased total power consumption of the module ($P_{\text{total}} = P_{\text{HV,LV}} \approx 2.7\,\text{W}$ at $V_{\text{bias}} = 600\,\text{V}$ and $T_{\text{sensor}} \approx -24\,^{\circ}\text{C}$). The temperature on the VTRx+ is the highest temperature on the module.

After reaching stable temperatures, the routine of calibrating the module and measuring the electronic noise is started. The low voltage power consumption increases again when the chips on the module are operated ($P_{\text{total}} = P_{\text{HV,LV}} \approx 4.8\,\text{W}$ at $V_{\text{bias}} = 600\,\text{V}$ and $T_{\text{sensor}} \approx -22.5\,^{\circ}\text{C}$). Thus, all temperatures on the module increase again. At about minute 21.5 the low voltage

[2] During the prototyping phase, Phase-2 Outer Tracker modules were sometimes powered with high voltage only. This is not foreseen during the later tracker operation and, especially for PS and irradiated modules, not recommended. Powering the readout chips of the modules compensates the leakage current which is, especially for the DC coupled macro-pixel sensors of the PS module, important to not damage the readout chips. With higher irradiation, the leakage current increases and thus, the low voltage powering gets more relevant. The operation with high voltage only has to be avoided during the Phase-2 Outer Tracker operation.

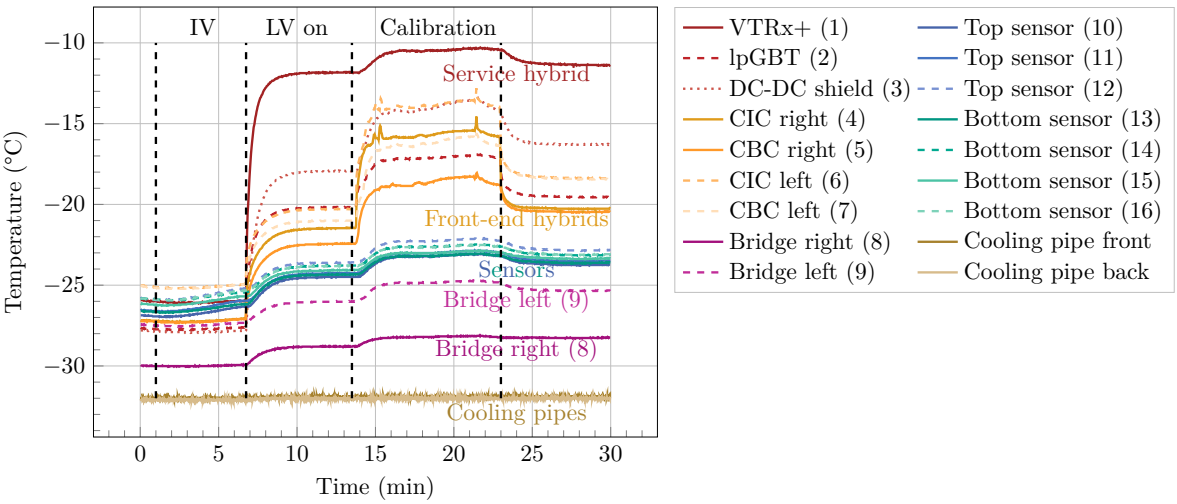

(a) Module temperatures on the irradiated module during module operation

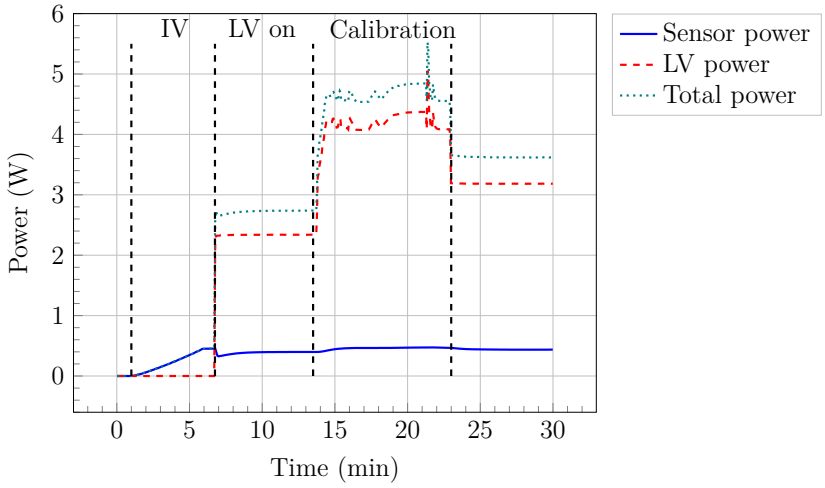

(b) Power consumption on the irradiated module during module operation

Figure 6.4.: Module temperatures and power consumption on the irradiated module during module operation. (a) The temperatures measured with the 16 temperature probes on the irradiated module as well as the temperature at the cooling pipe upstream and downstream of the modules are shown. The temperatures on different parts of the module are plotted with different colors (Service hybrid: red, Front-end hybrids: orange, Top sensor: blue, Bottom sensor: green, Bridges: purple, Cooling pipes: brown). The temperatures of the right module side are plotted with solid lines while for the left sides temperatures are depicted with dashed lines. The time ranges of the measurements performed on the module are indicated with dashed vertical lines. (b) The high and low voltage power consumption is shown separately as well as summed up to the total power consumption. The sensor power consumption is higher at the end of the IV curve than in the "LV on" and "Calibration" section since the IV curve was taken up to 800 V while it is set to 600 V during the calibration. The peaks at about minute 21.5 in the low voltage power and in the CIC and CBC temperatures occur when the 50 % percent occupancy level is scanned during the noise measurement.

power shows a peak. This power consumption peak coincides with the temperatures on the CICs and CBCs and occurs while scanning the 50 % occupancy during the noise measurement. At hit occupancies around 50 % the amount of bit flips in the data streams is higher than at other occupancies. Thus, the power consumption is at its maximum when reading out data with 50 % occupancy.

After finishing the measurements the low voltage power consumption and thus temperatures remain higher than before calibrating the module ($P_{\text{total}} = P_{\text{HV,LV}} \approx 3.6\,\text{W}$ at $V_{\text{bias}} = 600\,\text{V}$ and $T_{\text{sensor}} \approx -23.5\,^{\circ}\text{C}$). Chip configurations different from the default values after the power up are the reason. For the thermal runaway measurements, all modules get calibrated beforehand to increase the power consumption across the whole ladder but to also have stable power conditions. As visible in figure 6.4b the mean power consumption during the calibration is about 1 W higher than the stable value after the calibration. Thus, the power consumption during module operation in the tracker could be about 1 W higher than during the performed measurements.

During the whole measurement time it can be seen that the temperatures on the right side of the module are lower than the ones on the left. This is due to the worse cooling path on the left side of the module since it is mounted there on the special ladder inserts that have worse cooling performance compared to the other inserts of the ladder. The bridges of the left and right module side show a temperature difference of about 3 °C. But nevertheless, the spread of the silicon sensor temperatures is within 1 °C meaning that the overall cooling performance under these conditions is sufficient to reach a homogeneous temperature profile across the silicon sensors. For stable operation of the modules in the tracker, the silicon sensor temperature should stay below −20 °C at a CO_2 set temperature between −35 °C and −33 °C. The measurements show that this is already the case during the module operation with a cooling pipe temperature of −32 °C.

6.1.3. Thermal Runaway Measurements

For stable operation of the modules in the Phase-2 Outer Tracker it is important that the cooling power of the cooling system together with the thermal contacts is able to compensate the heating power of the modules and to keep the silicon sensor temperature below −20 °C. Thermal runaway means that the system enters an uncontrolled self-heating loop when the cooling power of the system is no more able to compensate the heating. The design of the Outer Tracker cooling concept was assisted by thermal *Finite Volume Method* (FVM) simulations also taking into account the higher power dissipation of irradiated modules. The design of the tracker was tuned with the simulations to reach a sufficient margin between the operation temperature and the thermal runaway temperature. The first simulation results were presented in the Technical Design Report of the CMS Tracker [CMS17f]. Therein it was stated that these simulations should be validated with measurements with near to final prototype material as soon as it is available. The thermal runaway measurements presented in this section are such measurements. All thermal simulation results shown in the following were produced by Cristiano Turrioni [Tur22] from INFN Perugia.

This section starts with an explanation of the adiabatic FVM simulations and continues with adaptations to the model to match the measurement conditions. Then, the data taking procedure is explained in more detail and the introduction of an air convection model to the simulations is shown. In the end, the data are compared with the simulation results and the observations are set in the context of the Phase-2 Tracker operation.

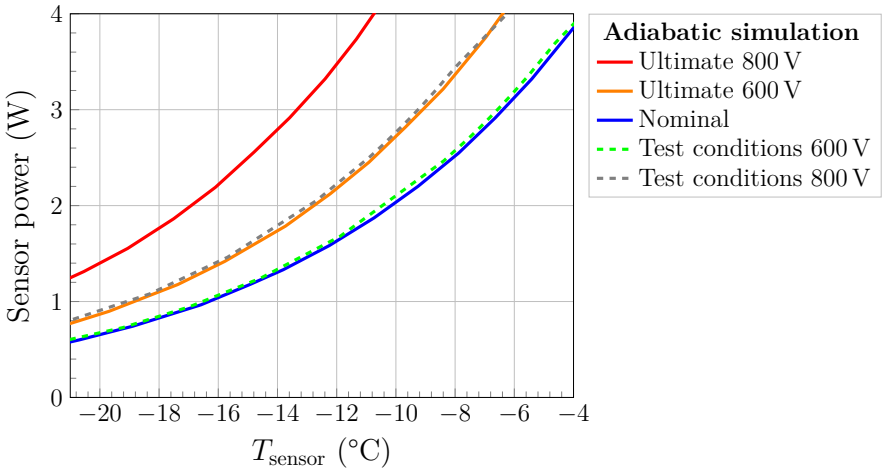

Figure 6.5.: Comparison of the sensor power of the adiabatic simulation. The sensor power is shown as a function of the mean silicon sensor temperature for the adiabatic simulations. All simulations were performed by Cristiano Turrioni [Tur22].

Adiabatic Baseline Simulations

The baseline and most pessimistic simulations are made for the adiabatic case where no heat exchange between the modules and the surrounding air is considered. Only the cooling of the modules by the cooling contacts from the bridges to the inserts of the ladder is taken into account. The geometry of the modules on the ladder and the cooling contact to the ladder inserts with the pipe are simulation parameters. The total power consumption of the module is split for the simulation to single power consumption contributions per electrical component on the module. Thus, the power distribution across the module is close to the real power distribution on the module. The simulations are performed for the nominal and ultimate scenario further described in section 3.2.3. The sensor power as a function of the silicon sensor temperature is an input to the simulation and plotted in figure 6.5. The sensor power is the leakage current defined in equation (3.12) multiplied by the applied bias voltage. For the nominal scenario a bias voltage of 600 V is used while the ultimate scenario is simulated with 600 V and 800 V since depending on the radiation damage to each individual module it is possible that the bias voltage has to be increased to 800 V during the tracker operation in this scenario. The sensor power of the ultimate scenario at 600 V is higher than of the nominal scenario since the radiation level of the simulated module is higher in the ultimate scenario. The power is then again increased at 800 V due to the higher bias voltage. The test conditions mentioned in the label of figure 6.5 are explained later in the text.

The simulation results in the adiabatic case are shown in figure 6.6. The difference of the sensor temperature T_{sensor} to the CO_2 temperature T_{CO2} is shown as a function of T_{CO2}. With increasing CO_2 temperature, the silicon sensor temperature increases as well. The point of the thermal runaway is reached when the sensor and CO_2 temperature diverge. For stable operation of the future tracker it is important that there is a safety margin between the envisaged CO_2 operation temperature (marked as gray area in figure 6.6) and the thermal runaway temperature. The safety margin describes the temperature difference of the CO_2 temperature of the thermal runaway and the −33 °C line which is the highest CO_2 operation temperature in the Outer Tracker. The safety margin is about 8 °C for the nominal scenario, 5.5 °C for the ultimate scenario at 600 V and just 1 °C for the ultimate at 800 V.

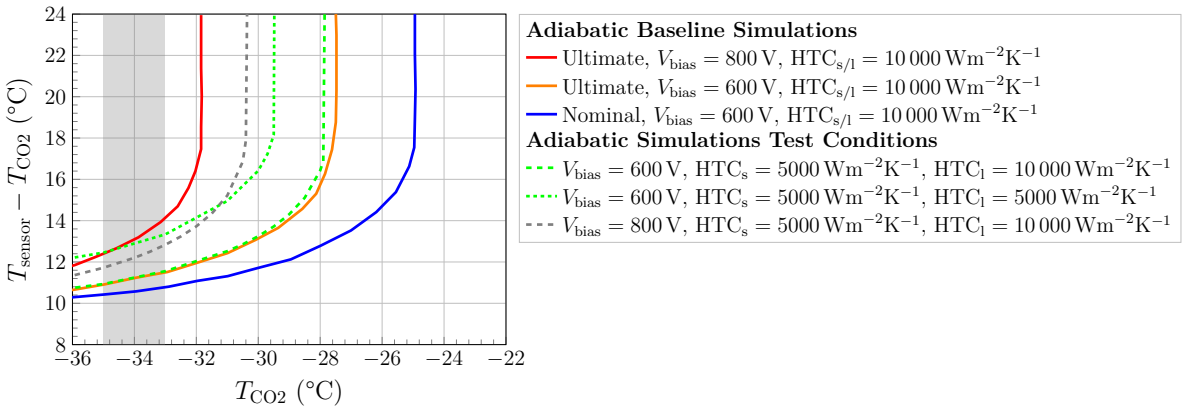

Figure 6.6.: Simulation results for the adiabatic model. The difference of the mean silicon sensor temperature to the CO_2 temperature is shown as a function of the CO_2 temperature. The CO_2 temperature of the Outer Tracker is shown in gray between $-35\,°\text{C}$ and $-33\,°\text{C}$. All simulations were performed by Cristiano Turrioni [Tur22].

Adiabatic Simulations Test Conditions

To be able to compare the simulation results with measurement data, the simulation model has to be adapted to measurement specific conditions. Changes that are input parameters of the simulation and that influence already the adiabatic model are described in this subsection. The annealing factor α of the sensors as well as the fluence they got irradiated to differ from the baseline values. These two variables change the sensor power as a function of the silicon temperature that is an input parameter of the simulation. This curve is shown in figure 6.5 also for the conditions during the measurements for a bias voltage of 600 V and 800 V. The sensor power of the test conditions at 600 V matches, by chance, well the simulation of the nominal scenario and the test conditions at 800 V match the ultimate scenario at 600 V.

The low voltage power dissipation also contributes to the heating power of the modules. Thus, this is an input parameter of the simulation as well. The low voltage power of the irradiated module and the module at position 2 during the presented measurements was about 4.2 W, which is lower than the baseline value of 5.159 W that is normally used for the simulations. The low voltage power during data taking in the tracker is expected to be somewhere in between these values. The sensor power dissipation of the module at position 2 is negligible since the sensors were unirradiated. These two changes to the model would yield better cooling performance.

The sixth cooling point of the modules is also removed for the new simulation model and the "old" spacer design without additional extra mass and therefore worse thermal conductivity is used. The modules are screwed to the ladder inserts with screws applied with a torque key. The torque τ applied allows an estimate of the heat transfer coefficient from the ladder inserts to the module bridges. The heat transfer coefficient of the special and long inserts $\text{HTC}_{\text{s/l}}$ that is normally set to $\text{HTC}_{\text{s/l}} = 10\,000\,\text{Wm}^{-2}\text{K}^{-1}$ for an applied torque of $\tau_{\text{s/l}} = 10\,\text{cNm}$ is reduced to $\text{HTC}_{\text{s/l}} = 5000\,\text{Wm}^{-2}\text{K}^{-1}$ during some measurements since the torque being applied during data taking was $\tau_{\text{s/l}} = 5.5\,\text{cNm}$ for individual configurations. This gives worse cooling conditions than in the baseline model. Measurements of the relation between the applied torque and the heat transfer coefficient can be found in [Rau20]. The values used for the shown simulations are slightly on the pessimistic side compared to these results.

Table 6.2.: Thermal runaway measurement conditions. The measurement conditions for the four thermal runaway measurements are listed in the table. The air temperature profile, the high voltage setting and the applied torque to the screws at the long inserts τ_l are the only parameters that were changed between the different measurements. The air temperature during the test at the first CO_2 set temperature of $-35\,°C$ is given to get an idea of the air temperature during this measurement.

Test name	V_bias	τ_s	τ_l	$T_\mathrm{air}(T_\mathrm{CO2} = -35\,°C)$
TR_ref	600 V	< 5.5 cNm	10 cNm	$-12\,°C$
TR_lowTemp	600 V	< 5.5 cNm	10 cNm	$-17\,°C$
TR_800V	800 V	< 5.5 cNm	10 cNm	$-19\,°C$
TR_lowTorque	600 V	< 5.5 cNm	5.5 cNm	$-19\,°C$

The adiabatic simulations with all these changes is also shown in figure 6.6. By chance, the test conditions at 600 V result in nearly the same thermal runaway curve as the ultimate at 600 V while the test conditions as 800 V show the thermal runaway for an about 2 °C higher CO_2 temperature than the ultimate at 800 V scenario. The simulation of the test conditions with reduced thermal contact on the special and long inserts has the thermal runaway at a CO_2 temperature about 1 °C higher than the 800 V case.

Measurements

For the thermal runaway measurements, dry air at a temperature of about $-19\,°C$ was flushed to the inner and the outer box until the air temperature measured inside the inner box was at least $-12\,°C$. The modules on the ladder were calibrated to increase the power consumption across the entire ladder. For the actual measurements that took about one to two hours, the dry air flux to both – the inner and outer box – was switched off completely to reduce the air convection during the measurements to a minimum. Due to the good isolation of the outer box, the dew point stayed far below the temperatures in the setup for the measurement time. After each thermal runaway measurement the dry air flux was switched on again.

Starting at the lowest possible CO_2 set temperature of about $-35\,°C$ at a CO_2 pressure of 12 bar, the pressure is increased in steps of 1 bar and thus the CO_2 temperature increases as well. At each temperature step, it was waited until the monitoring temperatures stabilized. All the necessary parameters for the comparison with the simulation such as the air temperature and the mean silicon sensor temperature are extracted from the monitoring data by averaging the values of the last 30 seconds at each temperature step.

During the 2024 test thermal runaway measurements were performed with four different test conditions. These tests are named TR_ref, TR_lowTemp, TR_800V and TR_lowTorque and the conditions of each measurement are given in table 6.2. The tests differ by the high voltage, the torque on the long inserts τ_l and the air temperature during the measurements. The reference measurement TR_ref was – besides the air temperature – measured with the same conditions as TR_lowTemp. TR_800V was measured with a high voltage of 800 V instead of 600 V and during TR_lowTorque the torque on the long inserts was reduced from $\tau_\mathrm{l} = 10$ cNm to $\tau_\mathrm{l} = 5.5$ cNm. The torque at the special inserts was $\tau_\mathrm{s} < 5.5$ cNm during all measurements since the threads for screwing the module at these inserts were already damaged from previous thermal qualification measurements of that ladder. The temperatures on the irradiated module as well as ambient temperatures during these four thermal runaway measurement are further described in appendix F.1 and plotted in figures F.1 to F.4.

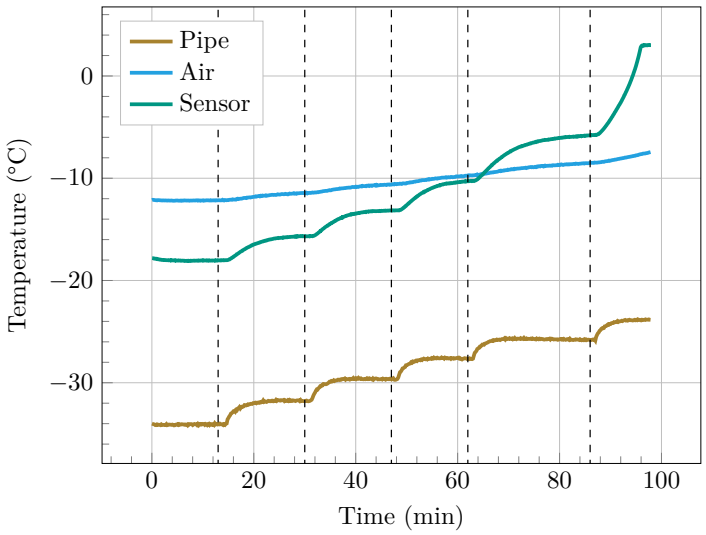

Figure 6.7.: Temperatures during TR_ref. The temperatures of the pipe, air and silicon sensor of the irradiated module are shown versus the measurement time. The vertical dashed lines indicate the times at which the data of the thermal runaway measurements were taken.

A simplified version of the temperatures measured during TR_ref can be found in figure 6.7. The CO_2 temperature is changed in steps and thus, the temperature measured at the pipe increases in steps and stabilizes after some minutes of waiting time. The silicon sensor temperature follows the temperature of the pipe. The air temperature is slightly increasing during the measurement time since no cold dry air is flushed into the measurement box. At the last measurement step, the temperature of the sensor increases drastically. The sensor went into thermal runaway. At the point between 90 and 100 minutes where the sensor temperature stayed at the same level, the current compliance of 12 mA of the high voltage power supply was reached. The vertical dashed lines indicate the time stamps at which the measurement data of the following thermal runaway plots were extracted from the data. At these points, the pipe and sensor temperatures had stabilized.

Convection Simulations

To be able to compare the data with the simulation, the simulation is adapted to take the air convection and heat transfer of the modules with the surrounding air into account. The heat transfer rate $\dot{Q}$ can be expressed by

$$\dot{Q} = \mathrm{HTC}_{\mathrm{air}} \cdot A \cdot (T_{\mathrm{air}} - T_{\mathrm{module\ surface}}) \ . \tag{6.1}$$

The temperature of the air inside the measurement box T_{air} is an input variable of the simulation and taken from the measurement results. The mean value of four pt1000 temperature sensors measuring the air temperature inside the inner box are used. The temperature of the modules surface $T_{\mathrm{module\ surface}}$ is extracted from the simulation itself for each simulation step. The heat transfer coefficient of the air $\mathrm{HTC}_{\mathrm{air}}$ is varied such that the simulation fits best to the data while the outer modules surface area A is known from the module geometry.

The influence of different values of $\mathrm{HTC}_{\mathrm{air}}$ is depicted in figure 6.8. As for all plots of the thermal runaway measurements, the difference of the temperature of the air and the sensor to the CO_2 temperature is plotted over the CO_2 temperature. The gray area marks the envisaged

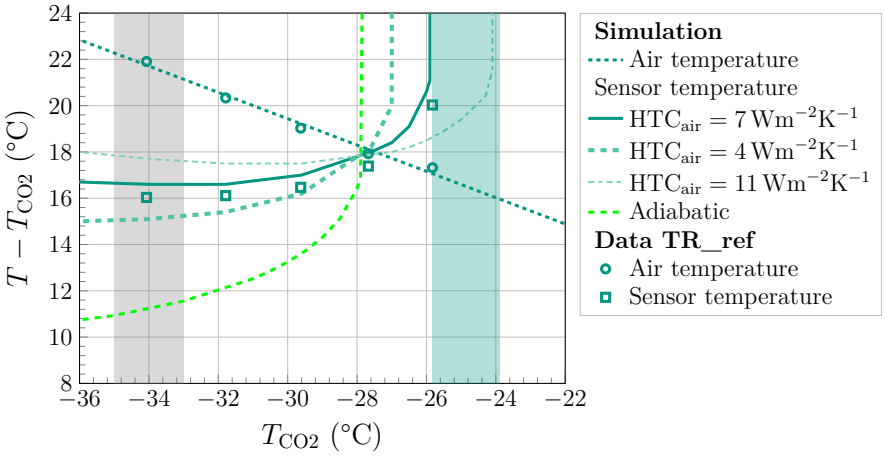

Figure 6.8.: Influence of the heat transfer coefficient of the air on the simulation results. The higher the heat transfer coefficient of the air to sensor, the closer is the sensor temperature to the air temperature. This is valid for both cases, higher and lower air temperature compared to the sensor temperature. In the point where the sensor and air temperature have the same value, the sensor temperature does not depend on the air temperature since this matches the adiabatic conditions where the sensor temperature is not influenced by the air. All simulations were performed by Cristiano Turrioni [Tur22].

CO_2 operation temperature from −35 °C to −33 °C of the Phase-2 Outer Tracker. The green area marks the temperature range of the measured thermal runaway. It starts at the last CO_2 temperature at which the temperature on the silicon sensors stabilized and ends at the CO_2 temperature at which the silicon sensors went into thermal runaway. The data of TR_ref is shown besides the simulation results for different values of HTC_{air}. The adiabatic simulation is shown as well. As expected, the air increases the sensor temperature with respect to the adiabatic case when it is higher than the sensor temperature of the adiabatic model and reduces the sensor temperature when it is lower. The larger HTC_{air} was set in the simulation, the higher is the influence of the air on the sensor temperature. At the point where the sensor temperature matches the air temperature, all simulation results are the same. In this single point, all convection simulations match with the adiabatic simulation. Since the measurement and simulation results match best for a value of $HTC_{air} = 7\,Wm^{-2}K^{-1}$, this was used for all the following simulations. This heat transfer coefficient of the air is absolutely reasonable for natural air convection as inside the measurement box

Figure 6.9 depicts again data and simulation results of TR_ref. This time, the heat transfer coefficients of the inserts are varied to see how this influences the simulation results. The baseline convection model uses a heat transfer coefficient of the special inserts $HTC_s = 5000\,Wm^{-2}K^{-1}$ and of the long inserts $HTC_l = 10\,000\,Wm^{-2}K^{-1}$. This accounts for the different torques that were used in the measurements (see table 6.2). The torque at the special inserts was about half of the torque at the long inserts. Assuming linear dependence of the torque and the thermal contact, the heat transfer coefficient was also halved at the special inserts. The simulation in which also the heat transfer coefficient of the long inserts was reduced to $HTC_l = 5000\,Wm^{-2}K^{-1}$ shows that this has a huge impact on the sensor temperature. It is increased by about 1.5 °C and also the thermal runaway occurs about 1.5 °C earlier. Contrary, increasing the heat transfer coefficient of the special inserts to $HTC_s = 10\,000\,Wm^{-2}K^{-1}$, results in a negligible sensor temperature reduction. The results show that for modules at

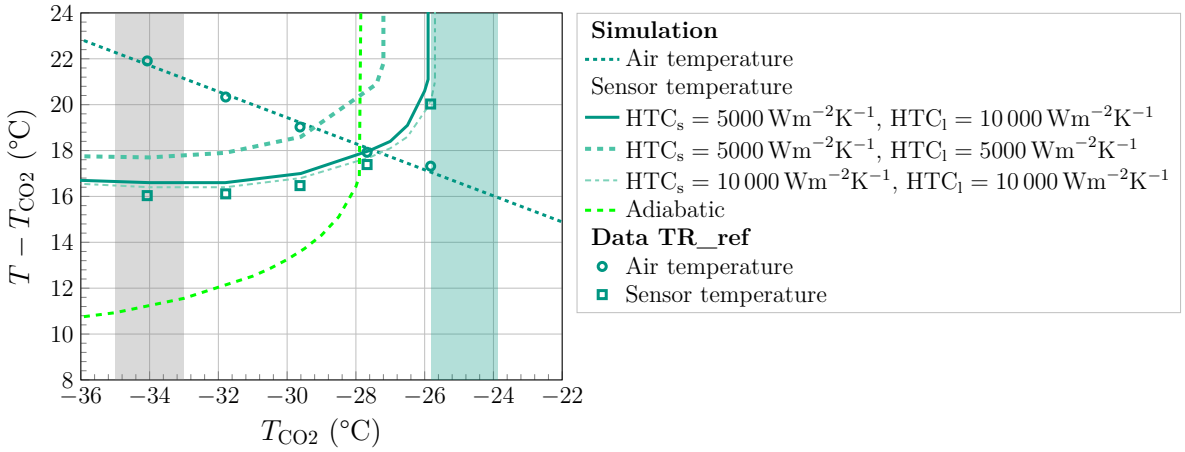

Figure 6.9.: Influence of the heat transfer coefficient of the thermal inserts on the simulation results. Reducing the thermal heat transfer coefficient of the long inserts has a bigger influence on the simulated sensor temperature than the reduction of the heat transfer coefficient of the special inserts. All simulations were performed by Cristiano Turrioni [Tur22].

position 1, the cooling performance is mainly driven by the long inserts since the cooling performance of them is much better than on the special inserts with the less good cooling contact to the pipe.

Comparison Simulation and Data

The comparison of the simulation and measurement results for the three remaining thermal runaway measurements TR_lowTemp, TR_800V and TR_lowTorque can be found in figure 6.10. The adiabatic simulation results are the same as plotted in figure 6.6. For each test, the adiabatic model with the test parameters are added as reference in the plot as well. TR_lowTemp was measured with exactly the same parameters as the already shown reference measurement TR_ref. Just the linear air profile was different. The simulation result of the sensor temperature matches the measurement well. TR_800V was measured with a bias voltage of $V_{bias} = 800\,V$ instead of 600 V. Thus, the thermal runaway occurs already at lower CO_2 temperatures than during the other measurements. The convection simulation fits again the data within 1 °C. During the last measurement TR_lowTorque, the torque at the long inserts was reduced to $\tau_l = 5.5\,cNm$. In figure 6.10c, the results of the simulation that takes the reduced contact into account as well as the baseline simulation are shown. The measurement results are unexpectedly closer to the baseline simulation than to the one taking the reduced contact into account. A reason for that could be that the torque at the screws was just reduced and not the whole module lifted and then mounted again with the reduced torque. Also, the irradiated module at position 1 was mounted on the top side of the ladder meaning that the weight of the module also presses it down a bit even though this is not much with about 40 g. Additionally, it is not clear if halving the screw torque has really a linear effect on the thermal contact. It could be that the thermal contact will stay more or less the same while reducing the torque until it drops dramatically. To answers these questions, even more detailed thermal measurements with an irradiated module would be needed.

During the thermal runaway measurements, the leakage current of the irradiated module was measured at various sensor temperatures. The data of both thermal tests is plotted together with the expectation in figure 6.11. The expectation is calculated as described in section 3.3.1.

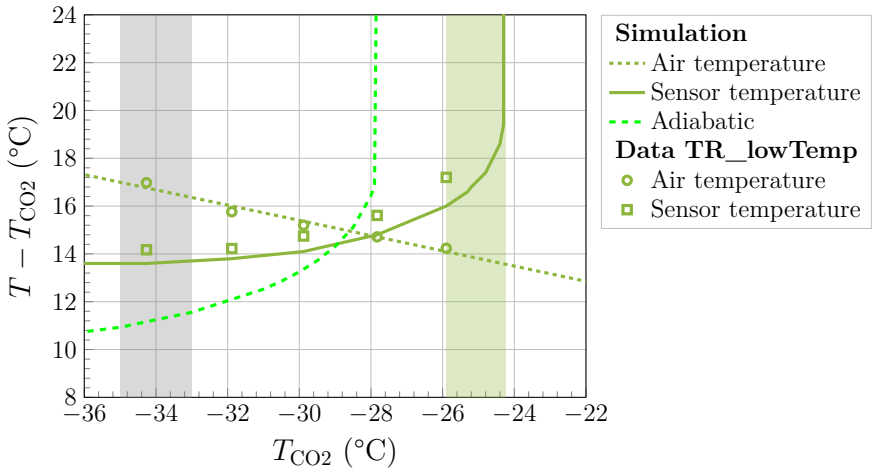

(a) TR_lowTemp

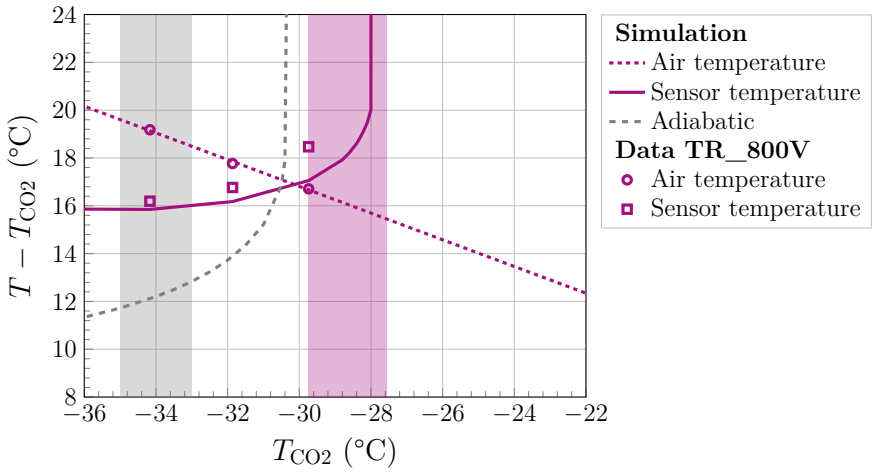

(b) TR_800V

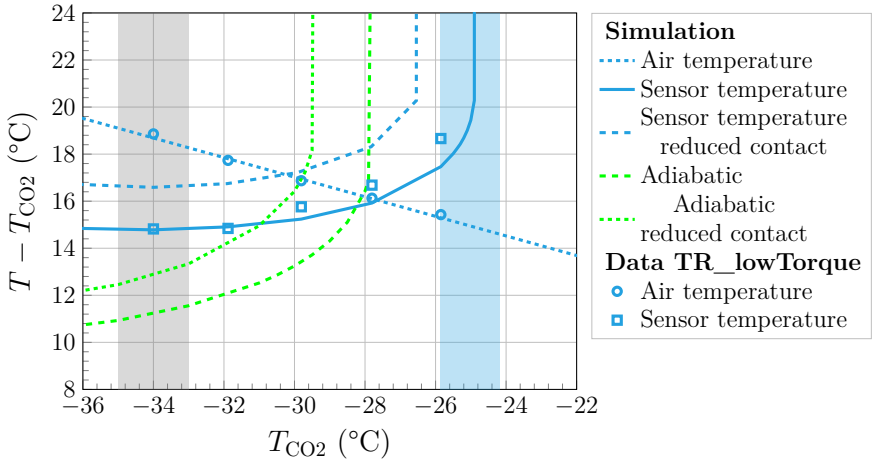

(c) TR_lowTorque

Figure 6.10.: Simulation results of the thermal runaway measurements. The simulated and measured sensor temperature match well. For TR_lowTorque the reduction of the torque on the long inserts cannot be seen as concisely as expected from the simulation. All simulations were performed by Cristiano Turrioni [Tur22].

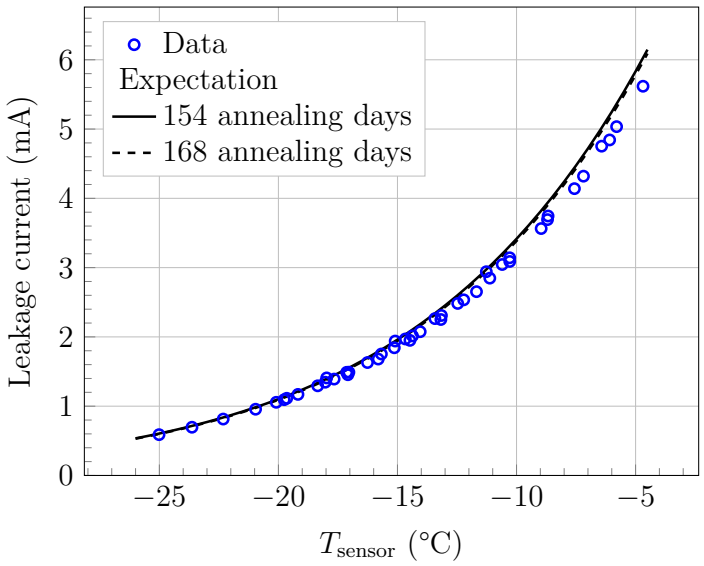

Figure 6.11.: Leakage current versus mean silicon sensor temperature. The leakage current of the irradiated module is shown as a function of the mean silicon sensor temperature. The calculated expectation is plotted separately for 154 and 168 annealing days at room temperature. The data fit the expectation well.

The radiation induced increase of the leakage current at 21 °C given in equation (3.7) is calculated separately for each sensor with their fluence levels and then summed leading to the equation

$$\Delta I(T) = \alpha \cdot (\Phi_{\text{top}} + \Phi_{\text{bottom}}) \cdot V_{\text{sensor}} \cdot \frac{I(T)}{I(21\,^{\circ}\text{C})} \tag{6.2}$$

for the expectation of the leakage current. The exponential temperature dependency $I(T)$ of the leakage current is given by equation (3.11). This is plotted in figure 6.11 for an annealing factor $\alpha = 2.959 \times 10^{-17}\,\text{Acm}^{-1}$ and $\alpha = 2.934 \times 10^{-17}\,\text{Acm}^{-1}$ for 154 days and 168 days annealing time at room temperature. The difference of the shown expectations is small since the annealing factor stays relatively constant with more annealing time in this time range as visible in figure 3.10. The measured leakage current fits the expectation well even though the expectation is extracted from data measured on diodes. The larger size of the 2S module sensors compared to these diodes explains the differences between data and expectation.

Figure F.5 shows the comparison of the sensor power as a function of the sensor temperature. The simulation takes for the leakage current the same input model as described in the paragraph above. Thus, the data and simulation input of the sensor power match as already observed in figure 6.11. The simulation input in figure F.5 is already shown in figure 6.5 compared to the input of the adiabatic baseline simulations. Figure 6.12 shows an output of the simulation, the sensor power over the CO_2 temperature. For all four measurement conditions, the convection simulation results show agreement with the measured data.

First Thermal TB2S Ladder Test in 2022

The results of the first thermal ladder test from 2022 are shown in appendix F.3. Due to a small dry air flux to the measurement box the heat transfer coefficient of the air is higher. Also, thermal runaway could not be observed during the measurements due to the current compliance of the high voltage power supply. The results of this test were presented at the Technology and

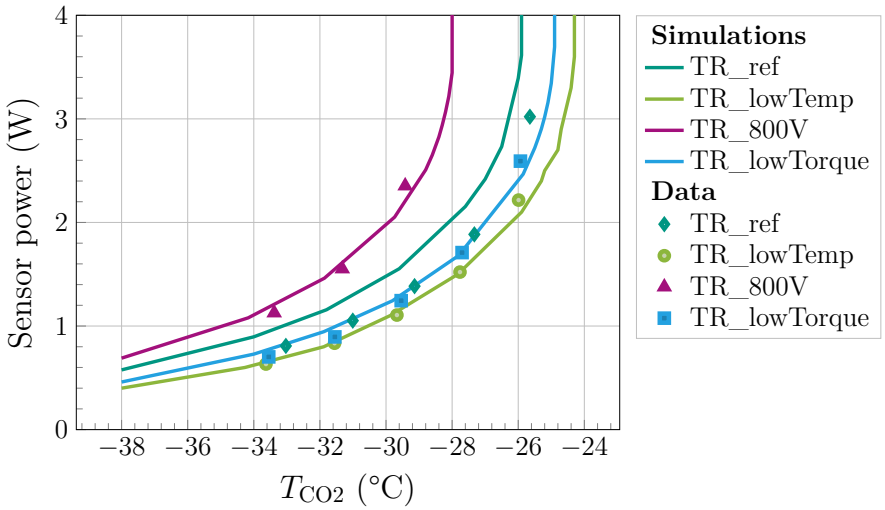

Figure 6.12.: Comparison of the sensor power from data and simulations. The sensor power is plotted as a function of the CO_2 temperature. This output of the convection simulations matches the data from the four measurement conditions well. All simulations were performed by Cristiano Turrioni [Tur22].

Instrumentation in Particle Physics (TIPP) conference 2023 [Sto23]. The proceedings can be found in [Sto25].

Operation of the Phase-2 Tracker

To bring all these observations in the context of the Phase-2 Tracker operation, it is important to understand the real environmental conditions that will be there. Generally, this is not known a priori, but the current tracker operated in CMS since more than 15 years can give hints of what can be expected in the Phase-2 Outer Tracker. In the current tracker, the temperature of the silicon sensors is at about −17 °C while the coolant is circulated at about −25 °C. This results in a temperature difference of about 8 °C. The mean air temperature measured in the tracker is also at about −17 °C. [Shv25] This means that the air temperature in the tracker is driven by the silicon sensor temperature which has the largest surface area inside the tracker. The air having the same temperature as the silicon is also an assumption for the Phase-2 Tracker. One can imagine that the air acts mainly as a heat exchanger between the modules with higher and lower silicon sensor temperature than the mean. It cools the warmest modules and heats the colder modules providing a relatively uniform temperature distribution inside the tracker. During that, the air is moving just due to the natural convection slightly increased by the movement of the “oxygen depleted air” with about 4 % of O_2 flushed to the tracker at the air supply. [Shv25] Since during the presented measurements the dry air supply was switched off completely and the air temperature was also above the silicon sensor temperature when having set the CO_2 temperature to its nominal operation conditions of −33 °C to −35 °C, the operation conditions in the Phase-2 Tracker are most likely even better than during the presented measurements. This would result in an even higher safety margin to the thermal runaway temperature than assumed by the simulation taking the air convection into account. These measurements were just first thermal measurements with near to final modules on final subdetector structures. Within the CMS Tracker group further investigations with respect to the cooling and operation are ongoing.

6.1.4. Noise and Pedestal Measurement Results

The noise measurements performed on the eleven kickoff modules during this test can be seen in figure 6.13. The noise was measured individually at room temperature before the integration and simultaneously on all modules on the ladder at 15 °C, −20 °C and −35 °C. There is no noise measurement after disassembling the modules from the ladder since the modules stayed on the ladder for further tests which are not part of this thesis. The bias voltage during the measurements before the integration was 350 V while it was set to 600 V during the measurements on the ladder.

As the noise was measured at three different CO_2 cooling set temperatures, the reduction of the noise with reduced temperature can be seen in figure 6.13 as well. Also, nearly all modules show some not connected strips with low noise as well as outliers that are plotted as individual points in the candle plot figure 6.13. All strip noise values that lie outside 1.5 times the interquartile range are plotted as outliers. This is not affected by the integration but was already present at the modules before the integration test. The noise on the ladder is similar to the noise before the integration for all modules except module 6. The problems with module 6 are explained later in the text.

As already shown in section 4.1.2, the noise of kickoff modules with a split plane SEH is higher than the noise of the modules with a common plane SEH. On the ladder, there were both types of modules mounted. Module 2, 3, 6, 7, 8 and 10 are assembled with a common plane SEH while the other modules have a split plane SEH. As expected, the noise of the common plane SEH modules is lower than of the others. All modules except module 4 had a ground balancer attached to the FEHs at the module side opposite the SEH. The noise of module 4 is, as expected, higher than the noise of the other split plane modules with a ground balancer connected.

The module at position 6 shows many unconnected strips on the ladder with noise values at about 2.5 V_{CTH} as well as channels with noise values up to 30 V_{CTH} meaning that these channels were not connected to high voltage during that measurement. The channels with increased noise belong to the bottom sensor where the high voltage connection to the sensor backside was already unstable before the integration on the ladder. It turned out that the disconnection of the bonds near the edges of the sensors was caused by mechanical stress on the module that was executed during screwing the module on the ladder inserts. A small plastic piece intended for temporal usage during assembly of the modules was not removed from the module that then clashed with the ladder insert during the integration. This accident demonstrated why a visual inspection at the assembly center before shipping out the modules is as important as a reception inspection at the integration centers before integrating modules on detector substructures such as TB2S ladders.

Before the noise measurement, the offsets of all channels get trimmed individually (see section 3.3.4) so that the pedestal at which the noise hit occupancy is 50 % is about the same for all channels. The pedestal values measured during the same runs for which the noise is shown in figure 6.13 are depicted in figure 6.14. The temperature dependence of the pedestal can be seen as well as the effect of trimming all modules to the same value. During the measurement before the integration, the modules are read out individually, resulting in different pedestal values due to different temperatures during the measurement. On the ladder, the pedestals of all channels get trimmed to the same value, which is the mean pedestal value of all module channels. Thus, the pedestals of all modules are the same and the measurement is not sensitive to potential pedestal differences due to different local temperatures. The pedestals of module 6 spread since it is the broken one.

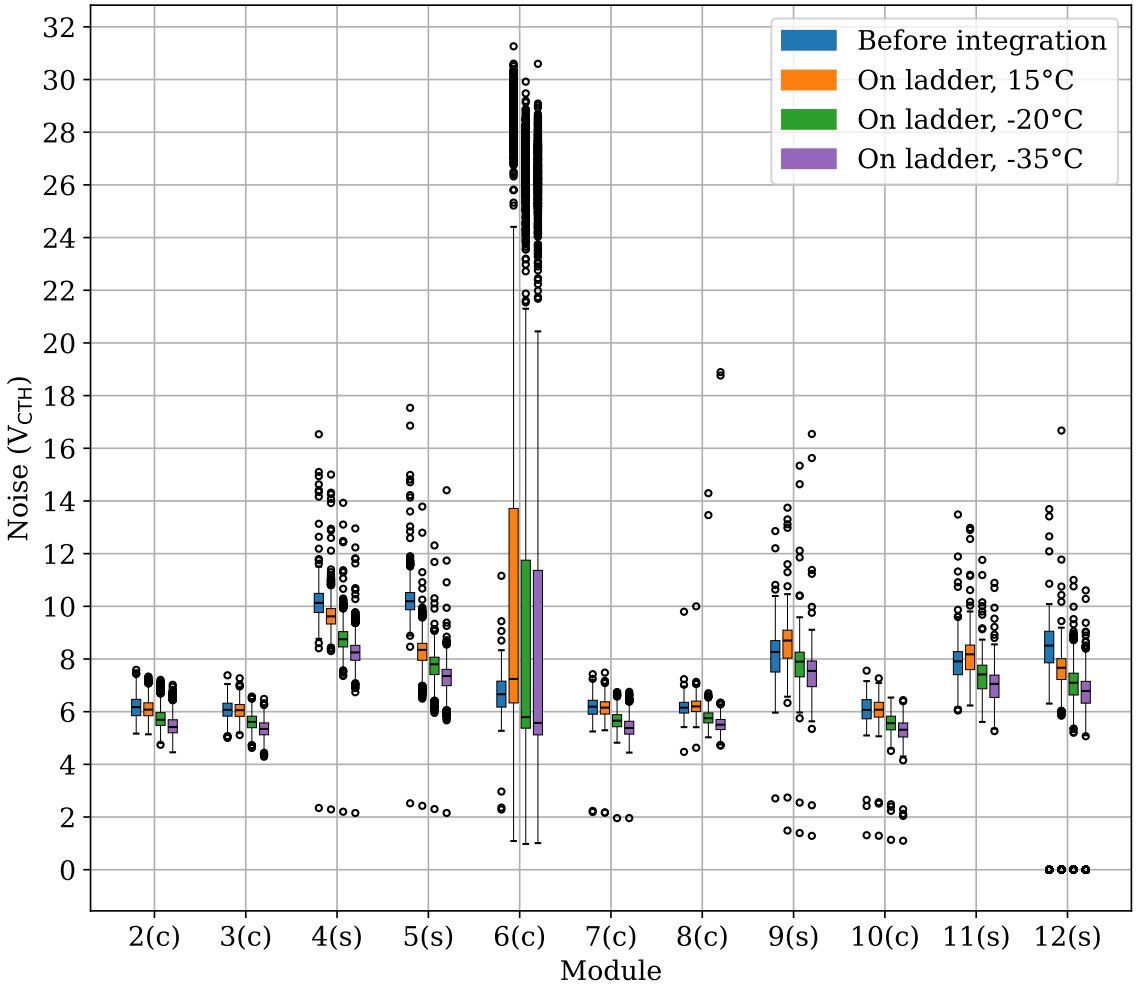

Figure 6.13.: Noise of the kickoff modules on the fully populated ladder during the thermal ladder integration test. The distribution of the strip noise of all eleven kickoff modules on the ladder next to the irradiated module is shown at different temperatures. The results are shown as a box plot with boxes extending from the first to third quartile and whiskers extending to the farthest data points lying within 1.5 times the interquartile range. The median is represented by the stroke within the box. The data points outside the whiskers are outliers and also shown. The letters in brackets behind the module number indicate which kind of module it is. (c) stands for common plane SEH design while (s) means that the module was built with a split plane SEH. A ground balancer was attached to all modules except number 4. As expected, the noise values do not change on the ladder compared to the measurement before the integration. The module mounted at position 6 broke during the integration on the ladder. Due to that it shows many not connected strips with noise values at about 2.5 V_{CTH}. In addition, it showed an already existent high voltage problem on the ladder resulting in noise values up to 30 V_{CTH} on the bottom sensor due to bad high voltage connection of the sensor backside.

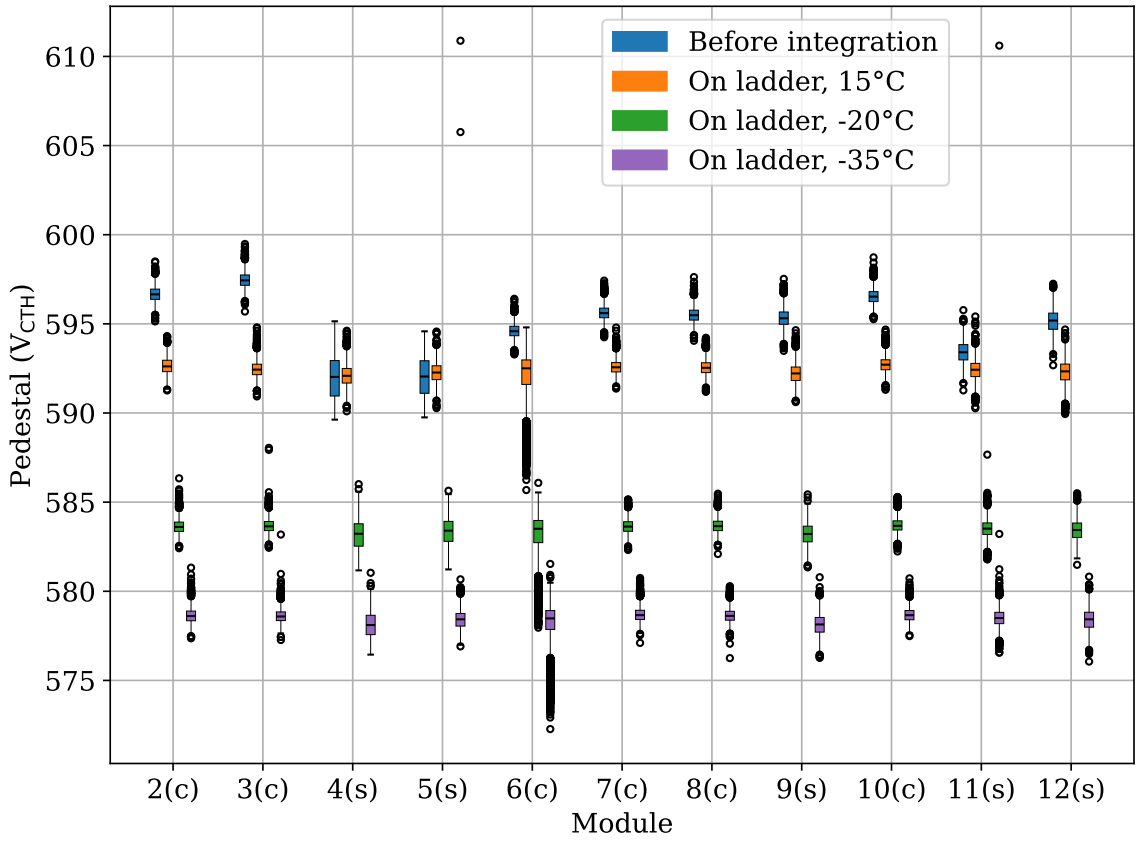

Figure 6.14.: Pedestal of the kickoff modules on the fully populated ladder during the thermal ladder integration test. The distribution of the pedestals of all sensor channels of all eleven kickoff modules on the ladder next to the irradiated module is shown at different temperatures. On the ladder, the pedestal of all modules is the same since all channels are trimmed to the same value.

6.1.5. Summary

During the thermal TB2S ladder integration tests, an irradiated 2S prototype module was operated successfully on a TB2S ladder cooled with evaporative CO_2 cooling. By increasing the CO_2 temperature, the thermal runaway of the silicon sensors of the irradiated module was provoked. The results of these measurements were compared with thermal simulations of the 2S modules showing good agreement between measurement and simulation results. Since the heat transfer coefficient of the air to the modules surface HTC_{air} is not known a priori, this simulation parameter was tuned according to the measurements. This tuning resulted in $HTC_{air} = 7\,Wm^{-2}K^{-1}$, which is reasonable for natural air convection as inside the measurement box. To really be able to test the conditions in the future tracker, the knowledge of the environmental conditions in the future tracker would be important to know. From the conditions in the current tracker, it can be assumed that the air in the Phase-2 Tracker will have about the same temperature as the silicon sensors. Since this is an even lower air temperature than during the presented measurements, the effect of the convective boundary conditions is assumed to be positive as it is expected to provide additional safety margin between the operation and thermal runaway temperature.

6.2. Full TB2S Ladder Integration Test

In December 2021 four 2S prototype modules were mounted on a TB2S ladder prototype. This was a first pretest for the full ladder integration test that was performed in January 2023 at IPHC in Strasbourg and that is described in detail in this chapter. The purpose of the full ladder test was to gain experience in module handling during ladder integration and to perform functional tests of the modules on the ladder. Section 6.2.1 gives a detailed explanation of the measurement setup while sections 6.2.2 to 6.2.5 summarize the results.

6.2.1. Experimental Setup

Since an integration test consists of multiple steps that are executed one after the other the setups and readout configurations are explained for all steps in the following subsections.

Reception

Before integrating the modules on the ladder it is crucial to test them individually to detect possible defects or damage during transport. For this purpose, an Outer Tracker Module Test Station as described in section 3.3.6 is used. During the reception test, noise measurements and IV curves were taken. High voltage tail adaptors were attached to all modules used during this test to have lower module noise and thus provide higher sensitivity to grounding effects that could influence the module noise on the ladder. The results of the comparison between the module noise with and without high voltage tail adaptors are given in section 4.1.1. The Outer Tracker Module Test Station is also used to test the modules after the integration as well when they are removed from the ladder and mounted again on their carrier. This ensures that potential damage during dismounting the modules gets detected before shipping them back to their home institutes.

Integration

For integrating the modules on the ladder, a rotation tool is used to be able to access the ladder safely from both sides. The tool as well as the fully equipped ladder can be seen in figure 6.15. The modules get placed manually with their bridges on the ladder inserts. When

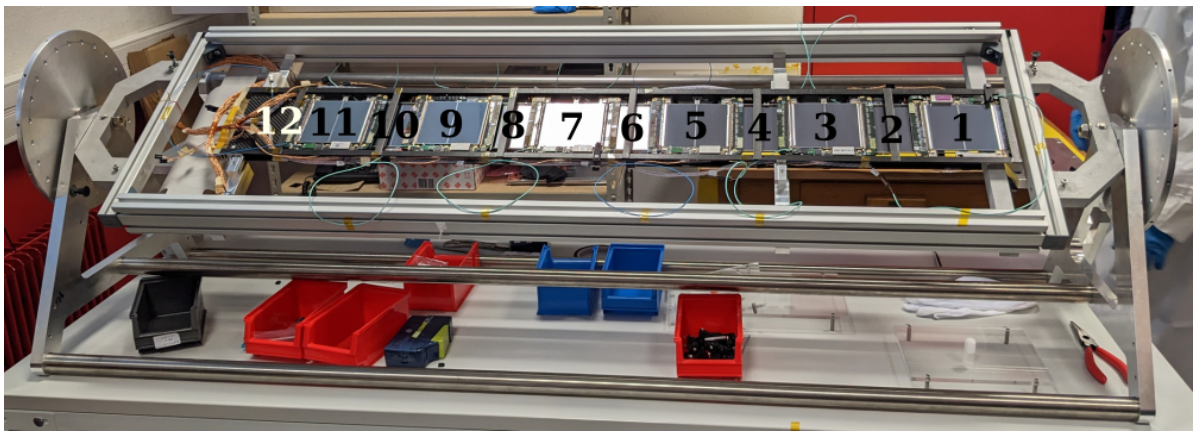

Figure 6.15.: TB2S ladder on the rotation tool fully equipped with 2S modules. The TB2S ladder is mounted in the rotation tool with its dedicated support structures that are used to hold the ladder inside the support wheel of the tracker. By a locking mechanism the rotation stage can get fixed at different angles and the ladder can be accessed from both sides for safe module integration. Twelve modules are mounted on the ladder and the electrical pigtail and optical fanout are attached to the modules. The modules are labeled according to table A.1.

placed they are screwed down by applying a torque of 8 cNm. After being screwed the ladder can safely be rotated to reach the other side. Since each module partially overlaps with the neighboring modules, the modules get integrated from one end to the other beginning with module 1 instead of first mounting all modules from one and then from the other side. The optical octopus and naked fanout get attached to the ladder already before starting the module integration. They have twelve ends with a connector at each end that fits to the optical and electrical pigtails of the module. A module that gets placed on the ladder has the optical and electrical pigtail attached. They get routed through holes in the C-profile by one person; at the same time another person places the module on the ladder. Also during the final integration, this is always done with two people. When a module is placed on the ladder, it gets first screwed to the inserts and then the optical and electrical pigtails get connected to the octopus and fanout. The frame of the rotation tool is also used to transport the equipped ladder and to hold it during the measurements in the measurement setup as depicted in figure 6.16a.

Electrical Measurements

For the measurements the ladder is placed in a box to be operated in dark and dry environment. The box is constantly flushed with dry air and the environmental conditions are monitored with a temperature and humidity sensor placed near module 7 and 8. The high and low voltage of the modules is routed via an electrical octopus to the modules. Two different power supplies were used during the measurements to power the modules with high and low voltage. A CAEN laboratory power supply (CAEN-SY5527 [CAE24]) which will also be used for the integration tests performed during tracker integration at IPHC and a prototype power supply (see figure 6.16b) as it will be used later during tracker operation in CMS. The power cable connecting the electrical octopus and the power supply is a 60 m cable prototype (see figure 6.16b) providing the same impedance from the power supply to the modules as it will be later in the tracker. The optical connection is made with a naked fanout that is connected to the FC7 (see figure 6.16b) for reading out the modules. The FC7 is inserted in a µTCA

Table 6.3.: CMS standard trigger rules. The standard CMS trigger rules are, by default, applied for triggers from the AMC13. The number in brackets is the number of bunch crossings of that trigger rule converted to seconds. All except rule 1 can be disabled to provide trigger rates above 670 kHz. Adapted from [Haz22] and values corrected according to [HT24; Var02].

Number	Description
1	Not more than 1 trigger per every 3 bunch crossings (75 ns)
2	Not more than 2 triggers per every 25 bunch crossings (625 ns)
3	Not more than 3 triggers per every 100 bunch crossings (2.5 µs)
4	Not more than 4 triggers per every 240 bunch crossings (6 µs)

crate to allow trigger signals from an AMC13 [Haz+13]. The modules are read out with the Ph2_ACF and the power supplies are remotely controlled. The currents and voltages are monitored during the whole measurement time.

Triggering

An AMC13 [Haz+13] is used to provide the high rate triggers for the high statistics measurements described in sections 6.2.4 and 6.2.6. The triggers are distributed to the FC7 via the backplane of the µTCA crate housing the AMC13 and the FC7. By default, the standard CMS trigger rules given in table 6.3 are applied to the triggers from the AMC13. These trigger rules are implemented in the CMS L1 Trigger Control System to minimize the buffer overflow probability by inducing a dead time of less than 1 %. The first rule ensures at least two untriggered bunch crossings in between two consecutive L1A signals, which is absolutely necessary for the tracker and preshower. The second rule facilitates firmware implementations for the pixel tracker readout and the last two are part of the history of the CMS design and still there for convenience. [HT24; Var02] For Phase-2 component testing they can be disabled except number 1 which does not allow more than one trigger per every three bunch crossings. [Haz22] Due to a mistake during data taking, the trigger rules two to four actually did not get disabled during the measurements.

The AMC13 triggers can be configured in two modes, the *constant trigger separation* (CTS) mode and *mean trigger separation* (MTS) mode. In CTS mode the triggers always have a constant trigger separation S_{CTS} in clock cycles between two subsequent triggers while in MTS mode the aimed mean trigger frequency can be set. The triggers will come randomly distributed with the predefined mean trigger frequency f_{MTS}. To convert trigger separations in bunch crossings (25 ns) in trigger frequencies in kHz the equation

$$f = \frac{1}{S\,[\text{bunch crossings}]} = \frac{1}{S \cdot 25 \cdot 10^{-9}\,\text{s}} = \frac{1}{S \cdot 25 \cdot 10^{-6}}\,\text{kHz} \tag{6.3}$$

can be used.

The AMC13 also provides the functionality of an orbit reset as it is present at the LHC. An orbit at the LHC contains 3564 bunch crossings. The *L1A ID* counts the bunch number in each orbit from 0 to 3563. During the LHC operation, a gap of some µs between bunches is used to initiate changes of the magnetic fields. This leads to an *orbit gap* in between two orbits, in which no triggers are allowed at all. The orbit gap can be used in the tracker for a resync of the electronics. The Trigger Control of the LHC sends fast controls that can be used by the experiments to identify the orbit gap. [Var00] The orbit gap can be configured for the AMC13 and was set to a width of 63 bunch crossings from L1A IDs of 3500 to 3563. For high

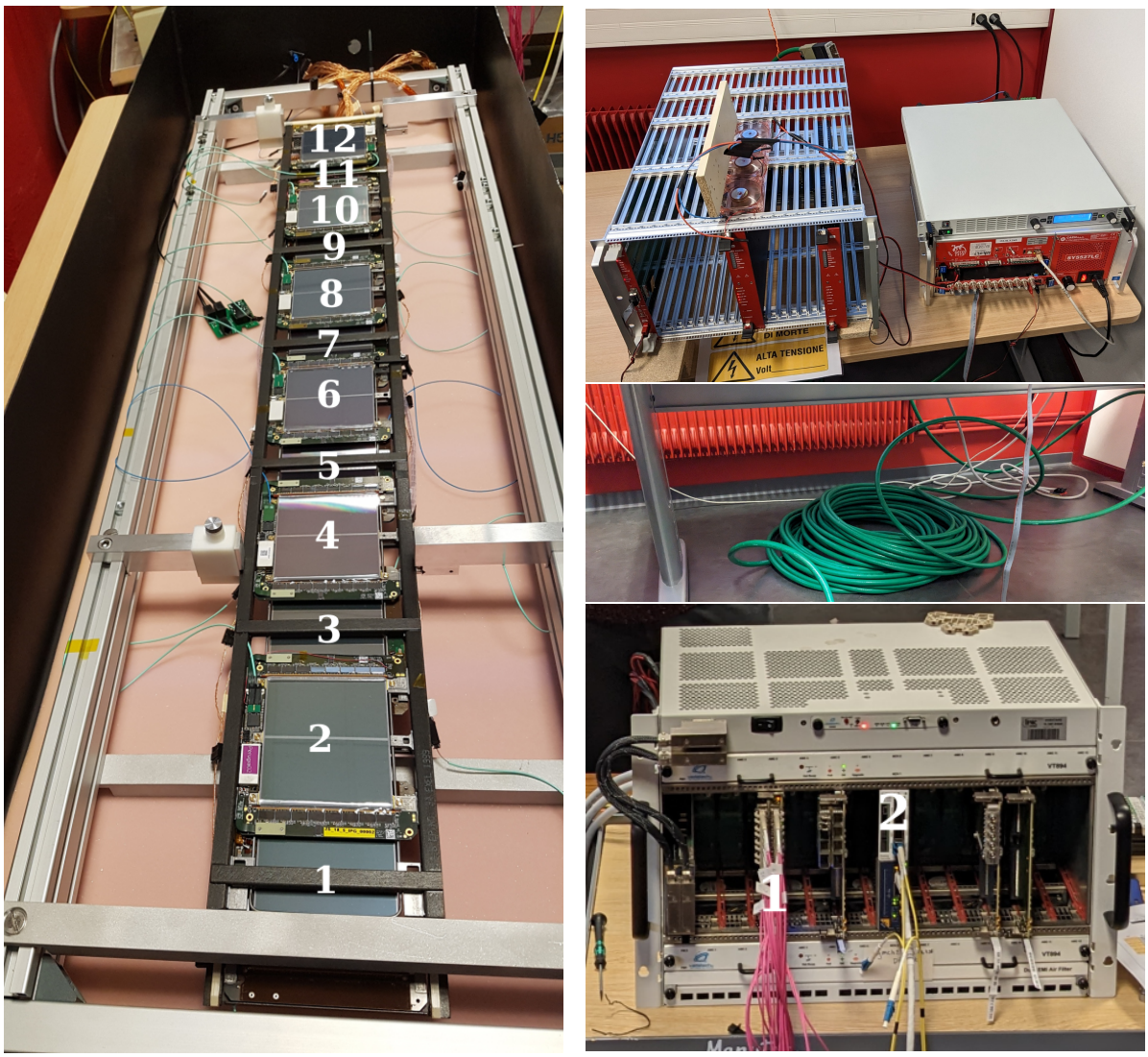

(a) Ladder in testbox

(b) Powering and readout components

Figure 6.16.: Measurement setup of the full ladder integration test. (a) The ladder is placed held by the aluminum frame in the measurement box. The modules are labeled according to table A.1. A humidity and temperature sensor for environmental monitoring is located near module 7 and 8. (b) From top to bottom: Prototype power supply for the Phase-2 Outer Tracker, 60 m long cable for module powering as it will be later during operation in CMS, FC7 with the optical fibers of the modules (label "1") and AMC13 (label "2") in a µTCA crate.

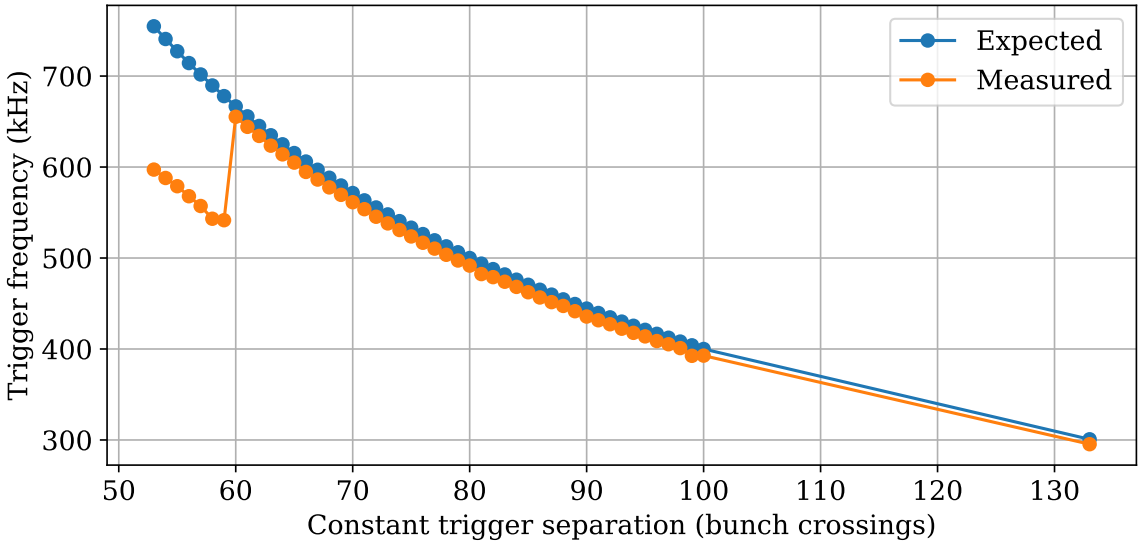

Figure 6.17.: Expected and measured trigger frequencies over the CTS value. The measured trigger frequency is always lower than the expectation since some triggers fall into the orbit gap and get rejected. The drop at a CTS value of 59 bunch crossings is caused by the CMS trigger rules (see table 6.3). Rule 4 becomes relevant as soon as the CTS value is below 60 bunch crossings.

rate triggers with the AMC13, the CMS trigger rules and orbit gaps influence the actual mean trigger separation compared to the set value. Thus, the mean trigger separation got extracted from the data by averaging all BX ID differences between two subsequent events if the BX ID is not reset in the same event. However, in this analysis one effect is not taken into account, which is the result of a missing trigger at the same time the BX ID reset is executed. The expected and measured trigger frequencies are plotted over the CTS set value in figure 6.17. The CMS trigger rules become relevant for trigger separations below 60 bunch crossings.

Readout

For the different measurements that were performed during this test, different readout configurations were used. The noise measurements were performed with internal triggers from the FC7 at 100 kHz and unsparsified readout mode as explained in section 3.3.4 in more detail.

The high statistics measurements described in sections 6.2.4 and 6.2.6 were taken in the sparsified readout mode with triggers from the AMC13. The modules were powered with 350 V high voltage. Further measurement configuration details are given when the results are presented.

6.2.2. IV Measurement Results

To have a first crosscheck that the silicon sensors of the modules did not break during the integration procedure, the current-voltage characteric as explained in section 3.3.1 can be used. IV curves from 0 V to 800 V were taken during the reception test as well as after the removal from the ladder. The reception IV was taken with low voltage off, and on the ladder, different combinations were measured. For better comparability, the comparison of the reception test, the measurement on the ladder with the same configuration (LV of measured module off, all other modules off) and the test after removal are shown in figure 6.18 for all twelve modules on

the ladder. The basic behavior of the leakage current with respect to the applied voltage is the same for all twelve modules, but the absolute current values differ from measurement to measurement. This is only caused by different temperatures during the measurements, since there was no light coming from the VTRx+ of the modules with LV off (see sections 3.3.1 and 3.3.3). Module 9 was only biased up to 350 V during all measurements since its wire-bonds were not encapsulated.[3] Also, module 1 had problems with a lost soldering connection in the HV line on the ladder. Due to that it was only powered to 350 V on the ladder. To avoid high currents on the ladder, the IV curve of module 11 was measured only up to 600 V, and it was decided to power this module like module 1 at 350 V during the further measurements.

The already shown IV measurements were all taken with the LV of all modules off to have no influence by light emitted from the VTRx+. The influence of the VTRx+ light was studied on the ladder as well. The results of these measurements are explained in the appendix in appendix G.1 and plotted in figure G.1. The reference measurements in figure G.1 with LV off (label "LV off") are the same that were already shown in figure 6.18 with the label "On ladder". Concluding, the effect of the VTRx+ light on the module leakage current in the ladder is extremely module dependent and no general statement about the absolute effect can be done. For the operation in the Phase-2 Outer Tracker the VTRx+ of all modules will be covered by a plastic light shield as visible in section 3.3.2. This reduces the effect of the VTRx+ light to a minimum.

When powering the modules with the prototype power supply for the Phase-2 Tracker, four modules are connected to one high voltage channel. Thus, the IV curves with that power supply are performed for four modules at once and the measured leakage current is the sum of the leakage currents of all four modules of that group. The plots of the three power groups are depicted in figure 6.19. Module 1 to 4, 5 to 8 and 9 to 12 are in the power groups 1 to 3, respectively. During the measurement performed with the prototype power supply (label "Other modules on"), all modules were powered with low voltage at 10.5 V and the high voltage of the modules not part of the measured group was set to 350 V. The sum of the leakage currents belonging to the modules of the respective group but measured with the laboratory power supply is also plotted in figure 6.19 with the label "LV all modules on". The individual curves per module can be found in figure G.1 with the same label. The absolute current values vary very much between the power groups, which is caused by the different influence of light on the modules from the different groups. The sum of these leakage currents from the reference measurements with the laboratory power supply is higher than the currents measured with the prototype power supply. Different temperatures during the measurements could be responsible for that. The important result of the IV curve measurements with the prototype power supply is the fact that the current measurement resolution of the prototype power supply is good enough to measure the sum of the currents of the four modules. Furthermore, it is important to check if powering the modules with that power supply changes the electrical performance of the modules, which is investigated in the following section 6.2.3.

6.2.3. Noise and Pedestal Measurement Results

The electronic noise of the modules is an important parameter that can be used to verify the module performance and their electrical grounding to the supporting structure. To be able to compare it throughout the whole integration test, the noise is measured individually for each module in an Outer Tracker Module Test Station (see section 3.3.6) before the integration,

[3] All wire bonds on the 2S modules get encapsulated with a silicone elastomer to protect the wire bonds during handling. [Mai19] During module production, the modules get not biased above 350 V before encapsulation. [Hei+23] For prototype modules without applied encapsulation this limit was also used during tests.

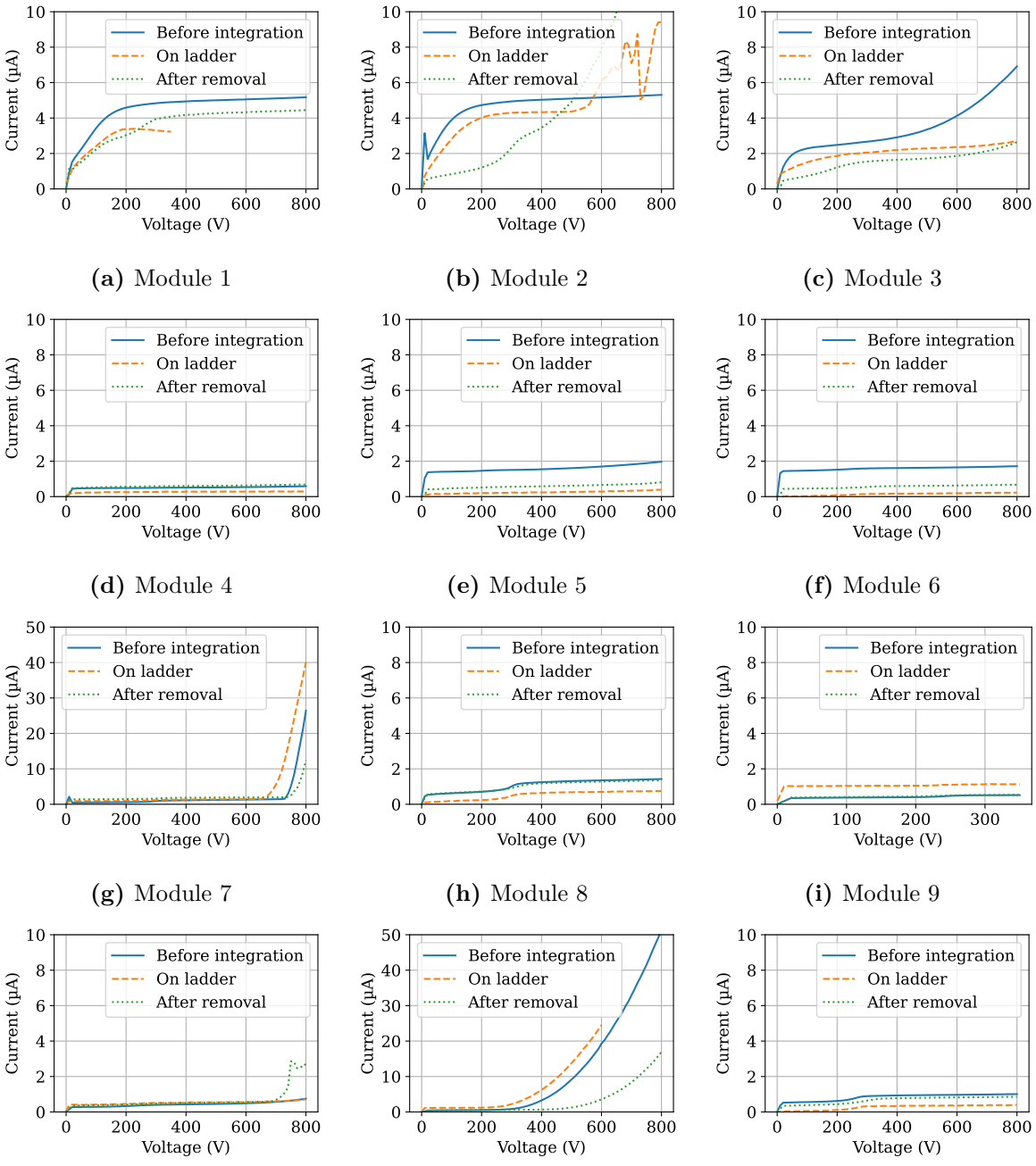

(a) Module 1 **(b)** Module 2 **(c)** Module 3

(d) Module 4 **(e)** Module 5 **(f)** Module 6

(g) Module 7 **(h)** Module 8 **(i)** Module 9

(j) Module 10 **(k)** Module 11 **(l)** Module 12

Figure 6.18.: IV curves of the modules on the fully integrated TB2S ladder. The IV curves are shown before the integration, on the ladder and after being removed from the ladder. The low voltage of all modules was switched off during the measurements.

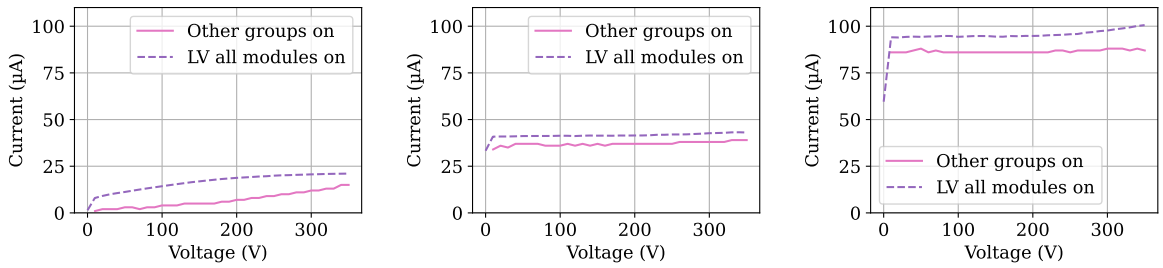

(a) Power group 1 **(b)** Power group 2 **(c)** Power group 3

Figure 6.19.: IV curves of the power groups on the fully integrated TB2S ladder. The IV curves are shown for the different power groups. Power group 1 consists of the modules 1 to 4 and so on. The low voltage of the four modules of the measured group were always on at 10.5 V while the LV power of the other modules varied according to the labels. During the simultaneous IV curve, all modules were powered with low voltage.

several times with different configurations on the ladder and then after dismounting the modules from the ladder again in the Outer Tracker Module Test Station. The mean value of all channel noise values of a module is called the module noise σ.

In figure 6.20 the module noise is shown for the twelve modules before the integration, on the ladder powered with the laboratory power supply and powered with the prototype power supply as well as individually after the removal. During the measurements, all modules were powered with a low voltage of 10.5 V and a high voltage of 350 V. There are two noisy channels in module 3 and four noisy channels in module 9, each having a noise value in the range of 15 V_{CTH} to 25 V_{CTH}. Module 11 also shows a strip with high noise, but this is not consistent over all four measurements. The noise values differ between the first three measurements and after the integration, the noisy channel is gone. Comparing the measurement before the integration and on the ladder shows that the channel noise of the different modules converges slightly when they are mounted on the same support structure with the same ground level. The noise measured when the modules were powered with the prototype power supply behaves as with the laboratory power supply. Thus, the different powering of the modules with the two power supplies does not influence their electrical performance. The higher impedance of the cable of the prototype power supply does not influence the noise measured on the modules. This is a very important result for the project since this was the first time powering fully functional modules with the Phase-2 power supplies. The measurement after removal demonstrates that there was no deterioration of any module during the integration procedure.

Module 1 shows large differences of the noise before the integration and after removal compared to on the ladder. This is due to a high voltage powering issue with this module. The bottom sensor HV tail was repaired with a soldering connection that got disconnected during integrating the module on the ladder and was repaired before the measurement after the integration. Thus, the bottom sensor was not biased during the noise measurements on the ladder resulting in very high bottom sensor noise of about 20 V_{CTH}. Due to this, figure 6.20 shows for module 1 just the top sensor noise, which is, compared to the other modules, rather low since the module noise is reduced when powering just one sensor as shown in [Kop22]. The rather high noise of the top sensor in the individual noise scan before and after integration is most likely caused by HV spark effects due to not optimal connection of the soldering connection to the bottom sensor. Due to this HV powering problem, the channels connected

to the bottom sensor of module 1 were masked during all the measurements presented in the following sections 6.2.4 to 6.2.6.

The pedestals of the twelve modules on the ladder are shown in figure 6.21 for the same runs of which the noise is depicted in figure 6.20. The pedestals before the integration and after the removal spread between the different modules since the chip temperature differed during the measurements. On the ladder, the modules were read out synchronously, resulting in same pedestal values due to trimming them to the same value across all channels of all modules. The pedestal differed by about $2\,V_{CTH}$ between the two measurements on the ladder (labels "On ladder" and "On ladder, prototype PS"). This difference can be used as an estimation how much the pedestal could have moved during the more detailed measurements on the ladder that are shown in the following sections 6.2.4 to 6.2.6. A zoomed out version of the plot can be found in the appendix in figure G.2.

6.2.4. Threshold Scan Results

A threshold scan is performed at different high rate trigger frequencies above 100 kHz. Thus, the sparsified readout mode with zero suppression and clustering from the CIC is used. At high trigger frequencies, the readout is limited by the CIC bandwidth limit given in equation (3.13). The triggers from the AMC13 are set to a specific trigger frequency with constant trigger separation and the threshold is changed in steps of $1\,V_{CTH}$ in a range that covers relative thresholds from about $1\,\sigma$ to $8\,\sigma$ with the module noise σ. At each threshold step five runs are recorded to have datasets of about 100 000 events to 500 000 events per step.

The mean number of clusters per event is extracted from the data and can be seen in figure 6.22 for trigger frequencies of 295 kHz and 597 kHz. The relative threshold on the x-axis is defined in equation (3.16). The expectation of the maximum mean number of clusters per event is indicated with vertical lines for a header size of 54 bits and 78 bits. The corresponding values can be found in table 6.4. The number of clusters per event for hybrid 0 and 1, which belong to module 1, does not reach the maximum given by the bandwidth limit since the bottom sensor channels were masked during the measurements (see section 6.2.3). The mean number of clusters per event saturates for all the other hybrids. This saturation occurs at a lower number of clusters per event than expected from the CIC bandwidth limit given in equation (3.13). The same effect was already observed in measurements within [Dro21]. There, a two-dimensional scan over the trigger frequency and number of clusters per event and front-end showed that the CIC cluster size perfectly matches the expectation of 14 bits/cluster but the header size resulting from the fit was 78 bits. As shown in figure 3.14b, the expected header size of the sparsified CIC data format is 54 bits, resulting in a 24 bits larger header size than expected. The CIC output formatter emits between two L1 data frames, an idle pattern of the bits 1010...10 of different length to the data stream. [Ber+24] The bandwidth limit measurement is sensitive to the average minimal length of this idle pattern when the CIC is operated at high data and trigger rates. Measurements with a kickoff module showed that the CIC output formatter also adds the pattern 0000 before and after each L1 word, which is referred to as the transition pattern. [Rav25] Even though the raw CIC data stream of the data shown in figure 6.22 was not stored to check for the exact idle and transition pattern, the measurements confirm the observations from [Dro21] that the average minimum length of the idle and transition pattern for 2S modules is 24 bits.[4]

When looking at even higher thresholds, the modules are operated more closely to the use-case in the tracker. Figure 6.23 shows the noise hit occupancy given by equation (3.17) with a logarithmically scaled y-axis. The occupancy values are independent of the trigger frequency

[4]The event header size of the sparsified CIC L1 data is not 52 bits as stated in [Ber+24], but 54 bits. Therefore, the absolute value stated in [Dro21] differs from the value in the text.

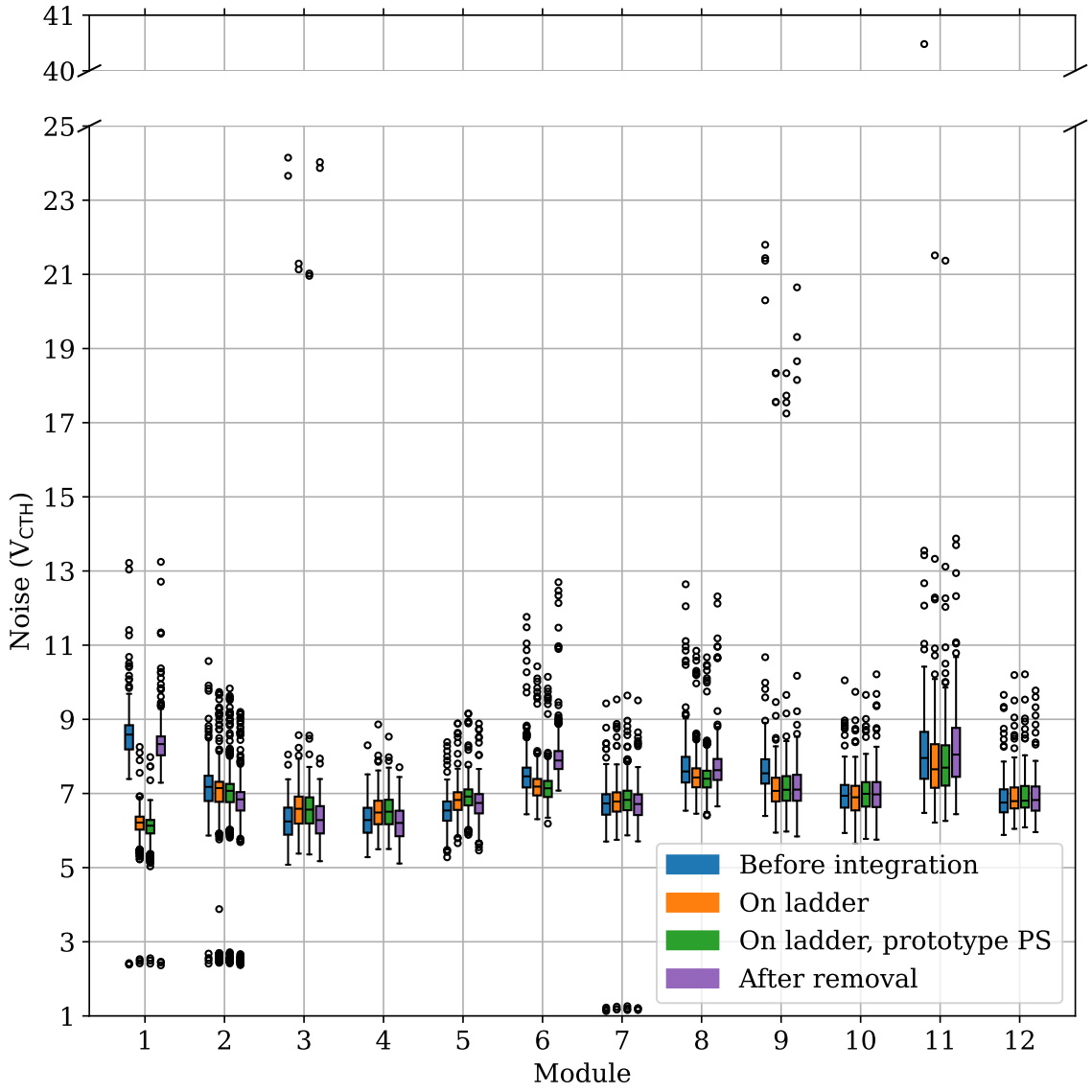

Figure 6.20.: Noise of the 2S modules during the TB2S ladder test. The strip noise of each of the twelve modules is shown with boxes extending from the first to the third quartile and whiskers extending to the farthest data points lying within 1.5 times the interquartile range. The median is represented by the stroke within the box. The data points outside the whiskers are outliers and also shown. The noise is plotted separately before the integration, on the ladder powered with both power supplies and after removal from the ladder. For module 1 just the top sensor noise is shown. The noise value is significantly reduced on the ladder because the bottom sensor was not biased during the measurements on the ladder. Further details can be found in the text.

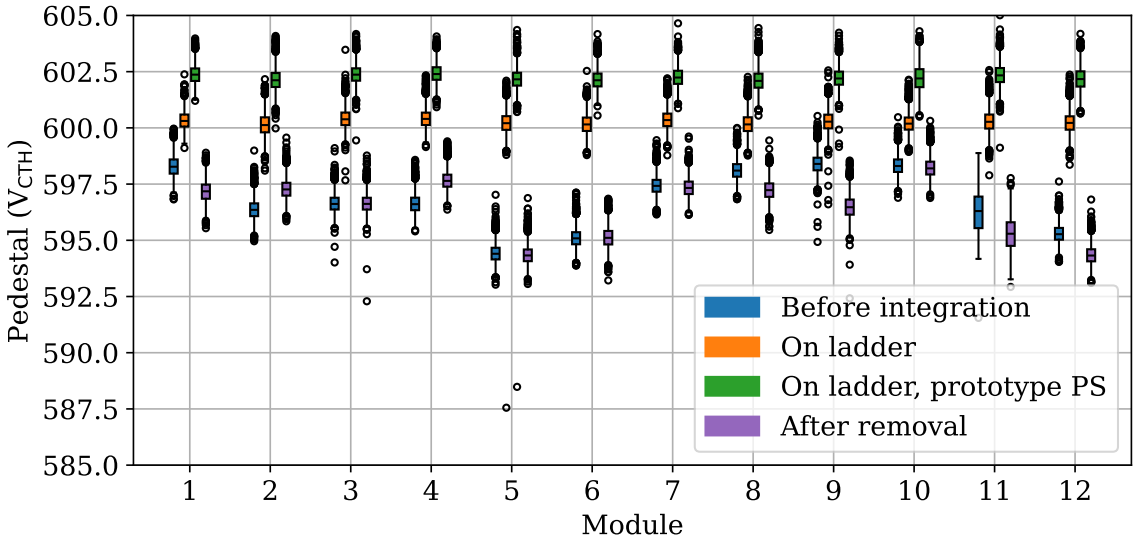

Figure 6.21.: Pedestal of the 2S modules during the TB2S ladder test. The pedestal differs from module to module for the runs during which the modules got read out individually and at different temperatures while it is the same value across all modules when they were trimmed accordingly. The pedestal differs about 2 V_{CTH} between the two measurements on the ladder with different power supplies.

Table 6.4.: CIC bandwidth limits. The table shows the average number of clusters n_{cl} that can be read out by the CIC for the measured trigger separations S and two different total event header sizes H, as explained in the text.

Frequency (kHz)	S (clock cycles)	H (bits)	average n_{cl}
295	135.4	54	73.5
		78	71.8
597	67.0	54	34.4
		78	32.7

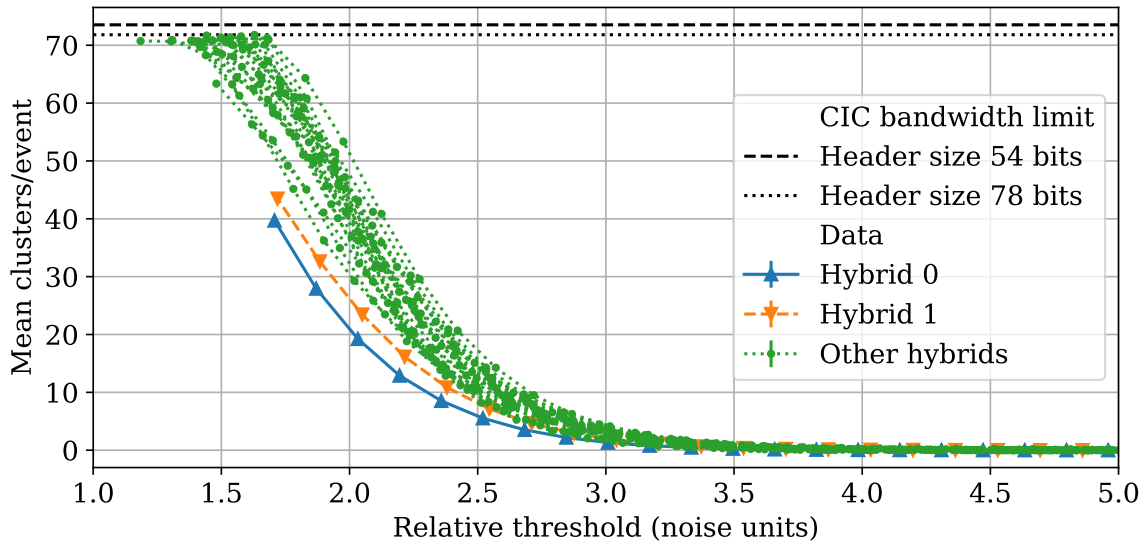

(a) 295 kHz

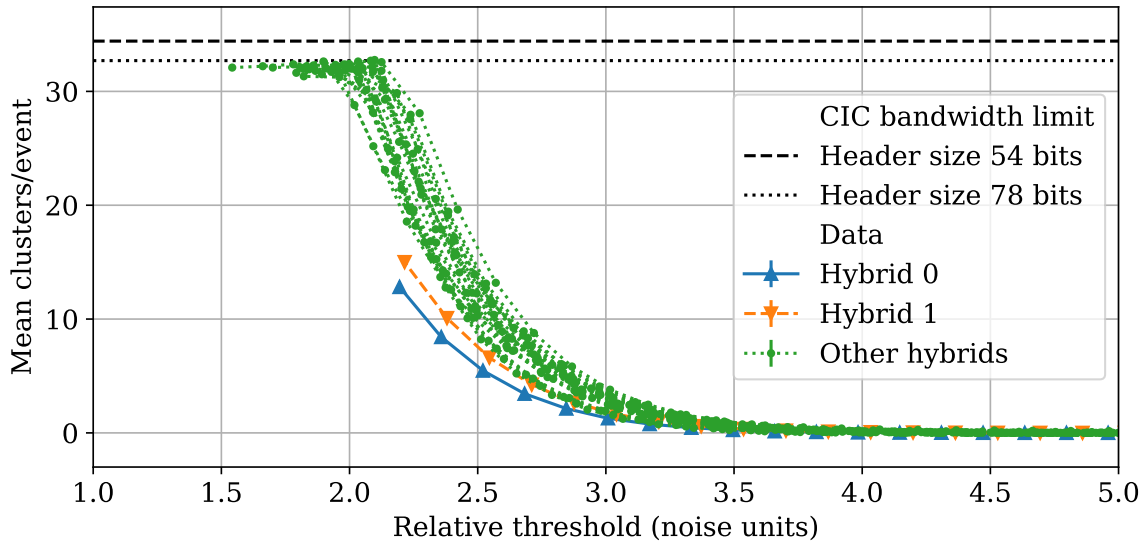

(b) 597 kHz

Figure 6.22.: Mean number of clusters per event of the high rate trigger threshold scan. The number of clusters per event over the relative threshold are shown at 295 kHz (a) and 597 kHz (b). The measured number of clusters per event fits the expectation from the bandwidth limit given in equation (3.13) with a total header size of 78 bits instead of the expected 54 bits. Hybrid 0 and 1 from module 1 do not reach the limit since the bottom sensor was not attached to high voltage. The channels of the bottom sensor got masked during data taking.

(295 kHz in figure 6.23a and 597 kHz in figure 6.23b). The noise hit occupancy of most of the hybrids is above the Gaussian expectation (see equation (3.15)), which indicates common mode noise. A more detailed analysis of the common mode noise is given in section 6.2.5. The hybrids 4, 16 and 17 belonging to module 3 and 9 show higher noise hit occupancies than the other hybrids. Individual noisy channels existing in these modules are the reason of this behavior. The noisy channels are the same that showed high noise values already in figure 6.20. Each of the affected hybrids has two noisy channels. The noise hit occupancy of hybrid 21, which belongs to module 11, shows the highest noise hit occupancy of the other hybrids. The relative threshold of $5\,\sigma$ that will be applied to the modules during the operation in the tracker is also plotted with the label "Relative threshold tracker". With this threshold applied, the noise hit occupancy should be below 10^{-5} (label "Noise hit occupancy tracker"). The hit occupancy produced by charged particles is expected to be at about 10^{-3} resulting in a sufficient signal-to-noise ratio of 100. [CMS17f] The area above a threshold of $5\,\sigma$ with good noise hit occupancies is indicated with a green area in figure 6.23. At a threshold of $5\,\sigma$, the hybrids with the noisy channels have a noise hit occupancy above the maximum of 10^{-5}, but the hybrids without noisy channels stay below the maximum noise hit occupancy. The noisy channels would get masked in the tracker. This masking was also performed during the analysis of the measurements shown in figure 6.23. With the masking of the six high noise channels, the noise hit occupancy of the hybrids 4, 16 and 17 reduces to the same values as the group of the other hybrids slightly above the Gaussian expectation. The corresponding analysis results are plotted in the appendix in figure G.3. If a module shows too many noisy channels during production it will get rejected. It is not yet decided within the Tracker community how many percent of dead or noisy strips per module will be allowed. The L1 tracking efficiency will reduce about 0.5 % (3 %) when 1 % (5 %) of all modules are randomly lost. [Ski24] However, detector inefficiencies due to strip loss, strip noise, or electronic noise would have a less drastic impact on the overall tracker than losing entire modules. Therefore, the exact amount of allowable random strip loss is difficult to quantify, but using the total amount of allowable module loss serves as reasonable starting point for this study. Thus, that assumption implies 40 masked strips per 2S module would then result in an L1 tracking efficiency loss of about 0.5 %. The experiences with the built prototype modules show that the number of dead strips per modules is expected to be much lower. The noise hit occupancy of hybrid 2, 8, 12 and 22 is below the Gaussian expectation. It could not be resolved why they behave unexpectedly. A pedestal shift of $+2\,\mathrm{V_{CTH}}$ would bring their results again above the expectation. This shift could be explained by a changing temperature compared to the noise runs presented in section 6.2.3. Since the pedestal difference between two different noise runs is in the order of $2\,\mathrm{V_{CTH}}$ as depicted in figure 6.21, such a pedestal shift could have happened. On the other hand, this explanation is not very likely because it is not obvious why the temperature and pedestal should have changed only at these four hybrids.

6.2.5. Common Mode Noise and Crosstalk

During measuring the noise of 2S modules as explained in section 3.3.4, a Gaussian fit is used to extrapolate the noise. Besides Gaussian contributions, also *common mode noise* can be present in 2S modules. It is quantified by noise hits in many strips in the same event. Within this section, the common mode noise of the twelve 2S modules on the TB2S ladder is investigated, and the observations are discussed in the context of the module operation in the Phase-2 Outer Tracker.

The common mode noise and crosstalk of the 2S modules in the TB2S integration test was already investigated within a bachelor thesis [Hub24]. This section summarizes the observations and shows if and how the results influence the Phase-2 Tracker operation.

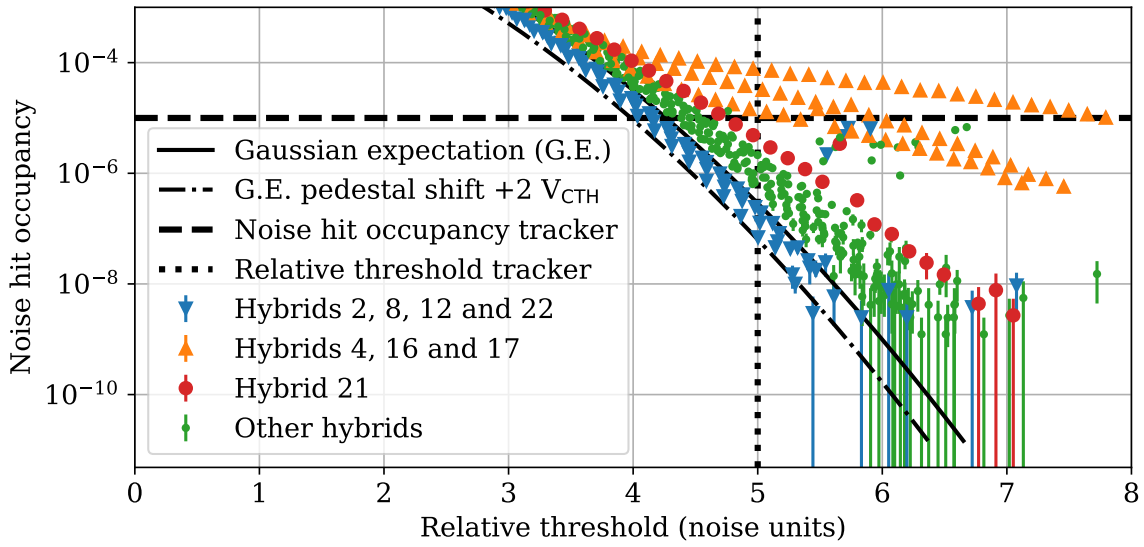

(a) 295 kHz

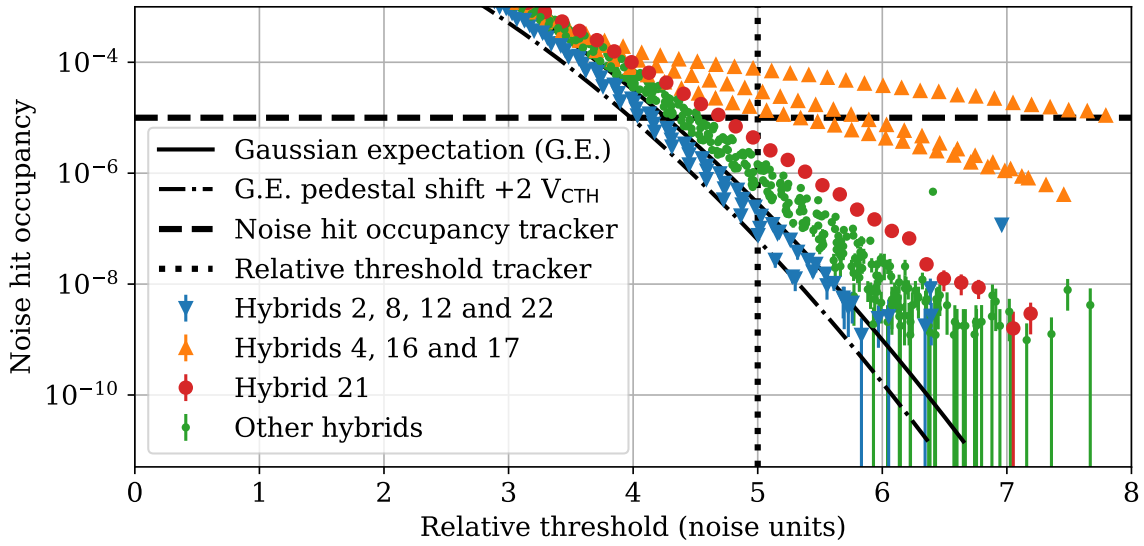

(b) 597 kHz

Figure 6.23.: Noise hit occupancy of the high rate trigger threshold scan. The noise hit occupancy is plotted over the relative threshold at 295 kHz (a) and 597 kHz (b). The Gaussian expectation for the measured pedestal values and a pedestal shifted by $2\,V_{CTH}$ as well as the aimed noise hit occupancy and relative threshold of the Phase-2 Outer Tracker are indicated in the plot. The hybrids 4, 16 and 17 show higher noise hit occupancy than the other hybrids due to two noisy channels each. With those the noise hit occupancy of that hybrids is above the upper limit of 10^{-5} at a relative threshold of $5\,\sigma$. The noise hit occupancies of the hybrids 2, 8, 12 and 22 are below the Gaussian expectation. Further details can be found in the text.

Within [Hub24], a first detailed look to the data of the high statistics measurements was performed. Event maps which show the strips that fired in an event as a function of the event number were used to get a first overview of which effects can be observed in the data. Also, the number of hits per event was analyzed. The observations will be explained in more detail in the paragraph after next. Also, correlation and anti-correlation matrices were calculated to investigate the correlation of noise hits within a module. It was observed that the hits in the top and bottom sensor of a module are correlated while the hits in both hybrids of the module are strongly anti-correlated. The same effect was also observed in common mode noise studies performed in [Ter24]. Additionally, the correlation between neighboring modules on the ladder was analyzed to study possible crosstalk between modules at close distances. The analysis showed that the modules did not influence each other on the ladder. The results of [Hub24] were used to continue with common mode noise analyses that are presented in this subsection.

For the common mode noise analysis presented in this subsection, data from the high rate trigger threshold scan presented in the previous section 6.2.4 are used. First, results at a low relative threshold are shown to further explain some observations in the histogram of the number of hits per event of [Hub24] and then, the data at a relative threshold of $5\,\sigma$ is analyzed regarding the common mode noise.

When looking at the data taken at high trigger frequencies at a low relative threshold, the noise features overlap with the effects of the CIC bandwidth and hard cluster limits introduced in section 3.3.3 and measured in section 6.2.4. In figure 6.24, the number of hits/event (figure 6.24a) and clusters/event (figure 6.24b) is histogrammed. The histograms are weighted such that the area under the curve is one. The data at a threshold of $589\,\mathrm{V_{CTH}}$ and a trigger rate of 597 kHz are shown, which corresponds to the data points at the very left side of figure 6.22b at low relative thresholds. The absolute relative threshold value differs from hybrid to hybrid since the noise of all hybrids is different. For the hybrids of module 1, it is at about $2.2\,\sigma$ and between $1.5\,\sigma$ and $2.0\,\sigma$ for the other hybrids. The modules 6, 8 and 11 show the highest noise in figure 6.20. Thus, the relative threshold of these modules is the lowest in the presented runs with an absolute threshold of $589\,\mathrm{V_{CTH}}$. The tail in figure 6.24a to the right to higher number of hits per event is larger for these modules. This is an indication for the presence of more common mode noise when having more Gaussian noise. For the hybrids of module 1 fewer hits per event are present because the channels of the bottom sensor got masked due to the HV powering problem of this sensor (see section 6.2.3). The number of hits per event varies from 0 to about 400 and peaks at 0 and about 130. The peak at about 130 hits per event is referred to as the *second peak* in [Hub24]. At the time of writing [Hub24] it was not clear why this second peak occurred in the data but the distribution of the number of clusters per event shown in figure 6.24b explains it. There, the bin at 0 clusters per event and 127 clusters per event show a peak. The peak at 127 clusters per event represents the hard cluster limit of the CIC (see section 3.3.3) meaning this bin acts as an overflow bin of all the events that contribute to the distribution of hits per events above the dashed line at 126 hits per event shown in figure 6.24a. The peak at zero clusters per event results from the fact that the CIC bandwidth limit is present as well, which results in a maximum mean number of clusters per event of 32.7 as visible in figure 6.22b and table 6.4. A comparison of this mean number of clusters per event for the threshold scan analysis explained in section 6.2.4 and the common mode noise analysis shown here can be found in the appendix in figure G.4a. As expected both analyses deliver the same results of the mean number of clusters per event. The height of the hit and cluster histograms for less than 127 hits and clusters is about the same, meaning that these clusters most likely have a width of one strip. The expectation of the histogram of the number of hits per event is very different to the observations. Assuming purely Gaussian noise one would, depending on the relative threshold of the respective hybrid, expect a Gaussian peak around a most probable number of hits per event. This distribution was simulated for the

data taking conditions and can be found in the appendix in figure G.5a. As this distribution does not match the measured one shown in figure 6.24a, there need to be common mode noise present in the 2S modules during the measurements. Nevertheless, the occupancies expected in the Phase-2 Outer Tracker are much lower than in the data shown in figure 6.24 and the common mode noise was analyzed for the threshold setting during later tracker operation as well which is shown in the next paragraph.

To check if the common mode noise will influence the module operation in the Phase-2 Tracker, it is also analyzed for the runs with a relative threshold of $5\,\sigma$. The number of hits per event for the corresponding runs are depicted in figure 6.25. During the analysis, the channels of hybrid 4, 16 and 17 that caused the increased noise hit occupancy of these hybrids in figure 6.23 were masked. Thus, these hybrids do not show increased noise compared to the others. All histograms are weighted to an integral of one. Nearly all events have zero hits. The percentage of events with one (two) hits is below 1 % (0.1 %). Only a few hybrids have even fewer events with three or four hits. The hybrids 2, 8, 12 and 22 that showed a noise hit occupancy lower than expected from Gaussian noise have just one hit in less than 0.1 % of the events. Only hybrid 21, which is part of module 11, shows a very small number of events with five to nine hits. There are two single events with eight and nine hits respectively and fewer than ten events with five and six hits each. Even though this is a slightly increased number of common mode events, this would not reduce the tracking performance. Mainly the strips at the sensor edges with noise values of about $9\,\mathrm{V_{CTH}}$ to $10\,\mathrm{V_{CTH}}$ show more frequent hits than the other strips of this hybrid. Since these strips have increased noise in nearly all 2S modules, it could also be decided to mask them in the entire Phase-2 Outer Tracker. The simulated expectation from purely Gaussian noise is depicted in the appendix in figure G.5b. The direct comparison of the simulation results and data for all hybrids is shown in the appendix in figure G.6. The expectation is that nearly all events have no noise hits at the relative threshold of $5\,\sigma$ and the fraction of events with one hit is in the order of 10^{-3} to 10^{-1} depending on the hybrid. In six hybrids also some events with two hits are expected, and one hybrid is expected to have three hits in less than 10^{-4} of all events. As already visible in figure 6.23, slightly more hits than expected from the Gaussian noise simulation are present in the data. In the hybrids 2, 8, 12 and 22 less hits are present than expected. Concluding, all effects seen in section 6.2.4 and section 6.2.5 are already visible in the normal noise plot depicted in figure 6.20.

In [Hub24], the correlation between neighboring modules and, especially, the overlapping parts of neighboring modules, was analyzed. The results show that there is no correlation between the module hits at the close distances on a TB2S ladder. Combined with the previously presented measurements, this shows that the modules can be operated in normal data taking conditions at a threshold of $5\,\sigma$ and with high rate triggers on the TB2S ladders as in single module test setups without influencing each other.

6.2.6. Trigger Frequency Scan Results

The other high statistics measurements performed are trigger frequency scans with different settings of other parameters like threshold, trigger latency and trigger mode. Trigger frequency scans can be used to check for trigger frequency and trigger mode related features in the hits. An observed feature can be probed in the use-case conditions of the tracker to check its relevance for the later data taking.

Figure 6.26 shows the noise hit occupancy for the CTS mode at two different thresholds of $585\,\mathrm{V_{CTH}}$ and $579\,\mathrm{V_{CTH}}$. The expected trigger separation between two consecutive triggers without considering rejections due to the CMS trigger rules are indicated on the x-axis. The real mean trigger frequencies belonging to the trigger separation values on the x-axis can be extracted from figure 6.17. The mean module noise hit occupancy is about 0.7 % at a threshold

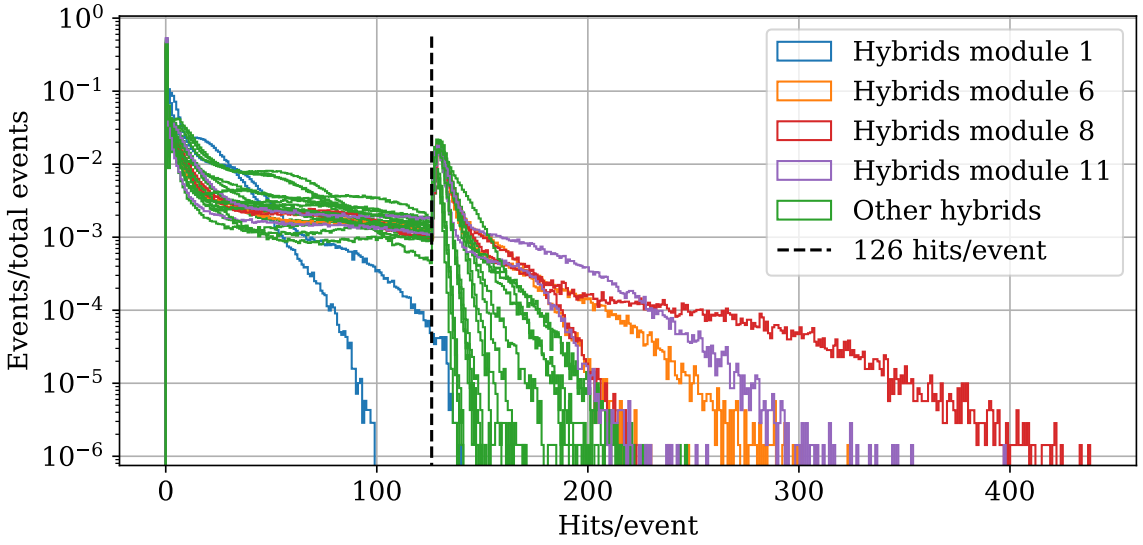

(a)

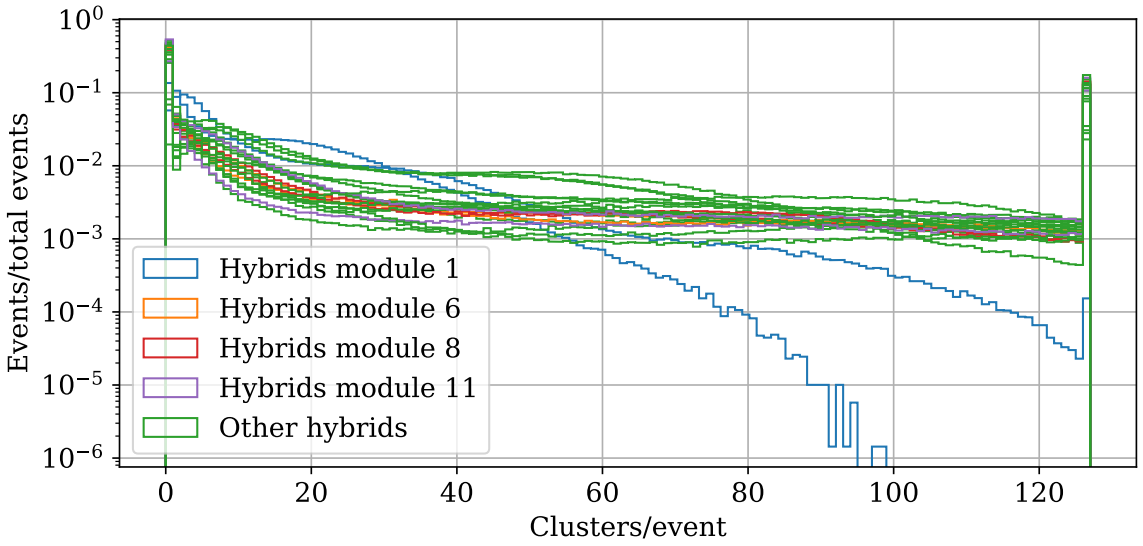

(b)

Figure 6.24.: Histograms of the number of hits and clusters per event. The data are recorded at a threshold of 589 V_{CTH} and a trigger frequency of 597 kHz. (a) The number of hits per event is shown as histograms for all 24 hybrids individually. The hybrids of modules that show special features are depicted with separate colors. The vertical line at 126 hits/event represents the number of hits per event that definitively do not come from a hard CIC cluster overflow. (b) The number of clusters per event is shown for the same data as in (a). At the hard cluster limit of 127 hits per events, the distribution shows a peak that is the sum of the events that are above the 126 hits/event line in (a).

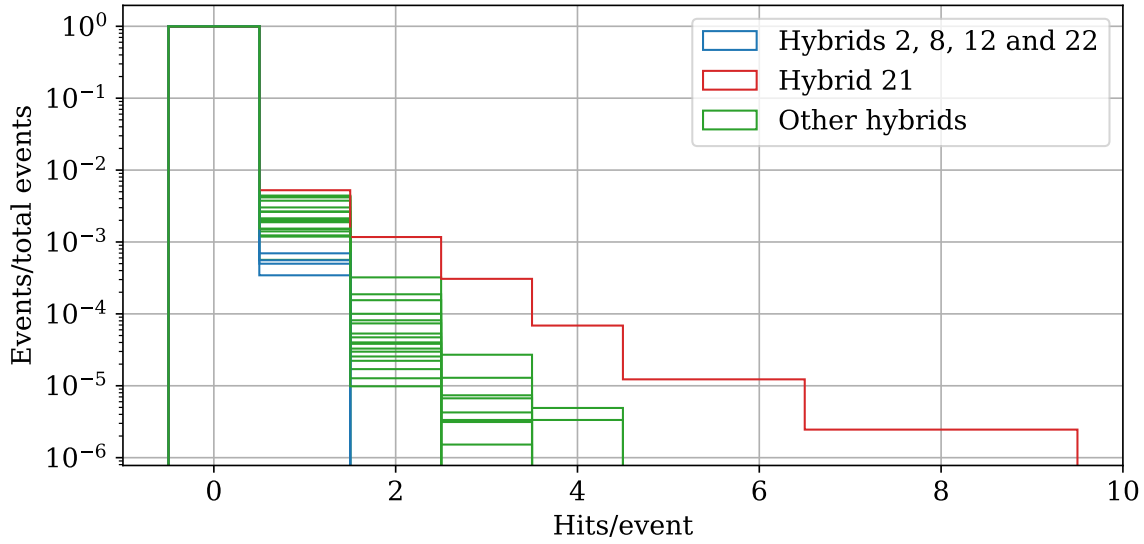

Figure 6.25.: Histogram of the number of hits per event at a threshold of $5\,\sigma$. The hybrids 2, 8, 12 and 22 show the smallest number of hits per event while hybrid 21 shows the largest noise of the 24 hybrids on the TB2S ladder.

of 585 V_{CTH} (see figure 6.26a) and 0.07 % at 579 V_{CTH} (see figure 6.26b). The modules with higher noise on the ladder in figure 6.20 show a higher noise hit occupancy at a globally set threshold as expected. In the plot, a peak at $S_{CTS} = 77$ bunch crossings can be seen followed by a dip at $S_{CTS} = 78$ bunch crossings. This behavior was already observed in [Mai19]. It can be explained by a baseline-oscillation of the pre-amplifier of the CBC when it receives a trigger and starts the readout process. The baseline drop results in higher module noise hit occupancies when the constant trigger separation is two bunch crossings higher than the readout latency (in this case 75 bunch crossings). The baseline increase results in lower noise hit occupancies when the constant trigger separation is three bunch crossings higher than the readout latency.

To confirm the relation between the occupancy oscillation and the module readout latency, the latency is set to different values for each module. The results are depicted in figure 6.27. It can be confirmed that the dip always occurs when the constant triggers come with a trigger separation two bunch crossings higher than the module readout latency. As the next paragraph shows, this will not be a problem during the data taking with randomly distributed triggers.

Figure 6.28 pictures the results of the frequency scan with random triggers at different mean trigger separations. Compared to the data plotted in figure 6.26 the only difference is the trigger mode. It can be seen that the occupancy oscillation vanishes for random triggers since there is no frequency setting anymore at which the triggering of an event and the readout of the previous event always happens at the same time distance. The mean noise hit occupancy is slightly reduced compared to the data shown in figure 6.26, resulting in about 0.6 % at a threshold of 585 V_{CTH} and 0.06 % at a threshold of 579 V_{CTH}. In the data taken at 585 V_{CTH}, an increase of the occupancy towards higher mean trigger separations is visible. Both effects can most likely be explained by a drift of the ambient temperature inside the measurement box. A lower temperature leads to a lower pedestal value and also a lower noise. Since the change of the noise is less than the change of the pedestal (see figures 6.13 and 6.14), the change of the noise with the temperature is not taken into account in the following explanation. The lower pedestal at lower temperature leads to a lower relative threshold when the absolute threshold stays the same. This results in a higher occupancy at lower temperature. The temperatures

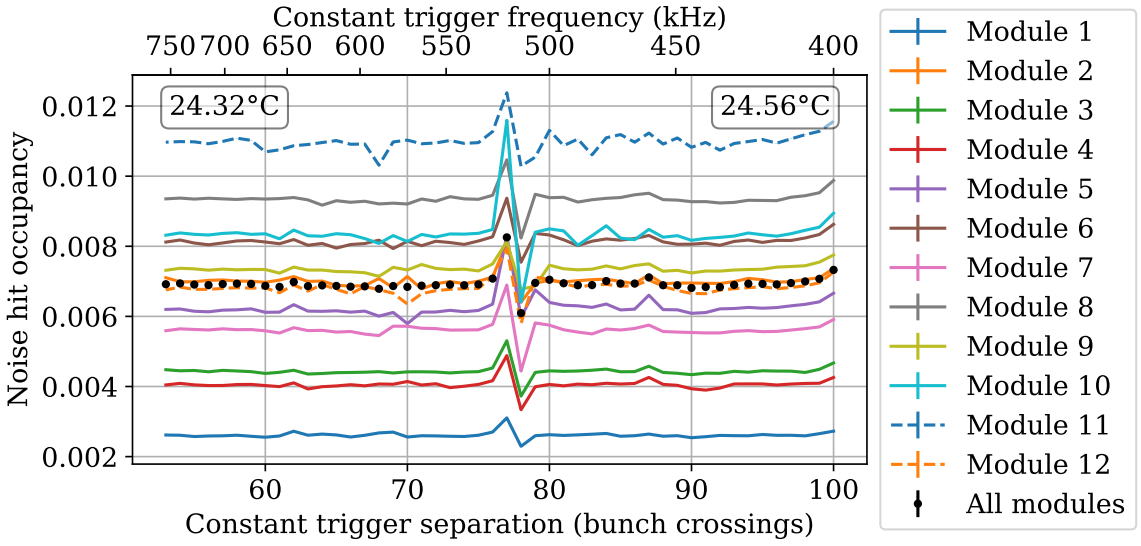

(a) 585 V_{CTH}

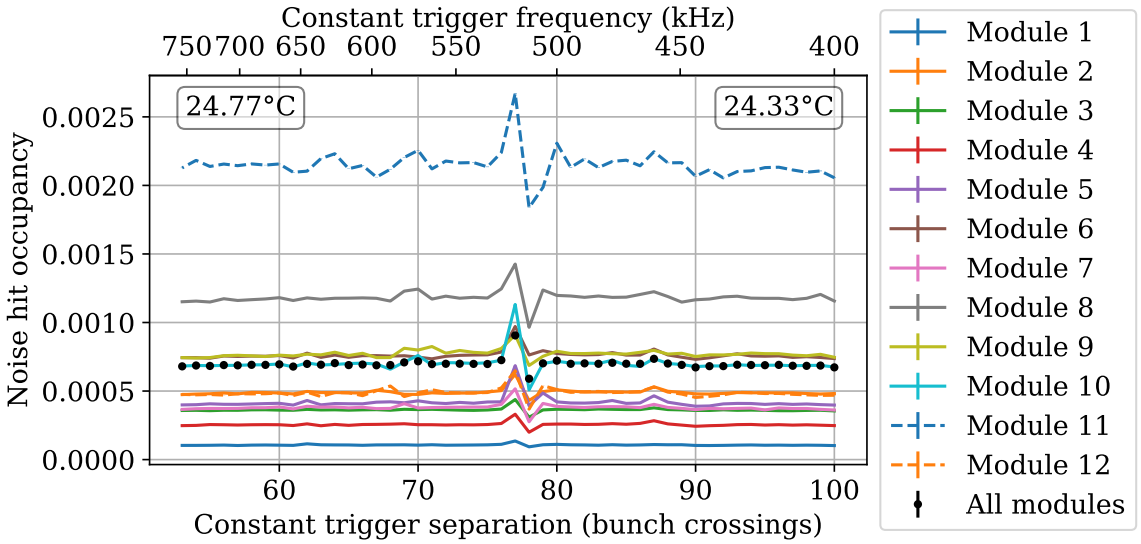

(b) 579 V_{CTH}

Figure 6.26.: Frequency scan with constant trigger separation at two thresholds. The noise hit occupancy of all twelve modules is shown for a frequency scan with constant trigger separation at a threshold of 585 V_{CTH} (a) and 579 V_{CTH} (b). The black dots represent the average of all modules. The occupancy is overall constant at different frequencies except for a trigger separation of 77 bunch crossings and 78 bunch crossings where an oscillation of the occupancy is observed. The readout latency was set to 75 clock cycles during the measurements. The temperatures measured in the box during the first and last run of the scan are given in the plot.

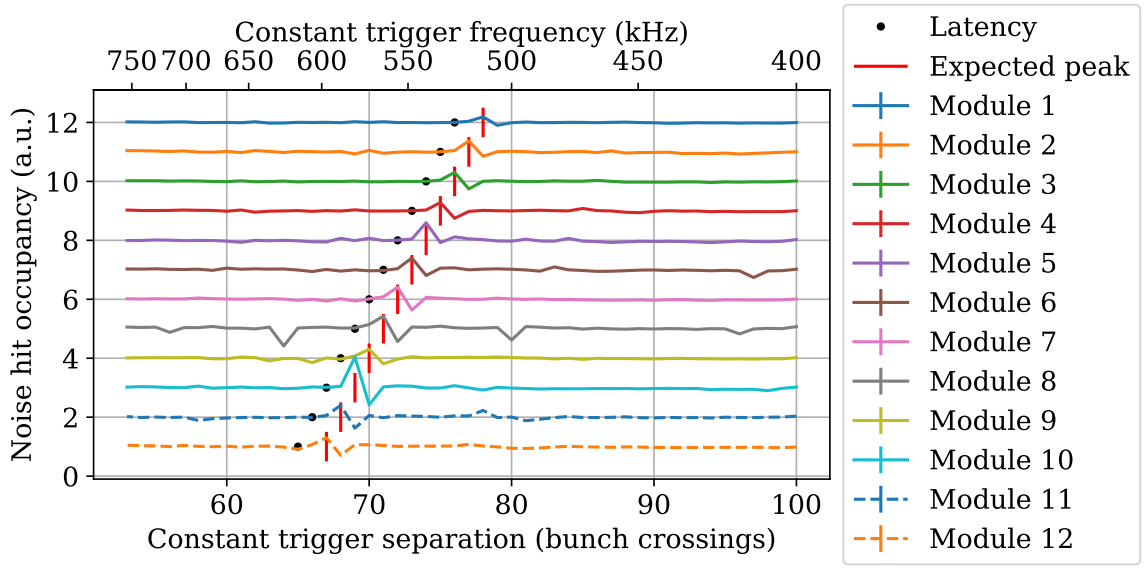

Figure 6.27.: Frequency scan with constant trigger separation and different latencies for all modules. The noise hit occupancy is shown in arbitrary units for all twelve modules read out with different trigger latencies. For better visualization the noise hit occupancy of the individual modules is shifted in y-direction by a constant offset per module. The latency and the expected occupancy peak are plotted as well. The expectation matches the data for all twelve modules.

during the last and first run of the scan are written in the plots of figures 6.26 and 6.28. The scan at a higher threshold of 579 V_{CTH} with a lower noise hit occupancy shown in figure 6.28b shows no temperature dependent drift in the noise hit occupancy. Being more at the tail of the S-curve the pedestal shift with the temperature has not that much of an effect on the occupancy. The results shown in figure 6.28b at a mean trigger separation of 53 bunch crossings are somehow near to the use-case in the later tracker operation. In the later tracker, the hit occupancy is expected to be about 10^{-3}. [CMS17f] Since during this integration test, no particles were detected with the 2S modules, the hits recorded by the modules purely result from noise. The mean noise hit occupancy of about 0.06 % in the data shown in figure 6.28b matches this expectation. The difference to the operation in the Phase-2 Tracker is the origin of the hits and the trigger frequency that will be about 750 kHz but was 597 kHz during the presented measurements.

6.2.7. Summary

This first full TB2S ladder integration test showed that the mechanical integration of the 2S modules on the ladder works as expected. IV curve and noise measurements at 100 kHz were used to demonstrate the electrical performance of the modules on the ladder compared to before the integration and after removal. Both measurements showed that the modules perform on the ladder as expected. Also, a prototype power supply for the Phase-2 Tracker operation was used to power the modules on the ladder. Neither this nor the 60 m long power cable influenced the module operation.

Additionally, high rate trigger measurements were performed to operate the modules on the ladder in near-to-use case conditions. A threshold scan from relative thresholds of about 1 σ to 8 σ was performed at two different high rate trigger frequencies 295 kHz and 597 kHz. With

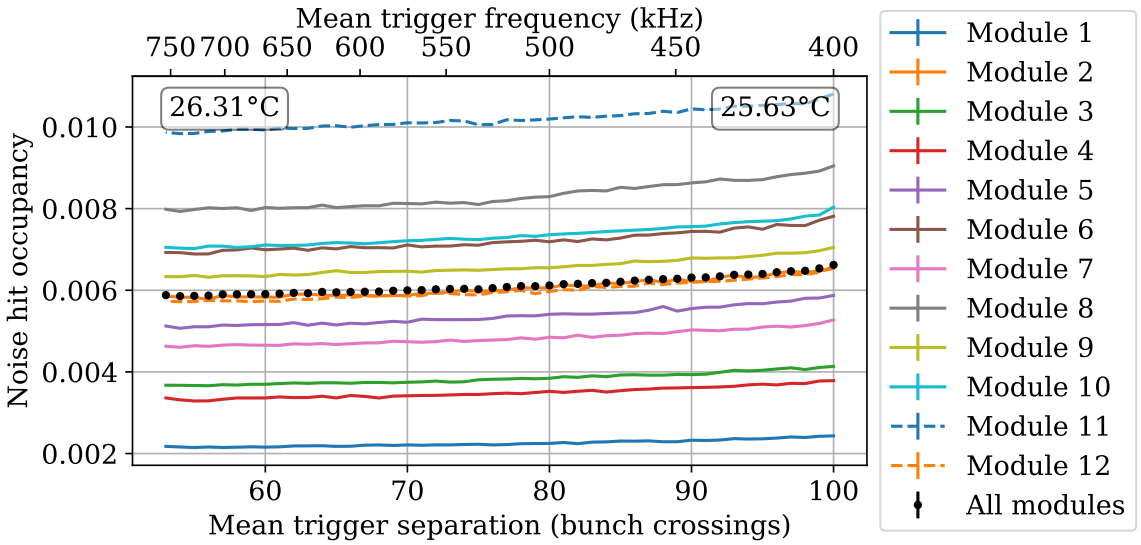

(a) 585 V_{CTH}

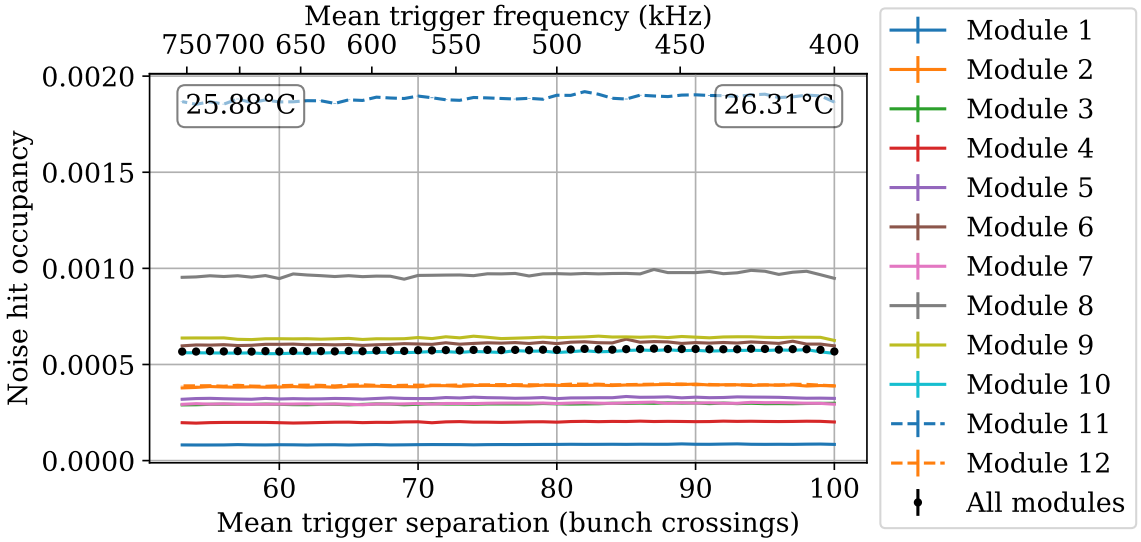

(b) 579 V_{CTH}

Figure 6.28.: Frequency scans with random triggers at two thresholds. The noise hit occupancy of all twelve modules is shown for a frequency scan with random triggers at a threshold of 585 V_{CTH} (a) and 579 V_{CTH} (b). The occupancy shows in (a) an increase towards higher trigger separations while it is constant over time in (b). The temperatures at the start and end of the scan are depicted in the plot.

this scan, the CIC cluster limits were measured with the low relative threshold runs and the behavior of the module noise at the foreseen relative threshold of $5\,\sigma$ was analyzed. The CIC bandwidth limit behaves as expected from previous measurements by [Dro21] and the noise hit occupancy of the modules is below the required 10^{-5} at a relative threshold of $5\,\sigma$. A common mode noise analysis of the noise data at use-case conditions shows that the module operation in the Phase-2 Outer Tracker will not be influenced by common mode noise events.

Several trigger frequency scans with constant and mean trigger separation settings were performed at two different thresholds, $585\,\mathrm{V_{CTH}}$ and $579\,\mathrm{V_{CTH}}$. The scans with constant trigger separation show a baseline-oscillation of the pre-amplifier of the CBCs resulting in a noise hit oscillation when the trigger separation is two bunch crossings higher than the latency. This effect cannot be observed with Poisson distributed random triggers and does thus not influence the data taking in use-case conditions. The trigger frequency scan with random triggers at a relative threshold that results in a mean noise hit occupancy of about 0.06 % shows that the 2S modules can be operated with a noise hit occupancy near the expected hit occupancy of 0.1 % in the tracker. Even though the hits were not generated by crossing particles, the operation conditions were similar to what is expected in the Phase-2 Tracker.

6.3. TEDD Dee Integration Test

In addition to the integration tests on the TB2S ladder, a first test on a TEDD dee was performed within this thesis in June 2023. The test was performed at DESY in Hamburg where dees will be integrated and double-disks will be assembled. During the test, experts from Lyon (dee integration), Louvain (dee integration and double-disk assembly), Bari (PS module assembly), Aachen (2S module assembly), DESY (PS module assembly, dee integration and double-disk assembly) and KIT (2S module assembly) were involved so that experts from all specific parts of the production chain could gain experience in the integration and module readout. The software preparation, measurement planning and data analysis were in my responsibility and are part of this thesis.

The goal of this integration test was to perform first measurements of the electrical performance of 2S modules on a TEDD dee. It was the first time ever 2S modules were mounted on a full prototype dee. With noise and IV curve measurements, the performance of the mounted modules was tested. Thermal qualification and testing was not in the scope of this integration test since cooled operation of the system was not possible with the setup at that time.

6.3.1. Experimental Setups

The measurement setup is explained below separately for the reception, integration and measurements on the dee.

Reception

As for other integration tests, a reception test was performed individually for all modules. For that the modules were placed inside the burn-in setup at DESY [Ven25] and the noise and IV curves were measured. The modules were powered with high and low voltage from a CAEN laboratory power supply and were read out with an FC7 inserted in a µTCA crate. The noise measurements and IV curves were taken individually for all modules while the others were not powered. After dismounting the modules from the dee they were measured again in the burn-in setup.

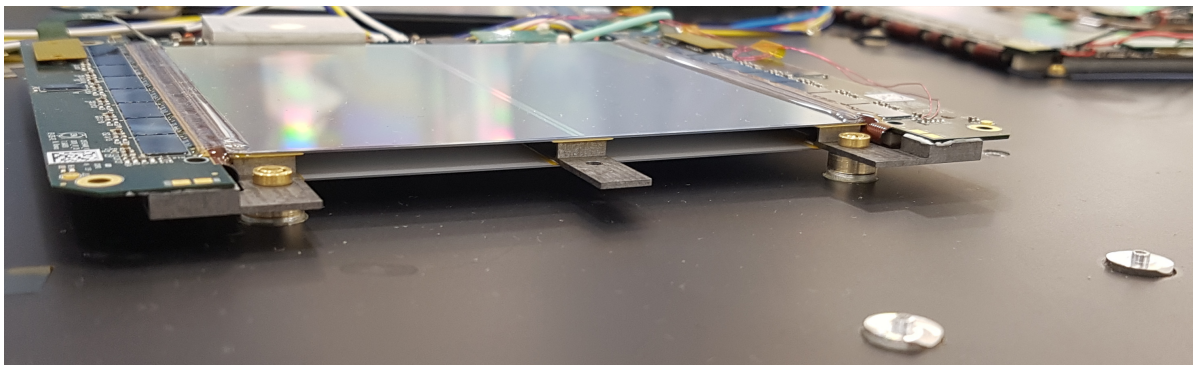

Figure 6.29.: Spacers for the 2S modules on the TEDD dee. The inserts of the dee can be seen in the bottom right corner of the picture while a 4.0 mm module is mounted on the dee inserts with additional spacers in between the inserts and the module.

Integration

The dee is mounted in an aluminum arc frame that is supporting the dee on the outer and inner side. The frame is mounted on a so-called "integration trolley" that is used to move and rotate the dee during the module integration. During this test the dee was not rotatable because the cooling pipe of the inner cooling segment of the dee was already connected to an evaporative CO_2 cooling system called MARTA (Monoblock Approach for a Refrigeration Technical Application) [CEB23]. Applying the final procedure, the module integration will start at smaller radii with the PS modules and proceed to larger radii. During this test, the 2S modules were ready to be integrated earlier than the PS modules and thus the 2S modules were mounted first. The modules were mounted in the center region of the dee because the transition area from the PS modules at lower radii and the 2S modules in the outer part is the most critical regarding the distances of the modules. The 2S modules are placed on inserts on the dee and then fixed with screws. Since HV tail adaptors as described in section 4.1.1 were plugged to the modules, the dee inserts were not high enough for the modules. They got extended with 3 mm high custom-made spacers as depicted in figure 6.29.

When the modules are mounted on the dee, the cables are routed in between the modules. This can be seen in figure 6.30.

Measurements

During the measurements the modules were covered with a light cover. The modules were powered with a CAEN laboratory power supply and read out with FC7 inserted in a µTCA crate. Since the PS and 2S modules needed different firmware versions the modules were read out with two FC7 for the PS modules and one FC7 for the 2S modules. On the dee, IV curves were taken, and the electronic noise was measured. The noise was measured with internal triggers from the FC7 at 100 kHz and unsparsified readout mode. At each threshold step 1000 events were recorded.

During the measurements presented in the following section 6.3.2 the evaporative CO_2 cooling system MARTA was not running, and the measurements were performed at a room temperature of about 21 °C. Measurements were also performed with the cooling system running and set to 12 °C but since the cooling connection of the 2S modules was not optimal due to the additional spacers these data are not presented in this thesis.

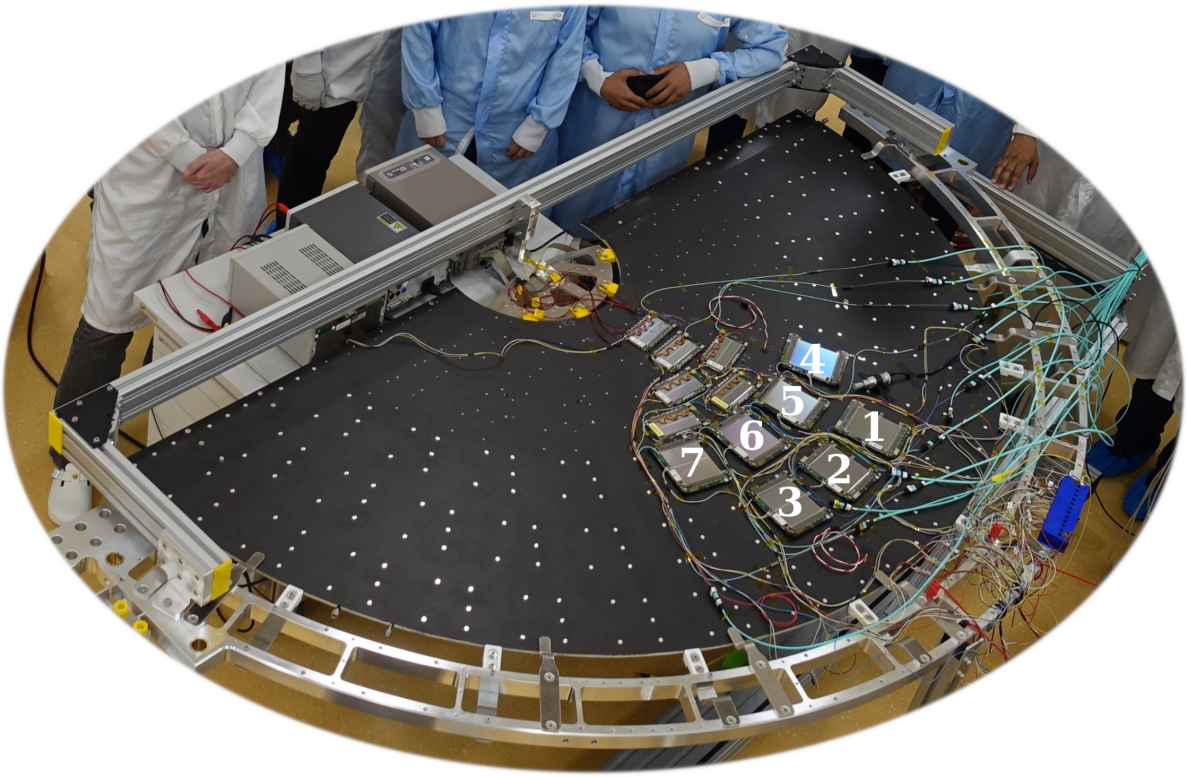

Figure 6.30.: PS and 2S modules mounted on the TEDD dee. The 2S modules are labeled according to table A.1. The not labeled modules at lower radii are the PS modules. The cable routing in between the modules is close to final, but the cables are custom-made for this test.

6.3.2. Results

The IV curves of the 2S modules during the reception test, on the dee and after the removal of the dee are depicted in figure 6.31. During all measurements, the other modules in the burn-in setup or on the dee were not powered by high or low voltage. The low voltage of the measured module was set to 10.5 V. Module 4 and 7 show different breakdown voltages at different setups, which is caused by different humidity conditions during the measurements. In [Wit23] it was shown that early sensor breakdowns of unirradiated sensors are correlated with the humidity conditions during the measurements. All modules show lower absolute leakage current values on the dee compared to the measurements in the burn-in setup. This results from different light conditions from the VTRx+ light during the measurements that influences the absolute leakage current values as explained in section 3.3.2. The surface reflections of the VTRx+ light differ in the different setups. The metallic surface of the burn-in setup is more reflective than the black surface of the dee and the cover on the dee. The absolute leakage current values also differ between the measurement before the integration to the one after removal, although they were both performed in the burn-in setup. Since the modules were not mounted in the same slot of the burn-in setup during both measurements, different reflections cause again the difference in the leakage current. Taking the described and understood effects into account, the IV curve results on the dee look as expected.

The noise of the 2S modules during the reception test, on the dee and after the removal of the dee is shown in figure 6.32. It can be seen that the noise of the modules on the dee did not change significantly compared to the reception measurements before the integration. The shown results were obtained by measuring the noise consecutively on all modules. A parallel noise measurement on all 2S modules led to the same result. The noise of module 1 was very high during the reception test. This was due to a not properly installed ground connection of the module to the carrier during this measurement. On the dee and after the removal the grounding of the module was correct, and thus the noise was reduced to a normal level. The number of not connected or noisy strips does not increase with the integration. Being the first time that 2S modules were mounted on a TEDD dee the measurements show that the modules work properly and the dee does not induce additional noise to the modules.

The results of some PS module measurements from the same integration test can be found in [Ven25].

Summarizing, the 2S modules showed good performance also on the TEDD dee prototype. Even though the presented measurements were not as detailed as the ones on the TB2S ladder, this first TEDD dee integration test with 2S and PS modules at once was a kickoff test for following integration tests that will be performed in the future.

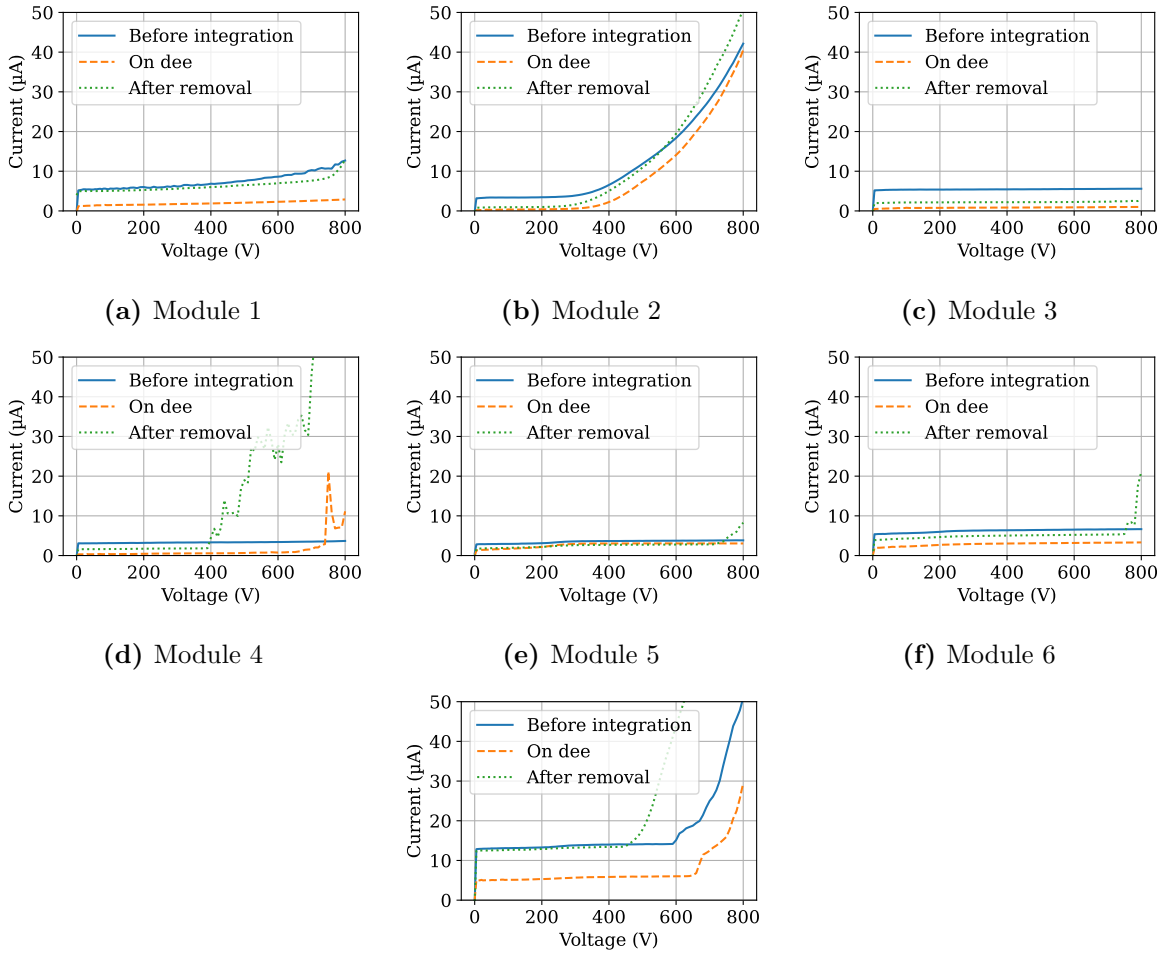

(a) Module 1 **(b)** Module 2 **(c)** Module 3

(d) Module 4 **(e)** Module 5 **(f)** Module 6

(g) Module 7

Figure 6.31.: IV curves of the 2S modules on the TEDD dee. The IV curves are shown before the integration, on the dee and after the removal from the dee. The low voltage of the measured module was set to 10.5 V while the other modules were not powered. Further details can be found in the text.

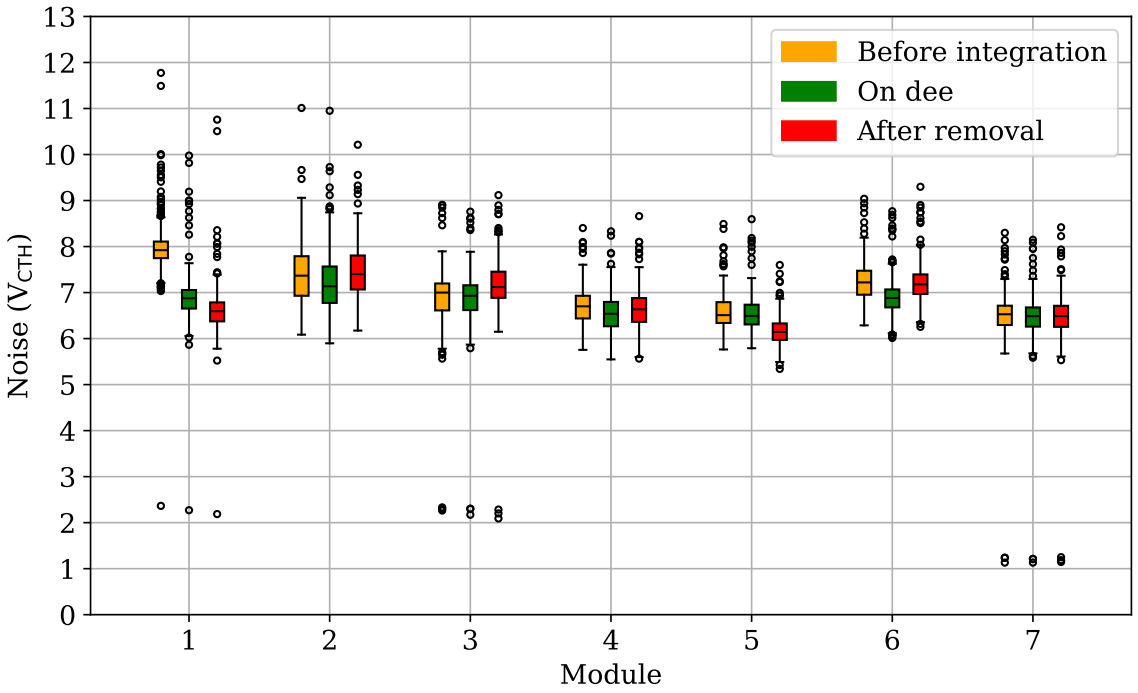

Figure 6.32.: Noise of the 2S modules on the TEDD dee. The distribution of the strip noise of the 2S modules mounted on the dee is depicted before the integration, on the dee and after removal. The results are shown as a box plot with boxes extending from the first to third quartile and whiskers extending to the farthest data points lying within 1.5 times the interquartile range. The median is represented by the stroke within the box. The data points outside the whiskers are outliers and also shown. The noise of the modules on the dee is not changed significantly compared to the reception measurements before the integration. The noise of module 1 is higher during the reception test compared to on the dee because it was not grounded properly to the carrier during this measurement. The number of outliers to low noise (not connected strips) and higher noise does not change with the integration process.

Part III.

Summary and Outlook

7
Summary and Outlook

The *Large Hadron Collider* (LHC) at the *European Organization for Nuclear Research* (CERN) is currently the largest particle accelerator in the world. To further exploit the physics potential of the LHC, it will be upgraded to the *High-Luminosity LHC* (HL-LHC) which will have increased integrated luminosity by a factor of ten compared to the LHC. The first beams at the HL-LHC are expected in 2030. With the accelerator upgrade, the requirements regarding the radiation levels and the overall particle densities in the detectors at the LHC will increase drastically.

The *Compact Muon Solenoid* (CMS) experiment at the LHC has to be upgraded for its operation during the HL-LHC era from 2030 to 2040. All upgrade activities are summarized in the *CMS Phase-2 Upgrade*. The innermost subdetector, the silicon tracker, will be fully replaced by a new silicon tracker. This will consist of an inner and an outer tracker. The *CMS Phase-2 Outer Tracker* will be built with 2S modules, which house two silicon strip sensors, and PS modules with one macro-pixel and one strip sensor each. Both module types are called p_{T}-modules because they can select particles traversing the modules based on their transverse momentum p_{T}. A selection of high p_{T} particles are processed to reconstruct tracks which are used at the L1 Trigger for event selection. When an L1 trigger signal is received, the full hit information of the modules is read out. In the Outer Tracker, the modules are arranged on different subdetector structures. In the *Tracker Barrel with 2S modules* (TB2S), the modules are mounted on *ladders* that house twelve 2S modules each. The modules on the ladder are overlapping to not lose any track. The *Tracker Endcap Double-Disks* (TEDD) are composed of *dees* on which 2S modules are mounted at larger radii while the inner region supports PS modules.

The *Institute of Experimental Particle Physics* (ETP) at the *Karlsruhe Institute of Technology* (KIT) is one of eight 2S module *assembly centers*. Prototype modules were built since 2016 to set up the assembly line and to perform functional tests with the prototype modules. Since 2021, the prototype modules have the final outer dimensions. The modules used within this thesis are called *2S prototype modules* and *2S kickoff modules*. As the CMS Phase-2 Outer Tracker project was moving from the R&D to the production phase during the time of this thesis, *integration tests* on subdetector structures got possible with multiple modules at once. The integration tests targeted different research aspects. Generally, the module integration itself, thermal behavior and electrical performance can be tested. At the *integration center Hubert Curien pluridisciplinary Institute* (IPHC) in Strasbourg, TB2S ladders will be integrated with 2S modules, and at *Deutsches Elektronen-Synchrotron* (DESY) in Hamburg, TEDD dees will be integrated with 2S and PS modules. Since modules and substructures are needed for integration tests, the integration tests performed within this thesis were done in cooperation with the groups at DESY and IPHC. The results of the system and integration tests performed in this thesis are summarized in the following paragraphs.

On the 2S prototype modules, the noise level turned out to be about one DAC value ($1\,\mathrm{V_{CTH}}$) higher than foreseen by the hybrids design. Special, self-made high voltage tail adaptors were used to successfully mitigate the noise of the 2S prototype modules by adding a $100\,\Omega$ resistance to the high voltage circuit. This additional resistance was also added to the final high voltage

tail design and ensures – together with a ground balancer – low enough module noise for the operation of the 2S modules in the Phase-2 Outer Tracker. The measurements within this thesis also required various software and firmware developments in order to properly configure the multi-module stub readout. The initial implementation was performed by Sarah Seif El Nasr-Storey but they were added to the repositories within this thesis. With these changes, the measurements in the burn-in stations housing up to ten modules at all burn-in centers and the integration tests at the integration centers can be performed.

As a first test-bench for the multi-module readout, 2S prototype modules were stacked in a 2S muon hodoscope. All modules were oriented in the same direction such that the strips of the sensors were all parallel. Taking the coincidence signal of scintillator panels above and below the modules allowed for tracking cosmic muons. The projection of the zenith angle to a plane perpendicular to the strips was measured with the 2S muon hodoscope by fitting tracks to the hits generated in the silicon sensors of the modules. The expected projection was simulated with a Monte-Carlo simulation taking the exact detector geometry of the 2S muon hodoscope into account. The measured distribution shows the basic shape of the expectation, but vertically incident contributions are missing in the data. This could be related to inefficient areas in the scintillators. Nevertheless, particle tracking was possible with the 2S muon hodoscope in the laboratory without the need of any extra particle source. The setup will be used for a laboratory exercise of the Master's detector lecture at KIT to allow students to work with state-of-the art detectors.

The particle detection performance of three 2S kickoff modules was measured during a beam test at the DESY II test beam facility. The modules were rotated within the electron beam to emulate high p_{T} particles crossing the silicon sensors of the modules. In this way, the turn-on characteristics of the stub detection efficiency with varying angle was measured for different stub window and offset sizes. The expected behavior was simulated and consistent results from simulation and data were found. Also, the stub data show clear correlation between the different modules meaning that the earlier mentioned developments regarding the multi-module stub readout work as expected. With these results, the 2S kickoff modules are proven to show the same particle detection efficiencies as their predecessors and the module production with the final, very similar, hybrid design can start.

Two integration tests with a TB2S ladder were performed at CERN together with the IPHC group. These tests focussed on the thermal performance of a 2S prototype module mounted on that ladder. The irradiated module was built with silicon sensors irradiated to 1 MeV neutron equivalent fluences above the maximum expected fluence of 2S modules in the TB2S. During both tests, the irradiated module was mounted at the ladder position 1 which provides the worst cooling performance. Also, the irradiated module was built with five instead of six cooling points which are generally intended for modules at position 1. The cooling pipe of the ladder was connected to an evaporative CO_2 cooling system. During both thermal integration tests, thermal runaway measurements were performed. Thermal runaway means that the system comes to an uncontrolled self-heating loop when the cooling power of the system is no longer able to compensate the heating power. For the measurements, the CO_2 set temperature was changed in steps until the silicon sensor temperature did not stabilize anymore at the new temperature. At this CO_2 temperature, thermal runaway was reached. The data of the silicon sensor temperature as a function of the CO_2 temperature were compared to thermal Finite Volume Method (FVM) simulations performed by Cristiano Turrioni [Tur22] from INFN Perugia. In contrast to the baseline simulations with an adiabatic model, the simulations for comparison with the measurement data was tuned to the measurement conditions and heat exchange of the modules with the surrounding air was taken into account. Measuring the thermal runaway with different conditions showed that the torque with which the irradiated module was applied to the ladder inserts, can be reduced, which would be needed to avoid

thread breakage during the integration procedure. The environmental conditions during the Phase-2 Tracker operation are not known a priori. From the over 15 years of operation of the current CMS Tracker, it can be estimated that the air temperature will be about at the silicon sensor temperature, resulting in even better cooling conditions than during the presented measurements. This means that the safety margin between the operation and thermal runaway temperature is even larger than simulated by the adiabatic model and measured during the thermal integration tests.

A first full TB2S ladder integration test was performed at IPHC, Strasbourg. Twelve 2S modules were mounted on a TB2S ladder and were operated synchronously with focus on the electrical properties. The ladder was powered with either a laboratory power supply or a prototype power supply for the Phase-2 Tracker. The electrical performance of the modules did not change on the ladder compared to the measurements before the integration. Also, the performance was not influenced by the prototype power supply with the 60 m long power cable. High statistics measurements with different high rate trigger and threshold settings were performed to be able to study the module performance during the operation on the ladder in more detail. Threshold scans at different high rate trigger frequencies were performed. The results showed that the bandwidth limit of the *Concentrator Integrated Circuit* (CIC) behaves as expected. The maximum number of clusters that can be read out in average is, as intended by the chip design, suitable for the 2S module operation in the Phase-2 Outer Tracker. It was measured that the noise hit occupancy of the modules was below the required 10^{-5} at relative thresholds above $5\,\sigma$. A common mode noise analysis of the data with a relative threshold of $5\,\sigma$, which corresponds to the use-case-conditions in the Phase-2 Outer Tracker, showed that the data taking will not be influenced by common mode noise events. Trigger frequency scans were performed to check for trigger related features during the 2S module operation. In the scans with constant trigger separation, a noise hit oscillation was observed which can be explained by a baseline-oscillation of the pre-amplifier of the *CMS binary chips* (CBCs). The effect was not seen in the data taken with Poisson distributed random triggers since the readout of the events does not always happen at the same time when a new signal enters the frontends. Thus, it will not influence the tracker operation. Additionally, high rate trigger frequency measurements with a noise hit occupancy of about 0.06 %, which is close to the expected hit occupancy of 0.1 % in the Phase-2 Tracker, were performed. This is, beside the fact that the hits were generated by noise instead of crossing particles, close to the operation conditions of the 2S modules in the tracker.

A TEDD dee integration test was performed at DESY, Hamburg. During this test, for the first time, 2S modules were mounted on a TEDD dee. Regarding the noise and current-voltage characteristics of the silicon sensors, the 2S modules showed very similar electrical behavior on the dee as in single module measurements before the integration. The tests also showed that the cabling scheme foreseen for the dees is tight but possible with real modules.

During the later tracker integration at the integration centers, the knowledge and experience gained from the presented tests can be used. Also, further integration tests are planned with the final (pre-)production Outer Tracker modules.

Summing up, the latest 2S prototype and kickoff modules showed very good performance in system and integration tests. Particle detection and p_{T} discrimination is possible as intended, and the modules show excellent thermal and electrical performance on subdetector structures. The Outer Tracker module production started in 2024. This is on schedule for beginning of data taking with the new Phase-2 Outer Tracker of CMS at the HL-LHC in 2030.

Part IV.

Appendix

A

Overview of Measured Modules

Appendices A.1 and A.2 provide an overview of the prototype and kickoff modules that were used for the tests within this thesis. For both module types, the official name, a short name of the test in which the module was used and the position that module had in the respective test, are given. The short test names are linked to the sections like following:

- "Full ladder": section 6.2 Full TB2S Ladder Integration Test
- "Dee": section 6.3 TEDD Dee Integration Test
- "Hodoscope": section 5.1 2S Muon Hodoscope
- "Thermal ladder": section 6.1 Thermal TB2S Ladder Integration Tests
- "Full thermal ladder": section 6.1 Thermal TB2S Ladder Integration Tests
- "Beam test": section 5.2 Beam Test

The module positions are the same as labeled in the setup pictures of the respective test.

A.1. Prototype Modules

In table A.1 besides the official name, test and position of the modules, it is indicated if they have an I^2C patch (explained in section 3.3.5), which lpGBT version is mounted on the SEH and which CIC version is mounted on the FEHs. In the column "Comments" special things are listed for some modules. "Patched kickoff SEH" means that this module had another SEH attached than for the previous tests. It is a common plane kickoff SEH that was fixed to be read out with FEC5 instead of FEC12 as the SEH of the kickoff modules are designed for. "Irradiated" refers to the irradiation of the silicon sensors of that module.

Table A.1.: 2S prototype modules used for measurements within this thesis. For each module all relevant parameters are listed in this table. Specialities can be found in the column for comments. They are further explained in the text.

Official name	Test	Position	I^2C patch	lpGBT version	CIC version	Comments
2S_18_5_IPG-00001	Full ladder	1		v0	CIC2.1	
2S_18_5_IPG-00002	Full ladder	2	Yes	v0	CIC2.1	
2S_40_6_BEL-00005	Full ladder	3		v0	CIC2.1	
2S_40_6_BEL-00006	Full ladder	4		v1	CIC2	
2S_18_5_BRN-00008	Full ladder	5	Yes	v0	CIC2.1	
2S_18_5_AAC-00002	Full ladder	6		v0	CIC2.1	
2S_18_5_KIT-00001	Full ladder	7		v0	CIC2.1	
	Dee	7				
2S_18_5_KIT-00002	Full ladder	8		v0	CIC2.1	
	Dee	6				
2S_40_6_KIT-00005	Full ladder	9	Yes	v0	CIC2.1	
	Hodoscope	2	No	v1		Patched kickoff SEH
2S_40_6_KIT-00007	Full ladder	10	Yes	v0	CIC2.1	
	Dee	4				
2S_40_6_KIT-00009	Full ladder	11		v1	CIC2.1	
	Dee	2				
	Hodoscope	3				Patched kickoff SEH
2S_18_5_KIT-00006	Full ladder	12		v0	CIC2.1	
	Hodoscope	1				
	Thermal ladder	3				
	Dee	5				
2S_18_5_KIT-00003	Thermal ladder	2		v0	CIC2	
2S_18_5_KIT-00004	Thermal ladder	1		v0	CIC2.1	Irradiated
	Full thermal ladder	1				
2S_18_5_AAC-00001	Dee	3		v0	CIC2	
2S_18_5_AAC-00004	Dee	1		v1	CIC2.1	

A.2. Kickoff Modules

In table A.2 the SEH type (common and split plane) of the used kickoff modules as well as if a ground balancer was attached during the measurements is indicated.

Table A.2.: 2S kickoff modules used for measurements within this thesis. For each module all relevant parameters are listed in this table. Specialities can be found in the column for comments.

Official name	Test	Position	SEH type	Ground balancer	Comments
2S_18_5_KIT-00104	Full thermal ladder	2	Common plane	Yes	
	Beam test	2			
2S_18_5_KIT-00101	Full thermal ladder	3	Common plane	Yes	
	Beam test	1			
2S_18_6_IPG-00101	Full thermal ladder	4	Split plane	No	
2S_18_5_NCP-00102	Full thermal ladder	5	Split plane	Yes	
2S_18_6_BEL-00104	Full thermal ladder	6	Common plane	Yes	Broken during full thermal ladder test.
2S_18_5_BRN-00102	Full thermal ladder	7	Common plane	Yes	
2S_18_5_FNL-00101	Full thermal ladder	8	Common plane	Yes	
2S_18_6_FNL-00103	Full thermal ladder	9	Split plane	Yes	
2S_18_6_BEL-00103	Full thermal ladder	10	Common plane	Yes	
2S_18_5_KIT-00102	Full thermal ladder	11	Split plane	Yes	
	Beam test	3			
2S_18_5_KIT-00105	Full thermal ladder	12	Split plane	Yes	

B
Noise Measurements

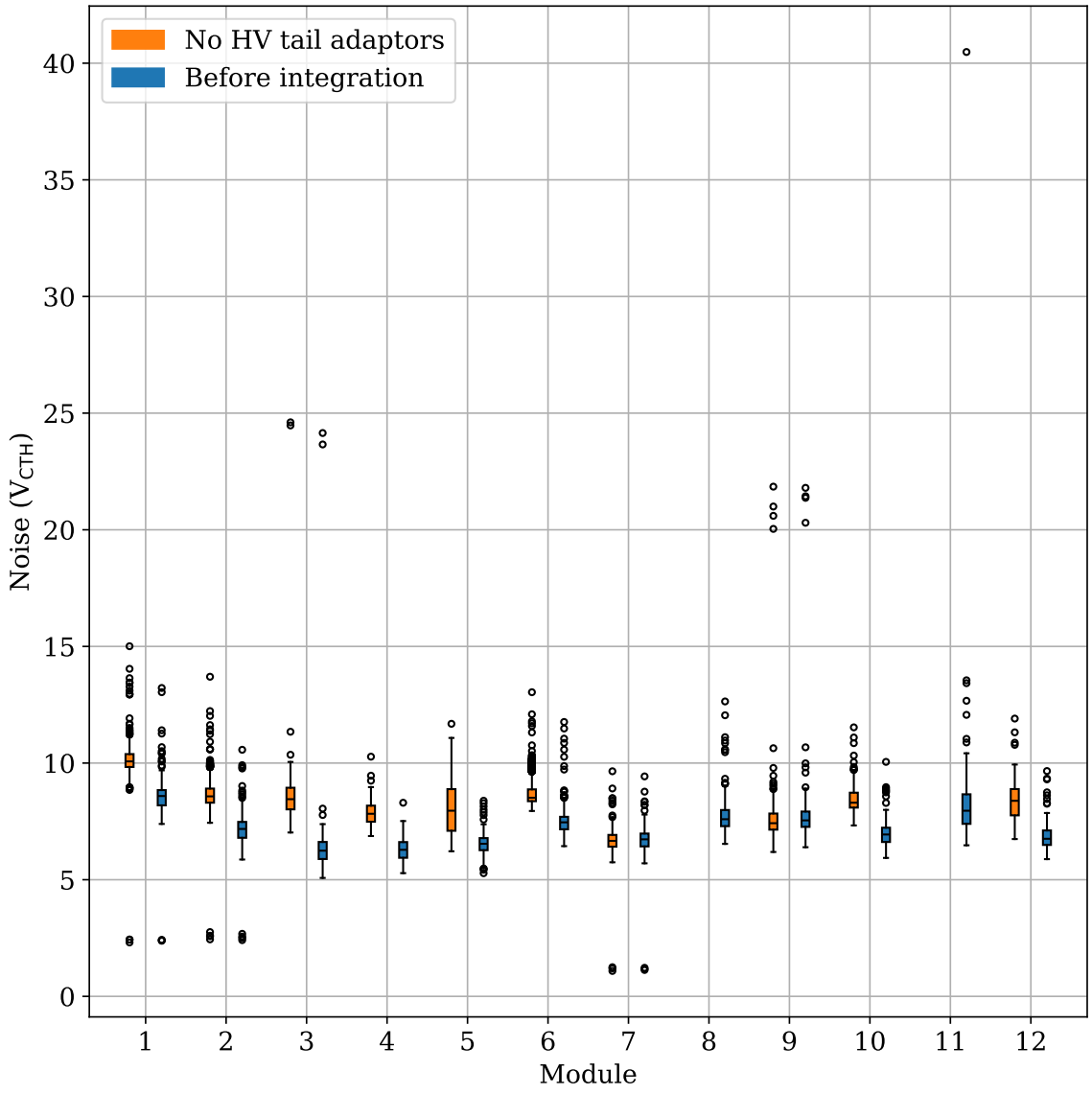

Figure B.1.: Comparison of the noise without and with HV tail adaptors. The plots shows the noise values already shown in figure 4.3 but without any zoom of the y-axis.

C

Software and Firmware Changes for the Multi-Module Stub Readout

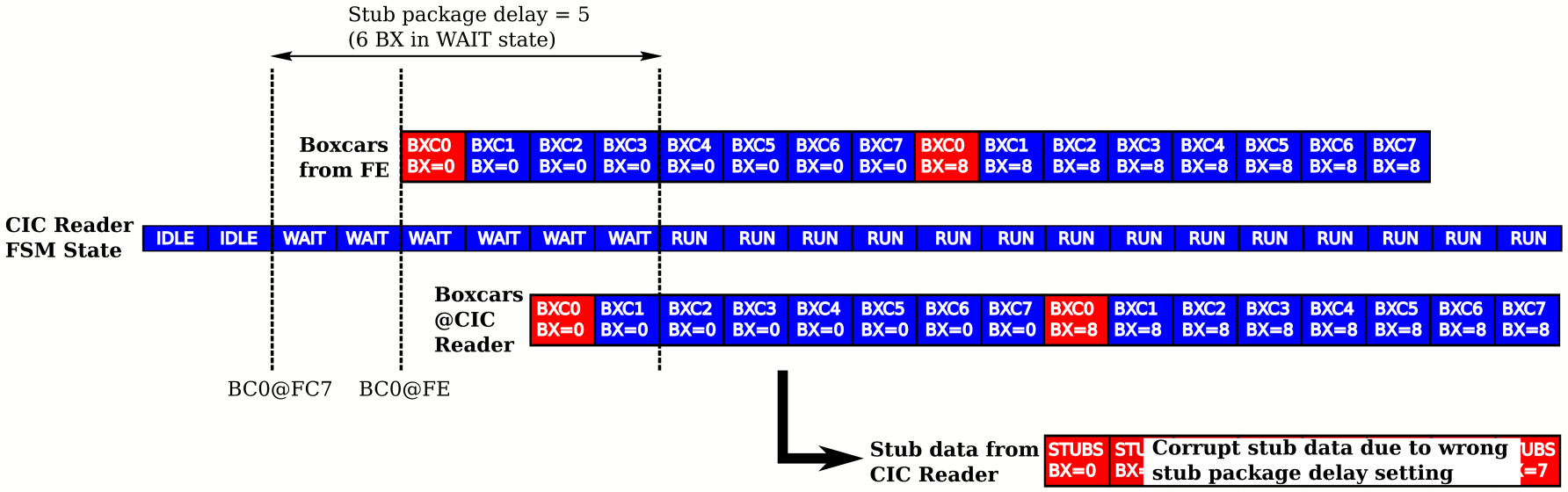

Figure C.1.: Illustration of the stub readout with a wrong stub package delay. A BC0 command resets the BX ID counter in the FE. When the BC0 command arrives at the FC7, the finite-state machine (FSM) of the CIC reader goes from the idle to the wait state. It remains there for the number of clock cycles equal to the stub package delay plus one. Then, the run state is entered, and the stub data are read out. The stub data are reasonable when the CIC reader starts reading the stub data at the boxcar 0 (BXC0). In this figure, this is not the case since the stub package delay is set to a wrong value of 5 bunch crossings. With the setting of 5 bunch crossings, the CIC reader starts reading the stubs at the boxcar 2 (BXC2). The read stub data are corrupt. The correct stub package delay would be 3 bunch crossings, which is depicted in figure 4.5. Adapted from [Mag24].

D
2S Muon Hodoscope

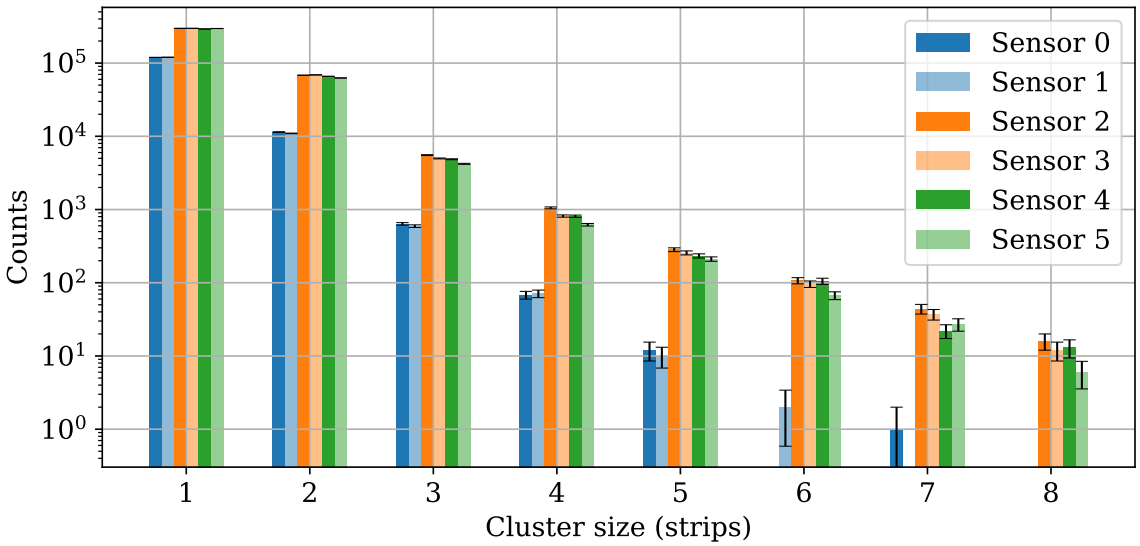

Figure D.1.: Cluster sizes of the sensors in the muon hodoscope. The cluster sizes of all six sensors of the hodoscope are histogrammed. Sensors with the same color but different opacity belong to the same module. The sensor with the lower number and higher opacity is the bottom sensor of the module. Sensor 0 and 1 belong to the bottom module 1 and so on.

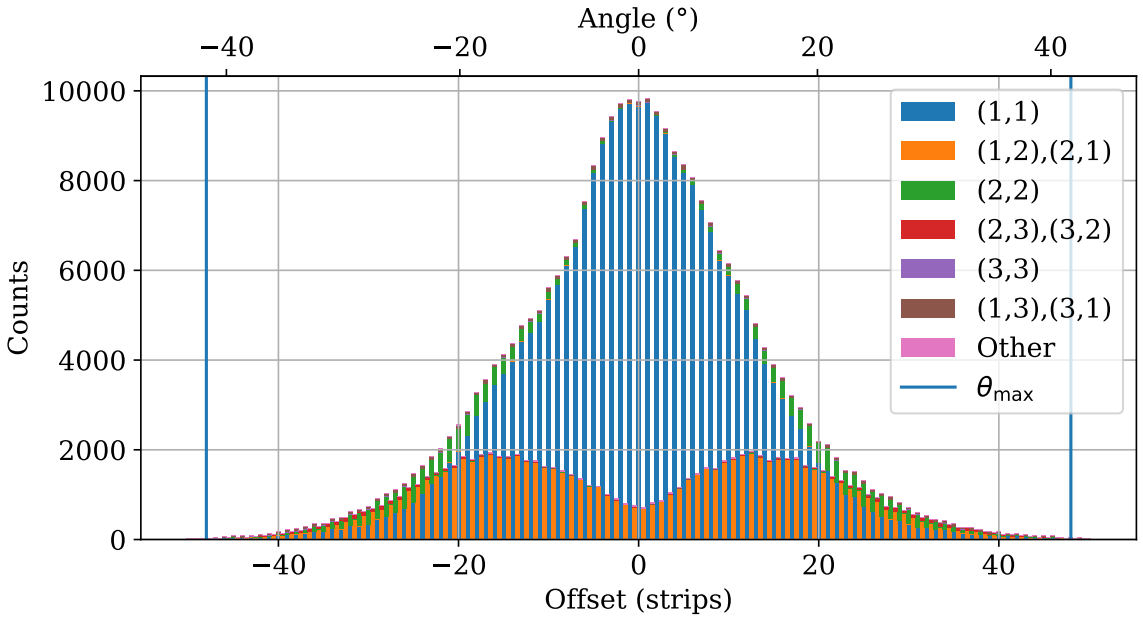

Figure D.2.: Offset of the clusters in the top and bottom sensor for module 3 (4.0 mm module). The offset values are plotted stacked for different combinations of the cluster width in the top and bottom sensor of each module. The cluster widths of both sensors are given as tuples in the legend. Cluster size differences of an even integer number result in integer offset values while cluster size differences of odd integer numbers result in half-integer offset values. The binning is chosen in half-integer steps such that each possible offset in strips is shown separately.

E
Beam Test

E.1. DUT Alignment

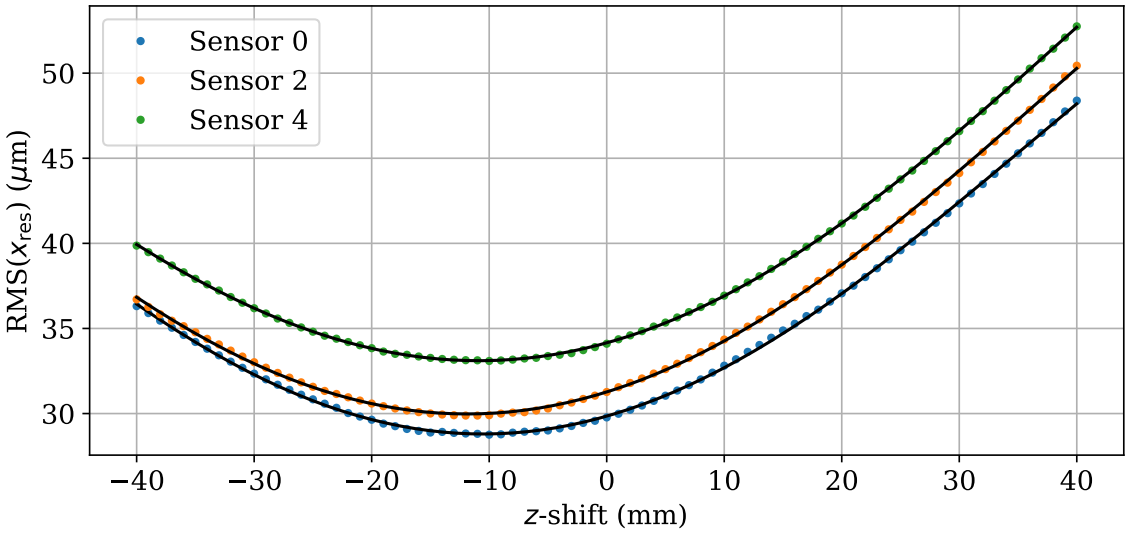

Figure E.1.: Illustration of the z-position alignment. The RMS of the x-residuals is plotted as a function of the applied z-shift during the DUT alignment. The z-shift at the minimum is applied as DUT alignment. The RMS of the x-residuals increases with the sensor number and thus the position along the beam. This effect is caused by multiple scattering at the silicon sensors.

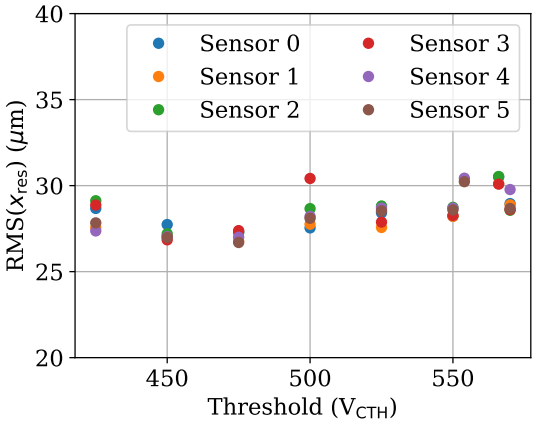

(a) Threshold scan

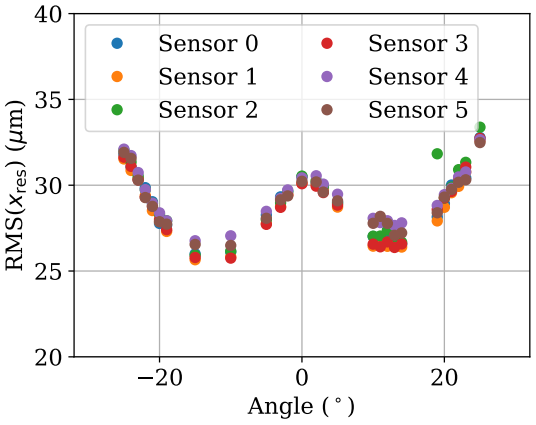

(b) Angular scan AS_Outer

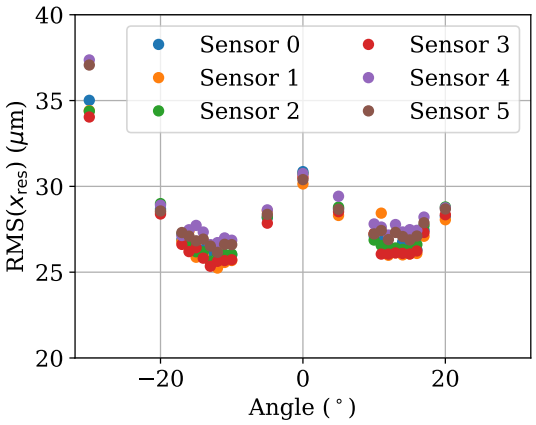

(c) Angular scan AS_Inner

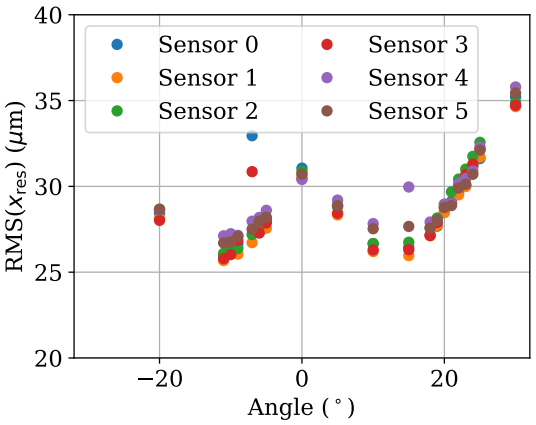

(d) Angular scan AS_Offset

Figure E.2.: RMS of the x-residuals after the DUT alignment. The RMS of the x-residuals after the DUT alignment is depicted for all runs presented in section 5.2.3. The results belonging to the threshold scan (a) are given as a function of the applied threshold while the results of the angular scans (b) to (d) are plotted as a function of the DUT rotation angle. The angular scan names in the captions refer to the names given in table 5.1.

E.2. Threshold Scan

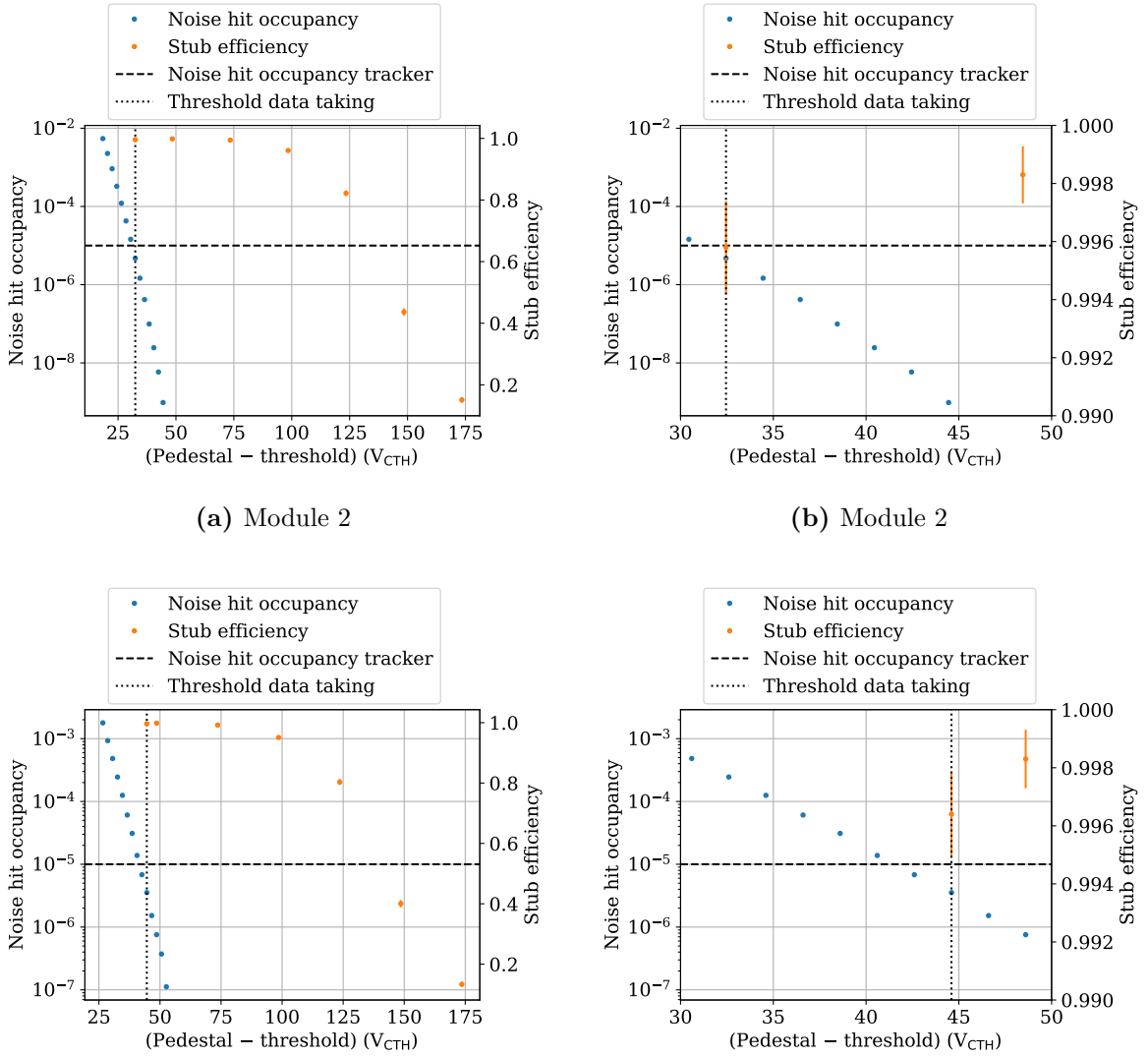

(a) Module 2

(b) Module 2

(c) Module 3

(d) Module 3

Figure E.3.: Threshold scan of module 2 an 3 during the beam test. The noise occupancy and the stub efficiency are shown as a function of the set threshold. (b) and (d) show a zoomed version of (a) and (c). At the threshold for data taking, the noise hit occupancy is as required below 10^{-5} and the stub efficiency above 99.6 %.

E.3. Angular Scans

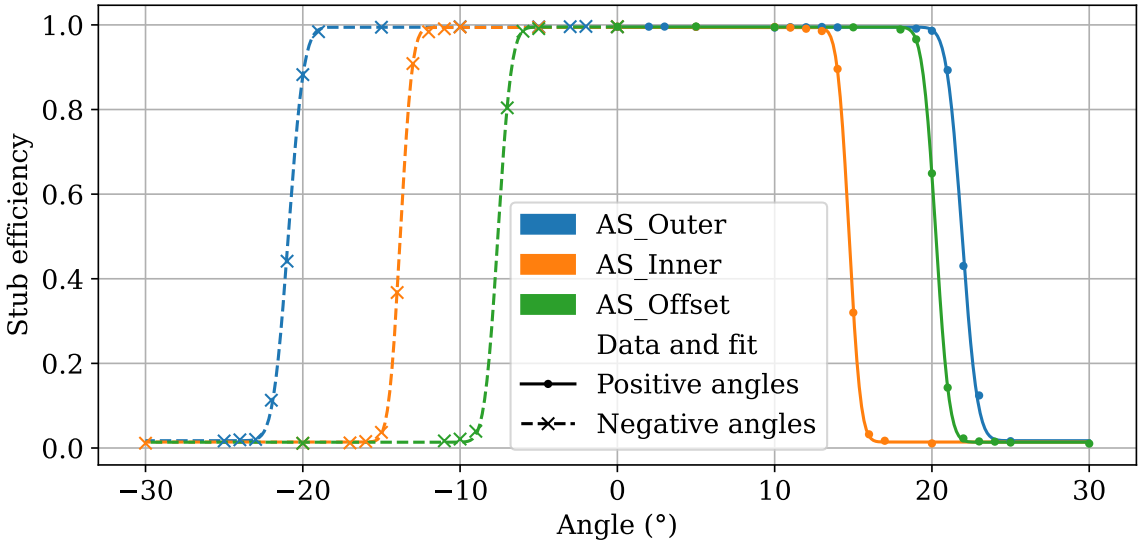

(a) Module 2

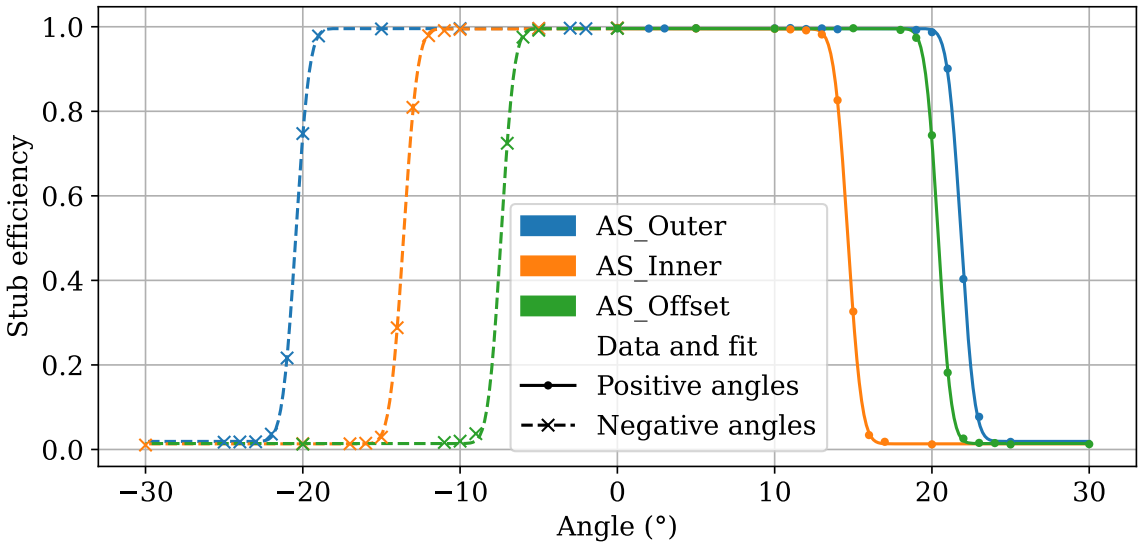

(b) Module 3

Figure E.4.: Stub efficiencies of module 2 and 3 for the angular scans. The stub efficiencies as a function of the module rotation angle are shown. The fits according to equation (5.12) with the resulting parameters given in table E.1 are also plotted. The scans are labeled according to table 5.1.

Table E.1.: Fit parameters of the turn-on characteristics for module 2 and 3. The parameters p_0, p_1 and p_3 are obtained from the fit to the positive angles while they are fixed in the fit to the negative angles. The parameter p_2 is given separately for the fit to positive angles $p_{2,\mathrm{pos}}$ and negative angles $p_{2,\mathrm{neg}}$. The statistical uncertainties are shown as well.

Module	Fit parameter	AS_Outer	AS_Inner	AS_offset
2	p_0	0.988 ± 0.004	0.992 ± 0.003	0.991 ± 0.001
2	p_1	0.978 ± 0.004	0.980 ± 0.003	0.981 ± 0.001
2	$p_{2,\mathrm{pos}}$ in °	21.91 ± 0.03	14.73 ± 0.02	20.25 ± 0.01
2	$p_{2,\mathrm{neg}}$ in °	20.91 ± 0.02	13.79 ± 0.02	7.59 ± 0.03
2	p_3 in °	1.09 ± 0.04	0.82 ± 0.03	0.95 ± 0.02
3	p_0	0.985 ± 0.003	0.992 ± 0.003	0.990 ± 0.002
3	p_1	0.977 ± 0.003	0.982 ± 0.003	0.982 ± 0.002
3	$p_{2,\mathrm{pos}}$ in °	21.85 ± 0.02	14.65 ± 0.02	20.40 ± 0.02
3	$p_{2,\mathrm{neg}}$ in °	20.44 ± 0.01	13.59 ± 0.02	7.391 ± 0.04
3	p_3 in °	0.96 ± 0.03	0.99 ± 0.03	0.92 ± 0.02

Table E.2.: Simulation parameters matching the measurement conditions. The simulation results shown in figures 5.14 and E.6 were obtained with these parameters.

Module	Parameter	AS_Outer	AS_Inner	AS_Offset
1	sensor distance in mm	1.679	1.669	1.685
1	σ_θ in °	0.0	0.332	0.0
2	sensor distance in mm	1.693	1.681	1.687
2	σ_θ in °	0.0	0.327	0.0
3	sensor distance in mm	1.797	1.700	1.695
3	σ_θ in °	0.0	0.427	0.0

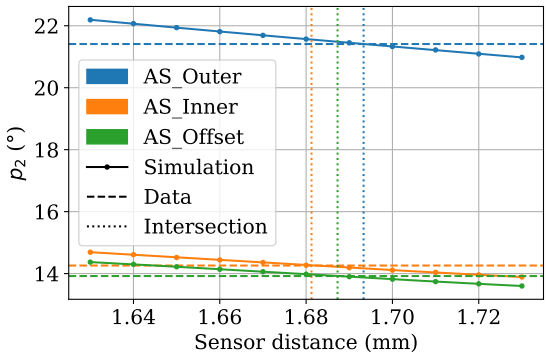

(a) Module 2

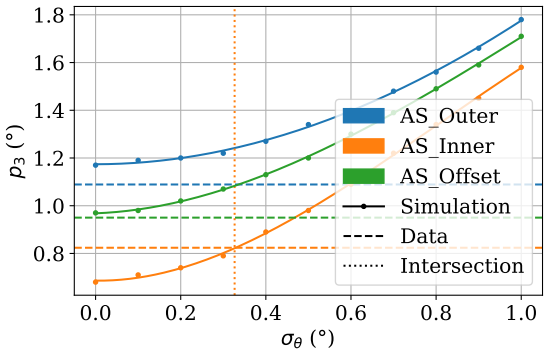

(b) Module 2

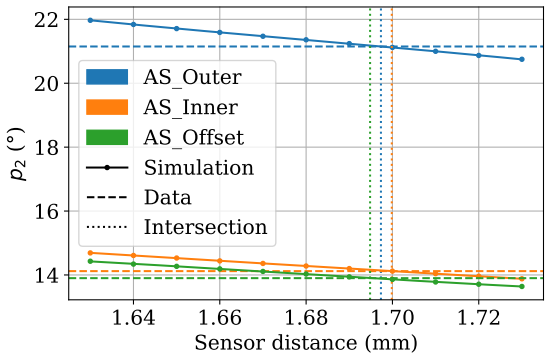

(c) Module 3

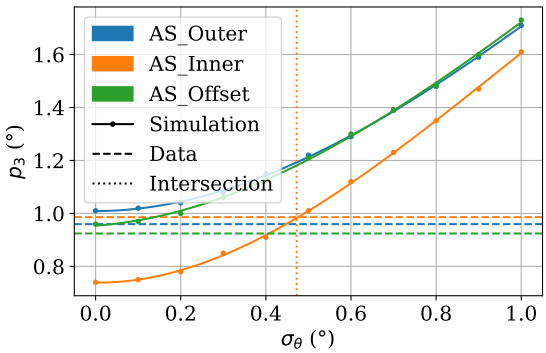

(d) Module 3

Figure E.5.: Comparison of the fit parameters obtained from data and simulation for module 2 and 3. The simulation was performed for different sensor distances (a) and (c) and standard deviations of the angle σ_θ (b) and (d). The fit parameters of the data are plotted as horizontal dashed lines while the intersection with the simulated parameters is depicted with a dotted vertical line.

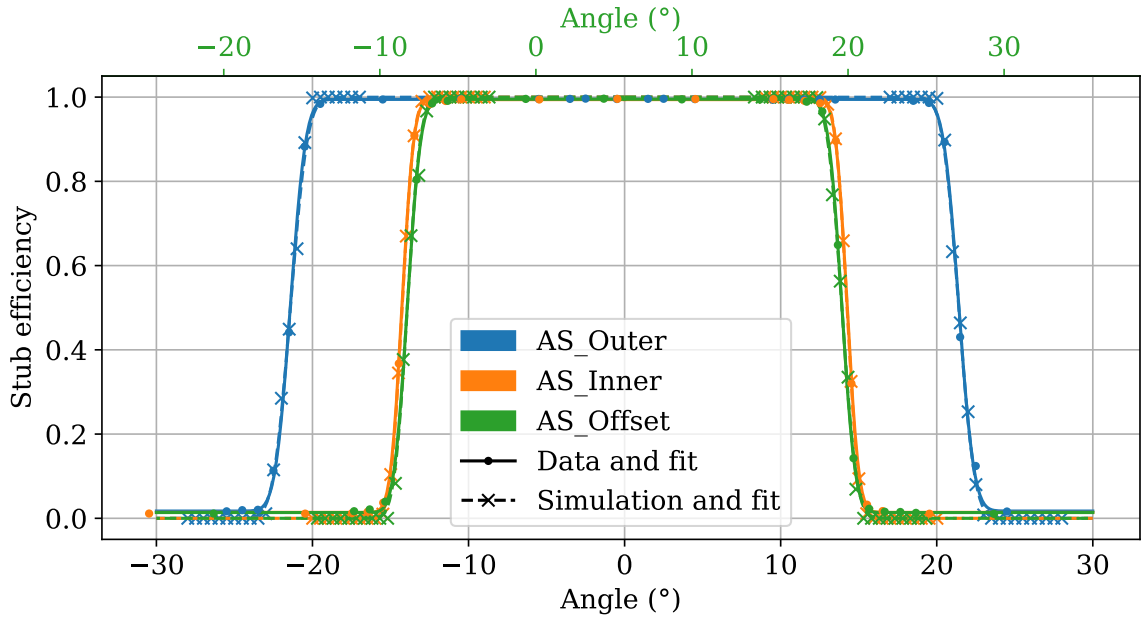

(a) Module 2

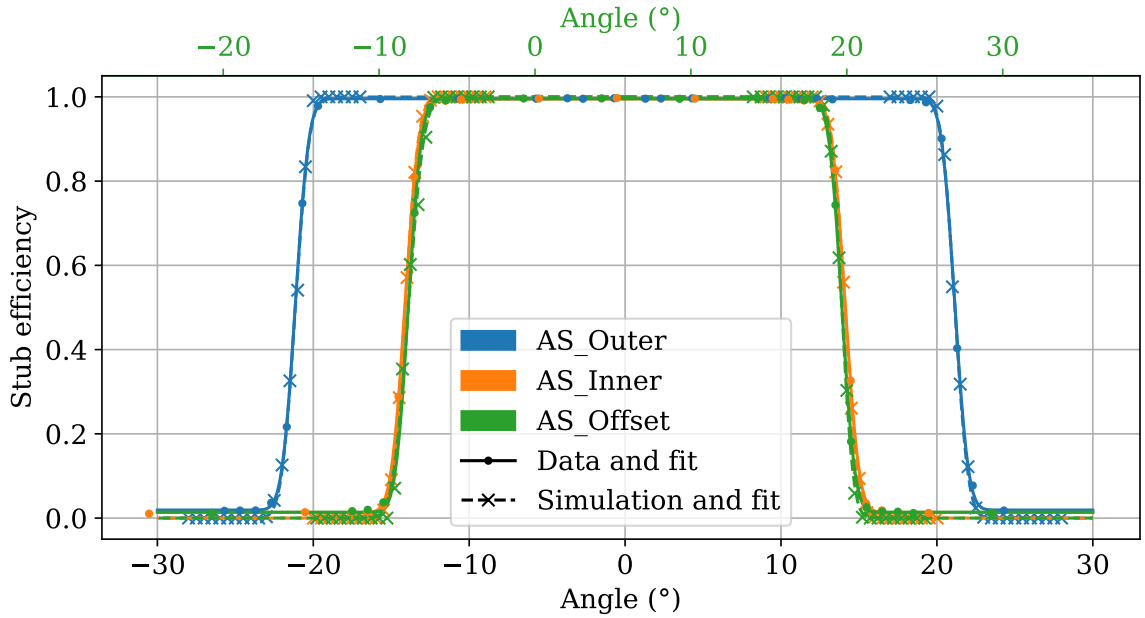

(b) Module 3

Figure E.6.: Comparison of data and simulation results for module 2 and 3. The measured and simulated stub efficiency turn-on curve is shown for all three angular scans. The turn-on curves were shifted such that they are symmetric around 0°. For AS_Offset, the not shifted angle is also indicated in a secondary x-axis. The simulation results match the measurement results.

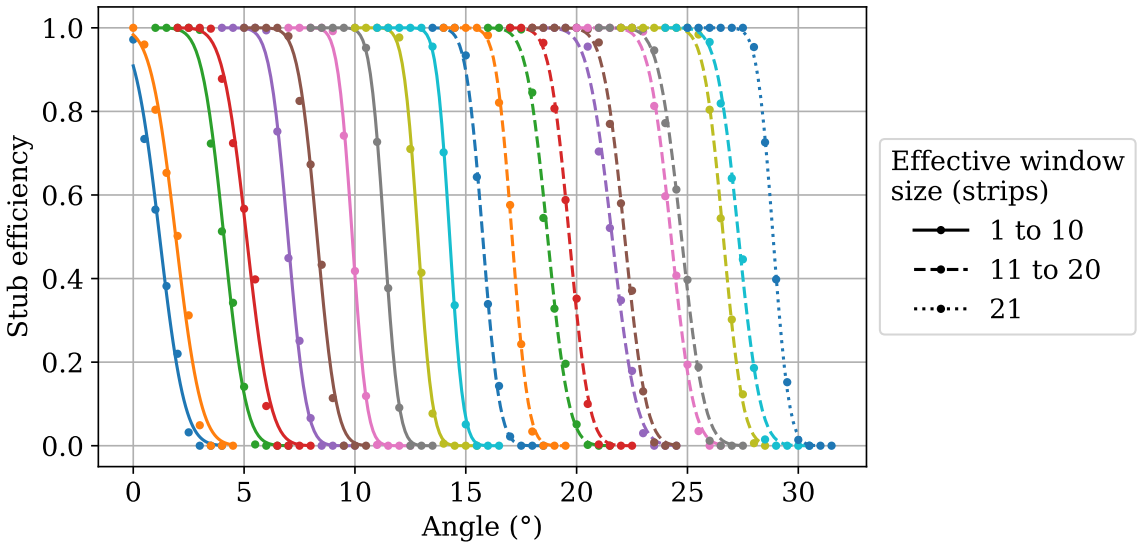

Figure E.7.: Stub efficiency turn-on simulation results of all possible effective stub window sizes. The results of the simulation of the stub efficiency are shown as a function of the rotation angle. The angle at which the decrease of the stub efficiency occurs depends on the applied effective stub window size.

F

Thermal TB2S Ladder Integration Tests

F.1. Thermal Runaway Measurement Conditions

The monitoring data during the thermal runaway measurements presented in section 6.1.3 are plotted in the figures F.1 to F.4. The numbers at the end of the labels of the temperatures measured on the irradiated module are referring to the number of the temperature sensor on the module (see figure 6.2b). The temperatures on the bridges of the irradiated module are plotted in purple while the temperatures on the top (bottom) silicon sensor are plotted in blue (green). The temperatures measured at several positions along the pipe are depicted in brown and the air temperatures are plotted in different light blue colors. The air temperature used as the input of the simulations shown in section 6.1.3 is the mean value of four pt100 temperature measurements that are labeled with "Air below", "Air left", "Air near" and "Air far" in figures F.1 to F.4. The temperature with the label "Air above" is not included to this mean value since it shows a larger difference to the other air temperatures and was measured with a 1-wire sensor. [Mou25b; Mou25a; FHE15] The pipe temperature shown in section 6.1.3 is the temperature that is labeled with "Outlet" in figures F.1 to F.4.

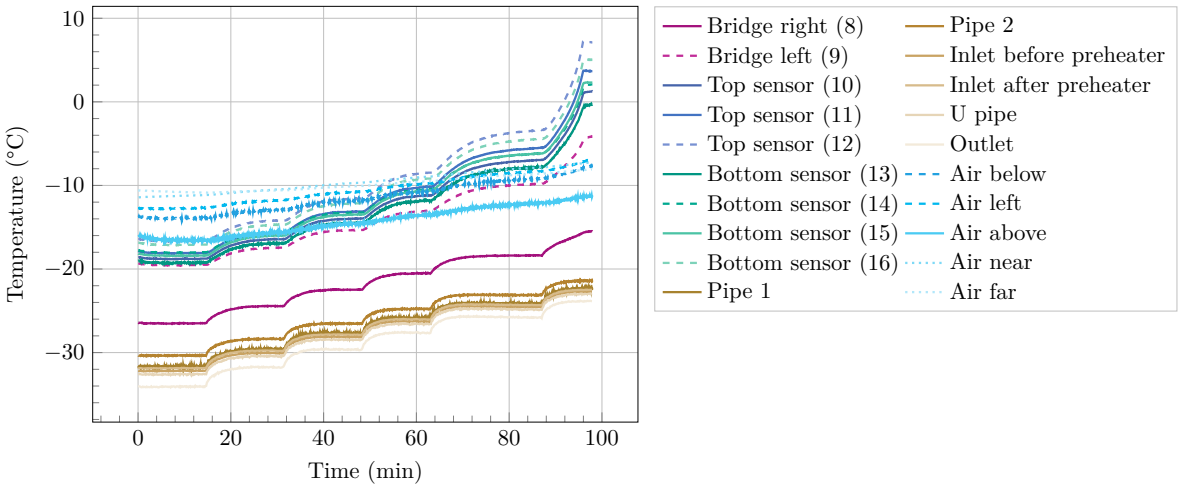

Figure F.1.: Temperatures during TR_ref. The silicon sensor temperatures of the irradiated module as well as the temperatures on the bridges, the cooling pipe and of the air in the measurement box are shown.

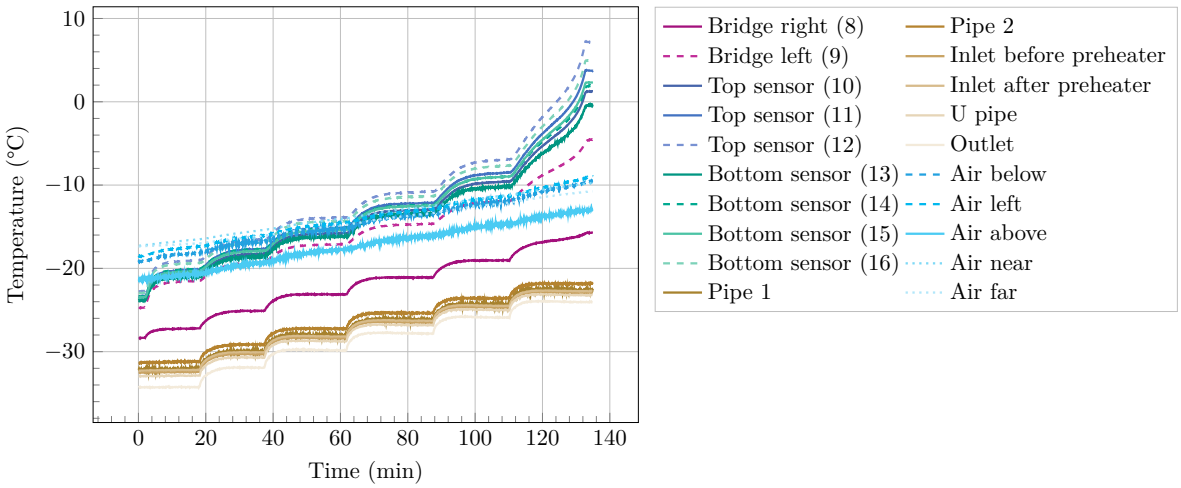

Figure F.2.: Temperatures during TR_lowTemp. The silicon sensor temperatures of the irradiated module as well as the temperatures on the bridges, the cooling pipe and of the air in the measurement box are shown.

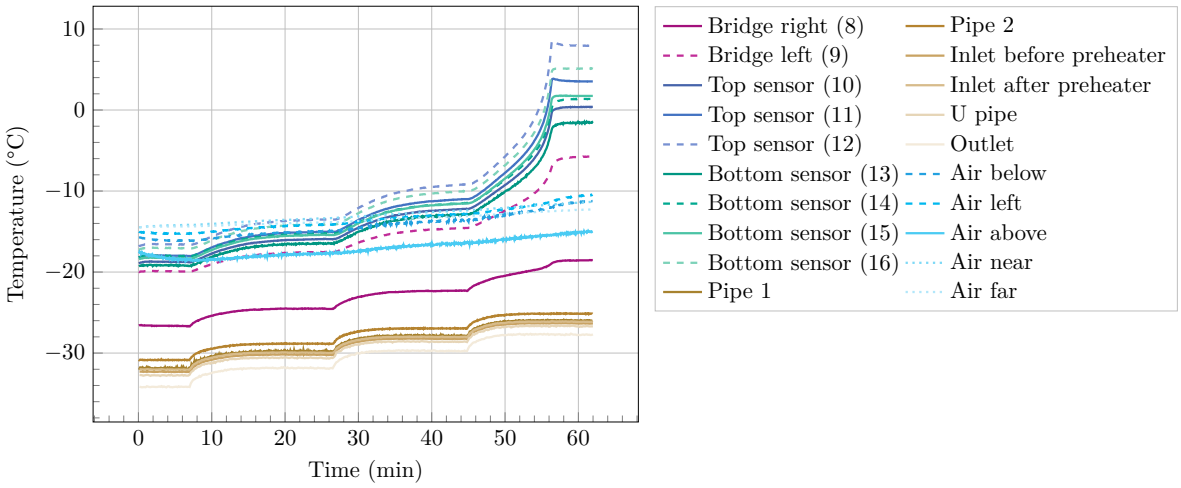

Figure F.3.: Temperatures during TR_800V. The silicon sensor temperatures of the irradiated module as well as the temperatures on the bridges, the cooling pipe and of the air in the measurement box are shown.

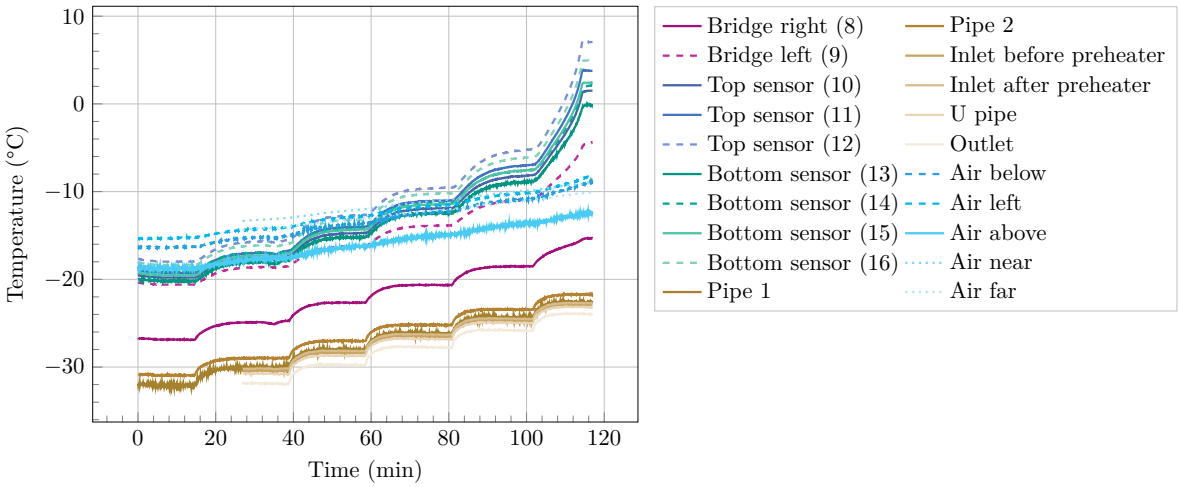

Figure F.4.: Temperatures during TR_lowTorque. The silicon sensor temperatures of the irradiated module as well as the temperatures on the bridges, the cooling pipe and of the air in the measurement box are shown. The data taking of some temperature sensors was started about 25 minutes delayed. The previous data points for the thermal runaway plots were extrapolated from the existing data.

F.2. Thermal Runaway Sensor Power Measurements

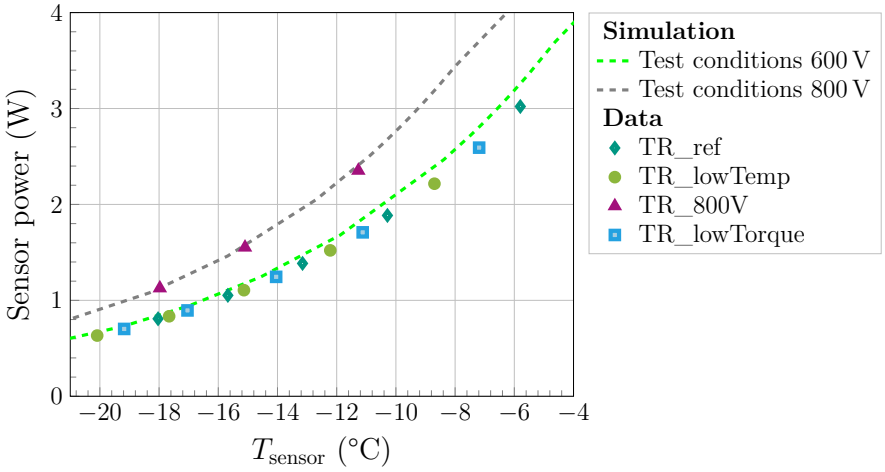

Figure F.5.: Comparison of the sensor power from data and simulations. The sensor power is shown as a function of the mean silicon sensor temperature. The simulation input matches well the data points. All simulations were performed by Cristiano Turrioni [Tur22].

F.3. Thermal Runaway Measurement Data from 2022

During the test performed in 2022, thermal runaway measurements with two environmental conditions were performed. Figure F.6 shows the comparison between these measurements and the results of the simulation performed by Cristiano Turrioni [Tur22]. The parameters such as high voltage, irradiation levels, materials and heat transfer coefficients of the simulation are taken as written in the figure. They match the measurement conditions. The only unknown parameter is the heat transfer coefficient of the air to the silicon sensors. With a value of $\text{HTC}_{\text{air}} = 15\,\text{Wm}^{-2}\text{K}^{-1}$, the simulation fits the data within 1 °C for two different air temperature conditions (colder air on the left side of figure F.6 and warmer air on the right side of figure F.6). The operation margin from −35 °C to −33 °C, which is aimed for stable operation of the Outer Tracker, is shown as a gray band in figure F.6. For stable operation of the future tracker it is important that there is a safety margin between the operation target temperature and the thermal runaway temperature, which is already the case for the adiabatic model. Taking air convection into account even increases this margin by almost 10 °C. During these measurements, the thermal runaway could actually not be observed in the data since the current limit of 5 mA of the HV power supply was reached before seeing the thermal runaway. Also, the heat transfer coefficient of the air of $\text{HTC}_{\text{air}} = 15\,\text{Wm}^{-2}\text{K}^{-1}$ is much higher than the one extracted from the data of 2024. The air flow during the 2022 measurements was not switched off completely as for the 2024 data taking. This is another indication that the data from 2024 fit better to the real conditions in the Phase-2 Outer Tracker. There, the air flow will probably also be reduced to a minimum and the air will behave like it does with just natural convection effects.

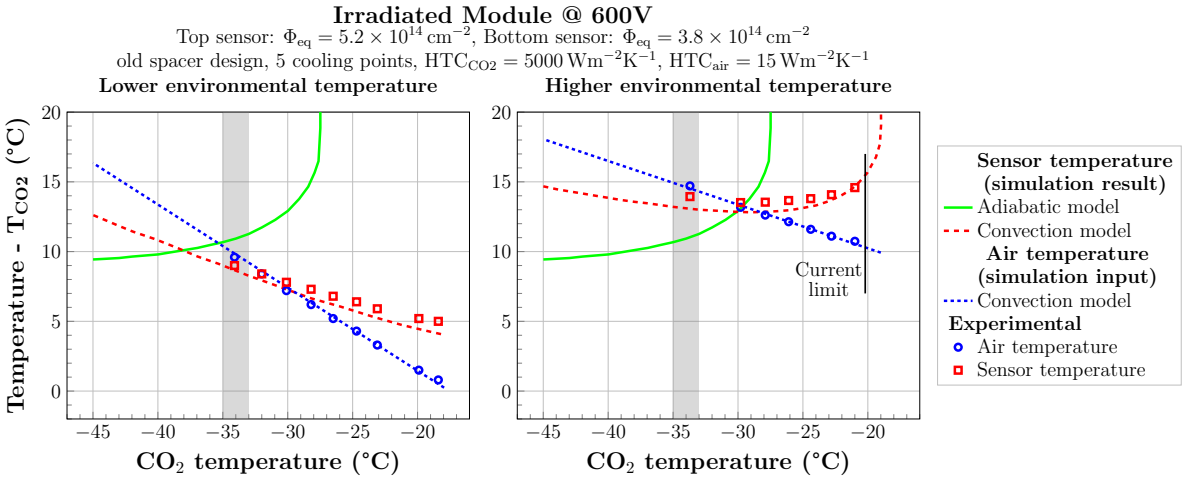

Figure F.6.: Comparison of data and simulation of the thermal runaway measurements. The aimed CO_2 temperature during tracker operation is indicated with the gray area between −35 °C and −33 °C. The solid green line shows the simulation result for the temperature difference between sensor and CO_2 using an adiabatic model while the dashed red curve shows simulation results taking air convection into account. The circles indicate the measured air temperature profile in the box as input for the simulation (dotted blue line). The squares show the measurement results for the sensor temperature. The vertical line in the right plot at about −20 °C indicates the temperature conditions during the measurements at which the current limit of 5 mA of the power supply was reached. All simulations were performed by Cristiano Turrioni [Tur22].

G

Full TB2S Ladder Integration Test

G.1. IV Measurement Results

The influence of the light emitted by the VTRx+ of the twelve modules on the ladder was studied during the full TB2S ladder integration test and is plotted in figure G.1. The comparison of the IV curve on the ladder with LV off, LV on and the LV of all modules on is shown. The difference in the leakage current between the measurements labeled with “LV off” and “LV on” shows the influence of the VTRx+ light of the measured module. This effect is very module dependent. On the modules 1, 2 and 3 this effect is expected to be the smallest since the VTRx+ of these modules was covered with black tape to reduce the light emission. The IV curve labeled with “LV all modules on” shows the impact of the VTRx+ light of all modules on the ladder on the leakage current of the measured module. The influence of this additional light is also varying from module to module. A statement about the expectation of the light influence cannot be done since this depends on how exactly the fibers are routed and bent, how the light gets reflected on metal surfaces inside the measurement box and many other not quantifiable parameters.

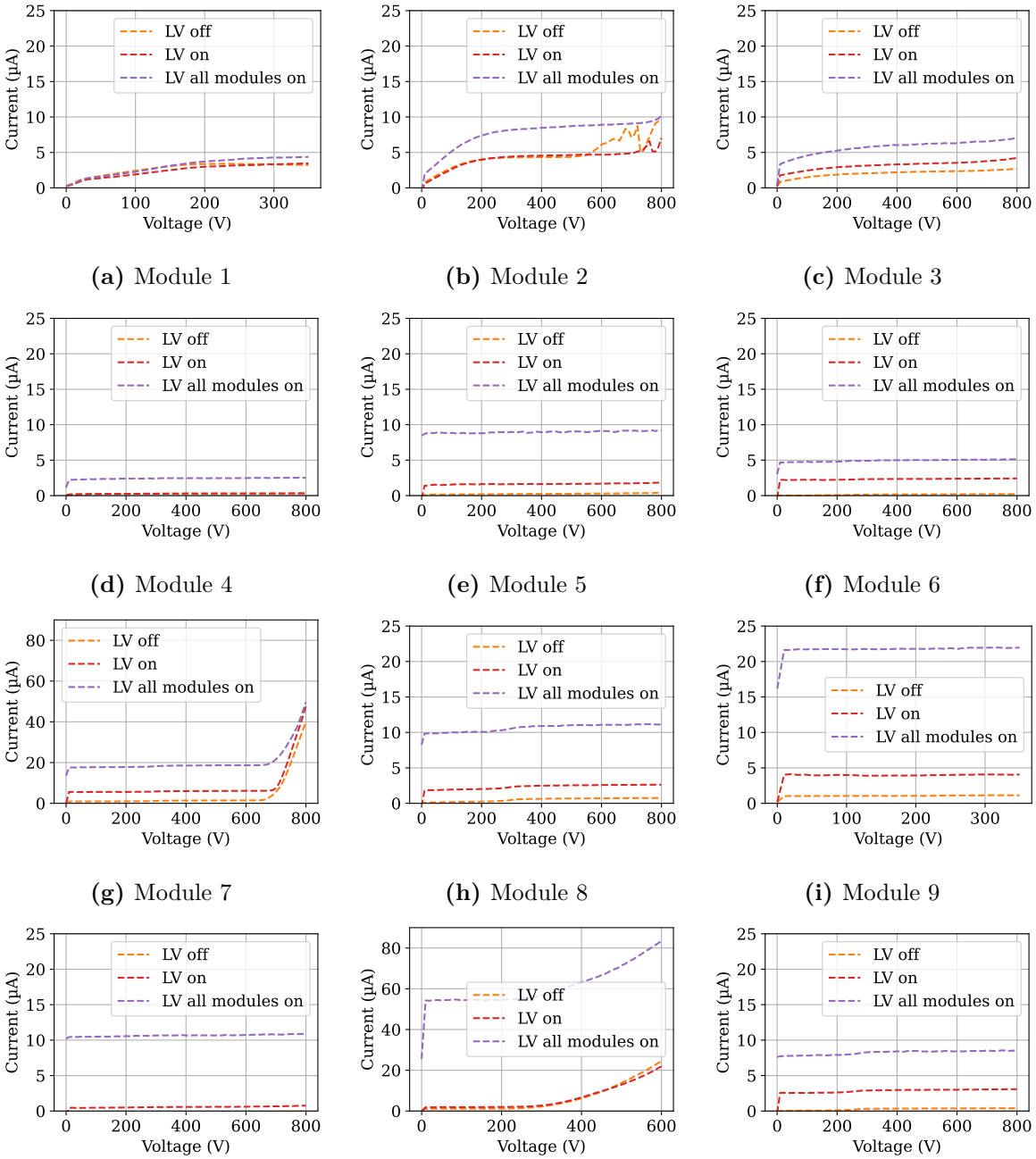

(a) Module 1 **(b)** Module 2 **(c)** Module 3

(d) Module 4 **(e)** Module 5 **(f)** Module 6

(g) Module 7 **(h)** Module 8 **(i)** Module 9

(j) Module 10 **(k)** Module 11 **(l)** Module 12

Figure G.1.: IV curves of modules on fully integrated TB2S ladder. The IV curves are shown for modules on the ladder with the LV of all modules off, the LV of just the measured module on, and the LV of all twelve modules on the ladder on. LV on means that the VTRx+ emits light. The y-axes for module 7 and 11 have a larger range than for the other modules. The IV curves with the label "LV off" are the same that are already shown in figure 6.18 with the label "On ladder".

G.2. Noise and Pedestal Measurement Results

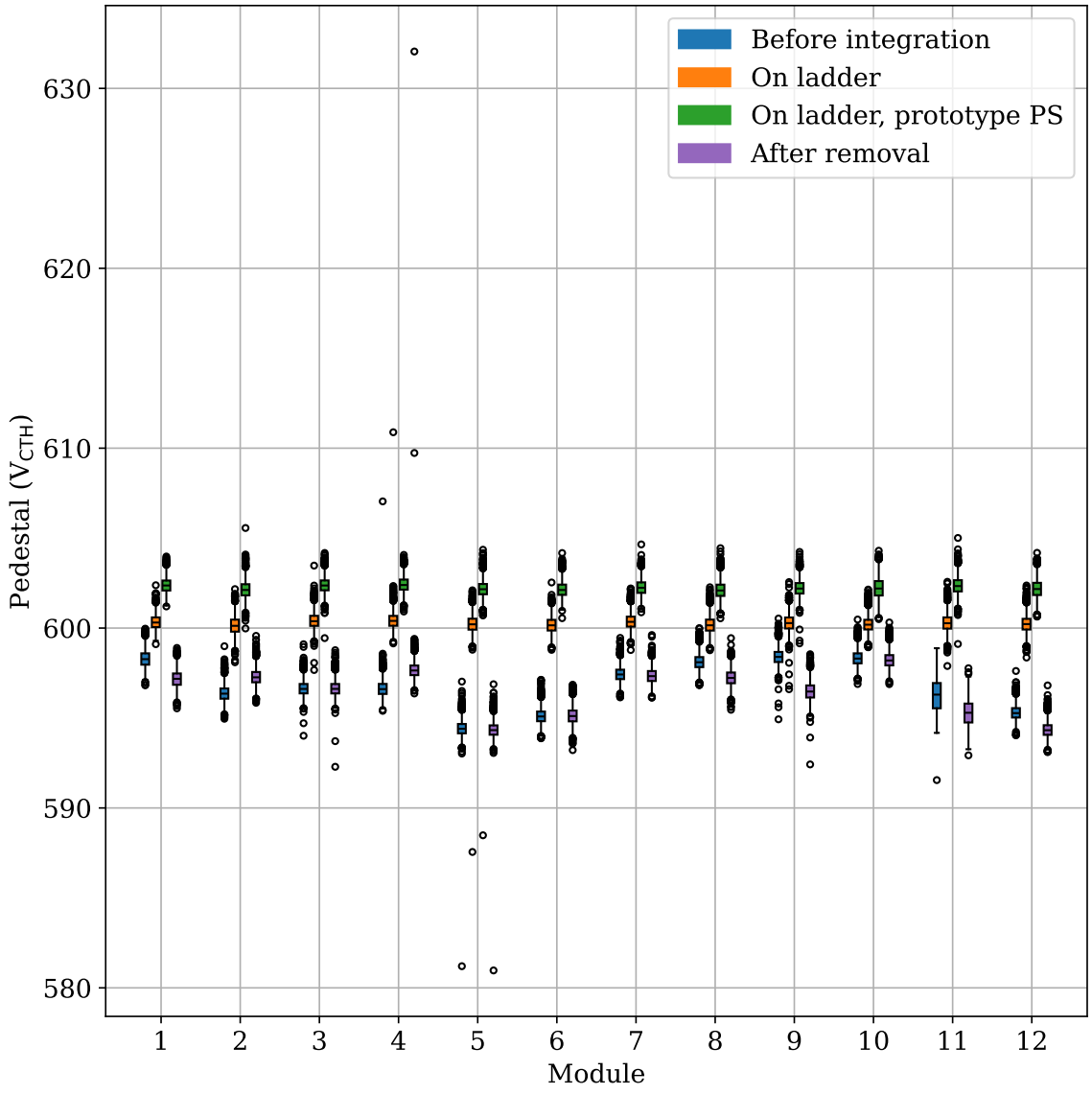

Figure G.2.: Pedestal of the 2S modules during the TB2S ladder test. The plot shows the pedestal values already shown in figure 6.21 but without any zoom of the y-axis.

G.3. Threshold Scan Results

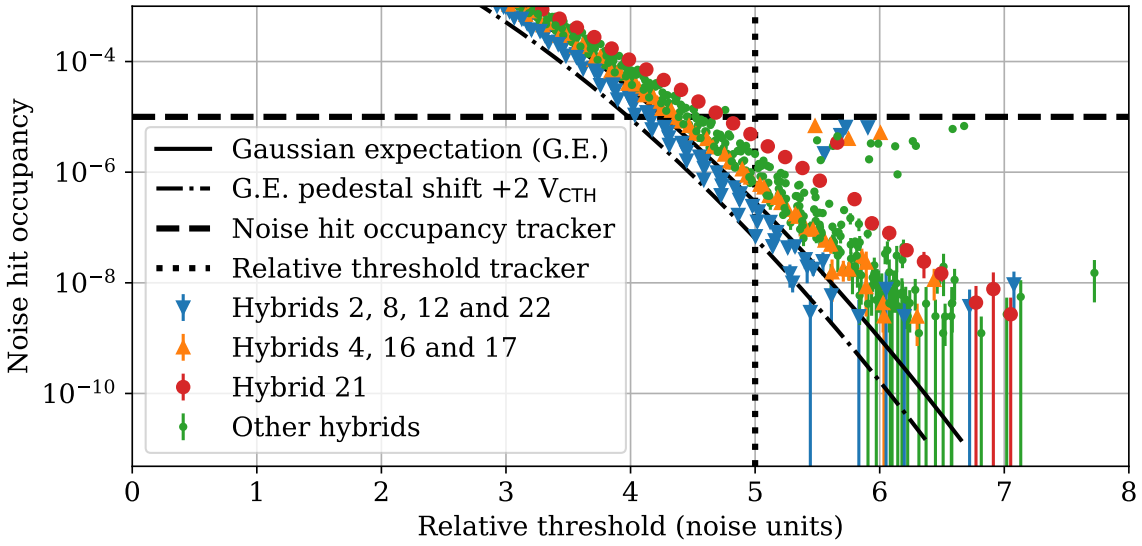

(a) 295 kHz

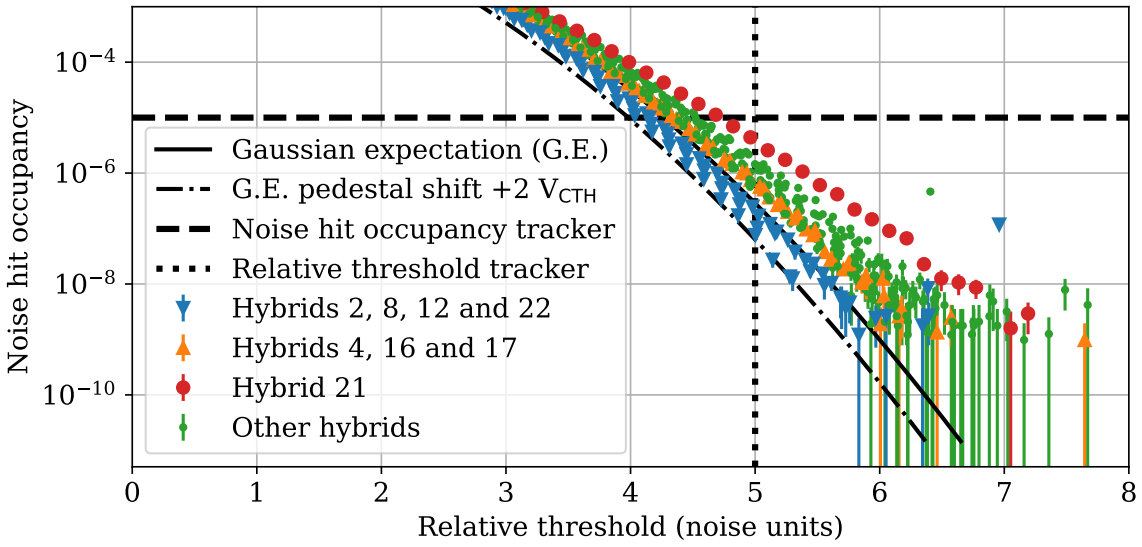

(b) 597 kHz

Figure G.3.: Noise hit occupancy of the high rate trigger threshold scan. The noise hit occupancy is plotted over the relative threshold at 295 kHz (a) and 597 kHz (b). The Gaussian expectation as well as the aimed noise hit occupancy and relative threshold of the Phase-2 Outer Tracker are indicated in the plot as well. The two noisy channels of each of the hybrids 4, 16 and 17 are masked during the analysis. With the masking the noise hit occupancy of that hybrids is also below the aimed 10^{-5} at a relative threshold of $5\,\sigma$.

G.4. Common Mode Noise and Crosstalk

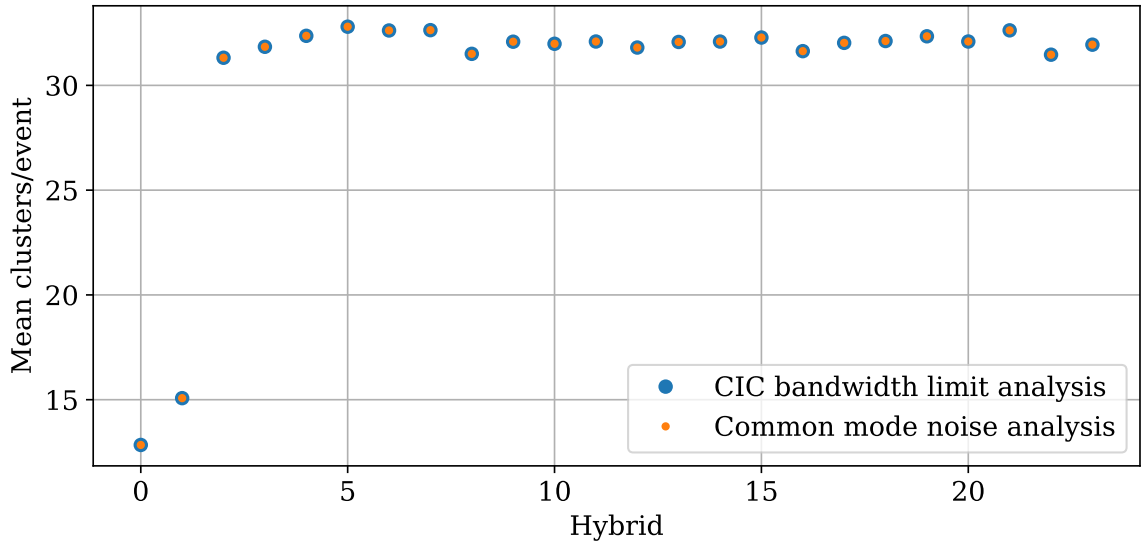

(a) $589\,V_{CTH}$

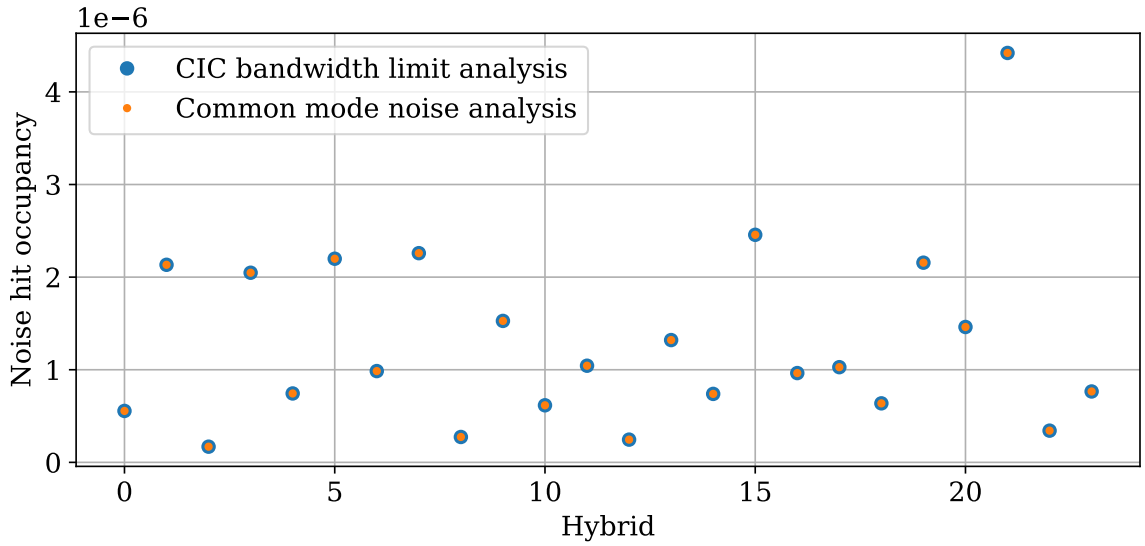

(b) $5\,\sigma$

Figure G.4.: Comparison of the CIC bandwidth and common mode noise analysis. (a) The mean number of clusters per event at a threshold of $589\,V_{CTH}$ is shown for the 24 hybrids of the twelve 2S on the fully populated TB2S ladder. (b) The noise hit occupancy at a threshold of $5\,\sigma$ is shown for the 24 hybrids. (a) + (b) The results of the CIC bandwidth limit analysis (see section 6.2.4) and the common mode noise analysis (see section 6.2.5) show the expected agreement.

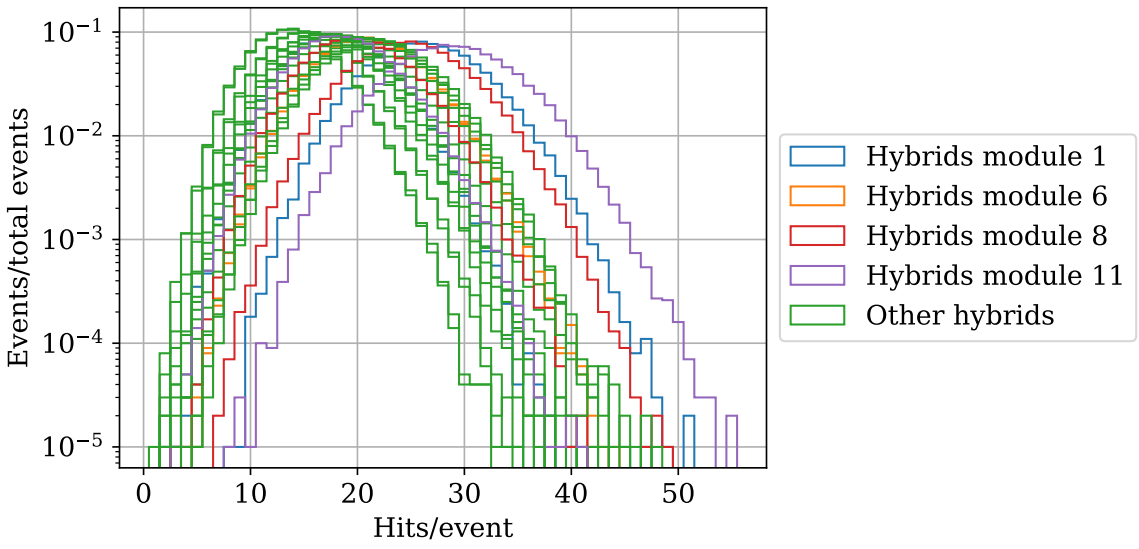

(a) $589\,\mathrm{V_{CTH}}$

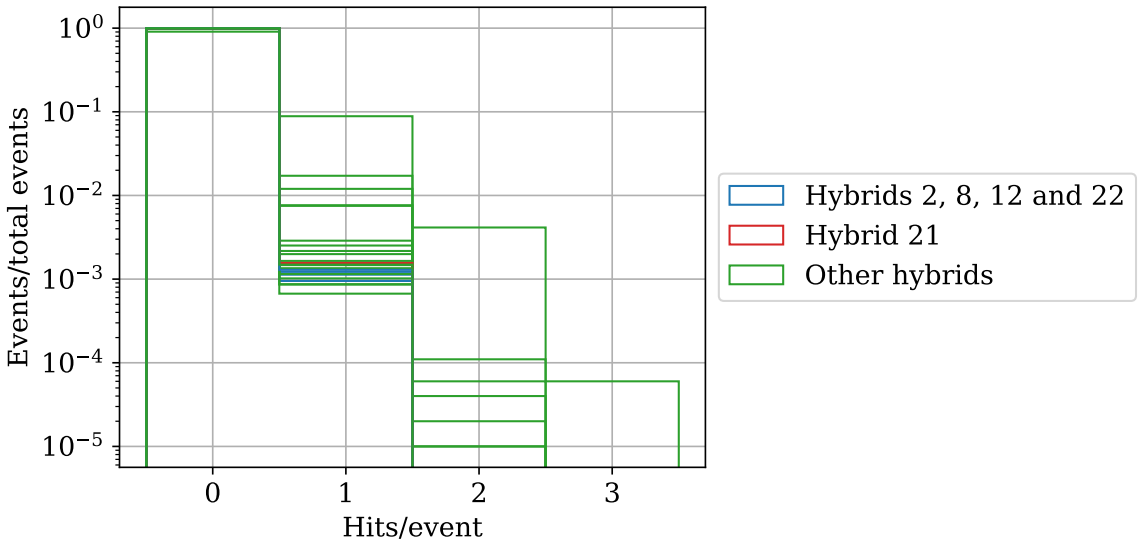

(b) $5\,\sigma$

Figure G.5.: Expectation of the number of hits per event and hybrid. The number of hits per event was simulated for a threshold of $589\,\mathrm{V_{CTH}}$ (a) and a relative threshold of $5\,\sigma$ (b) and the noise and pedestal values of all strips measured during the noise measurements presented in section 6.2.3.

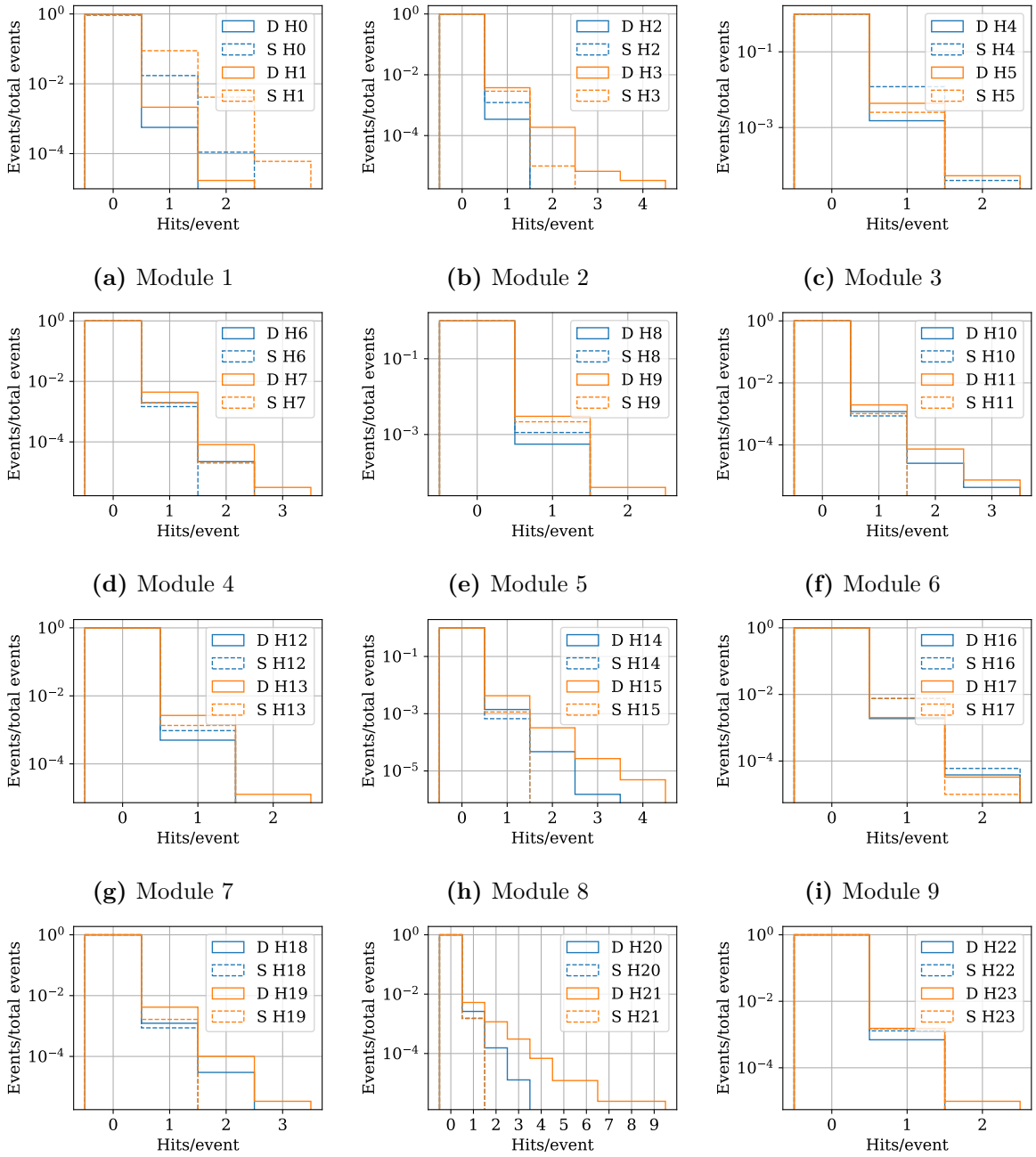

(a) Module 1 **(b)** Module 2 **(c)** Module 3

(d) Module 4 **(e)** Module 5 **(f)** Module 6

(g) Module 7 **(h)** Module 8 **(i)** Module 9

(j) Module 10 **(k)** Module 11 **(l)** Module 12

Figure G.6.: Comparison of data and simulation per hybrid. The data (label "D") and simulation (label "S") are shown separately for each hybrid sorted by the modules they belong to.

List of Figures

List of Tables

Bibliography

[Ada+17] W. Adam et al. *P-Type Silicon Strip Sensors for the new CMS Tracker at HL-LHC*. In: Journal of Instrumentation 12.06 (June 2017), P06018. DOI: 10.1088/1748-0221/12/06/P06018 (cited on p. 10).

[Ada+21a] W. Adam et al. *Selection of the silicon sensor thickness for the Phase-2 upgrade of the CMS Outer Tracker*. In: Journal of Instrumentation 16.11 (June 2021), P11028. DOI: 10.1088/1748-0221/16/11/p11028 (cited on p. 16).

[Ada+21b] W. Adam et al. *The CMS Phase-1 pixel detector upgrade*. In: Journal of Instrumentation 16.02 (Feb. 2021), P02027. DOI: 10.1088/1748-0221/16/02/P02027 (cited on pp. 10, 64).

[Ago+03] S. Agostinelli et al. *Geant4—a simulation toolkit*. In: Nuclear Instruments and Methods in Physics Research Section A: Accelerators, Spectrometers, Detectors and Associated Equipment 506.3 (2003), pp. 250–303. ISSN: 0168-9002. DOI: https://doi.org/10.1016/S0168-9002(03)01368-8 (cited on p. 53).

[Apl+12] S. Aplin et al. *LCIO: A persistency framework and event data model for HEP*. In: *2012 IEEE Nuclear Science Symposium and Medical Imaging Conference Record (NSS/MIC)*. 2012, pp. 2075–2079. DOI: 10.1109/NSSMIC.2012.6551478 (cited on p. 66).

[Apo+17] G. Apollinari et al. *High-Luminosity Large Hadron Collider (HL-LHC): Technical Design Report V. 0.1*. Geneva, 2017. DOI: 10.23731/CYRM-2017-004 (cited on p. 8).

[ATL12] ATLAS Collaboration. *Observation of a new particle in the search for the Standard Model Higgs boson with the ATLAS detector at the LHC*. In: Physics Letters B 716.1 (Sept. 2012), pp. 1–29. DOI: 10.1016/j.physletb.2012.08.020 (cited on pp. 3, 5).

[Bal24] Ball, A. and Contardo, D. *New paradigms for the CMS Phase-2 Upgrades*. 2024. URL: https://cms.cern/news/new-paradigms-cms-phase-2-upgrades (visited on 09/06/2024) (cited on p. 8).

[Bau+09] J. Baudot et al. *First test results Of MIMOSA-26, a fast CMOS sensor with integrated zero suppression and digitized output*. In: *2009 IEEE Nuclear Science Symposium Conference Record (NSS/MIC)*. 2009, pp. 1169–1173. DOI: 10.1109/NSSMIC.2009.5402399 (cited on p. 64).

[BCG19] P. Baesso, D. Cussans, and J. Goldstein. *The AIDA-2020 TLU: a flexible trigger logic unit for test beam facilities*. In: Journal of Instrumentation 14.09 (Sept. 2019), P09019. DOI: 10.1088/1748-0221/14/09/P09019 (cited on p. 64).

[Ber+19] T. Bergauer et al. *History, status and prospects of producing silicon sensors for HEP experiments at Infineon Technologies*. In: Nuclear Instruments and Methods in Physics Research Section A: Accelerators, Spectrometers, Detectors and Associated Equipment 924 (2019). 11th International Hiroshima Symposium on Development and Application of Semiconductor Tracking Detectors, pp. 1–6. ISSN: 0168-9002. DOI: https://doi.org/10.1016/j.nima.2018.06.069 (cited on p. 22).

[Ber+24] G. Bergamin et al. *CIC2.1 Technical Specification*. Limited access. 2024. URL: https://edms.cern.ch/document/2797497/1 (visited on 01/24/2025) (cited on pp. 29, 31, 33, 106).

[Bil16] B. Bilki. *CMS Forward Calorimeters Phase II Upgrade*. Tech. rep. Geneva: CERN, 2016. DOI: 10.1109/NSSMIC.2014.7431116 (cited on p. 11).

[Bis+20] T. Bisanz et al. *EUTelescope: A modular reconstruction framework for beam telescope data*. In: Journal of Instrumentation 15.09 (Sept. 2020), P09020–P09020. ISSN: 1748-0221. DOI: 10.1088/1748-0221/15/09/p09020 (cited on p. 66).

[Bla12] J. Blanchard. *A Measurement of the Angular Distribution of Cosmic Muons*. 2012. URL: https://www.physics.mcgill.ca/~francois/projects/spark/Reports/201209_blanchard_spark.pdf (visited on 12/20/2024) (cited on p. 55).

[Blo07] V. Blobel. *Millepede II - Linear Least Squares Fits with a Large Number of Parameters*. 2007. URL: http://www.desy.de/~blobel/Mptwo.pdf (cited on p. 67).

[Bro24] C. Brown. *CMS Level-1 Track Finder for the Phase-2 Upgrade*. In: PoS VERTEX2023 (2024), p. 022. DOI: 10.22323/1.448.0022 (cited on p. 13).

[Bru+97] R. Brun et al. *ROOT — An object oriented data analysis framework*. In: Nuclear Instruments and Methods in Physics Research Section A: Accelerators, Spectrometers, Detectors and Associated Equipment 389.1 (1997). New Computing Techniques in Physics Research V, pp. 81–86. ISSN: 0168-9002. DOI: https://doi.org/10.1016/S0168-9002(97)00048-X (cited on pp. 66, 67).

[BWL23] E. van der Bij, T. Wlostowski, and M. Lipinski. *fmc-dio-5chttla FMC 5-channel Digital I/O module*. 2023. URL: https://ohwr.org/project/fmc-dio-5chttla/wikis/home (visited on 01/08/2025) (cited on p. 34).

[CAE24] CAEN S.p.A. *SY5527: Universal Multichannel Power Supply System*. 2024. URL: https://www.caen.it/products/sy5527/ (visited on 09/05/2024) (cited on p. 99).

[CEB23] CEBEA. *MARTA (Monoblock Approach for a Refrigeration Technical Application)*. 2023. URL: https://cebeabochnia.pl/martac02/ (visited on 09/10/2024) (cited on p. 120).

[CER20] CERN. *RD-53 Collaboration Home*. 2020. URL: https://rd53.web.cern.ch/ (visited on 01/14/2025) (cited on p. 8).

[CER22] CERN. *bPOL2V5_V3.3 Radiation tolerant Synchronous Step-Down Buck DC/DC converter*. 2022. URL: https://power-distribution.web.cern.ch/assets/datasheets/bPOL2V5_V3.3%20datasheet%20rev3.pdf (visited on 01/05/2025) (cited on pp. 34, 37).

[CER24a] CERN. *bPOL12V_V6 Radiation tolerant 10W Synchronous Step-Down Buck DC/DC converter*. 2024. URL: https://power-distribution.web.cern.ch/assets/datasheets/bPOL12V_V6%20datasheet%20V1.9.pdf (visited on 01/05/2025) (cited on pp. 34, 37).

[CER24b] CERN. *TRACI II*. 2024. URL: https://ep-dep-dt.web.cern.ch/co2-cooling-plants/traci-geneva (visited on 11/15/2024) (cited on p. 80).

[CER25] CERN. *The HL-LHC project*. 2025. URL: https://hilumilhc.web.cern.ch/content/hl-lhc-project (visited on 01/31/2025) (cited on p. 7).

[Chi13] A. Chilingarov. *Temperature dependence of the current generated in Si bulk*. In: Journal of Instrumentation 8.10 (Oct. 2013), P10003–P10003. DOI: 10.1088/1748-0221/8/10/p10003 (cited on p. 25).

[CMS12a] CMS Collaboration. *CMS Technical Design Report for the Pixel Detector Upgrade*. Tech. rep. CERN-LHCC-2012-016. CMS-TDR-11. CERN, 2012. URL: https://cds.cern.ch/record/1481838 (cited on p. 10).

[CMS12b] CMS Collaboration. *Observation of a new boson at a mass of 125 GeV with the CMS experiment at the LHC*. In: Physics Letters B 716.1 (2012), pp. 30–61. DOI: 10.1016/j.physletb.2012.08.021 (cited on pp. 3, 5).

[CMS14] CMS Collaboration. *Alignment of the CMS tracker with LHC and cosmic ray data*. In: Journal of Instrumentation 9.06 (June 2014), P06009–P06009. ISSN: 1748-0221. DOI: 10.1088/1748-0221/9/06/p06009 (cited on p. 62).

[CMS17a] CMS Collaboration. *The CMS trigger system*. In: Journal of Instrumentation 12.01 (2017), P01020. DOI: 10.1088/1748-0221/12/01/p01020 (cited on p. 13).

[CMS17b] CMS Collaboration. *The Phase-2 Upgrade of the CMS Barrel Calorimeters*. Tech. rep. Geneva: CERN, 2017. URL: http://cds.cern.ch/record/2283187 (cited on p. 11).

[CMS17c] CMS Collaboration. *The Phase-2 Upgrade of the CMS Endcap Calorimeter*. Tech. rep. Geneva: CERN, 2017. DOI: 10.17181/CERN.IV8M.1JY2 (cited on pp. 11, 12).

[CMS17d] CMS Collaboration. *The Phase-2 Upgrade of the CMS Level-1 Trigger Interim Technical Design Report*. Tech. rep. CERN-LHCC-2017-013. CMS-TDR-017. Geneva: CERN, 2017. URL: https://cds.cern.ch/record/2283192 (cited on p. 13).

[CMS17e] CMS Collaboration. *The Phase-2 Upgrade of the CMS Muon Detectors*. Tech. rep. Geneva: CERN, 2017. URL: https://cds.cern.ch/record/2283189 (cited on pp. 13, 14).

[CMS17f] CMS Collaboration. *The Phase-2 Upgrade of the CMS Tracker*. Tech. rep. Geneva: CERN, June 2017. DOI: 10.17181/CERN.QZ28.FLHW (cited on pp. 10, 16–18, 21, 22, 25, 70, 85, 110, 117).

[CMS19] CMS Collaboration. *A MIP Timing Detector for the CMS Phase-2 Upgrade*. Tech. rep. Geneva: CERN, 2019. URL: https://cds.cern.ch/record/2667167 (cited on p. 11).

[CMS24a] CMS Collaboration. *CMS Tracker Phase2 Acquisition & Control Framework*. 2024. URL: https://gitlab.cern.ch/cms_tk_ph2/Ph2_ACF (visited on 08/19/2024) (cited on p. 34).

[CMS24b] CMS HGCAL collaboration. *Timing performance of the CMS High Granularity Calorimeter prototype*. In: Journal of Instrumentation 19.04 (Apr. 2024), P04015. ISSN: 1748-0221. DOI: 10.1088/1748-0221/19/04/p04015 (cited on p. 11).

[CMS24c] CMS Outer Tracker Modules Working Group. *Module Assembly and Integration Flow*. Limited access. 2024. URL: https://edms.cern.ch/document/2798680/13 (visited on 01/07/2025) (cited on p. 40).

[CMS25] CMS Collaboration. *d19c-firmware*. Limited access. 2025. URL: https://gitlab.cern.ch/cms_tk_ph2/d19c-firmware (visited on 02/01/2025) (cited on p. 34).

[CS09] L. Caminada and A. Starodumov. *Building and commissioning of the CMS pixel barrel detector*. In: Journal of Instrumentation 4.03 (Mar. 2009), P03017. DOI: 10.1088/1748-0221/4/03/P03017 (cited on p. 10).

[Die+19] R. Diener et al. *The DESY II test beam facility*. In: Nuclear Instruments and Methods in Physics Research Section A: Accelerators, Spectrometers, Detectors and Associated Equipment 922 (2019), pp. 265–286. ISSN: 0168-9002. DOI: https://doi.org/10.1016/j.nima.2018.11.133 (cited on p. 64).

[Dig14] Digilent/AVNET. *ZedBoard (Zynq Evaluation and Development) Hardware User's Guide*. Version Version 2.2. 2014. URL: https://files.digilent.com/resources/programmable-logic/zedboard/ZedBoard_HW_UG_v2_2.pdf (visited on 12/16/2024) (cited on p. 53).

[DM24] A. Dierlamm and S. Maier. *Kickoff modules noise summary plots approval*. Limited access. 2024. URL: https://indico.cern.ch/event/1441644/#2-kickoff-modules-noise-summar (visited on 02/24/2025) (cited on pp. 48, 49).

[Dro21] A. Droll. *Performance Studies on 2S Module Prototypes for the Phase-2 Upgrade of the CMS Outer Tracker*. PhD thesis. Karlsruhe Institute of Technology (KIT), 2021. URL: https://publish.etp.kit.edu/record/22088 (cited on pp. 32, 106, 119).

[Fer+05] A. Ferrari et al. *FLUKA: A Multi-Particle Transport Code*. Tech. rep. SLAC National Accelerator Lab., Menlo Park, CA (United States), Dec. 2005. DOI: 10.2172/877507 (cited on p. 21).

[FHE15] FHEM e.V. *1-Wire Feuchtemessung*. 2015. URL: https://wiki.fhem.de/wiki/1-Wire_Feuchtemessung (visited on 01/29/2025) (cited on pp. 80, 151).

[FK21] R. Fabio and D. Karri. *Report about I2C patch for 2S Modules*. Limited access. 2021. URL: https://indico.cern.ch/event/1043642/#4-report-about-i2c-patch-for-2 (visited on 01/05/2025) (cited on p. 37).

[Gos24] F. Gostner. *An FPGA-Based Trigger System for Lab Exercises in Experimental Particle Physics*. Bachelor's thesis. Karlsruhe Institute of Technology (KIT), 2024. URL: https://publish.etp.kit.edu/record/22247 (cited on p. 53).

[Har17] F. Hartmann. *Evolution of Silicon Sensor Technology in Particle Physics*. 2nd ed. Springer, Nov. 3, 2017. ISBN: 978-3-319-64434-9. DOI: 10.1007/978-3-319-64436-3 (cited on pp. 23, 24, 71).

[Haz+13] E. Hazen et al. *The AMC13XG: a new generation clock/timing/DAQ module for CMS MicroTCA*. In: Journal of Instrumentation 8 (Dec. 2013), pp. C12036–C12036. DOI: 10.1088/1748-0221/8/12/C12036 (cited on pp. 34, 100).

[Haz22] Hazen, Eric. *AMC13Tool2*. 2022. URL: https://bucms.bu.edu//twiki/bin/view/BUCMSPublic/AMC13Tool2 (visited on 08/26/2024) (cited on p. 100).

[Hei+23] U. Heintz et al. *QC Document*. Limited access. 2023. URL: https://edms.cern.ch/document/2915025/1 (visited on 03/11/2025) (cited on p. 103).

[Her00] A. Hervé. *The CMS detector magnet*. In: IEEE Trans. Appl. Supercond. 10.1 (2000), pp. 389–94. DOI: 10.1109/77.828255 (cited on p. 8).

[HM06] W. Herr and B. Muratori. *Concept of luminosity*. In: (2006). DOI: 10.5170/CERN-2006-002.361 (cited on p. 7).

[HRM22] A. Honma, A. L. Rosa, and A. Mussgiller. *2S Module Specifications*. Limited access. 2022. URL: https://edms.cern.ch/document/2642509/3 (visited on 03/27/2025) (cited on p. 57).

[HT24] J. Hegeman and J. Troska. *Documentation of the post-LS1 Trigger Distribution and Control System for CMS*. Limited access. 2024. URL: https://twiki.cern.ch/twiki/bin/viewauth/CMS/TcdsNotes (visited on 01/21/2025) (cited on p. 100).

[Hub24] L. Huber. *Common Mode Noise Analysis of 2S Modules for the CMS Phase-2 Outer Tracker Upgrade*. Bachelor's thesis. Karlsruhe Institute of Technology (KIT), 2024. URL: https://publish.etp.kit.edu/record/22301 (cited on pp. 110, 112, 113).

[Kat+23] R. Kataria et al. *Muon flux measurements and their angular distribution with the new muon telescope at GRAPES-3 experiment*. In: PoS ICRC2023 (2023), p. 1361. DOI: 10.22323/1.444.1361 (cited on p. 54).

[Kle12] C. Kleinwort. *General broken lines as advanced track fitting method*. In: Nuclear Instruments and Methods in Physics Research Section A: Accelerators, Spectrometers, Detectors and Associated Equipment 673 (2012), pp. 107–110. DOI: 10.1016/j.nima.2012.01.024 (cited on p. 67).

[Kop22] R. Koppenhöfer. *Noise and Detection Efficiency Studies on Full-Size 2S Module Prototypes for the Phase-2 Upgrade of the CMS Experiment*. PhD thesis. Karlsruhe Institute of Technology (KIT), 2022. URL: https://publish.etp.kit.edu/record/22134 (cited on pp. 23, 37, 39, 45, 57, 60, 66, 68, 70–72, 76, 105).

[Kov+23] M. Kovacs et al. *2S-SEH designs for kickoff*. Limited access. 2023. URL: https://indico.cern.ch/event/1247868/#16-2s-seh-kick-off-designs (visited on 01/06/2025) (cited on p. 38).

[Liu+19] Y. Liu et al. *EUDAQ2—A flexible data acquisition software framework for common test beams*. In: Journal of Instrumentation 14.10 (Oct. 2019), P10033–P10033. DOI: 10.1088/1748-0221/14/10/p10033 (cited on p. 64).

[Lop22] E. Lopienska. *The CERN accelerator complex, layout in 2022. Complexe des accélérateurs du CERN en janvier 2022*. In: (2022). General Photo. URL: https://cds.cern.ch/record/2800984 (cited on p. 6).

[lpG22] lpGBT Design Team. *lpGBT Manual*. 2022. URL: https://lpgbt.web.cern.ch/lpgbt/v0/ (visited on 01/05/2025) (cited on p. 37).

[lpG24] lpGBT Design Team. *lpGBTv1 Manual*. 2024. URL: https://lpgbt.web.cern.ch/lpgbt/v1/ (visited on 01/05/2025) (cited on p. 37).

[Mag24] G. Magazzù. *Update on FC7 firmware: FW for test with multiple modules*. Limited access. 2024. URL: https://indico.cern.ch/event/1369971/#6-update-on-fc7-firmware (visited on 02/25/2025) (cited on pp. 51, 52, 140).

[Mai19] S. Maier. *Assembly and qualification procedures of 2S modules and high rate tests of the CMS Binary Chip for the Phase 2 Upgrade of the CMS Outer Tracker*. PhD thesis. Karlsruhe Institute of Technology (KIT), 2019. URL: https://publish.etp.kit.edu/record/21941 (cited on pp. 35, 39, 48, 71, 72, 103, 115).

[Mol99] M. Moll. *Radiation Damage in Silicon Particle Detectors*. PhD thesis. Universtiy of Hamburg, 1999. URL: https://mmoll.web.cern.ch/thesis/ (cited on p. 25).

[Mor+24] P. Moreira et al. *lpGBT: Low-power radiation-hard multipurpose high-speed transceiver ASIC for high-energy physics experiments*. In: IEEE Transactions on Nuclear Science (2024), pp. 1–1. DOI: 10.1109/TNS.2024.3506753 (cited on pp. 32, 37).

[Mou25a] Mouser Electronics. *DS2438Z+*. 2025. URL: https://www.mouser.de/ProductDetail/Analog-Devices-Maxim-Integrated/DS2438Z%2b?qs=0Y9aZN%252BMVCXYzd1djJeYaw%3D%3D (visited on 01/29/2025) (cited on pp. 80, 151).

[Mou25b] Mouser Electronics. *HIH-4030-001*. 2025. URL: https://www.mouser.de/ProductDetail/Honeywell/HIH-4030-001?qs=yJVtgANCw00QC6hykt%252Ba7w%3D%3D (visited on 01/29/2025) (cited on pp. 80, 151).

[Mur+16] F. Murphy-Armando et al. *Mind the drain from strain: Effects of strain on the leakage current of Si diodes*. In: *2016 13th IEEE International Conference on Solid-State and Integrated Circuit Technology (ICSICT)*. 2016, pp. 802–804. DOI: 10.1109/ICSICT.2016.7999046 (cited on pp. 24, 25).

[Ola+20] L. Olantera et al. *Versatile Link+ Transceiver Production Readiness*. In: PoS TWEPP2019 (2020), p. 055. DOI: 10.22323/1.370.0055 (cited on pp. 32, 37).

[Orf20] S. Orfanelli. *The Phase 2 Upgrade of the CMS Inner Tracker*. Tech. rep. Geneva: CERN, 2020. DOI: 10.1016/j.nima.2020.164396 (cited on p. 10).

[Pau24] A. Pauls. *Development and Implementation of Test Infrastructure and its Application during the Development and Prototyping of Service Hybrids for the Phase-2 Upgrade of the CMS Outer Tracker*. PhD thesis. RWTH Aachen University, 2024. DOI: 10.18154/RWTH-2024-11777 (cited on pp. 32, 38, 46, 48).

[Pes+15] M. Pesaresi et al. *The FC7 AMC for generic DAQ & control applications in CMS*. In: Journal of Instrumentation 10.03 (Mar. 2015), p. C03036. DOI: 10.1088/1748-0221/10/03/C03036 (cited on p. 34).

[PIC25a] PICMG. *MicroTCA Overview*. 2025. URL: https://www.picmg.org/openstandards/microtca/ (visited on 02/20/2025) (cited on p. 34).

[PIC25b] PICMG. *VT895*. 2025. URL: https://www.picmg.org/spec-product/vt895/ (visited on 02/20/2025) (cited on p. 34).

[Pry19] M. Prydderch. *CBC3.1 user Manual*. 2019. URL: http://www.hep.ph.ic.ac.uk/ASIC/CBC_documentation/CBC3p1_User_Manual_V1p4.pdf (cited on pp. 27, 30, 31).

[Ras24] D. Rastorguev. *Test-beam qualification of the PS modules for the CMS Phase-2 Outer Tracker*. 2024. URL: https://indico.cern.ch/event/1323113/contributions/5823797/ (visited on 10/21/2024) (cited on p. 64).

[Rau20] M. P. Rauch. *Thermal Measurements and Characterizations for the CMS Phase-1 Barrel Pixel Detector and the CMS Phase-2 Upgrade Tracker 2S Module with Evaporative CO_2 Cooling Systems*. Presented on 20 May 2020. RWTH Aachen U., 2020. URL: https://cds.cern.ch/record/2740861 (cited on p. 87).

[Rav25] F. Ravera. *CIC output data format*. private communication. 2025 (cited on p. 106).

[Ros+19] A. W. Rose et al. *Serenity: An ATCA prototyping platform for CMS Phase-2*. In: PoS TWEPP2018 (2019), p. 115. DOI: 10.22323/1.343.0115 (cited on p. 34).

[Ros03] L. Rossi. *The LHC Main Dipoles and Quadrupoles Toward Series Production*. In: IEEE Transactions on Applied Superconductivity 13.2 (2003), pp. 1221–1228. DOI: 10.1109/TASC.2003.812639 (cited on p. 7).

[Sak19] T. Sakuma. *Cutaway diagrams of CMS detector*. In: (2019). URL: https://cds.cern.ch/record/2665537 (visited on 09/06/2024) (cited on p. 9).

[Shv25] I. Shvetsov. *Environmental conditions in the CMS tracker*. private communication. 2025 (cited on p. 94).

[Ski24] L. Skinnari. *Impact of module losses on L1 tracking performance*. Limited access. 2024. URL: https://indico.cern.ch/event/1484072/#8-impact-of-module-losses-on-l (visited on 02/14/2025) (cited on p. 110).

[Sto21] L. Stockmeier. *Laboratory and Integration Tests with 2S Module Prototypes for the Phase-2 Upgrade of the CMS Outer Tracker*. Master's thesis. Karlsruhe Institute of Technology (KIT), 2021. URL: https://publish.etp.kit.edu/record/22070 (cited on pp. 16, 53, 57, 59).

[Sto23] L. Stockmeier. *Integration Tests with 2S Module Prototypes for the Phase-2 Upgrade of the CMS Outer Tracker*. 2023. URL: https://indico.tlabs.ac.za/event/112/contributions/2798/ (visited on 11/26/2024) (cited on p. 94).

[Sto25] L. Stockmeier. *Integration Tests with 2S Module Prototypes for the Phase-2 Upgrade of the CMS Outer Tracker*. In: *Proceedings of Technology & Instrumentation in Particle Physics — PoS(TIPP2023)*. Vol. 468. 2025, p. 066. DOI: 10.22323/1.468.0066 (cited on p. 94).

[Ter24] J. Terörde. *Untersuchung von korreliertem Rauschen in 2S-Siliziumstreifenmodulen für das CMS Phase-2 Tracker Upgrade*. Bachelor's thesis. RWTH Aachen University, 2024. URL: https://cds.cern.ch/record/2926441 (cited on p. 112).

[tkL23] tkLayout developers. *OT801_IT701 layouts*. 2023. URL: https://cms-tklayout.web.cern.ch/cms-tklayout/layouts/recent-layouts/OT801_IT701/ (visited on 09/10/2024) (cited on pp. 10, 21, 82, 83).

[Tor22] M. Tornago. *The CMS MTD Endcap Timing Layer: Precision Timing with Low Gain Avalanche Detectors*. In: PoS ICHEP2022 (2022), p. 650. DOI: 10.22323/1.414.0650 (cited on p. 13).

[Tur22] C. Turrioni. *Thermal Performance Analysis and optimizations of systems and components for the CMS Phase-2 Tracker Upgrade*. PhD thesis. Università degli Studi di Perugia, 2022 (cited on pp. 85–87, 90–92, 94, 128, 154, 155).

[Var00] J. Varela. *Timing and synchronization in the LHC experiments*. Tech. rep. Geneva: CERN, 2000. DOI: 10.5170/CERN-2000-010.77 (cited on p. 100).

[Var02] J. Varela. *CMS L1 Trigger Control System*. Tech. rep. Geneva: CERN, 2002. URL: http://cds.cern.ch/record/687458 (cited on p. 100).

[Ven25] A. Ventura Barroso. *From detectors to data: Thermal Characterization of CMS Outer Tracker Modules and Measurement of the top quark mass using $t\bar{t}$+jet events*. Dissertation, Bergische Universität Wuppertal, 2025. Dissertation. Hamburg: Bergische Universität Wuppertal, 2025, p. 248. DOI: 10.3204/PUBDB-2025-00758 (cited on pp. 119, 122).

[Vir+22] S. Viret et al. *CIC2: a radiation tolerant 65 nm data aggregation ASIC for the future CMS tracker*. In: JINST 17.05 (2022), p. C05016. DOI: 10.1088/1748-0221/17/05/C05016 (cited on p. 37).

[Wit23] F. Wittig. *Qualification of Silicon Sensors for the Phase-2 Upgrade of the CMS Outer Tracker*. PhD thesis. Karlsruhe Institute of Technology (KIT), 2023. URL: https://publish.etp.kit.edu/record/22194 (cited on pp. 24, 25, 57, 60, 64, 82, 122).

[Yoh20] R. Yohay. *The CMS High Granularity Calorimeter for High Luminosity LHC*. In: Nuclear Instruments and Methods in Physics Research Section A: Accelerators, Spectrometers, Detectors and Associated Equipment 958 (2020). Proceedings of the Vienna Conference on Instrumentation 2019, p. 162151. ISSN: 0168-9002. DOI: https://doi.org/10.1016/j.nima.2019.04.105 (cited on p. 12).

[ZAG24] ZAG Zyklotron AG. *ZAG Zyklotron AG: Radioisotope für Technik und Medizin.* 2024. URL: `https://www.zyklotron-ag.de/` (visited on 11/15/2024) (cited on p. 80).

[Zog+22] A. Zografos et al. *CMS Outer Tracker Phase-2 Upgrade module noise and mitigation.* In: Journal of Instrumentation 17.12 (Dec. 2022), p. C12008. DOI: `10.1088/1748-0221/17/12/C12008` (cited on p. 45).

Acknowledgments — Danksagung

The present work would not have been possible without the support of many people, to whom I express my greatest thanks! Die vorliegende Arbeit wäre ohne die Unterstützung zahlreicher Mitmenschen nicht möglich gewesen. Euch möchte ich an dieser Stelle meinen aufrichtigen Dank aussprechen.

Zuallererst möchte ich Prof. Dr. Ulrich Husemann für die Möglichkeit, meine Promotion am Institut für Experimentelle Teilchenphysik durchzuführen, danken. Bei Fragen und Anliegen stand er immer direkt und sehr hilfreich zur Verfügung.
Außerdem danke ich Prof. Dr. Thomas Müller für die Übernahme des Korreferats und dass er mich nach der Bachelorprüfung für die Bachelorarbeit ans ETP holte.

Bei Dr. Alexander Dierlamm und Dr. Stefan Maier bedanke ich mich für die wunderbare Betreuung während der Promotionszeit.
Dr. Alexander Dierlamm danke ich insbesondere für das gründliche Korrekturlesen dieser Arbeit in einem sehr frühen Stadium, sodass die dabei entstandenen Diskussionen die Ergebnisse umso tiefer haben werden lassen.
Bei Dr. Stefan Maier bedanke ich mich dafür, dass er mich auf die ersten Messkampagnen begleitet hat und ich dadurch lernen konnte, wie man effektiv unter Stress und Zeitdruck arbeiten kann.

Auch Dr. Roland Koppenhöfer möchte ich einen gesonderten Dank aussprechen. Er hat mich bereits während der Masterarbeit hervorragend betreut und stand auch nach seiner Zeit bei uns am ETP immer für Fragen jeglicher Form zur Verfügung. Ich hoffe, dass diese Arbeit den “Roland approves”-Stempel erhalten wird.

Special thanks go to Dr. Cristiano Turrioni for the thermal simulations matching my measurement conditions.

Guido Magazzù, Dr. Fabio Ravera and Dr. Sarah Seif El Nasr-Storey, thank you for making the multi-module readout possible!

Allen Korrekturlesenden, Dr. Alexander Dierlamm, Dr. Frank Hartmann, Dr. Roland Koppenhöfer, Guido Magazzù, Dr. Stefan Maier und Dr. Brendan Regnery, möchte ich an dieser Stelle meinen Dank aussprechen.

Bärbel Bräunling, Peichen Chen und Diana Fellner möchte ich für die Hilfe bei allen administrativen Angelegenheiten danken.

I would like to thank all the colleagues from the different groups that I worked together with during the integration and beam tests.

From IPHC, Strasbourg: Dr. Jérémy Andrea, Dr. Saskia Falke and Clément Haas.

From DESY, Hamburg: Dr. Moritz Guthoff, Dr. Andreas Nürnberg, Daniil Rastorguev, Oskar Reichelt, Dr. Paul Schütze, Anastasiia Velyka and Ana Ventura.

From CERN: Pier Filippo Cianchetta and Dr. Giovanni Zevi Della Porta.

From KIT: Lorenzo Asfour, Baudry Bartels, Tobias Barvich, Bernd Berger, Luc Brandl, Yi-Mu Chen, Alexander Dierlamm, Alexander Droll, Umut Elicabuk, Filipp Gostner, Leander Grimm, Lorena Hahn, Frank Hartmann, Lars Huber, Christina Klauda, Gani Kösker, Roland Koppenhöfer, Kai Krämer, Robert Lahmann, Jay Lawhorn, Aurora Losana, Matthias Ludwig, Stefan Maier, Pietro Marchesi, Oskar Moritz, Dominik Münch, Marius Neufeld, Andreas Nürnberg, Martin Pittermann, Kristof Purpus, Niyathi Radhakrishnan, Marek Recknagel, Brendan Regnery, Waldemar Rehm, Thomas Renkhoff, Alexander Salameh, Linus Schlee, Philipp Schnitzius, Felix Schuckert, Tatiana Selezneva, Ivan Shvetsov, Leon Siebert, Andreas Siemens, Hans Jürgen Simonis, Pia Steck, Maria Toms, Bogdan Topko, Fabio Trenner, Nicolo Trevisani, Florian Wittig, Dowling Wong and Xunwu Zuo.
Ich danke euch, der Hardware-Gruppe des ETP, für die schöne Atmosphäre beim Mittagessen und in den Kaffeerunden.

Meiner Familie und meinen Freunden danke ich für die Unterstützung in allen Phasen der Schule, des Studiums und der Promotion. Gabriel Moser danke ich dafür, dass er mir den Übergang in die Schreibphase erleichtert hat.

Das allergrößte Dankeschön gilt aber meinem wundervollen Pferd Milo, der mich seit der Masterarbeit begleitet. Während der Zeiten am Stall und auf schönen Ausritten in Zweisamkeit konnte ich den Alltag immer hinter mir lassen.

Der Landesgraduiertenförderung des Landes Baden-Württemberg und der Karlsruhe School of Elementary Particle and Astroparticle Physics: Science and Technology (KSETA) möchte ich für die Unterstützung während der Promotion danken.

I acknowledge funding by the Federal ministry of Education and Research of Germany in the framework of the project "Fortführung des CMS-Experiments zum Einsatz am HL-LHC: Verbesserung des Spurdetektors für das Phase-II-Upgrade des CMS-Experiments" under the grants 05H21VKCC9 and 05H24VK9.

The measurements leading to these results have been performed at the Test Beam Facility at DESY Hamburg (Germany), a member of the Helmholtz Association (HGF).

Declaration

I declare that the work in this dissertation was carried out in accordance with the requirements of the University's Regulations and that it has not been submitted for any other academic award. Except where indicated by specific reference in the text, the work is the candidate's own work. Work done in collaboration with, or with the assistance of, others is indicated as such.

Karlsruhe, March 2025

Lea Stockmeier